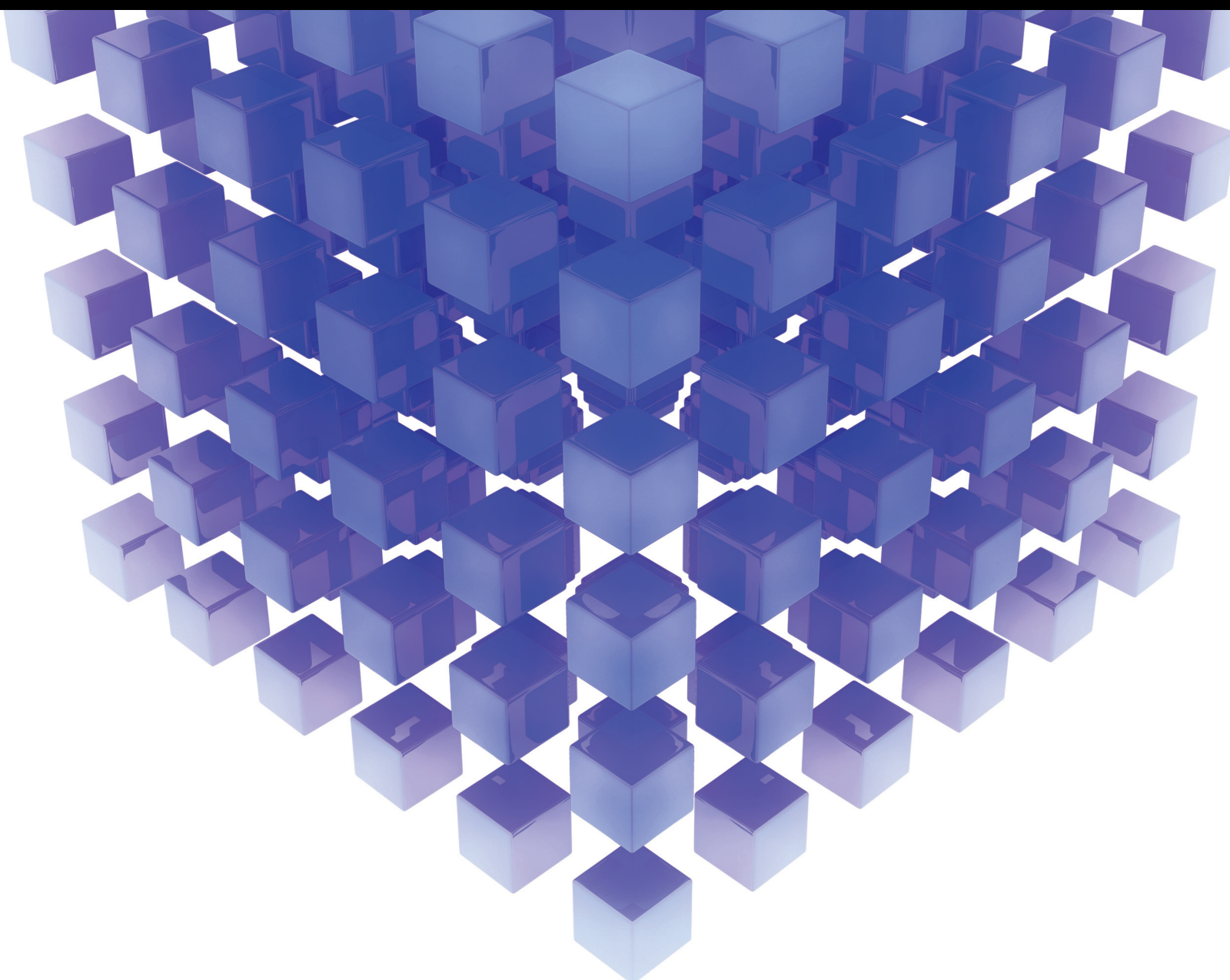


Mathematical Problems in Engineering

Advanced Theories and Methods for Computer Numerical Control Machining

Lead Guest Editor: Qiang Guo

Guest Editors: Jinting Xu, Shanglei Jiang, and Chigbogu G. Ozoegwu





Advanced Theories and Methods for Computer Numerical Control Machining

Mathematical Problems in Engineering

**Advanced Theories and Methods
for Computer Numerical Control
Machining**

Lead Guest Editor: Qiang Guo

Guest Editors: Jinting Xu, Shanglei Jiang, and
Chigbogu G. Ozoegwu



Copyright © 2021 Hindawi Limited. All rights reserved.

This is a special issue published in “Mathematical Problems in Engineering.” All articles are open access articles distributed under the Creative Commons Attribution License, which permits unrestricted use, distribution, and reproduction in any medium, provided the original work is properly cited.

Chief Editor

Guangming Xie , China

Academic Editors

Kumaravel A , India
Waqas Abbasi, Pakistan
Mohamed Abd El Aziz , Egypt
Mahmoud Abdel-Aty , Egypt
Mohammed S. Abdo, Yemen
Mohammad Yaghoub Abdollahzadeh
Jamalabadi , Republic of Korea
Rahib Abiyev , Turkey
Leonardo Acho , Spain
Daniela Addessi , Italy
Arooj Adeel , Pakistan
Waleed Adel , Egypt
Ramesh Agarwal , USA
Francesco Aggogeri , Italy
Ricardo Aguilar-Lopez , Mexico
Afaq Ahmad , Pakistan
Naveed Ahmed , Pakistan
Elias Aifantis , USA
Akif Akgul , Turkey
Tareq Al-shami , Yemen
Guido Ala, Italy
Andrea Alaimo , Italy
Reza Alam, USA
Osamah Albahri , Malaysia
Nicholas Alexander , United Kingdom
Salvatore Alfonzetti, Italy
Ghous Ali , Pakistan
Nouman Ali , Pakistan
Mohammad D. Aliyu , Canada
Juan A. Almendral , Spain
A.K. Alomari, Jordan
José Domingo Álvarez , Spain
Cláudio Alves , Portugal
Juan P. Amezcua-Sanchez, Mexico
Mukherjee Amitava, India
Lionel Amodeo, France
Sebastian Anita, Romania
Costanza Arico , Italy
Sabri Arik, Turkey
Fausto Arpino , Italy
Rashad Asharabi , Saudi Arabia
Farhad Aslani , Australia
Mohsen Asle Zaem , USA

Andrea Avanzini , Italy
Richard I. Avery , USA
Viktor Avrutin , Germany
Mohammed A. Awadallah , Malaysia
Francesco Aymerich , Italy
Sajad Azizi , Belgium
Michele Bacciocchi , Italy
Seungik Baek , USA
Khaled Bahlali, France
M.V.A Raju Bahubalendruni, India
Pedro Balaguer , Spain
P. Balasubramaniam, India
Stefan Balint , Romania
Ines Tejado Balsera , Spain
Alfonso Banos , Spain
Jerzy Baranowski , Poland
Tudor Barbu , Romania
Andrzej Bartoszewicz , Poland
Sergio Baselga , Spain
S. Caglar Baslamisli , Turkey
David Bassir , France
Chiara Bedon , Italy
Azeddine Beghdadi, France
Andriette Bekker , South Africa
Francisco Beltran-Carbajal , Mexico
Abdellatif Ben Makhlof , Saudi Arabia
Denis Benasciutti , Italy
Ivano Benedetti , Italy
Rosa M. Benito , Spain
Elena Benvenuti , Italy
Giovanni Berselli, Italy
Michele Betti , Italy
Pietro Bia , Italy
Carlo Bianca , France
Simone Bianco , Italy
Vincenzo Bianco, Italy
Vittorio Bianco, Italy
David Bigaud , France
Sardar Muhammad Bilal , Pakistan
Antonio Bilotta , Italy
Sylvio R. Bistafa, Brazil
Chiara Boccaletti , Italy
Rodolfo Bontempo , Italy
Alberto Borboni , Italy
Marco Bortolini, Italy

Paolo Boscariol, Italy
Daniela Boso , Italy
Guillermo Botella-Juan, Spain
Abdesselem Boulkroune , Algeria
Boulaïd Boulkroune, Belgium
Fabio Bovenga , Italy
Francesco Braghin , Italy
Ricardo Branco, Portugal
Julien Bruchon , France
Matteo Bruggi , Italy
Michele Brun , Italy
Maria Elena Bruni, Italy
Maria Angela Butturi , Italy
Bartłomiej Błachowski , Poland
Dhanamjayulu C , India
Raquel Caballero-Águila , Spain
Filippo Cacace , Italy
Salvatore Caddemi , Italy
Zuowei Cai , China
Roberto Caldelli , Italy
Francesco Cannizzaro , Italy
Maosen Cao , China
Ana Carpio, Spain
Rodrigo Carvajal , Chile
Caterina Casavola, Italy
Sara Casciati, Italy
Federica Caselli , Italy
Carmen Castillo , Spain
Inmaculada T. Castro , Spain
Miguel Castro , Portugal
Giuseppe Catalanotti , United Kingdom
Alberto Cavallo , Italy
Gabriele Cazzulani , Italy
Fatih Vehbi Celebi, Turkey
Miguel Cerrolaza , Venezuela
Gregory Chagnon , France
Ching-Ter Chang , Taiwan
Kuei-Lun Chang , Taiwan
Qing Chang , USA
Xiaoheng Chang , China
Prasenjit Chatterjee , Lithuania
Kacem Chehdi, France
Peter N. Cheimets, USA
Chih-Chiang Chen , Taiwan
He Chen , China

Kebing Chen , China
Mengxin Chen , China
Shyi-Ming Chen , Taiwan
Xizhong Chen , Ireland
Xue-Bo Chen , China
Zhiwen Chen , China
Qiang Cheng, USA
Zeyang Cheng, China
Luca Chiapponi , Italy
Francisco Chicano , Spain
Tirivanhu Chinyoka , South Africa
Adrian Chmielewski , Poland
Seongim Choi , USA
Gautam Choubey , India
Hung-Yuan Chung , Taiwan
Yusheng Ci, China
Simone Cinquemani , Italy
Roberto G. Citarella , Italy
Joaquim Ciurana , Spain
John D. Clayton , USA
Piero Colajanni , Italy
Giuseppina Colicchio, Italy
Vassilios Constantoudis , Greece
Enrico Conte, Italy
Alessandro Contento , USA
Mario Cools , Belgium
Gino Cortellessa, Italy
Carlo Cosentino , Italy
Paolo Crippa , Italy
Erik Cuevas , Mexico
Guozeng Cui , China
Mehmet Cunkas , Turkey
Giuseppe D'Aniello , Italy
Peter Dabnichki, Australia
Weizhong Dai , USA
Zhifeng Dai , China
Purushothaman Damodaran , USA
Sergey Dashkovskiy, Germany
Adiel T. De Almeida-Filho , Brazil
Fabio De Angelis , Italy
Samuele De Bartolo , Italy
Stefano De Miranda , Italy
Filippo De Monte , Italy

José António Fonseca De Oliveira
Correia , Portugal
Jose Renato De Sousa , Brazil
Michael Defoort, France
Alessandro Della Corte, Italy
Laurent Dewasme , Belgium
Sanku Dey , India
Gianpaolo Di Bona , Italy
Roberta Di Pace , Italy
Francesca Di Puccio , Italy
Ramón I. Diego , Spain
Yannis Dimakopoulos , Greece
Hasan Dinçer , Turkey
José M. Domínguez , Spain
Georgios Dounias, Greece
Bo Du , China
Emil Dumic, Croatia
Madalina Dumitriu , United Kingdom
Premraj Durairaj , India
Saeed Eftekhari Azam, USA
Said El Kafhali , Morocco
Antonio Elipse , Spain
R. Emre Erkmen, Canada
John Escobar , Colombia
Leandro F. F. Miguel , Brazil
FRANCESCO FOTI , Italy
Andrea L. Facci , Italy
Shahla Faisal , Pakistan
Giovanni Falsone , Italy
Hua Fan, China
Jianguang Fang, Australia
Nicholas Fantuzzi , Italy
Muhammad Shahid Farid , Pakistan
Hamed Faruqi, Iran
Yann Favennec, France
Fiorenzo A. Fazzolari , United Kingdom
Giuseppe Fedele , Italy
Roberto Fedele , Italy
Baowei Feng , China
Mohammad Ferdows , Bangladesh
Arturo J. Fernández , Spain
Jesus M. Fernandez Oro, Spain
Francesco Ferrise, Italy
Eric Feulvarch , France
Thierry Floquet, France

Eric Florentin , France
Gerardo Flores, Mexico
Antonio Forcina , Italy
Alessandro Formisano, Italy
Francesco Franco , Italy
Elisa Francomano , Italy
Juan Frausto-Solis, Mexico
Shujun Fu , China
Juan C. G. Prada , Spain
HECTOR GOMEZ , Chile
Matteo Gaeta , Italy
Mauro Gaggero , Italy
Zoran Gajic , USA
Jaime Gallardo-Alvarado , Mexico
Mosè Gallo , Italy
Akemi Gálvez , Spain
Maria L. Gandarias , Spain
Hao Gao , Hong Kong
Xingbao Gao , China
Yan Gao , China
Zhiwei Gao , United Kingdom
Giovanni Garcea , Italy
José García , Chile
Harish Garg , India
Alessandro Gasparetto , Italy
Stylianos Georgantzinou, Greece
Fotios Georgiades , India
Parviz Ghadimi , Iran
Ştefan Cristian Gherghina , Romania
Georgios I. Giannopoulos , Greece
Agathoklis Giaralis , United Kingdom
Anna M. Gil-Lafuente , Spain
Ivan Giorgio , Italy
Gaetano Giunta , Luxembourg
Jefferson L.M.A. Gomes , United Kingdom
Emilio Gómez-Déniz , Spain
Antonio M. Gonçalves de Lima , Brazil
Qunxi Gong , China
Chris Goodrich, USA
Rama S. R. Gorla, USA
Veena Goswami , India
Xunjie Gou , Spain
Jakub Grabski , Poland

Antoine Grall , France
George A. Gravvanis , Greece
Fabrizio Greco , Italy
David Greiner , Spain
Jason Gu , Canada
Federico Guarracino , Italy
Michele Guida , Italy
Muhammet Gul , Turkey
Dong-Sheng Guo , China
Hu Guo , China
Zhaoxia Guo, China
Yusuf Gurefe, Turkey
Salim HEDDAM , Algeria
ABID HUSSANAN, China
Quang Phuc Ha, Australia
Li Haitao , China
Petr Hájek , Czech Republic
Mohamed Hamdy , Egypt
Muhammad Hamid , United Kingdom
Renke Han , United Kingdom
Weimin Han , USA
Xingsi Han, China
Zhen-Lai Han , China
Thomas Hanne , Switzerland
Xinan Hao , China
Mohammad A. Hariri-Ardebili , USA
Khalid Hattaf , Morocco
Defeng He , China
Xiao-Qiao He, China
Yanchao He, China
Yu-Ling He , China
Ramdane Hedjar , Saudi Arabia
Jude Hemanth , India
Reza Hemmati, Iran
Nicolae Herisanu , Romania
Alfredo G. Hernández-Díaz , Spain
M.I. Herreros , Spain
Eckhard Hitzer , Japan
Paul Honeine , France
Jaromir Horacek , Czech Republic
Lei Hou , China
Yingkun Hou , China
Yu-Chen Hu , Taiwan
Yunfeng Hu, China
Can Huang , China
Gordon Huang , Canada
Linsheng Huo , China
Sajid Hussain, Canada
Asier Ibeas , Spain
Orest V. Iftime , The Netherlands
Przemyslaw Ignaciuk , Poland
Giacomo Innocenti , Italy
Emilio Insfran Pelozo , Spain
Azeem Irshad, Pakistan
Alessio Ishizaka, France
Benjamin Ivorra , Spain
Breno Jacob , Brazil
Reema Jain , India
Tushar Jain , India
Amin Jajarmi , Iran
Chiranjibe Jana , India
Łukasz Jankowski , Poland
Samuel N. Jator , USA
Juan Carlos Jáuregui-Correa , Mexico
Kandasamy Jayakrishna, India
Reza Jazar, Australia
Khalide Jbilou, France
Isabel S. Jesus , Portugal
Chao Ji , China
Qing-Chao Jiang , China
Peng-fei Jiao , China
Ricardo Fabricio Escobar Jiménez , Mexico
Emilio Jiménez Macías , Spain
Maolin Jin, Republic of Korea
Zhuo Jin, Australia
Ramash Kumar K , India
BHABEN KALITA , USA
MOHAMMAD REZA KHEDMATI , Iran
Viacheslav Kalashnikov , Mexico
Mathiyalagan Kalidass , India
Tamas Kalmar-Nagy , Hungary
Rajesh Kaluri , India
Jyottheswara Reddy Kalvakurthi, India
Zhao Kang , China
Ramani Kannan , Malaysia
Tomasz Kapitaniak , Poland
Julius Kaplunov, United Kingdom
Konstantinos Karamanos, Belgium
Michal Kawulok, Poland

Irfan Kaymaz , Turkey
Vahid Kayvanfar , Qatar
Krzysztof Kecik , Poland
Mohamed Khader , Egypt
Chaudry M. Khalique , South Africa
Mukhtaj Khan , Pakistan
Shahid Khan , Pakistan
Nam-Il Kim, Republic of Korea
Philipp V. Kiryukhantsev-Korneev ,
Russia
P.V.V Kishore , India
Jan Koci , Czech Republic
Ioannis Kostavelis , Greece
Sotiris B. Kotsiantis , Greece
Frederic Kratz , France
Vamsi Krishna , India
Edyta Kucharska, Poland
Krzysztof S. Kulpa , Poland
Kamal Kumar, India
Prof. Ashwani Kumar , India
Michal Kunicki , Poland
Cedrick A. K. Kwuimy , USA
Kyandoghere Kyamakya, Austria
Ivan Kyrchei , Ukraine
Márcio J. Lacerda , Brazil
Eduardo Lalla , The Netherlands
Giovanni Lancioni , Italy
Jaroslaw Latalski , Poland
Hervé Laurent , France
Agostino Lauria , Italy
Aimé Lay-Ekuakille , Italy
Nicolas J. Leconte , France
Kun-Chou Lee , Taiwan
Dimitri Lefebvre , France
Eric Lefevre , France
Marek Lefik, Poland
Yaguo Lei , China
Kauko Leiviskä , Finland
Ervin Lenzi , Brazil
ChenFeng Li , China
Jian Li , USA
Jun Li , China
Yueyang Li , China
Zhao Li , China

Zhen Li , China
En-Qiang Lin, USA
Jian Lin , China
Qibin Lin, China
Yao-Jin Lin, China
Zhiyun Lin , China
Bin Liu , China
Bo Liu , China
Heng Liu , China
Jianxu Liu , Thailand
Lei Liu , China
Sixin Liu , China
Wanquan Liu , China
Yu Liu , China
Yuanchang Liu , United Kingdom
Bonifacio Llamazares , Spain
Alessandro Lo Schiavo , Italy
Jean Jacques Loiseau , France
Francesco Lolli , Italy
Paolo Lonetti , Italy
António M. Lopes , Portugal
Sebastian López, Spain
Luis M. López-Ochoa , Spain
Vassilios C. Loukopoulos, Greece
Gabriele Maria Lozito , Italy
Zhiguo Luo , China
Gabriel Luque , Spain
Valentin Lychagin, Norway
YUE MEI, China
Junwei Ma , China
Xuanlong Ma , China
Antonio Madeo , Italy
Alessandro Magnani , Belgium
Toqeer Mahmood , Pakistan
Fazal M. Mahomed , South Africa
Arunava Majumder , India
Sarfranz Nawaz Malik, Pakistan
Paolo Manfredi , Italy
Adnan Maqsood , Pakistan
Muazzam Maqsood, Pakistan
Giuseppe Carlo Marano , Italy
Damijan Markovic, France
Filipe J. Marques , Portugal
Luca Martinelli , Italy
Denizar Cruz Martins, Brazil

Francisco J. Martos , Spain
Elio Masciari , Italy
Paolo Massioni , France
Alessandro Mauro , Italy
Jonathan Mayo-Maldonado , Mexico
Pier Luigi Mazzeo , Italy
Laura Mazzola, Italy
Driss Mehdi , France
Zahid Mehmood , Pakistan
Roderick Melnik , Canada
Xiangyu Meng , USA
Jose Merodio , Spain
Alessio Merola , Italy
Mahmoud Mesbah , Iran
Luciano Mescia , Italy
Laurent Mevel , France
Constantine Michailides , Cyprus
Mariusz Michta , Poland
Prankul Middha, Norway
Aki Mikkola , Finland
Giovanni Minafò , Italy
Edmondo Minisci , United Kingdom
Hiroyuki Mino , Japan
Dimitrios Mitsotakis , New Zealand
Ardashir Mohammadzadeh , Iran
Francisco J. Montáns , Spain
Francesco Montefusco , Italy
Gisele Mophou , France
Rafael Morales , Spain
Marco Morandini , Italy
Javier Moreno-Valenzuela , Mexico
Simone Morganti , Italy
Caroline Mota , Brazil
Aziz Moukrim , France
Shen Mouquan , China
Dimitris Mourtzis , Greece
Emiliano Mucchi , Italy
Taseer Muhammad, Saudi Arabia
Ghulam Muhiuddin, Saudi Arabia
Amitava Mukherjee , India
Josefa Mula , Spain
Jose J. Muñoz , Spain
Giuseppe Muscolino, Italy
Marco Mussetta , Italy

Hariharan Muthusamy, India
Alessandro Naddeo , Italy
Raj Nandkeolyar, India
Keivan Navaie , United Kingdom
Soumya Nayak, India
Adrian Neagu , USA
Erivelton Geraldo Nepomuceno , Brazil
AMA Neves, Portugal
Ha Quang Thinh Ngo , Vietnam
Nhon Nguyen-Thanh, Singapore
Papakostas Nikolaos , Ireland
Jelena Nikolic , Serbia
Tatsushi Nishi, Japan
Shanzhou Niu , China
Ben T. Nohara , Japan
Mohammed Nouari , France
Mustapha Nourelfath, Canada
Kazem Nouri , Iran
Ciro Núñez-Gutiérrez , Mexico
Włodzimierz Ogryczak, Poland
Roger Ohayon, France
Krzysztof Okarma , Poland
Mitsuhiro Okayasu, Japan
Murat Olgun , Turkey
Diego Oliva, Mexico
Alberto Olivares , Spain
Enrique Onieva , Spain
Calogero Orlando , Italy
Susana Ortega-Cisneros , Mexico
Sergio Ortobelli, Italy
Naohisa Otsuka , Japan
Sid Ahmed Ould Ahmed Mahmoud , Saudi Arabia
Taoreed Owolabi , Nigeria
EUGENIA PETROPOULOU , Greece
Arturo Pagano, Italy
Madhumangal Pal, India
Pasquale Palumbo , Italy
Dragan Pamučar, Serbia
Weifeng Pan , China
Chandan Pandey, India
Rui Pang, United Kingdom
Jürgen Pannek , Germany
Elena Panteley, France
Achille Paolone, Italy

George A. Papakostas , Greece
Xosé M. Pardo , Spain
You-Jin Park, Taiwan
Manuel Pastor, Spain
Pubudu N. Pathirana , Australia
Surajit Kumar Paul , India
Luis Payá , Spain
Igor Pažanin , Croatia
Libor Pekař , Czech Republic
Francesco Pellicano , Italy
Marcello Pellicciari , Italy
Jian Peng , China
Mingshu Peng, China
Xiang Peng , China
Xindong Peng, China
Yueqing Peng, China
Marzio Pennisi , Italy
Maria Patrizia Pera , Italy
Matjaz Perc , Slovenia
A. M. Bastos Pereira , Portugal
Wesley Peres, Brazil
F. Javier Pérez-Pinal , Mexico
Michele Perrella, Italy
Francesco Pesavento , Italy
Francesco Petrini , Italy
Hoang Vu Phan, Republic of Korea
Lukasz Pieczonka , Poland
Dario Piga , Switzerland
Marco Pizzarelli , Italy
Javier Plaza , Spain
Goutam Pohit , India
Dragan Poljak , Croatia
Jorge Pomares , Spain
Hiram Ponce , Mexico
Sébastien Poncet , Canada
Volodymyr Ponomaryov , Mexico
Jean-Christophe Ponsart , France
Mauro Pontani , Italy
Sivakumar Poruran, India
Francesc Pozo , Spain
Aditya Rio Prabowo , Indonesia
Anchasa Pramuanjaroenkij , Thailand
Leonardo Primavera , Italy
B Rajanarayan Prusty, India

Krzysztof Puszynski , Poland
Chuan Qin , China
Dongdong Qin, China
Jianlong Qiu , China
Giuseppe Quaranta , Italy
DR. RITU RAJ , India
Vitomir Racic , Italy
Carlo Rainieri , Italy
Kumbakonam Ramamani Rajagopal, USA
Ali Ramazani , USA
Angel Manuel Ramos , Spain
Higinio Ramos , Spain
Muhammad Afzal Rana , Pakistan
Muhammad Rashid, Saudi Arabia
Manoj Rastogi, India
Alessandro Rasulo , Italy
S.S. Ravindran , USA
Abdolrahman Razani , Iran
Alessandro Reali , Italy
Jose A. Reinoso , Spain
Oscar Reinoso , Spain
Haijun Ren , China
Carlo Renno , Italy
Fabrizio Renno , Italy
Shahram Rezapour , Iran
Ricardo Rianza , Spain
Francesco Riganti-Fulginei , Italy
Gerasimos Rigatos , Greece
Francesco Ripamonti , Italy
Jorge Rivera , Mexico
Eugenio Roanes-Lozano , Spain
Ana Maria A. C. Rocha , Portugal
Luigi Rodino , Italy
Francisco Rodríguez , Spain
Rosana Rodríguez López, Spain
Francisco Rossomando , Argentina
Jose de Jesus Rubio , Mexico
Weiguo Rui , China
Rubén Ruiz , Spain
Ivan D. Rukhlenko , Australia
Dr. Eswaramoorthi S. , India
Weichao SHI , United Kingdom
Chaman Lal Sabharwal , USA
Andrés Sáez , Spain

Bekir Sahin, Turkey
Laxminarayan Sahoo , India
John S. Sakellariou , Greece
Michael Sakellariou , Greece
Salvatore Salamone, USA
Jose Vicente Salcedo , Spain
Alejandro Salcido , Mexico
Alejandro Salcido, Mexico
Nunzio Salerno , Italy
Rohit Salgotra , India
Miguel A. Salido , Spain
Sinan Salih , Iraq
Alessandro Salvini , Italy
Abdus Samad , India
Sovan Samanta, India
Nikolaos Samaras , Greece
Ramon Sancibrian , Spain
Giuseppe Sanfilippo , Italy
Omar-Jacobo Santos, Mexico
J Santos-Reyes , Mexico
José A. Sanz-Herrera , Spain
Musavarah Sarwar, Pakistan
Shahzad Sarwar, Saudi Arabia
Marcelo A. Savi , Brazil
Andrey V. Savkin, Australia
Tadeusz Sawik , Poland
Roberta Sburlati, Italy
Gustavo Scaglia , Argentina
Thomas Schuster , Germany
Hamid M. Sedighi , Iran
Mijanur Rahaman Seikh, India
Tapan Senapati , China
Lotfi Senhadji , France
Junwon Seo, USA
Michele Serpilli, Italy
Silvestar Šesnić , Croatia
Gerardo Severino, Italy
Ruben Sevilla , United Kingdom
Stefano Sfarra , Italy
Dr. Ismail Shah , Pakistan
Leonid Shaikhet , Israel
Vimal Shanmuganathan , India
Prayas Sharma, India
Bo Shen , Germany
Hang Shen, China

Xin Pu Shen, China
Dimitri O. Shepelsky, Ukraine
Jian Shi , China
Amin Shokrollahi, Australia
Suzanne M. Shontz , USA
Babak Shotorban , USA
Zhan Shu , Canada
Angelo Sifaleras , Greece
Nuno Simões , Portugal
Mehakpreet Singh , Ireland
Piyush Pratap Singh , India
Rajiv Singh, India
Seralathan Sivamani , India
S. Sivasankaran , Malaysia
Christos H. Skiadas, Greece
Konstantina Skouri , Greece
Neale R. Smith , Mexico
Bogdan Smolka, Poland
Delfim Soares Jr. , Brazil
Alba Sofi , Italy
Francesco Soldovieri , Italy
Raffaele Solimene , Italy
Yang Song , Norway
Jussi Sopanen , Finland
Marco Spadini , Italy
Paolo Spagnolo , Italy
Ruben Specogna , Italy
Vasilios Spitas , Greece
Ivanka Stamova , USA
Rafał Stanisławski , Poland
Miladin Stefanović , Serbia
Salvatore Strano , Italy
Yakov Strelniker, Israel
Kangkang Sun , China
Qiuqin Sun , China
Shuaishuai Sun, Australia
Yanchao Sun , China
Zong-Yao Sun , China
Kumarasamy Suresh , India
Sergey A. Suslov , Australia
D.L. Suthar, Ethiopia
D.L. Suthar , Ethiopia
Andrzej Swierniak, Poland
Andras Szekrenyes , Hungary
Kumar K. Tamma, USA

Yong (Aaron) Tan, United Kingdom
Marco Antonio Taneco-Hernández , Mexico
Lu Tang , China
Tianyou Tao, China
Hafez Tari , USA
Alessandro Tasora , Italy
Sergio Teggi , Italy
Adriana del Carmen Téllez-Anguiano , Mexico
Ana C. Teodoro , Portugal
Efstathios E. Theotokoglou , Greece
Jing-Feng Tian, China
Alexander Timokha , Norway
Stefania Tomasiello , Italy
Gisella Tomasini , Italy
Isabella Torcicollo , Italy
Francesco Tornabene , Italy
Mariano Torrisi , Italy
Thang nguyen Trung, Vietnam
George Tsiatas , Greece
Le Anh Tuan , Vietnam
Nerio Tullini , Italy
Emilio Turco , Italy
Ilhan Tuzcu , USA
Efstratios Tzirtzilakis , Greece
FRANCISCO UREÑA , Spain
Filippo Ubertini , Italy
Mohammad Uddin , Australia
Mohammad Safi Ullah , Bangladesh
Serdar Ulubeyli , Turkey
Mati Ur Rahman , Pakistan
Panayiotis Vafeas , Greece
Giuseppe Vairo , Italy
Jesus Valdez-Resendiz , Mexico
Eusebio Valero, Spain
Stefano Valvano , Italy
Carlos-Renato Vázquez , Mexico
Martin Velasco Villa , Mexico
Franck J. Vernerey, USA
Georgios Veronis , USA
Vincenzo Vespri , Italy
Renato Vidoni , Italy
Venkatesh Vijayaraghavan, Australia

Anna Vila, Spain
Francisco R. Villatoro , Spain
Francesca Vipiana , Italy
Stanislav Vitek , Czech Republic
Jan Vorel , Czech Republic
Michael Vynnycky , Sweden
Mohammad W. Alomari, Jordan
Roman Wan-Wendner , Austria
Bingchang Wang, China
C. H. Wang , Taiwan
Dagang Wang, China
Guoqiang Wang , China
Huaiyu Wang, China
Hui Wang , China
J.G. Wang, China
Ji Wang , China
Kang-Jia Wang , China
Lei Wang , China
Qiang Wang, China
Qingling Wang , China
Weiwei Wang , China
Xinyu Wang , China
Yong Wang , China
Yung-Chung Wang , Taiwan
Zhenbo Wang , USA
Zhibo Wang, China
Waldemar T. Wójcik, Poland
Chi Wu , Australia
Qihong Wu, China
Yuqiang Wu, China
Zhibin Wu , China
Zhizheng Wu , China
Michalis Xenos , Greece
Hao Xiao , China
Xiao Ping Xie , China
Qingzheng Xu , China
Binghan Xue , China
Yi Xue , China
Joseph J. Yame , France
Chuanliang Yan , China
Xinggang Yan , United Kingdom
Hongtai Yang , China
Jixiang Yang , China
Mijia Yang, USA
Ray-Yeng Yang, Taiwan

Zaoli Yang , China
Jun Ye , China
Min Ye , China
Luis J. Yebra , Spain
Peng-Yeng Yin , Taiwan
Muhammad Haroon Yousaf , Pakistan
Yuan Yuan, United Kingdom
Qin Yuming, China
Elena Zaitseva , Slovakia
Arkadiusz Zak , Poland
Mohammad Zakwan , India
Ernesto Zambrano-Serrano , Mexico
Francesco Zammori , Italy
Jessica Zangari , Italy
Rafal Zdunek , Poland
Ibrahim Zeid, USA
Nianyin Zeng , China
Junyong Zhai , China
Hao Zhang , China
Haopeng Zhang , USA
Jian Zhang , China
Kai Zhang, China
Lingfan Zhang , China
Mingjie Zhang , Norway
Qian Zhang , China
Tianwei Zhang , China
Tongqian Zhang , China
Wenyu Zhang , China
Xianming Zhang , Australia
Xuping Zhang , Denmark
Yinyan Zhang, China
Yifan Zhao , United Kingdom
Debao Zhou, USA
Heng Zhou , China
Jian G. Zhou , United Kingdom
Junyong Zhou , China
Xueqian Zhou , United Kingdom
Zhe Zhou , China
Wu-Le Zhu, China
Gaetano Zizzo , Italy
Mingcheng Zuo, China

Contents

Optimization of Cryogenic Process Parameters for the Minimization of Surface Residual Stress in Pure Iron Using Taguchi Design

Meng Zheng , Jinxing Kong , and Yuwen Sun 

Research Article (12 pages), Article ID 2047044, Volume 2021 (2021)

X-Ray Image Recognition Based on Improved Mask R-CNN Algorithm

Jicun Zhang , Xueping Song , Jiawei Feng , and Jiyou Fei 

Research Article (14 pages), Article ID 6544325, Volume 2021 (2021)

The Local and Parallel Finite Element Scheme for Electric Structure Eigenvalue Problems

Fubiao Lin , Junying Cao , and Zhixin Liu 

Research Article (11 pages), Article ID 1049917, Volume 2021 (2021)

Prediction of Frequency Response Function for Cylindrical Thin-Walled Workpiece with Fixture Support Constraints

Jinjie Jia , Yuwen Sun , and Jinbo Niu 

Research Article (16 pages), Article ID 9946310, Volume 2021 (2021)

Design and Error Compensation Performance of a Precision Micro-Drive Rotary System

Manzhi Yang , Gang Jing , Zhenyang Lv, Wei Guo, Yumei Huang, Kaiyang Wei , Linyue Li , Bin Feng, Hongyu Ge, and Shuaitian Li

Research Article (13 pages), Article ID 3199915, Volume 2021 (2021)

High-Precision Guide Stiffness Analysis Method for Micromechanism Based on the Boundary Element Method

Manzhi Yang , Zhenyang Lv , Gang Jing , Wei Guo, Yumei Huang, Linyue Li , Kaiyang Wei , Bin Feng, and Hongyu Ge

Research Article (14 pages), Article ID 7516669, Volume 2021 (2021)

Simulation of Constant-Volume Removal Rate Machining of Middle-Convex and Varying Ellipse Piston

Yanwei Xu , Yinhao Wang, and Tancheng Xie

Research Article (10 pages), Article ID 5363992, Volume 2021 (2021)

Research Article

Optimization of Cryogenic Process Parameters for the Minimization of Surface Residual Stress in Pure Iron Using Taguchi Design

Meng Zheng ¹, Jinxing Kong ², and Yuwen Sun ¹

¹Key Laboratory for Precision and Non-Traditional Machining Technology of the Ministry of Education, Dalian University of Technology, Dalian 116024, China

²Machinery Manufacturing Technology, China Academy of Engineering Physics, Mianyang 621999, China

Correspondence should be addressed to Jinxing Kong; kjxmc106@163.com

Received 24 April 2021; Revised 19 June 2021; Accepted 13 October 2021; Published 2 November 2021

Academic Editor: Kamal Kumar

Copyright © 2021 Meng Zheng et al. This is an open access article distributed under the Creative Commons Attribution License, which permits unrestricted use, distribution, and reproduction in any medium, provided the original work is properly cited.

The plastic deformation produced in the machining process can cause residual stress. As an effective way to control the residual stresses, the cryogenic process is used in modern industries such as aerospace, automobile, and shipping industry. Focusing on the minimization of surface stress in the cryogenic process of pure iron, the Taguchi design is used in this paper. The effect of cryogenic temperature (77–193 K), holding time (8–24 H), cooling rate (2–6 K/min), and warming-up rate (0.5–1.5 K/min) on surface residual stress is discussed and the optimal combination of cryogenic parameters is obtained using signal-to-noise (S/N) ratios. To overcome the weakness of the Taguchi method that cannot calculate stresses, an exponential model to predict residual stresses considering cryogenic parameters is developed. The coefficients of this mathematical model are obtained using multilinear regressive analysis based on the database of the Taguchi experiment. After this, the optimization process is conducted with this model using the genetic algorithm (GA). The optimized results using both ways coincide with each other. The optimal cryogenic parameters are obtained, i.e., cryogenic temperature of 193 K, holding time of 24 h, cooling rate of 2 K/min, and warming-up rate of 0.5 K/min. When the optimum cryogenic parameters are used, the surface residual stress is reduced by 42.9% in the cutting direction and 46.2% in the feeding direction. The method can be applied to the actual machining engineering to realize the low-stress control on the cutting surface.

1. Introduction

The stress, which retains in part even after the external loads are removed, is defined as residual stress [1, 2]. Compared with compressive stress, tensile stress is undesirable due to its negative effects on the machining dimension and fatigue life, etc. [2, 3]. Especially for pure iron, as a typical difficult-to-cut material, large tensile residual stress is inevitably generated on the surface of the workpiece because of its high plasticity [2]. As an effective way to control stresses, the cryogenic process is a reasonable way to treat pure iron. Therefore, the control of cryogenic process parameters becomes essential to get the minstress.

By now, residual stress of the machined surface is mainly controlled by reducing the mechanical-thermal effect in the

machining process. This method usually reduces surface stress through reasonable selection and design of tools [4–6], optimization of cutting parameters [1, 7–9], and improvement of lubrication methods [10]. For example, Yen et al. [4] studied the effect of tool edge geometry on the cutting process, contact stress, cutting temperature, and sliding velocity between the tool and chip, and tool geometry is optimized through finite element analysis. Experiments were performed in [1] based on response surface methodology to develop a statistical model of residual stress. The authors analyzed the effect of parameters in the ultrasonic-assisted turning process and their interactions on residual stresses. Results reveal that percentage intensity and feed rate significantly affect the generation of residual stresses. The regression model of residual stress under different lubrication

modes is established in [10] to realize the optimization of residual stress.

The above researching works make great efforts to investigate residual stresses. However, they did not study material processing techniques before or after machining, such as heat treatment. Heat treatment can effectively eliminate the material internal stress. The postweld heat treatment of P91 steel has a great effect on residual stresses, reducing peak stresses from around 600 MPa to 20 MPa [11]. It is found in [12] that the heat treatment temperature has the greatest effect on the reduction of residual stresses and distortion compared with the holding time and cooling rate. Additionally, the postswaging annealing of Ti-6Al-4V alloy at 400°C can just relieve 80% of the residual stress, while a higher temperature at 500°C can relieve 97% of the residual stress to achieve the almost stress-free state [13]. However, the heat treatment can make the grain coarsening and the carbide solid solution supersaturation of the material. Moreover, the retained residual stress after heat treatment may reduce the fatigue strength and other mechanical properties of the material, which will easily lead to the deformation of the workpiece in the stress release process.

As a new material treatment technology, the cryogenic process can effectively diminish deficiencies of heat treatment. It can eliminate the internal residual stress, refine the grain structure, improve the wear resistance, and ensure the dimensional stability of the workpiece, which will enhance the machining accuracy and service life of the workpiece [14]. Hence it is wildly used in manufacturing, automotive, aerospace, and medical treatment [15]. Li et al. [16] found that cryogenic laser peening can significantly induce a higher density of dislocation and smaller-size grain of the 2024-T351 aluminum alloy compared with room temperature laser peening. Meanwhile, the tensile strength and elongation were simultaneously increased by 9.36% and 7.10%, respectively. Li et al. [17] found that the wear resistance is improved by lowering the cryogenic temperature and prolonging the holding time through the wear test of M2 steel. The wear resistance became saturated and reached the highest when the cryogenic treatment is 77 K, the holding time is 24 h, and the cooling rate is 2 K/min. Hariharan et al. [18] found that the AISI D7 steel tool treated by the cryogenic has a Vickers hardness improvement by 2.9 HV greater than that of normal tool hardness. The material removal rate of mild steel workpiece is slightly increased and accuracy in dimensions along surface finish is significantly upgraded while this material is turned by the cryogenically treated tool. Sert and Celik [19] presented that the cryogenic treatment of tungsten carbide cutting tools can cause martensitic transformation. This transformation rate is high with lower cryogenic treatment. Also, the use of cryogenic cycling allows changing the structure of material including recovery of a partially crystalline structure [20]. Bensely et al. [21] found that cryogenic treatment can improve the overall fatigue life of 71% over conventionally heat-treated En 353 steel. Han et al. [22] found that the brittleness of shale increases at low temperatures. This phenomenon can be attributed to the shrinkage of mineral grains and the freezing of pore water.

Cryogenic treatment is used to reduce the internal stress mainly through changing the atomic lattice constant caused by volume contraction at low temperatures. In the warming-up and tempering process, the diffusion ability of carbon atoms increases and the formation of ultra-fine carbides, thus the residual stress is reduced. The cryogenic process is mainly used in steel to reduce internal stress. Alexandru and Bulancea [23] pointed out that the strain caused by phase transition can change the state of residual stress. Bensely et al. [24] studied the effect of cryogenic treatment on the residual stress distribution of case-carburized En 353 steel. The results showed that cryogenic treatment would produce large compressive stress, and the compressive residual stress would decrease in the tempering process. This phenomenon could be explained as the increased precipitation of fine carbides in specimens subjected to deep cryogenic treatment with tempering. Senthilkumar et al. [25] found that the tensile residual stress is generated during the traditional heat treatment and the high cryogenic temperature (−80°C) for 4140 steel, while the compressive residual stress is generated under the low cryogenic temperature (−196°C). Xu et al. [26] found that residual stress is largely reduced by cryogenic treatment for electron-beam-welded Ti-6Al-4V joints. However, the reduction effect of residual stress is no longer obvious when the holding time of cryogenic treatment exceeds 24 h. Sachin et al. [27] showed that, compared with MQL and dry environment diamond burnishing, the compressive residual stress strength of 17–4 pH stainless steel is increased by 20% and 44%, respectively, in cryogenic environments.

The research work on pure iron mainly focuses on the control of tool wear and lubrication, the stability prediction of the machining process, and the control of machining-induced surface residual stress. Kong et al. [28] researched the notch wear mechanism in the turning process of pure iron under different cooling/lubrication conditions and find that the wear rates reached the maximum in wet cutting followed by dry cutting, rapeseed oil lubrication, and minimum quantity lubrication (MQL) condition. Jiang et al. [29] developed a three-dimensional exponential model for cutting forces by taking the nose radius into account and realized the prediction of chatter stability in turning of pure iron analytically. Luo and Sun [2] optimized process parameters for the minimization of surface residual stress based on central composite design turning experiments data. Their works play a tremendous role in the improvement of machining quality for the pure iron component.

As mentioned above, only a few works focus on the machining of pure iron, and none of them is involved in the cryogenic treatment to reduce the surface residual stress. Meanwhile, how to achieve optimal cryogenic process parameters is not well handled yet. Therefore, in this paper, optimization of cryogenic parameters to minimize the surface residual stress in the cryogenic process is proposed. The research route is shown in Figure 1. Focusing on the minimization of surface residual stress in the cryogenic process of pure iron, an efficient optimization method by using the Taguchi design is proposed. Then, the effects of cryogenic parameter variables including cryogenic

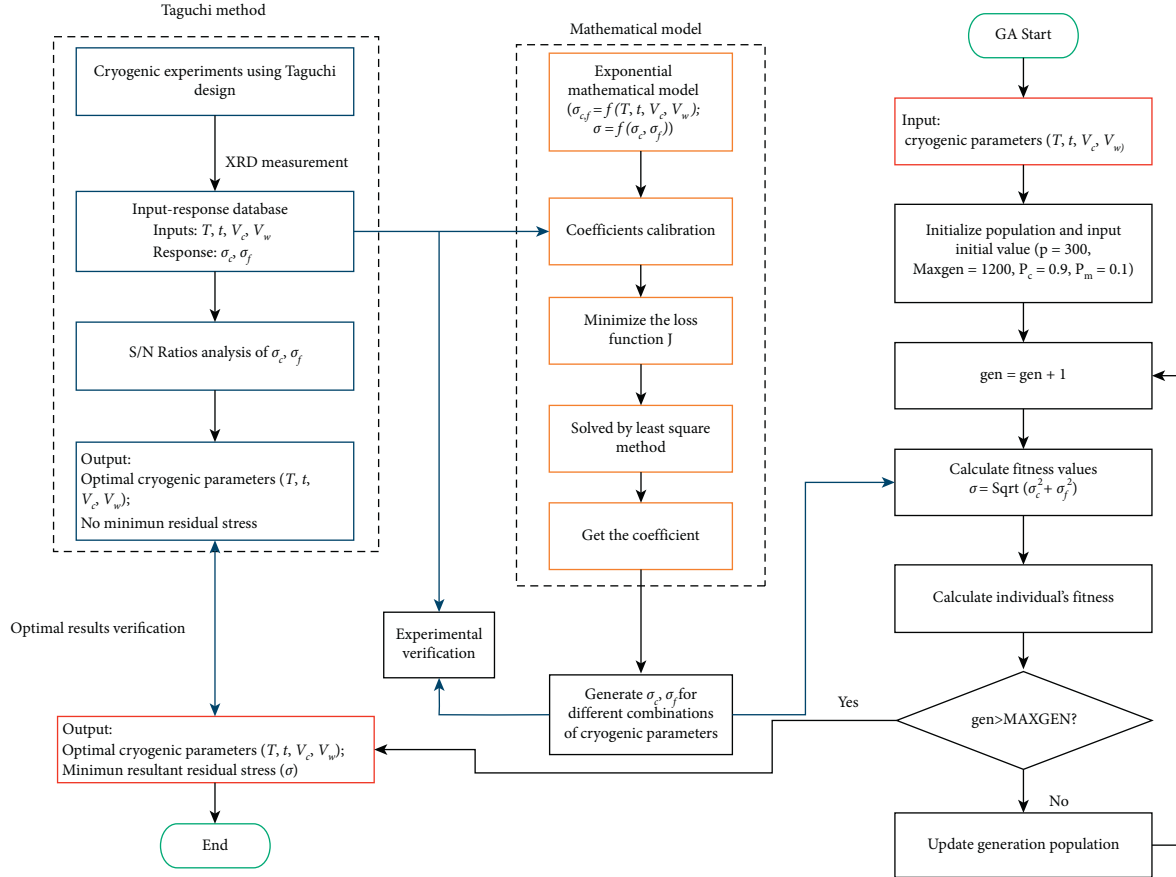


FIGURE 1: The flowchart of optimization.

temperature, holding time, cooling rate, and warming-up rate on output variables (cutting residual stress and feeding residual stress) are analyzed. Subsequently, the optimized parameters are calculated by means of the main effect plot of S/N ratios. To solve the difficulty of the Taguchi method to calculate stresses, an exponential model is proposed to predict residual stresses and then a genetic algorithm (GA) is used for the optimization procedure. The structure of this paper is designed as follows. The method applied for the minimization of surface residual stress is shown in Section 2. Meanwhile, the optimal combination of process parameters is deduced. Section 3 develops a residual stresses prediction modeling. Section 4 investigates the detailed procedures of related residual stress measurements to verify the validity of the proposed model. Section 5 is the conclusion of the paper. It is expected to provide technical support for the control of residual stress on the machined surface of pure iron components.

2. Methodology of Cryogenic Parameters Optimization

The process of minimizing surface residual stress is realized using the combination of the cryogenic process parameters based on the following steps:

- (1) The design of the Taguchi experimental strategy
- (2) Optimization of cryogenic process parameters by Taguchi experiments with S/N ratios analysis

2.1. The Design of Taguchi Experiments. The experimental design by orthogonal array can enhance efficiency and saving costs. So it is applied to design the cryogenic experiment. In this paper, the surface residual stresses (σ_c, σ_f) in the cutting and feeding direction are taken as the response characteristics. Input control factors include cryogenic process parameters, i.e., cryogenic temperature T , holding time t , cooling rate V_c , and warming-up rate V_w . The selected levels of the control factors are listed in Table 1.

Based on the Taguchi method, total degrees of freedom C can be calculated using the formula

$$C = m(T) + m(t) + m(V_c) + m(V_w) - 4, \quad (1)$$

where m stands for the number of levels for each control factor. Here, this value for all the factors is 3. Then, the number of experiment groups equals total degrees plus 1, that is, 9. Therefore, Taguchi L9 orthogonal array is used to conduct the cryogenic treatment experiments, which is shown in Table 2. The loss function is defined using the

TABLE 1: Levels of the control factors.

Control factors	Level 1	Level 2	Level 3
T (K)	193	135	77
t (H)	8	16	24
V_c (K/min)	2	4	6
V_w (K/min)	1.5	1	0.5

TABLE 2: L9 experimental program.

Exp. no.	T	t	V_c	V_w
1	193	8	2	1.5
2	193	16	4	1.0
3	193	24	6	0.5
4	135	8	4	0.5
5	135	16	6	1.5
6	135	24	2	1.0
7	77	8	6	1.0
8	77	16	2	0.5
9	77	24	4	1.5

relationship between real and ideal values of the residual stresses.

$$L(\sigma_x) = K\sigma_x^2, \quad x = c \text{ or } f, \quad (2)$$

where $L(\sigma_x)$ is the actual stress quality characteristics and K is the loss coefficient.

$$\frac{S}{N} = -10 \log \left(\sum_{i=1}^n \left(\frac{L(\sigma_{xi})}{K} \right)^2 \right), \quad x = c \text{ or } f. \quad (3)$$

When the loss function is obtained, the next step is to calculate the values of signal-to-noise (S/N) ratios. The signal can be expressed as the mean of the measured stresses, and the standard deviation is the noise. To get the minimization of the stress, the following S/N formula is used:

In this formula, n is the total number of experiments and i is the i^{th} experiment in Table 2. The optimized parameters can be obtained using the maximum value of S/N.

2.2. Optimization of Cryogenic Parameters. Based on the design of the experiment in the above subsection, cryogenic parameters can be optimized using the S/N ratios. Residual stresses of the machined surface are measured using a Pulstec μ -X360s X-ray residual stress analyzer shown in Figure 2.

The measured residual stress results and calculated S/N ratios are obtained in Table 3. From this table, it can be seen that the surface residual stresses along the cutting and feeding directions are tensile. Furthermore, the residual stress along the cutting direction is higher than that along the other direction. The maximum and minimum cutting residual stresses are 563 MPa and 352 MPa. For the other direction, these two values are 299 MPa and 194 MPa, respectively. Another phenomenon can be found that control factors of the cryogenic process in Table 1 influence residual stress significantly. Therefore, the optimization process is introduced here to get the minimization of the stresses.

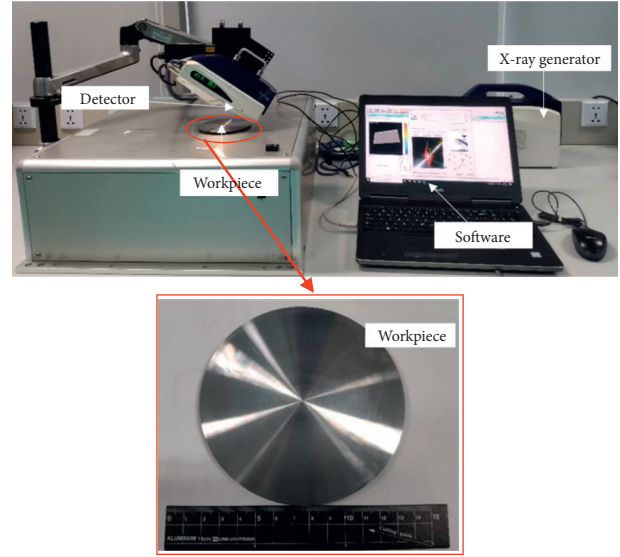
FIGURE 2: Residual stress measurement using μ -X360s equipment.

TABLE 3: L9 experimental program.

Exp. no.	σ_c	σ_f	$S/N(\sigma_c)$	$S/N(\sigma_f)$
1	431	230	-52.6895	-47.2346
2	399	195	-52.0195	-45.8007
3	352	194	-50.9309	-45.756
4	517	272	-54.2698	-48.7126
5	509	239	-54.1344	-47.568
6	420	220	-52.465	-46.8485
7	563	299	-55.0102	-49.5134
8	510	242	-54.1514	-47.6763
9	462	249	-53.2928	-47.924

Figure 3 shows the main effects plot for cutting residual stress and feeding residual stress using the data of the Taguchi experiment. In this figure, the temperature affects stresses most effectively compared with the other three parameters. The next one is cryogenic time. The other two parameters influence stresses relatively small. The residual stresses are reduced with increasing cryogenic temperature and holding time. However, with the increase of cooling rate and warming-up rate, the residual stresses show a reverse trend.

To get the minimum stresses, the maximum values of S/N are chosen as the green circles in Figure 3. That means, along the cutting and feeding directions, the optimized parameters are

$$\begin{cases} T = 193 \text{ K}, \\ t = 24 \text{ H}, \\ V_c = 2 \text{ K/min}, \\ V_w = 0.5 \text{ K/min}. \end{cases} \quad (4)$$

Through the above analysis, optimal cryogenic parameters can be finely obtained. However, it is unable to obtain the concrete magnitude of the residual stresses by using this method. Although more experiments can be conducted to investigate the residual stresses under different combinations of cryogenic process parameters, it is costly and time-consuming. Therefore, in the next section, a new model is

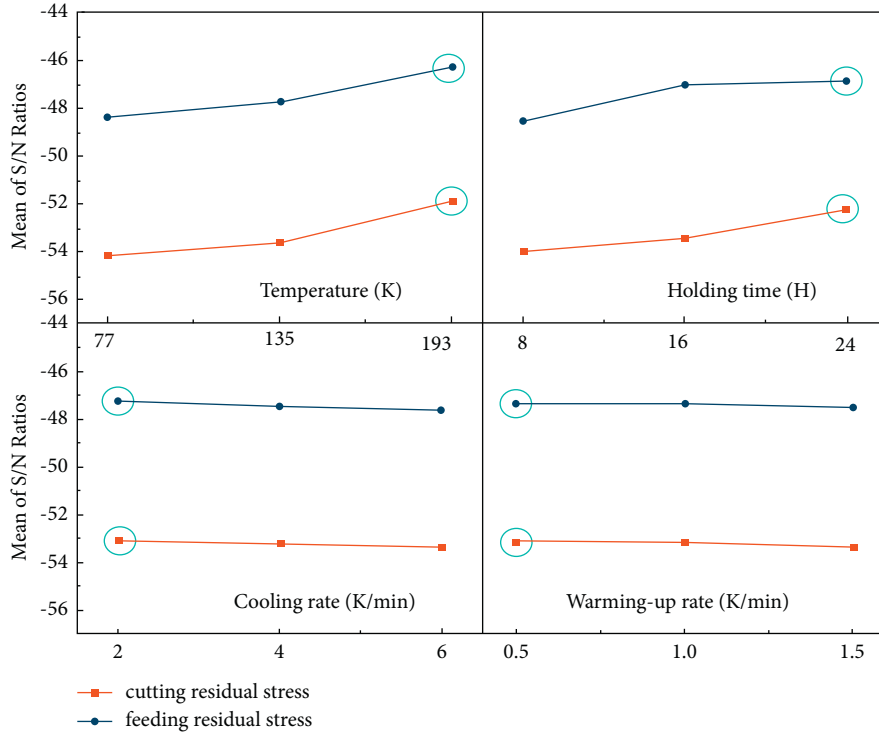


FIGURE 3: Main effect plot of S/N ratios.

constructed to predict the residual stress of pure iron under different cryogenic process parameters.

3. Residual Stresses Modeling

3.1. Exponential Model of Surface Residual Stress. Using the four parameters mentioned in the above section, a mathematical model is induced using

$$\begin{cases} \sigma_c = F_c c_c T^{k_c} t^{l_c} V_c^{m_c} V_w^{n_c}, \\ \sigma_f = F_f c_f T^{k_f} t^{l_f} V_c^{m_f} V_w^{n_f}, \\ \sigma = \sqrt{(\sigma_c)^2 + (\sigma_f)^2}, \end{cases} \quad (5)$$

where σ is the resultant stress, F_c and F_f are the correction coefficient, c_c and c_f are the residual stress constant, and $k_c, l_c, m_c, n_c, k_f, l_f, m_f, n_f$ are exponent constants.

To obtain these coefficients, equation (5) is changed into another form:

$$\begin{cases} \ln \sigma_c = \ln c_c + k_c T + l_c t + m_c V_c + n_c V_w, \\ \ln \sigma_f = \ln c_f + k_f T + l_f t + m_f V_c + n_f V_w. \end{cases} \quad (6)$$

Then, the mean square error as a loss function is defined as

$$\begin{aligned} J(\ln c_x, k_x, l_x, m_x, n_x) \\ = \frac{1}{M} \sum_{i=1}^M (\ln \sigma_{xi} - (\ln c_x + k_x T_x + l_x t_x + m_x V_{xi} + n_x V_{wi}))^2, \quad x = c \text{ or } f, \end{aligned} \quad (7)$$

where M is the number of experiments. When the minvalue of equation (7) is obtained, the coefficients in equation (5) can be derived. To realize this, equation (7) is rewritten as the matrix form:

$$J(\mathbf{C}) = (\mathbf{Y} - \mathbf{XC})^T (\mathbf{Y} - \mathbf{XC}). \quad (8)$$

We have

$$\begin{cases} \mathbf{C} = [\ln c_x \quad k_x \quad l_x \quad m_x \quad n_x]^T, \quad x = c \text{ or } f, \\ \mathbf{X} = \begin{bmatrix} 1 & T_1 & t_1 & V_{c1} & V_{w1} \\ 1 & T_2 & t_2 & V_{c2} & V_{w2} \\ \vdots & \vdots & \vdots & \vdots & \vdots \\ 1 & T_N & t_N & V_{cN} & V_{wM} \end{bmatrix}, \\ \mathbf{Y} = [Y_0 \quad Y_1 \quad Y_2 \quad \dots \quad Y_M]^T. \end{cases} \quad (9)$$

Therefore, coefficients can be calculated using the partial derivative which is set to zero.

$$\frac{\partial J}{\partial c_x} = 0, \quad x = c \text{ or } f. \quad (10)$$

Finally, coefficients vector \mathbf{C} is solved using the following equation:

$$\mathbf{C} = (\mathbf{X}^T \mathbf{X})^{-1} \mathbf{X}^T \mathbf{Y}. \quad (11)$$

Using the experimental results listed in Table 3, the coefficients are calculated and the results are

$$\begin{cases} F_c = 1.17, & c_c = 1236.2, & k_c = -0.25262, \\ l_c = -0.25262, & m_c = 0.03765, & n_c = 0.01823, \\ F_f = 1.28, & \sigma_f = 2602.5, & k_f = -0.26892, \\ l_f = -0.26892, & m_f = 0.02563, & n_f = 0.02468. \end{cases} \quad (12)$$

Analysis of variance (ANOVA) is employed to determine the adequacy of residual stress models and the degree of correlation among model terms. The F test is used to determine the significance test. The level of confidence equals 95%. The adequacy of the model is checked by correlation coefficient "Adj. R-Squared." The results of ANOVA for the cutting residual stress regression model are shown in Table 4. For the developed exponential model, regression is not significant since P value is more than 0.05. However, the P value which equals 0.06419 is very close to 0.05. The "Adj. R-Squared" of the proposed model is 0.69111. It can verify the predictive ability of the model. The results of ANOVA for the feeding residual stress regression model are shown in Table 5. For the developed model, regression is significant since P -value (0.02596) is less than 0.05. The "Adj. R-Squared" for feeding residual stress model is 0.80768 which indicates the good predictive ability and high significance of the model.

Using the presented model, the surface residual stresses for a random combination of cryogenic parameters can be predicted. Figure 4 shows the results calculated using the introduced model in (5). In this figure, single factors are considered. For example, for the up-left image, the temperature is changing. However, the other three parameters are fixed as $t = 24$ H, $V_c = 2$ K/min, and $V_w = 0.5$ K/min. The first phenomenon found in this figure is that the effect of each parameter on the residual stress can be illustrated. For temperature, the higher T is, the lower the stresses are. This shows a similar trend as in Figure 3. For the other three parameters, the same regular as that in Figure 3 can be found.

3.2. Optimization Based on Genetic Algorithm (GA). Furthermore, using this model, the combination of cryogenic parameters can also be optimized. Therefore, this section proposes a way to deal with this issue. The optimization function is set as

TABLE 4: Analysis of variance for cutting residual stress model.

Source	Regression	Residual error	Total
Df	4	4	8
Sum of squares	0.15185	0.02774	0.17958
Mean square	0.03796	0.00693	
F value	5.4748		
Prob > F	0.06419		
Remarks	Not significant		

TABLE 5: Analysis of variance for feeding residual stress model.

Source	Regression	Residual error	Total
Df	4	4	8
Sum of squares	0.14544	0.01547	0.16091
Mean square	0.03636	0.00387	
F value	9.39923		
Prob > F	0.02596		
Remarks	Significant		

$$\begin{cases} \min & (\sigma) = \min\left(\sqrt{\sigma_c^2 + \sigma_f^2}\right) \\ \text{s.t.} & \begin{cases} T_{\min} < T < T_{\max}, \\ t_{\min} < t < t_{\max}, \\ V_{c \min} < V_c < V_{c \max}, \\ V_{w \min} < V_w < V_{w \max}, \end{cases} \end{cases} \quad (13)$$

where x_{\min} and x_{\max} , $x = T, t, V_c$ or V_w are the extreme values for each parameter.

The genetic algorithm (GA) is suitable for solving constrained or unconstrained optimization problems and can ensure global optimal solutions with a high probability. Thus, for optimization, the GA method is used to obtain the minimization stress and the corresponding combination of cryogenic parameters. The optimization steps are as follows.

Step 1. Set initial values.

The initial population size of genetic algorithm P is 300, the maximum genetic generation $\text{MaxGen} = 1200$, maximum iteration time span $L = 20$ s, crossover fraction $P_c = 0.9$, and mutation rate P_m is set to 0.1. The genetic algebra is set $\text{gen} = 0$.

Step 2. Binary code the independent variables including cryogenic temperature T , cryogenic time t , cooling rate V_c , and the warming-up rate V_w .

These variables are binary coded based on their ranges, and the initial population is generated randomly. The length of chromosomes is set to 80. Then the counts $\text{gen} = \text{gen} + 1$ are performed.

Step 3. Calculating the fitness of individuals in the population.

The robust chromosomes which have a smaller fitness are more likely generated in $(u + 1)^{\text{th}}$ generation. Nevertheless, those chromosomes whose fitness is large have less opportunity generated in $(u + 1)^{\text{th}}$ generation.

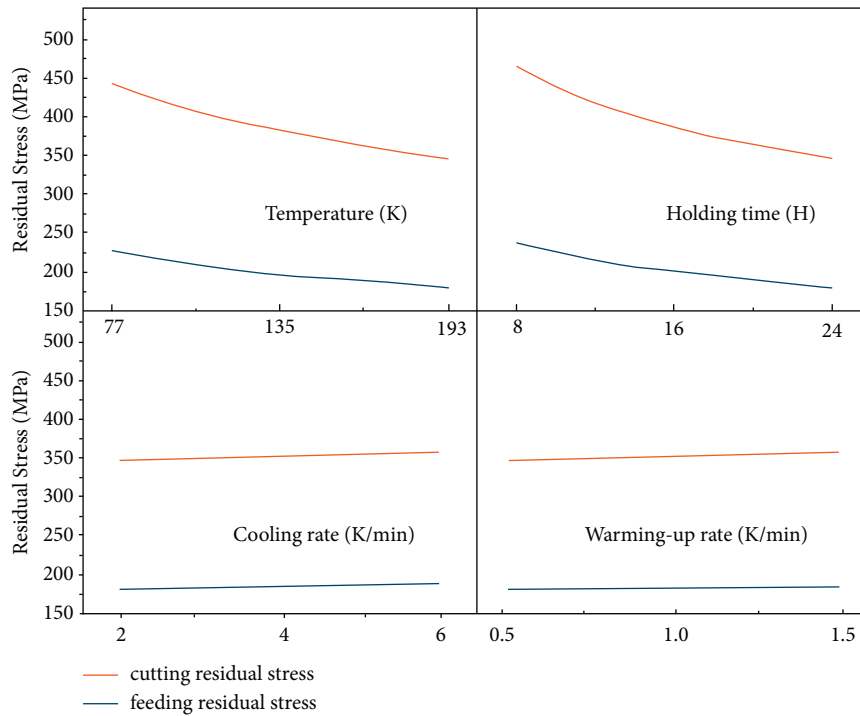


FIGURE 4: Prediction of the residual stress using the presented model.

Step 4. Crossover operation in the $(u + 1)^{\text{th}}$ generation.

According to individual fitness, samples of individuals from the u^{th} generation are selected and transformed to the $(u + 1)^{\text{th}}$ generation for crossover operation.

Step 5. Create new individuals.

A pair of individuals in the group are taken as parents. Using the crossover probability, a single crossover operation is carried out and two new individuals are created.

Step 6. Mutation operation.

Individuals are selected randomly in the population with a certain probability for mutation operation. New individuals are generated by changing some of the individual's genes.

Step 7. Terminate the iterative process.

If $\text{gen} \leq \text{MaxGen}$, go to Step 2; if $\text{gen} > \text{MaxGen}$ or the value of average fitness changes continuously less than a constant over a certain algebra, the obtained individual with maximum adaptation is taken as the optimal solution, and the iterative process can be terminated.

Step 8. Obtain the optimal cryogenic parameters.

Through translation of optimal solution code, the optimal parameters can be found.

As evolution progresses, individuals with low fitness are gradually eliminated. On the other hand, individuals with high fitness can survive in the vicinity of the optimal value. Finally, the optimal values are found. According to the above steps, the cryogenic parameters T , t , V_c , and V_w are optimized. The algorithm is run using the optimization tool in

MATLAB R2014a software. The iterative process is shown in Figure 5.

In this figure, after 310 iterations, the genetic algorithm converges and the target residual stress σ is 395 MPa, and corresponding cryogenic temperature $T = 193$ K, cryogenic time $t = 24$ H, cooling rate $V_c = 2$ K/min, and warming-up rate $V_w = 0.5$ K/min. This is proved by the Taguchi method.

4. Results and Discussion

This section introduces an experimental strategy to measure the surface residual stress. Simultaneously, the correctness of the introduced model can be verified using the experimental database.

4.1. Measurement Strategy. The disc-like DT4E pure iron blanks with a diameter of 120 mm and an initial thickness of 5.5 mm are selected for the experiment of cryogenic treatment. The cryogenic treatment is conducted using the equipment named SL-500. The cryogenic equipment uses liquid nitrogen as the cold source which is stored in the liquid nitrogen tank. This liquid flows into the cryogenic box through the transfer pipeline in the working process. This equipment can control temperature, holding time, cooling rate, and warming-up rate automatically through a PCL touch screen. In one cryogenic cycle, the temperature is gradually declined to one of its levels. Then the workpieces are held in this situation for certain durations. Finally, the workpiece is warmed up gradually to room temperature. The temperature deviation is controlled within ± 2 K. The range of temperature is from 77 K to 303 K.

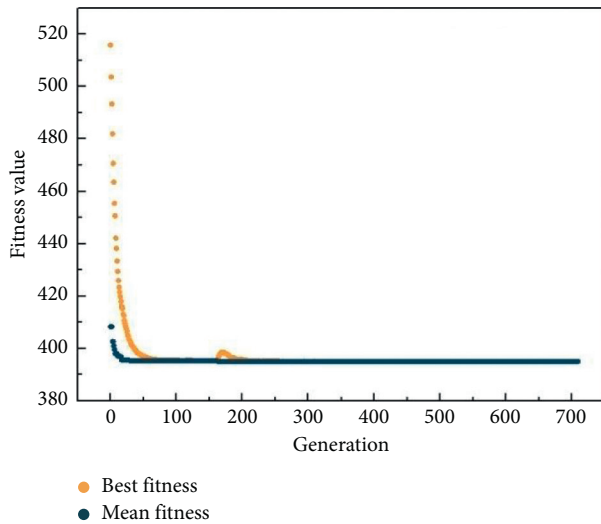


FIGURE 5: Optimization of cryogenic parameters using GA.

To obtain the rational surface, which is suitable to detect residual stress using the μ -X360s X-ray residual stress analyzer, the pure iron is machined by finish turning with the same cutting parameters. The turning process is conducted in a CNC lathe MJ520 with the same cutting parameters and cooling or lubrication conditions. The turning insert DCGT11T302-HP mounted in an SDJCL2525M11 right-hand tool holder is used for the machining of pure iron. The chemical compositions of pure iron blanks are illustrated in Table 6 and the cutting parameters are listed in Table 7. Then, the samples are put on the mobile platform of the X-ray residual stress analyzer for measurement. The residual stress of each workpiece is measured four times and the average value is taken. The obtained data are shown in Figure 6.

The Debye ring at the given point on the sample surface is measured as shown in Figure 6(a). Based on this ring, the Debye profile in the range of 360 degrees can be gained. The plot between the strain and $\cos(\alpha)$ in Figure 6(c) is also derived. Based on these pieces of information, the relationship between diffraction angle vs. a can be calculated, which is shown in Figure 6(e). The half-value is calculated using the Debye profile. At the same time, full width at half maxima (FWHM) is computed. In the last image, the peak strength is evaluated. Finally, the calculation of residual stress uses the cosine a method. Measuring conditions are shown in Table 8.

Electron backscatter diffraction (EBSD) is performed to determine the texture orientation of the optimal cryogenically treated sample and without cryogenically treated sample. It is equipped with a Nordlys II Nano EBSD camera (maximum resolution: 1344×1024 pixels) from Oxford Instruments. The samples are vibration polished and argon ion polished to fully remove the surface stress layer after standard metallographic polishing is completed. The inclination angle 70° , working distance 15 mm, high voltage 20 KV, and beam current approximately 10 nA are used during data collection. The EBSD data is processed using HKL Technologies Channel 5 software for orientation analysis.

TABLE 6: The chemical composition of pure iron blanks.

Element	$W_i\%$
Fe	>99.8
C	0.013
Si	0.028
Mn	0.029
Ni	0.035
S	0.02
Cr	0.02
Cu	0.034
P	0.0072
Al	0.0023

TABLE 7: The cutting parameters.

Parameters	Value
Cutting speed V (m/min)	200
Depth of cut a_p (mm)	0.05
Feed f (mm/rev)	0.12

4.2. Model Verification. To verify the model in (5), the predicted values of stress with different parameters are compared with that in the experiment. The comparison results are shown in Figure 7. It can be seen that the predicted residual stresses closely agree with the measured ones in both directions. The maximum error of the surface residual stresses is around 11.7% in the cutting direction and 9.18% in the feeding direction. Hence, the developed exponent mathematical model can be used to predict the surface residual stress of cryogenically treated pure iron material.

The experiments to verify the validity of the proposed residual stress model are conducted with the optimal cryogenic parameters, which are cryogenic temperature 193 K, cryogenic time 24 H, cooling rate 2 K/min, and tempering rate 0.5 K/min. The surface residual stress is also measured using μ -X360s equipment. The results of verified experiments are shown in Table 9. It can be found that the prediction error of the proposed mathematical model for surface residual stress calculation is less than 5.17% in the cutting direction and 7.14% in the feeding direction. Therefore, the model is of high accuracy.

Meanwhile, to illustrate the advantage of cryogenic treatment on reducing surface residual stress, the residual stress without cryogenic treat is also measured by the XRD. Compared with the results before treatment, the surface residual stress of the treated workpiece using optimal parameters is 329 MPa in the cutting direction and 168 MPa in the feed direction. The amount of reduction from the untreated state is 247 MPa in the cutting direction and 144 MPa in the other direction.

In the cryogenic process, the homogeneously distributed carbides and small-sized particles are formed. These carbide particles lead to an improvement in wear resistance and mechanical properties, such as the increase of the hardness and lifetime, the reduction of wear, and the change of microstructure after cryogenic treatment. This may lead to a

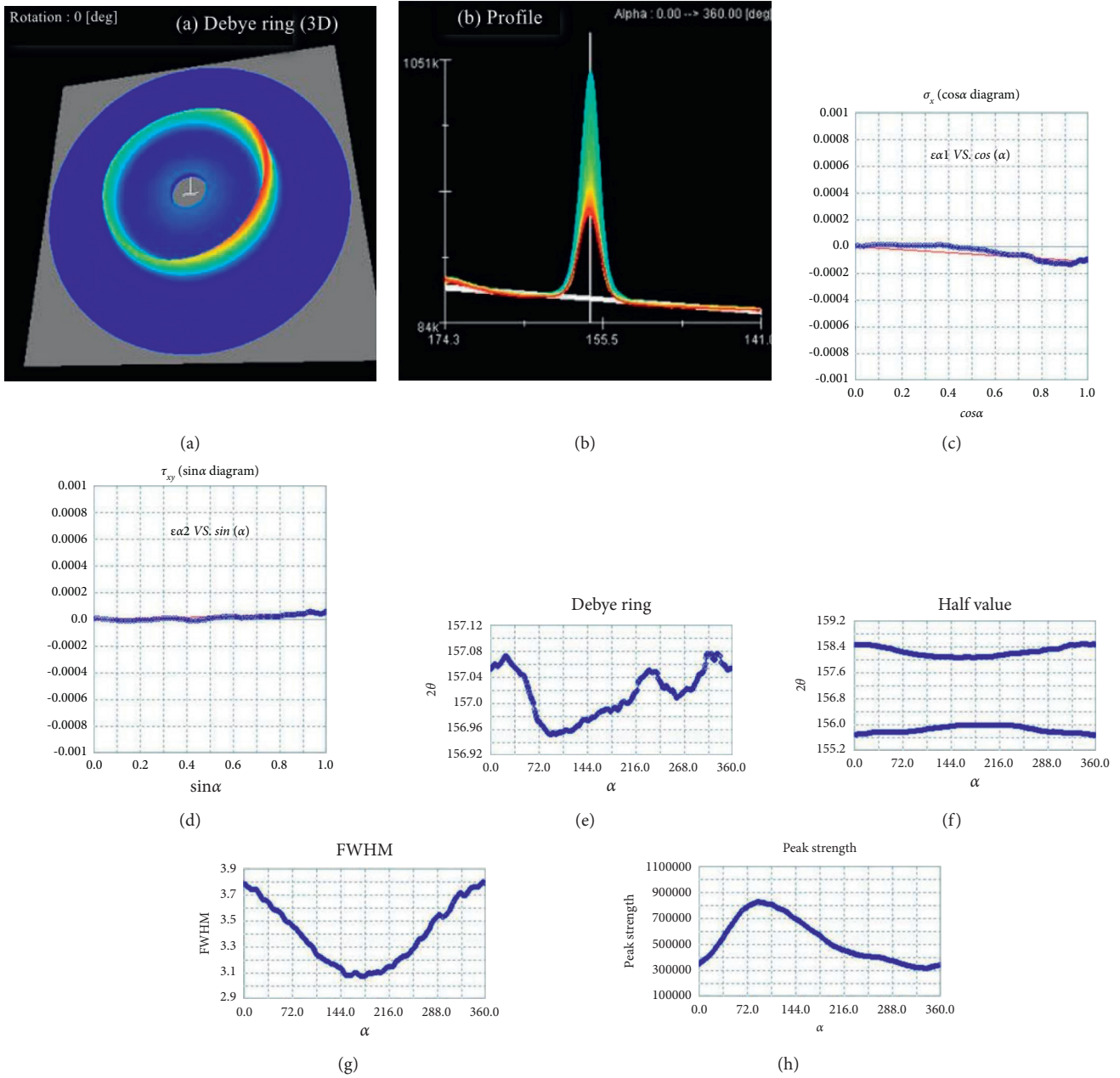


FIGURE 6: Measured stress result using the X-ray residual stress analyzer. (a) Debye ring (3D). (b) Profile. (c) σ_x (cos α diagram). (d) τ_{xy} (sin α diagram). (e) Debye ring. (f) Half-value. (g) FWHM. (h) Peak strength.

TABLE 8: Measuring conditions of X-ray equipment.

Item	Value
Characteristics X-ray	CrK α
Diffraction line	211
Crystal structure	B.C.C
Tube voltage (kV)	30
Tube current (mA)	0.1
X-ray incident angle, ψ_0 (deg)	35
Young's modulus E (GPa)	224
Poisson's ratio ν	0.28
Diffraction angle 2θ (deg)	156.396

decrease in the surface tensile residual stress of the pure iron. In the other aspect, the residual stress is reduced mainly through the change of atomic lattice constant caused by volume contraction in the cryogenic environment. In the warming-up process, the diffusion ability of carbon atoms increased. The segregation of carbon atoms from the octahedral or tetrahedral site of ferrite lattice to the defect regions causes more refining grain. And the more stable tissue performance results in the reduction of residual stress. This can be proved by the inverse pole (Figures 8(a) and 8(b)) obtained by electron backscatter diffraction. The microstructure of pure iron shows a (111)

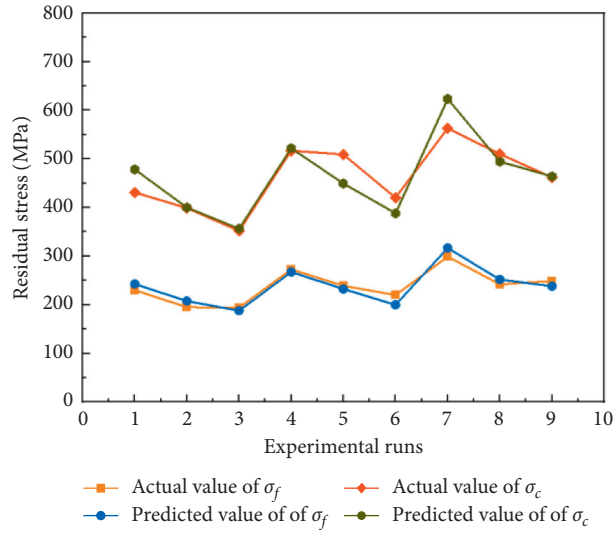


FIGURE 7: Actual and predicted values of surface residual stress.

TABLE 9: Results of verification test.

Item	σ_c (MPa)	σ_f (MPa)
Experiment	329	168
Model	346	180
Error	5.17%	7.14%

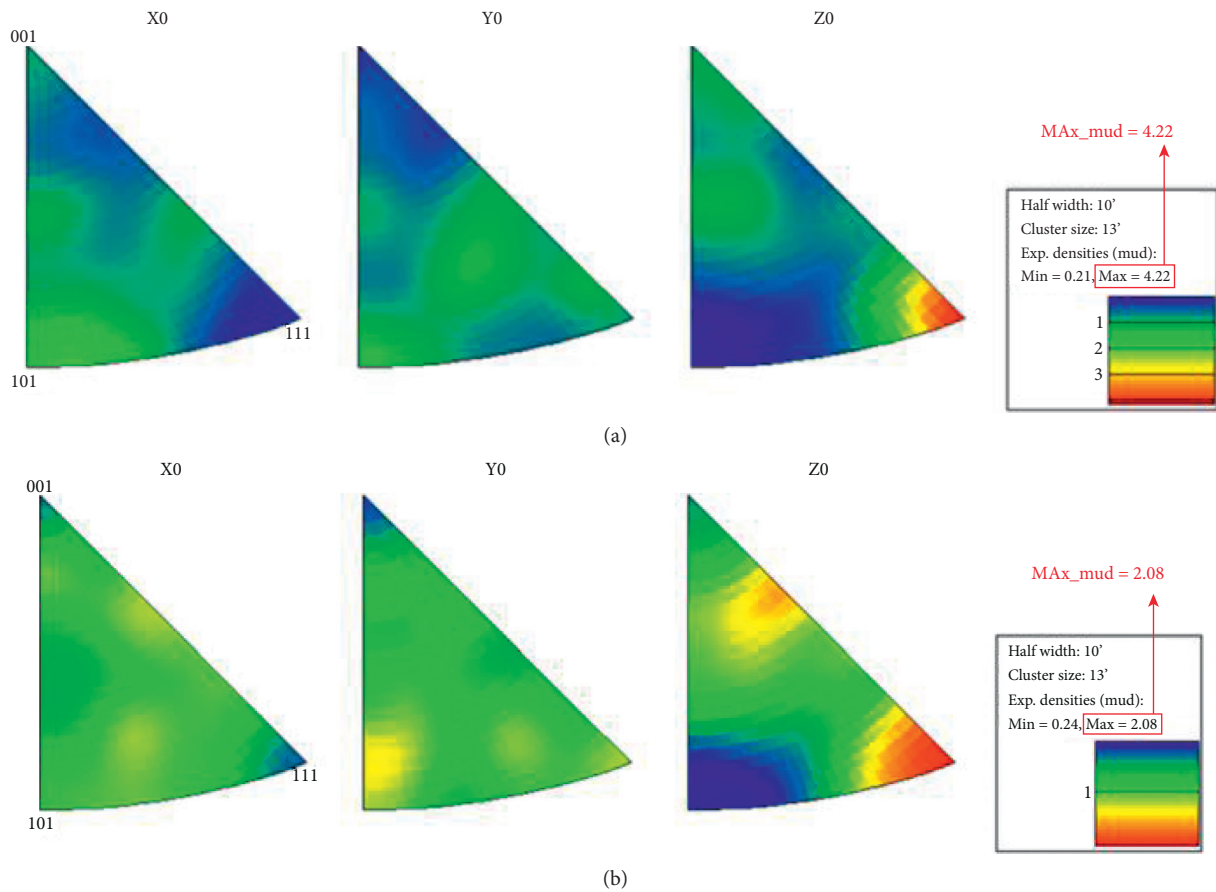


FIGURE 8: The inverse pole image of pure iron material. (a) Without cryogenic treatment. (b) Optimal cryogenic treatment.

textural trend. However, using the optimum cryogenic parameter, the texture is improved and maximum extreme density intensity (MUD) is reduced from 4.22 to 2.08.

5. Conclusion

The Taguchi design is introduced to minimize the surface residual stress in the cryogenic process of pure iron. In this process, the influence of cryogenic process parameters on the surface cutting residual stress and feeding residual stress are studied by using the signal-to-noise ratios (S/N) analysis. Simultaneously, a mathematical model for predicting the residual stress is established based on multiple linear regression analysis to overcome the difficulty of the Taguchi method. The following conclusions can be drawn:

- (1) It is found by Taguchi's S/N ratios analysis that, with the increase of cryogenic temperature and holding time, the surface residual stress of cryogenically treated pure iron both in the cutting and feeding directions is all reduced. In contrast, the influences of the other two parameters on stresses show a different trend.
- (2) The developed mathematical model is used to calculate the surface residual stress. Compared with the experimental data, the residual stress prediction error is less than 11.7% in the cutting direction and 9.18% in the feeding direction, which indicates that the mathematical model established can predict surface residual stress of cryogenically treated pure iron with high accuracy.
- (3) Within the given parameter range, the optimal cryogenic parameters for generating minimum surface stress are determined by Taguchi's S/N ratios as cryogenic temperature 193 K, cryogenic time 24 H, cooling rate 2 K/min, and tempering rate 0.5 K/min.
- (4) The obtained optimal cryogenic parameters by using a genetic algorithm are consistent with the results of Taguchi's S/N ratios analysis for residual stress.
- (5) Compared with the no cryogenically treated work-piece, using the obtained optimum parameters for the cryogenic treatment of pure iron, the surface residual stress is reduced by 42.9% in the cutting direction and 46.2% in the feeding direction, respectively.

Data Availability

The data used to support the findings of this study are available within the article or from the corresponding author upon request.

Conflicts of Interest

The authors declare that they do not have any commercial or associative interest that represents conflicts of interest in connection with the work submitted.

Acknowledgments

This work was supported by the Science Challenge Project, no. JDZZ2016006-01, and the National Natural Science Foundation of China, no. 51805498.

References

- [1] V. Sharma and P. M. Pandey, "Optimization of machining and vibration parameters for residual stresses minimization in ultrasonic assisted turning of 4340 hardened steel," *Ultrasonics*, vol. 70, pp. 172–182, 2016.
- [2] J. Luo and Y. Sun, "Optimization of process parameters for the minimization of surface residual stress in turning pure iron material using central composite design," *Measurement*, vol. 163, Article ID 108001, 2020.
- [3] N. Masmiahi, A. A. D. Sarhan, M. A. N. Hassan, and M. Hamdi, "Optimization of cutting conditions for minimum residual stress, cutting force and surface roughness in end milling of S50C medium carbon steel," *Measurement*, vol. 86, pp. 253–265, 2016.
- [4] Y.-C. Yen, A. Jain, and T. Altan, "A finite element analysis of orthogonal machining using different tool edge geometries," *Journal of Materials Processing Technology*, vol. 146, no. 1, pp. 72–81, 2004.
- [5] X. Cheng, X. Zha, and F. Jiang, "Optimizing the geometric parameters of cutting edge for rough machining Fe-Cr-Ni stainless steel," *International Journal of Advanced Manufacturing Technology*, vol. 85, no. 1–4, pp. 683–693, 2016.
- [6] X. Cheng, S. Jin, T. Liao, and F. Jiang, "Optimizing the geometric parameters of chamfered edge for rough machining Fe-Cr-Ni stainless steel," *International Journal of Advanced Manufacturing Technology*, vol. 91, no. 1–4, pp. 137–146, 2017.
- [7] E. Capello, "Residual stresses in turning," *Journal of Materials Processing Technology*, vol. 160, no. 2, pp. 221–228, 2005.
- [8] S. Saini, I. S. Ahuja, and V. S. Sharma, "Modelling the effects of cutting parameters on residual stresses in hard turning of AISI H11 tool steel," *International Journal of Advanced Manufacturing Technology*, vol. 65, no. 5–8, pp. 667–678, 2013.
- [9] L. Meng, N. He, Y. Yang, and W. Zhao, "Measurement of surface residual stresses generated by turning thin-wall Ti6Al4V tubes using different cutting parameters," *Rare Metal Materials & Engineering*, vol. 44, no. 10, pp. 2381–2386, 2015.
- [10] T. Leppert and R. L. Peng, "Residual stresses in surface layer after dry and MQL turning of AISI 316L steel," *Production Engineering*, vol. 6, no. 4–5, pp. 367–374, 2012.
- [11] A. H. Yaghi, T. H. Hyde, A. A. Becker et al., "Comparison of measured and modelled residual stresses in a welded P91 steel pipe undergoing post weld heat treatment," *International Journal of Pressure Vessels and Piping*, vol. 181, Article ID 104076, 2020.
- [12] B. Huang, J. Liu, S. Zhang, Q. Chen, and L. Chen, "Effect of post-weld heat treatment on the residual stress and deformation of 20/0Cr18Ni9 dissimilar metal welded joint by experiments and simulations," *Journal of Materials Research and Technology*, vol. 9, no. 3, pp. 6186–6200, 2020.
- [13] L. Yuan, W. Wang, Y. Li, M. Yang, H. Zhang, and W. Zhang, "Effect of annealing temperature on texture and residual stress of Ti-6Al-4V alloy seamless tubing processed by cold rotary swaging," *Vacuum*, vol. 177, Article ID 109399, 2020.

- [14] T. H. Guan, H. M. Liu, Y. B. Xu, C. Q. Wu, and Y. Lv, "Research status and application prospect of deep cryogenic treatment technology on cemented carbide," *Advanced Materials Research*, vol. 989–994, pp. 871–875, 2014.
- [15] T. Sonar, S. Lomte, and C. Gogte, "Cryogenic treatment of metal-a review," *Materials Today: Proceedings*, vol. 5, no. 11, pp. 25219–25228, 2018.
- [16] J. Li, J. Zhou, A. Feng et al., "Analysis of microstructure and tensile properties produced by cryogenic laser peening on 2024-T351 aluminum alloy," *Vacuum*, vol. 158, pp. 141–145, 2018.
- [17] J. Li, X. Yan, X. Liang, H. Guo, and D. Y. Li, "Influence of different cryogenic treatments on high-temperature wear behavior of M2 steel," *Wear*, vol. 376–377, pp. 1112–1121, 2017.
- [18] KB. Hariharan, S. Saravanan, and N. Parkunam, "Life time improvement of D7 tool steel by cryogenic treatment," *Materials Today: Proceedings*, vol. 21, no. 1, pp. 619–621, 2019.
- [19] A. Sert and O. N. Celik, "Characterization of the mechanism of cryogenic treatment on the microstructural changes in tungsten carbide cutting tools," *Materials Characterization*, vol. 150, pp. 1–7, 2019.
- [20] G. Abrosimova, N. Volkov, T. Pershina, and A. Aronin, "Cryogenic rejuvenation of Al-based amorphous-nanocrystalline alloys," *Materials Letters*, vol. 240, pp. 150–152, 2019.
- [21] A. Bensely, L. Shyamala, S. Harish et al., "Fatigue behaviour and fracture mechanism of cryogenically treated En 353 steel," *Materials & Design*, vol. 30, no. 8, pp. 2955–2962, 2009.
- [22] S. Han, Q. Gao, Y. Cheng, C. Yan, Z. Han, and X. Shi, "Experimental study on brittle response of shale to cryogenic fluid nitrogen treatment," *Journal of Petroleum Science and Engineering*, vol. 194, Article ID 107463, 2020.
- [23] I. Alexandru and V. Bulancea, "Effect of cryogenic cooling on residual stresses, structure and substructure," from: in *Handbook of Residual stress and Deformation of Steel*, G. Totten, M. Howes, and T. Inoue, Eds., pp. 331–334, ASM International, Ohio, 2002.
- [24] A. Bensely, S. Venkatesh, D. M. Lal, G. Nagarajan, A. Rajadurai, and K. Junik, "Effect of cryogenic treatment on distribution of residual stress in case carburized En 353 steel," *Materials Science and Engineering A*, vol. 479, no. 1–2, pp. 229–235, 2008.
- [25] D. Senthilkumar, I. Rajendran, M. Pellizzari, and J. Siiriainen, "Influence of shallow and deep cryogenic treatment on the residual state of stress of 4140 steel," *Journal of Materials Processing Technology*, vol. 211, no. 3, pp. 396–401, 2011.
- [26] L. Y. Xu, J. Zhu, H. Y. Jing, L. Zhao, X. Q. Lv, and Y. D. Han, "Effects of deep cryogenic treatment on the residual stress and mechanical properties of electron-beam-welded Ti-6Al-4V joints," *Materials Science and Engineering A*, vol. 673, pp. 503–510, 2016.
- [27] B. Sachin, S. Narendranath, and D. Chakradhar, "Effect of cryogenic diamond burnishing on residual stress and microhardness of 17-4 ph stainless steel," *Materials Today: Proceedings*, vol. 5, no. 9, pp. 18393–18399, 2018.
- [28] J. Kong, Z. Xia, D. Xu, and N. He, "Investigation on notch wear mechanism in finish turning pure iron material with uncoated carbide tools under different cooling/lubrication conditions," *International Journal of Advanced Manufacturing Technology*, vol. 86, no. 1–4, pp. 97–105, 2016.
- [29] S. Jiang, S. Yan, Y. Liu, C. Duan, J. Xu, and Y. Sun, "Analytical prediction of chatter stability in turning of low-stiffness pure iron parts by nosed tool," *International Journal of Advanced Manufacturing Technology*, vol. 102, no. 5–8, pp. 1227–1237, 2019.

Research Article

X-Ray Image Recognition Based on Improved Mask R-CNN Algorithm

Jicun Zhang ^{1,2}, Xueping Song ¹, Jiawei Feng ², and Jiyou Fei ¹

¹School of Mechanical Engineering, Dalian Jiaotong University, Dalian, Liaoning 116028, China

²Neusoft Group (Dalian) Co., Ltd., Dalian, Liaoning 116085, China

Correspondence should be addressed to Jicun Zhang; zhangjicun89@163.com and Jiyou Fei; fjy@djtu.edu.cn

Received 1 August 2021; Accepted 21 August 2021; Published 7 September 2021

Academic Editor: Shanglei Jiang

Copyright © 2021 Jicun Zhang et al. This is an open access article distributed under the Creative Commons Attribution License, which permits unrestricted use, distribution, and reproduction in any medium, provided the original work is properly cited.

It is an important part of security inspection to carry out security and safety screening with X-ray scanners. Computer vision plays an important role in detection, recognition, and location analysis in intelligent manufacturing. The object detection algorithm is an important part of the intelligent X-ray machine. Existing threat object detection algorithms in X-ray images have low detection precision and are prone to missed and false detection. In order to increase the precision, a new improved Mask R-CNN algorithm is proposed in this paper. In the feature extraction network, an enhancement path is added to fuse the features of the lower layer into the higher layer, which reduces the loss of feature information. By adding an edge detection module, the training effect of the sample model can be improved without accurate labeling. The distance, overlap rate, and scale difference between objects and region proposals are solved using DIoU to improve the stability of the region proposal's regression, thus improving the accuracy of object detection; SoftNMS algorithm is used to overcome the problem of missed detection when the objects to be detected overlap each other. The experimental results indicate that the mean Average Precision (mAP) of the improved algorithm is 9.32% higher than that of the Mask R-CNN algorithm, especially for knife and portable batteries, which are small in size, simple in shape, and easy to be mistakenly detected, and the Average Precision (AP) is increased by 13.41% and 15.92%, respectively. The results of the study have important implications for the practical application of threat object detection in X-ray images.

1. Introduction

At present, in the express logistics industry, high-speed railway stations, airports, and other public transportation fields, the security detection of parcels, baggage, and other items is mainly realized by X-ray security machines plus manual detection by human inspectors. The detection results mainly rely on the experience of screeners, which has high input cost and low efficiency. There are many kinds of items to be detected, which may be likely to be covered by other items, so the false detection and missed detection of manual detection occur from time to time.

Computer vision plays an important role in detection, recognition, and location analysis in intelligent manufacturing. With the development of artificial intelligence, automatic detection can be realized with the help of

computer vision technology to replace manual detection. The object detection algorithm is an important part of computer vision.

Recently, deep learning has shown promising results in many image-based tasks. Convolutional neural networks (CNNs) [1] are the derivatives of deep learning, which have been widely used in various applications, such as medical image analysis and applications [2–4], face detection [5], speech recognition [6], pose estimation [7], and other computer vision tasks.

The image recognition technology is integrated into the X-ray security scanning machine to realize the automatic detection of threat items, which can greatly reduce the workload of human inspectors and improve detection efficiency and precision. It has important significance in the field of security inspection of intelligent logistics and intelligent transportation.

The research of threat object detection in X-ray images has also made some progress [8–10]. In order to generate a large number of X-ray images of bags with threat objects, Threat Image Projection (TIP) [11] was developed. A real-time TIP model based on deep learning was proposed. Therefore, this model can be used to train screeners to recognize threat objects in real-time TIP images and can be applied to automated detection of threat objects research in the future.

Mery et al. [12] attempt to make a contribution to the field of object recognition in X-ray testing by evaluating different computer vision strategies that have been proposed in the last years, such as BoWs, sparse representations, deep learning, and classic pattern recognition schemes, among others. The author believes that a CNN trained with X-ray images (instead of optical images) would lead to better results in X-ray testing.

Akcay et al. [10] compare several object detection methods and come to a conclusion: it shows that contemporary Faster R-CNN, R-FCN, and YOLOv2 approaches outperform SW-CNN, which is already empirically shown to outperform handcrafted features regarding both speed and accuracy. CNN features achieve superior performance to handcrafted BoVW features.

Gao et al. [13] propose the combination of Faster R-CNN algorithm and Feature Pyramid Network to realize the detection of small items on clothes, which shows that Faster R-CNN is effective for small items detection.

Gaus et al. [14] propose a dual CNN architecture to firstly isolate liquid and electrical objects by type and subsequently screen them for abnormalities.

The abovementioned convolutional neural networks have made some achievements in the field of threat object detection in an X-ray image, but they cannot reach the practical application level for the safe detection of Real-time X-ray images. The main difficulties in X-ray detection of threat objects are as follows: (1) Objects are blocked and overlapped, which are easy to be undetected. (2) Some threat objects are small in size and simple in shape, such as knives and portable batteries, which are easily confused with other items in X-ray images, and the object detection precision is low.

There are two kinds of object detection algorithms based on the neural network: one-stage detection algorithm and two-stage algorithm. One-stage detection algorithm is represented by YOLO [15] and SSD [16]. The full name of YOLO is “You Only Look Once,” which means that the algorithm only needs one CNN operation. YOLO uses an end-to-end unified, fully convolutional network structure that predicts the objectless assurance and the bounding boxes concurrently over the whole image. YOLO resizes the input image, runs a single convolutional network on the image, and thresholds the resulting detections by model’s confidence.

The full name of SSD algorithm is “single shot multibox detector.” Single shot indicates that SSD algorithm belongs to the one-stage method, and multibox indicates that SSD is multibox prediction. It combined the anchor mechanism in the Faster R-CNN and the regression idea in YOLO, as the

input image feature extraction using a small convolution filter, and the feature of the different scales with different aspect ratio classification prediction.

The one-stage algorithm directly extracts features from the network to predict object classification and location, the speed is fast, but the accuracy is not as high as that of the two-stage algorithm. It is widely used in the field of video stream object detection with high real-time requirements [17–21].

The two-stage detection algorithm is represented by the R-CNN algorithm. The two-stage algorithm needs to generate a region proposal (a preselected box that may contain the object to be inspected) and then classify each candidate box (the position will also be corrected). This kind of algorithm is relatively slow because it needs to run the detection and classification process many times, but the accuracy is high.

The application scene of X-ray image threat object detection requires high recognition accuracy. So, the R-CNN algorithm with two-stage detection is more suitable for this scene. In this paper, the Mask R-CNN algorithm, which has a good effect in the field of object detection, is selected and optimized. The optimized algorithm has improved the mean Average Precision (mAP) more than the original Mask R-CNN algorithm and also improved a lot compared with other algorithms, which has the practical value of threat object detection in X-ray images.

The main contributions of this paper are as follows:

- (1) An improved algorithm based on Mask R-CNN is proposed. By optimizing in the network layer, the loss of feature information is reduced; online hard negative example mining (OHEM) is used to improve the robustness of the model.
- (2) Using DIoU instead of IoU makes the object region overlap more with the region proposal and the regression effect is better; SoftNMS algorithm is used to replace the NMS algorithm, which increases the object detection rate in the overlapping area of threat objects.
- (3) We propose an X-ray image dataset for model training and testing. Our experimental results show that the performance of the proposed method outperforms the state-of-the-art object detection method in precision and recall rate, especially for overlapped objects and threat objects with small sizes and simple shapes.

2. Materials and Methods

The development process of the R-CNN algorithm is shown in Figure 1, from R-CNN [22], Fast R-CNN [23], Faster R-CNN [24] to the most advanced Mask R-CNN [25] algorithm at present, which is manifested in the continuous improvement of precision and speed, covering various fields from classification to detection, segmentation and positioning [26–30]. The two-stage detection has high detection precision and strong robustness, but the detection speed is slow. The one-stage detection has a simple structure and fast

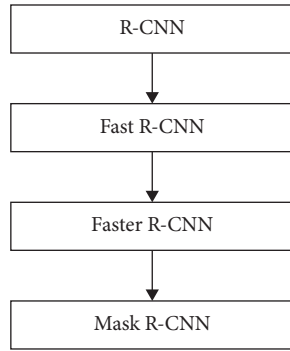


FIGURE 1: The development process of R-CNN algorithm, from R-CNN to Mask R-CNN.

detection speed but low detection precision and poor anti-interference ability. From the detection speed of CNN, Faster R-CNN is slower than YOLO and other one-stage algorithms when using GPU, but it can also reach the detection speed of 5FPS [31], which can fully meet the security requirements of X-ray machines.

2.1. Mask R-CNN. Based on Faster R-CNN, Mask R-CNN introduced the segmentation branch, which is composed of four convolutions, one deconvolution, and one convolution to realize instance segmentation. Moreover, ROI Align is proposed to fix the misalignment problem of ROI pooling, which could greatly improve the segmentation accuracy. The backbone of Mask R-CNN is ResNet [32] and Feature Pyramid Networks (FPN) [33]. The backbone uses residual learning to precisely extract object features and uses the feature pyramid to fuse multiscale features so as to construct high-quality feature maps.

After feature map extraction, RPNs are applied to extract ROIs from the feature maps. Then the ROIs are aligned and pooled by ROI Align. The aligned ROIs are used to instance segmentation by convolution and fully connected networks. The structure of MaskR-CNN is shown in Figure 2.

Mask R-CNN has many applications in image segmentation [34]. Mask R-CNN incorporates the advantages of previous algorithms and improves them to make the recognition more accurate, the training speed faster, and the effect better. In particular, the feature extraction structure of ResNet residual network + FPN is introduced, which solves the problem of difficult detection of small objects and has been applied in many fields. Mask R-CNN has significantly improved the effect on small object detection [35].

2.1.1. Feature Extraction Network. Mask R-CNN uses a feature extraction network composed with a feature pyramid structure by the residual network [36], which is divided into top-down and bottom-up parts. ResNet network is used in the bottom-up path, and five feature maps with different coarse granularities are generated through C_1 to C_5 modules. Each module is composed of multiple residual learning structures. For example, the structure of C_3 is $\{1 \times 1, 128; 3 \times 3, 128; 1 \times 1, 512\} \times 4$. This means that four residual

learning structures are included, each of which consists of 3 convolution layers, with convolution kernels of 1×1 , 3×3 and 1×1 , and the number of channels of 128, 128, and 512, respectively. In the bottom-up path, the step size of the first convolution kernel in each stage is 2, and the step size of other convolution kernels is 1. Therefore, the size of the feature map is halved every time it passes through a module, and feature maps with different sizes can be obtained in this way.

In the top-down path, the high-level features are sampled twice, then the features obtained by 1×1 convolution are fused with those obtained by the bottom-up path, and finally a new feature map P2~P5 is obtained by 3×3 convolution. As shown in Figure 3, when an image with a size of 1024×1024 is input, the final feature map size is $\{32 \times 32, 64 \times 64, 128 \times 128, 256 \times 256\}$.

2.1.2. Region Proposal Network. Region Proposal Network [37] (RPN) is a full convolution neural network that uses the feature map to calculate the position of objects in images and can accept images of different sizes as input.

Different from the traditional Selective Search [38], the input of the RPN network is the feature map obtained by the feature extraction network. As shown in Figure 4, a multiscale anchor is generated by a sliding window in the feature map.

Further, as shown in Figure 5, RPN regresses each feature vector in the feature map to obtain a correction vector to correct the anchor. The correction value includes two confidences of foreground and background and four-position information, among which the correction mode of position information is shown in formula (1). Windows are generally represented by four-dimensional vectors (x, y, w, h) . x, y is the coordinate of the center point, and w and h are the width and height of the candidate bounding box. By moving and zooming, the candidate bounding box is closer to its real position.

A large number of candidate bounding boxes can be obtained after the correction of anchor, and the foreground and background scores of these candidate bounding boxes are calculated, and the more accurate candidate bounding boxes are filtered out by nonmaximum suppression (NMS) [39].

$$\begin{cases} x = (1 + \Delta x) \cdot x, \\ y = (1 + \Delta y) \cdot y, \\ w = \exp(\Delta w) \cdot w, \\ h = \exp(\Delta h) \cdot h. \end{cases} \quad (1)$$

2.1.3. ROI Align. Since there is a certain correspondence between the image to be detected and the feature map of the image, mapping the target region in the image to the feature map is called a region of interest (ROI) mapping. In the Faster R-CNN algorithm, this process is completed in the ROI pooling layer, which converts input images of different sizes into a fixed dimensional feature vector output for

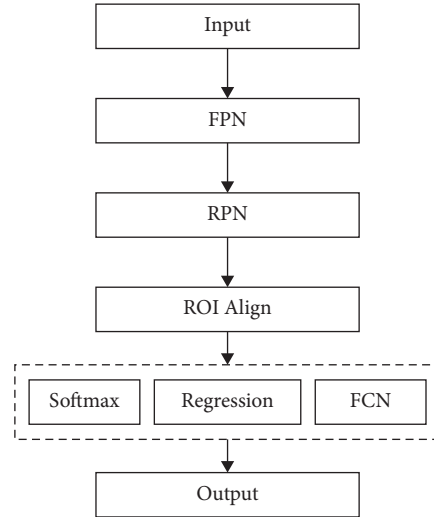


FIGURE 2: Mask R-CNN algorithm flow.

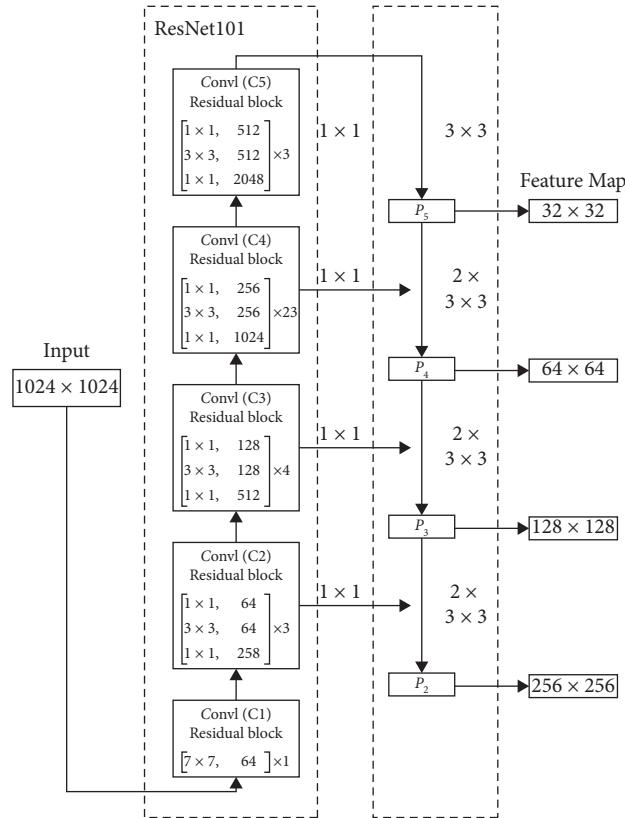


FIGURE 3: Feature extraction network using ResNet101.

subsequent head network training. The ROI Pooling uses the nearest-neighbor interpolation for region scaling, so if floating-point numbers are encountered in the process of pooling, they will be rounded off, resulting in the loss of information and then affecting the accuracy of detection.

The Mask R-CNN algorithms use ROI Align instead of ROI Pooling to avoid the loss of information. As shown in Figure 6, ROI Align uses bilinear interpolation in the process

of region scaling, and the specific steps are traversing each candidate region, retaining the region boundary of floating-point numbers and dividing the candidate region into $k \times k$ cells, and the boundary of each cell also retains floating-point numbers.

The bilinear interpolation is used to calculate the fixed four candidate regions and divide them into $k \times k$ cells, and the boundaries of each cell are also preserved as floating-

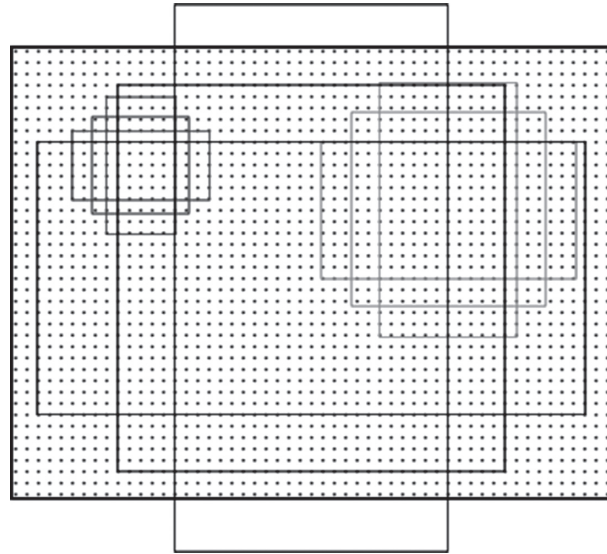


FIGURE 4: A multiscale anchor, generated by sliding window.

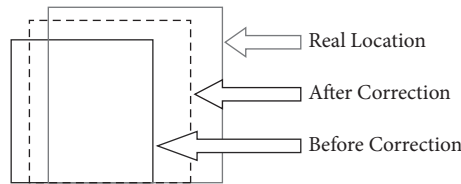


FIGURE 5: Correction process, the candidate bounding box is closer to its real position.

point numbers. Finally, the bilinear interpolation is used to calculate the values of fixed four coordinate positions, and then the max-pooling is carried out. ROI Align solves the problem of information loss in ROI Pooling by introducing bilinear interpolation for pooling, which turns the original discrete pooling process into a continuous process.

2.1.4. Network Header. Similar to Faster R-CNN, the network header of Mask R-CNN calculates the input characteristics of ROI Align. A fully connected layer plus Softmax is usually used to classify region proposals. At the same time, the region proposal is modified by two-stage regression in the same way as in the RPN process.

In addition, on the basis of classification and regression, Mask R-CNN obtains the accurate position information of the object through an FCN segmentation network [40] according to the obtained object border.

As shown in Figure 7, the input of the FCN segmentation network is the 14×14 characteristic map output by ROI Align, and the original 14×14 size is maintained using four 3×3 convolutional layers, then the size is boosted to 28×28 by a 2×2 deconvolution layer, and finally the 28×28 output is obtained by a 1×1 convolutional layer with a sigmoid activation layer. Each point in the output is the confidence of foreground and background in the region proposal, and the points are classified with a threshold of 0.5 to finally get the precise region of the target object.

2.2. Optimization of Mask R-CNN Algorithm. The process of using the Mask R-CNN algorithm to detect threat objects from an X-ray image is shown in Figure 8. Through network optimization, IoU index optimization, optimizer improvement, and prediction optimization of Mask R-CNN, the accuracy of threat object detection through X-ray by Mask R-CNN is improved.

2.2.1. Network Optimization. (1). Feature Extraction Optimization. In the feature extraction network, the high-level features focus on the overall object and the low-level features focus on the texture of the object, and the object can be better detected and localized by the low-level features. In the original feature extraction network shown in Figure 3, much information is lost in the lower layers, and the local texture of the object plays a greater role in the effectiveness of object detection due to the particularity of the X-ray image. Therefore, the original feature extraction network has room for improvement. Referring to the feature extraction network in PANet proposed in [41], as shown in Figure 9, this paper adds a bottom-up enhancement path after the top-down feature network in Figure 3 and fuses the low-level features into the high-level features again to avoid the loss of information.

(2) Online Hard Negative Example Mining. Traditional RPN network needs to take out ROI according to positive and negative samples of 1 : 3, in which the judgment condition of

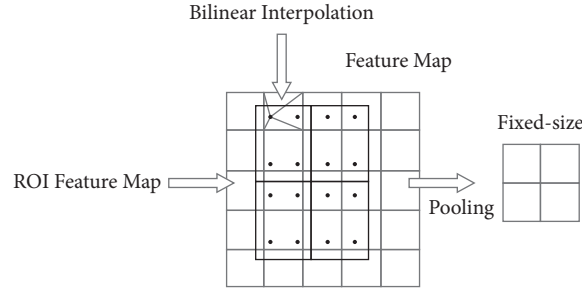


FIGURE 6: ROI Align, using bilinear interpolation to avoid the loss of information.

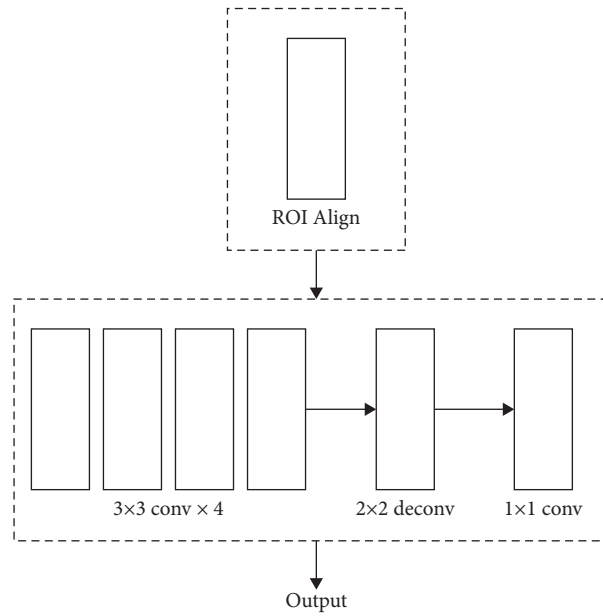


FIGURE 7: FCN segmentation network, output by ROI Align.

positive samples is that IoU is greater than 0.5, and the judgment condition of negative samples is that IoU is between [0.1, 0.5). The reason why it needs to be greater than 0.1 is to do a heuristic mining of hard examples. However, compared with online hard example mining (OHEM) [42], this heuristic hard example mining only uses prior hyper-parameters, and OHEM can mine online hard examples, so it is more suitable for the iterative training mode of Mask R-CNN.

In the Mask R-CNN algorithm, ROI Align and its subsequent networks are called ROI networks. OHEM accomplishes online hard example mining by building two ROI networks. The idea is as follows: in the model training network, more ROIs are generated by the RPN network.

As shown in Figure 10, these ROIs are first passed to an OHEM network the same as the original ROI network, and the information of this network is only passed forward. The OHEM network calculates the loss of all ROIs and then sorts the ROIs by Loss, selects the specified number of ROIs with larger loss, and passes these ROIs to the ROI network for model training. Obviously, compared with selecting positive and negative samples through prior parameters, this online

hard example mining can filter out more hard examples, and the robustness of the model can be improved by this training method.

(3) *Edge Detection.* X-ray image labeling often cannot be accurately labeled to the edges of objects, and most cases are labeled with rectangular boxes. Therefore, when using the Mask R-CNN algorithm directly, the accuracy of the Mask part will be affected. That is, the calculated L_{Mask} cannot accurately reflect the actual situation. In order to reduce the error, the Sobel operator is introduced before calculation, and the Mask_{new} and GT_{new} are generated by the Sobel operator interacting with Mask and GT (Ground Truth) after Gaussian filter denoising.

Sobel operator is a commonly used edge detection operator [43], which interacts with Mask by using the Sobel operator. Sobel operator contains two sets of 3×3 matrices, representing horizontal and vertical, respectively. The horizontal and vertical luminance difference approximations can be obtained by plane convolution with the image. G_x and G_y represent the image gray values of edge detection by horizontal and vertical, respectively.

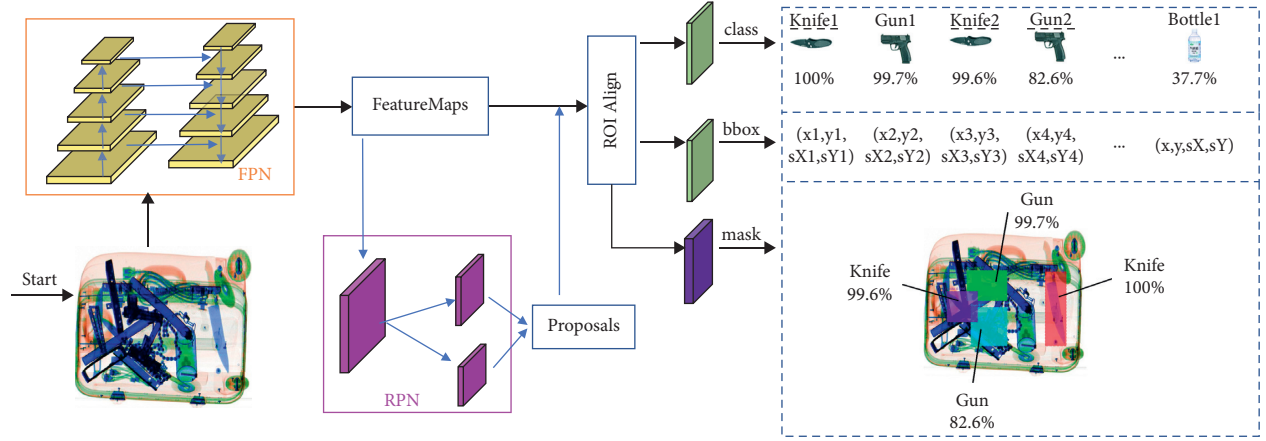


FIGURE 8: Mask R-CNN structure, from the input image to object classification and prediction.

The derivatives are derived in both directions as shown in equations (2) and (3), and then for each point of the image, the approximate gradient is derived as shown in equation (4).

$$G_x = \begin{bmatrix} -1 & 0 & 1 \\ -2 & 0 & 2 \\ -1 & 0 & 1 \end{bmatrix} * \text{Mask}, \quad (2)$$

$$G_y = \begin{bmatrix} -1 & -2 & -1 \\ 0 & 0 & 0 \\ 1 & 2 & 1 \end{bmatrix} * \text{Mask}, \quad (3)$$

$$\text{Mask}_{\text{new}} = G = \sqrt{G_x^2 + G_y^2}. \quad (4)$$

Sobel operator can make the features of edges in Mask and GT more prominent while weakening the nonedge part, so using the processed Mask_{new} and GT_{new} to calculate L_{mask} can make the Mask part fit more accurately.

2.2.2. IoU Index Optimization. In the traditional Mask R-CNN algorithm, IoU is used as a measure of the overlap degree of candidate regions. By calculating IoU, positive and negative samples can be determined, and the distance between candidate regions and the target objects can also be evaluated. Its advantage is that it is insensitive to scale and is not affected by the image to be detected and the size of the object.

However, IoU still has some limitations. For example, IoU cannot accurately reflect the coincidence degree between the two regions. As shown in Figure 11, when two regions overlap in different ways, the same IoU may be obtained. Obviously, the two regions in the first group have high overlap and better regression, while the last group has low overlap and poor regression.

To avoid these problems, DIoU (Distance-IoU) [44] can be used instead of IoU, which is more suitable for regression of candidate regions than traditional IoU. DIoU takes into account the distance, overlap rate, and scale between the object and the candidate region, and the regression of the

candidate region can be more stable by using DIoU. The definition of DIoU is shown in the following formula:

$$\text{DIoU} = \text{IoU} - \frac{\rho^2(b, b^{gt})}{c^2}, \quad (5)$$

where $\rho(b, b^{gt})$ represents the Euclidean distance between the center points of the two regions and c represents the diagonal distance of the minimum closed region containing both candidate regions, as shown in Figure 12. Compared with the traditional IoU, DIoU can directly minimize the distance between the center point of the prediction box and the real box, accelerate convergence, reduce errors, make the regression effect better, and make the results obtained in the process of SoftNMS more reasonable and effective.

2.2.3. Optimizer Improvement. When using the existing algorithms, the parameters of the model are updated by Mini-Batching. Because the image takes up too much video memory, in most cases, the hardware conditions cannot meet the requirement of training all samples at the same time. The idea of Mini-Batching is that during the training process of the model, each Epoch disrupts all the samples and generates multiple fixed-size subsets (Mini-Batch). The optimizer trains one Mini-Batch at a time and averages and updates the parameters trained by each sample in this Mini-Batch to the model. When the size of Mini-Batch is too small, this method almost degenerates to stochastic gradient descent (SGD) [45]. Compared with object detection in other scenarios, X-ray images tend to have fewer positive examples, which can lead to very few positive examples trained in each Mini-Batch when the size of the Mini-Batch is too small, resulting in greater randomness in model optimization.

To reduce the effect, this paper introduces a hyper-parameter (integer n). In the training process of the model, the weight updating of the model is not carried out after each training of Mini-Batch. When n Mini-Batches are trained, the mean value of the weights in multiple Mini-Batches is calculated, and the model

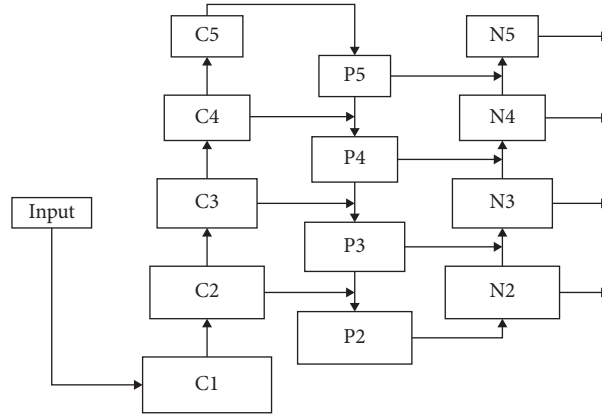


FIGURE 9: Improved feature extraction network from N2 to N5.

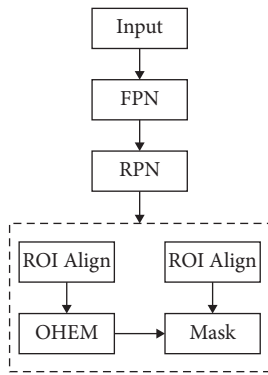


FIGURE 10: Training network with OHEM.

weights are updated. The purpose of expanding the size of Mini-Batch is achieved by this method.

2.2.4. Prediction Optimization. In the process of RPN, after the anchor is modified, the candidate regions need to be filtered by the NMS algorithm, and all the candidate regions are sorted according to their scores. The candidate region A_0 with the highest score is selected, and the intersection of union (IoU) of A_0 with another candidate region A_i is calculated. For A_i , whose IoU is higher than the specified threshold, it will be deleted, and then the one with the highest score is selected from the remaining candidate regions to repeat this step until no candidate regions can be deleted.

By this method, redundant candidate regions can be eliminated and the best detection position can be found. However, the NMS algorithm still has some limitations. On the one hand, it is a challenge to set a suitable threshold value. If the threshold value is set too high, fewer candidate regions will be removed, resulting in the ineffectiveness of the NMS algorithm; on the contrary, if the setting is too low, more candidate regions may be deleted, resulting in missed detection. On the other hand, if there are two objects with high coincidence in the image to be detected, the NMS algorithm will delete the objects with relatively low scores, so in this case, it is very likely to cause the missed detection of threat objects. The reason for this problem is

that the NMS algorithm only considers the coincidence degree of other candidate regions and the candidate regions with the highest score but does not pay attention to the scores of these candidate regions. Through the recognition precision of NMS and SoftNMS [46], SoftNMS improves the effect significantly. To solve this problem, SoftNMS is used instead of the NMS algorithm, as shown in formula (6), where S_i is the classification confidence, N_t is the threshold, and M is the box with the highest confidence.

$$S_i = \begin{cases} S_i, & \text{IoU}(M, b_i) < N_t, \\ 0, & \text{IoU}(M, b_i) \geq N_t. \end{cases} \quad (6)$$

In the NMS algorithm, the candidate region that overlaps with the highest scoring candidate region M will be deleted with a score of 0. In the SoftNMS algorithm, the score of the candidate region is deducted by multiplying the score of the candidate region by Gaussian weight, as shown in the following formula:

$$S_i = S_i e^{-iou(M, b_i)^2 / \sigma}. \quad (7)$$

When the overlapping candidate region has a high score, this method can avoid the candidate region being filtered out.

Taking the knife as an example, when the image to be detected is shown in Figure 13, the part marked by the color box is the threat object, and the two knives marked by the green box and blue box on the far left have more overlap. The result of the detection using the NMS algorithm is shown in Figure 14(a), and the knife with a lower score on the left side (corresponding to the green box in Figure 13) is filtered by the NMS algorithm, resulting in missed detection.

The detection results after replacing the NMS algorithm in Figure 14(a) with the SoftNMS algorithm are shown in Figure 14(b). Although the prediction probability of the missed detection of knives caused by the NMS algorithm is lower, they are not filtered out by the SoftNMS algorithm. Therefore, in this way, under the condition of ensuring the same detection precision of other items, the problem of missed detection by the NMS algorithm when there are multiple overlapping objects in the image can be effectively avoided.

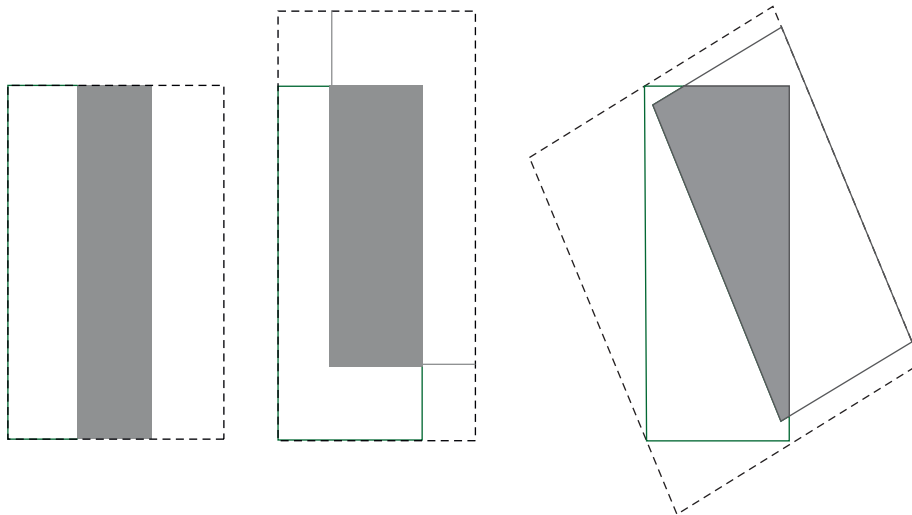


FIGURE 11: Different overlapping ways of the same IoU.

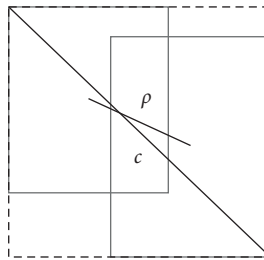


FIGURE 12: DIoU loss for bounding box regression.

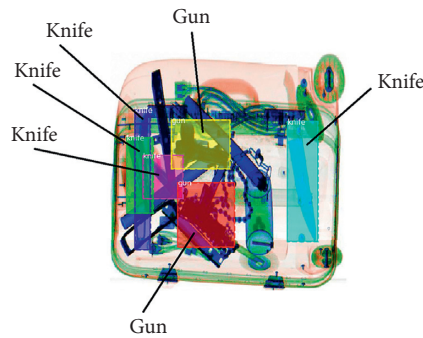


FIGURE 13: An example with ground truth.

3. Results and Discussion

3.1. *Preprocessing of X-Ray Image Data.* The original X-ray image contains many redundant parts, such as the text in the upper and lower parts and the blank background in Figure 15(a), but only the region marked by the dashed line in the figure is useful for algorithm training and prediction.

If the original image is directly used for algorithm training, on the one hand, there will be redundant noise which may lead to an inefficient training effect, and on the

other hand, the size of the image passed into the training will be too large to slow down the speed of the algorithm training. Therefore, it is necessary to preprocess the original image before accessing the algorithm training and image analysis module. The contour detection algorithm in OPENCV can effectively identify the cargo in the original image, and the image processed by the algorithm is shown in Figure 15(b). Since the model training is implemented on the GPU, the redundant parts of the image are eliminated after preprocessing, the occupied video memory becomes smaller, and more images

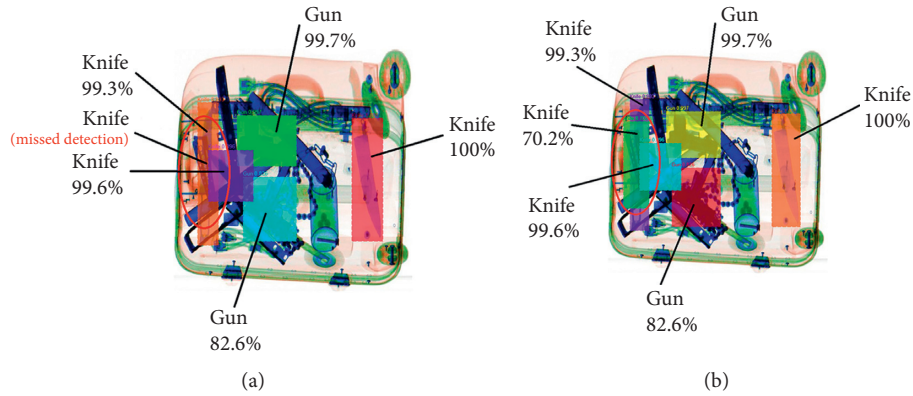


FIGURE 14: Detection results using NMS algorithm and SoftNMS algorithm. (a) Result of NMS. (b) Result of SoftNMS.

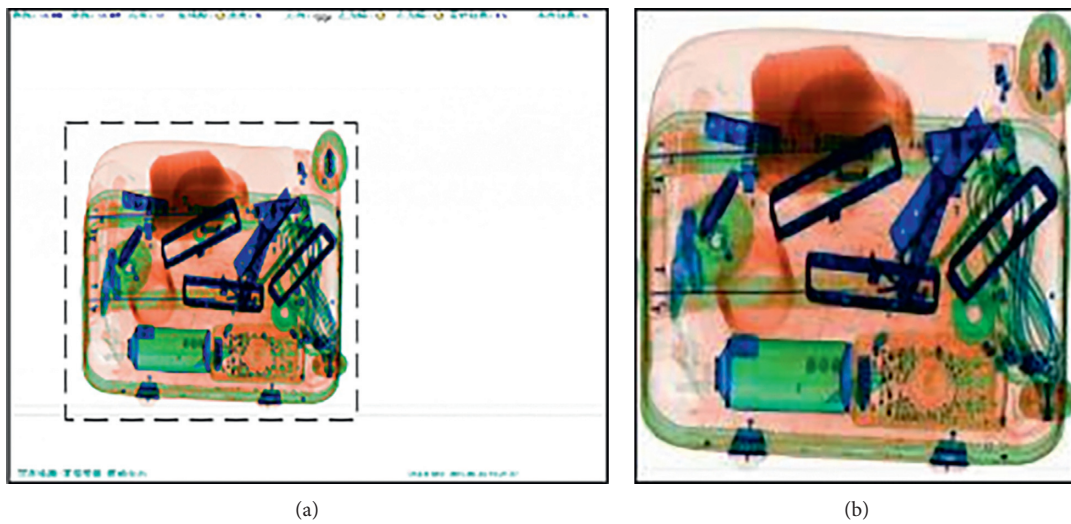


FIGURE 15: X-ray image preprocessing. (a) Original X-ray image. (b) Preprocessed image; the blank area was removed.

can be trained each time, so the effectiveness and efficiency of the algorithm training can be improved.

3.2. Experimental Environment and Parameter Settings. The hardware used in the experiment is shown in Table 1, and the software environment is shown in Table 2:

The X-ray image dataset is shown in Figure 16. We chose images from SIXray dataset [47] and simulated threat object images from the X-ray machine. It contains 5 classes of threat objects: knife, gun, liquid, mobile phone, and portable battery, with 6155 images in the train set and 560 images in the validation set. The algorithm parameters are set to train 2 images each time, and each Epoch contains 1000 trainings. The learning rate of the first 120 Epoch is 0.001, and then it is adjusted to 0.0001. The final algorithm achieves the best convergence effect at 160.

In order to verify the effectiveness of the improved algorithm, Mask R-CNN and other object detection algorithms are used to train the same dataset, and the training results are compared.

3.3. Comparison between Improved Algorithm and Mask R-CNN. In order to verify the effectiveness of the improved parts, the training results of the Mask R-CNN algorithm are compared with the detection results of the improved algorithm, and the results are shown in Figure 17.

The horizontal axis in Figure 17 is the recall rate, the vertical axis is the precision rate, and the three curves represent the detection effect under different IoU thresholds. The area below the curve is the AP value. It can be seen that in the results of the two algorithms, liquid, gun, and cell phone can be detected effectively. This is because the features of liquid, gun, and cell phone are obvious, and the objects and background are easy to distinguish, so recall and precision are both high; the knife and the portable battery have simple shapes, no obvious features, and it is not easy to distinguish between objects and background, so recall and precision are low. In the original Mask R-CNN algorithm, the detection effect of the knife and the portable battery are poor, while in the improved algorithm, the detection effect has been significantly improved.

It can be seen that the recall rate of the two classes of items, knife, and portable battery, is significantly increased

TABLE 1: Hardware environment.

CPU	Inter (R) Core (TM) i7-2600 CPU @3.40 GHz
GPU	TitanX 12G
Memory size	32 GB

TABLE 2: Software environment.

Operation System	CentOS 7
Development language	Python 3.6
Deep-learning API	Keras 2.0
Deep-learning framework	TensorFlow 1.3

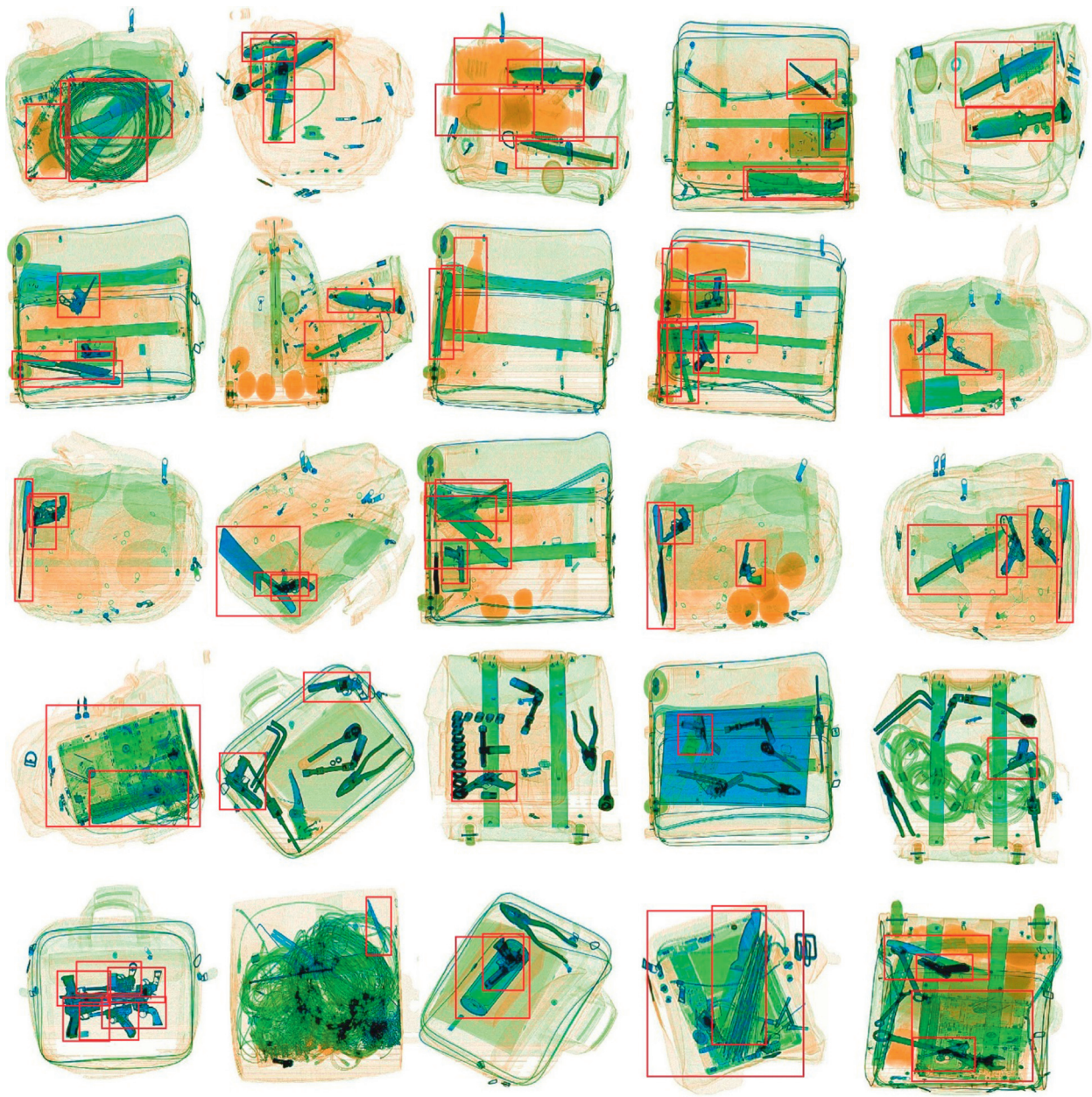


FIGURE 16: X-ray image dataset, including 5 classes of threat objects: knife, gun, liquid, mobile phone, and portable battery.

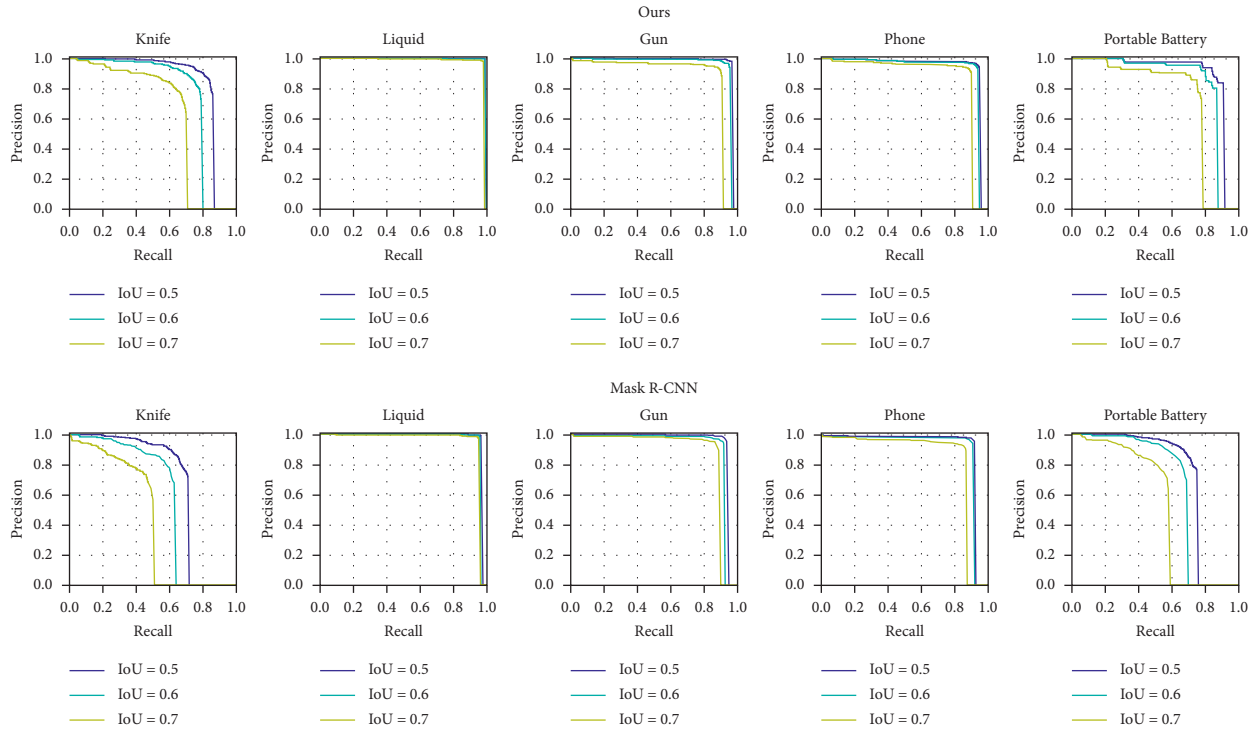


FIGURE 17: Comparison of detection effects of multiple objects.

in the improved algorithm (shown in the figure as the right shift of the intersection of the curve with the X -axis), and the accuracy rate is also obviously improved (shown in the figure as the upward shift of the curve, i.e., the increase of the value of Y for the same value of X).

From the aspect of algorithm structure, the improved algorithm has made a variety of optimizations in the network part (adding PANet enhancement path, introducing online hard example mining, introducing edge detection operator, optimizing IoU index, and improving optimizer), which has significantly improved the extraction effect of feature information and training effect of the algorithm. At the same time, SoftNMS is used to replace NMS in the inference part of the model, which reduces the cases where the detection objects are filtered out due to overlap and thus improves the recall rate of the algorithm model.

3.4. Comprehensive Comparison. The detection effect of the improved algorithm is compared with Mask R-CNN, Faster R-CNN, YOLOv3, and SSD513, and AP50 is used as the criterion. The results are shown in Table 3.

As can be seen, the detection effect of the one-stage algorithm (YOLOv3 and SSD513) is obviously lower than that of the two-stage algorithm due to its relatively simple network. The Mask R-CNN is improved based on Faster R-CNN, so the detection effect is better than that of Faster R-CNN, which is also a two-stage algorithm. Compared with the original Mask R-CNN algorithm, the improved algorithm in this paper has a significant improvement in detection effect because of the various optimizations mentioned above. The improved Mask R-CNN algorithm

TABLE 3: Comparison of algorithm recognition results (AP50).

Threat objects						
Algorithm	Knife (%)	Liquid (%)	Gun (%)	Phone (%)	Portable battery (%)	Mean (%)
Ours	83.75	99.01	96.74	93.74	88.74	92.40
Mask R-CNN	70.34	94.43	90.22	87.60	72.82	83.08
Faster R-CNN	45.74	90.63	86.78	73.77	71.86	73.76
YOLOv3	39.16	90.12	85.77	70.03	69.53	70.92
SSD513	38.51	84.35	76.74	63.42	61.92	64.99

increases the value of mAP by 9.32%, and the AP values of the knife and portable battery with poor detection effect in the original Mask R-CNN algorithm is increased by 13.41% and 15.92%, respectively.

4. Conclusions

In order to realize the intelligent manufacturing of X-ray machine equipment, it is necessary to improve the accuracy of object detection. An improved algorithm based on Mask R-CNN is proposed in this paper, aiming at the problems of irregular placement, occlusion and overlap, small size, and simple shape in X-ray security inspection images.

- (1) We optimized the network layer: bottom-up enhancement paths are added to fuse the features of the lower layers into the higher ones; we used OHEM to improve the robustness of the model. The training effect of sample model when accurate labeling is not

possible is improved by adding an edge detection module.

- (2) We used DIoU instead of IoU to make the coincidence degree of object region and candidate region higher and the regression effect better. We selected the SoftNMS algorithm to replace the original NMS algorithm, which increased the object detection rate in the overlapping area of threat objects.
- (3) We made an X-ray images dataset which included 5 classes of threat objects: knife, gun, liquid, mobile phone, and portable battery. The experimental results showed that the improved Mask R-CNN algorithm increases the mAP value by 9.32% compared with the original Mask R-CNN algorithm, and the AP values of knife and portable battery with poor detection effect increase by 13.41% and 15.92%, respectively.
- (4) The proposed algorithm compared with other advanced algorithms such as Faster R-CNN, YOLOv3, SSD513. The results also indicated that the improved Mask R-CNN accomplished the most accurate precision attaining a mean accuracy precision of 92.40% with the test data set.

In summary, the results show the effectiveness and robustness of our proposed algorithm for threat object detection in X-ray images. Therefore, more research will be conducted to improve the accuracy of the small object such as knives and portable batteries with relatively low AP values.

Data Availability

The data used to support the findings of this study are included within the article.

Conflicts of Interest

The authors declare that they have no conflicts of interest regarding the publication of this study.

Acknowledgments

This work was supported by the National Natural Science Foundation of China (grant no. 51605069).

References

- [1] A. Krizhevsky, I. Sutskever, and G. E. Hinton, "ImageNet classification with deep convolutional neural networks," *Communications of the ACM*, vol. 60, no. 6, pp. 84–90, 2017.
- [2] P. Christos, C. A. Frantidis, P. T. Gkivogkli, P. D. Bamidis, and C. Kourtidou-Papadeli, "Automatic sleep staging employing convolutional neural networks and cortical connectivity images," *IEEE Transactions on Neural Networks and Learning Systems*, vol. 31, no. 1, pp. 113–123, 2020.
- [3] H. Kang, "Accelerator-aware pruning for convolutional neural networks," *In IEEE Transactions on Circuits and Systems for Video Technology*, vol. 30, no. 7, pp. 2093–2103, 2020.
- [4] H. Chen, C. Wu, B. Du, L. Zhang, and L. Wang, "Change detection in multisource VHR images via deep siamese convolutional multiple-layers recurrent neural network," *IEEE Transactions on Geoscience and Remote Sensing*, vol. 58, no. 4, pp. 2848–2864, 2020.
- [5] J. Deng, J. Guo, and S. Zafeiriou, "Single-stage joint face detection and alignment," in *Proceedings of the IEEE/CVF International Conference on Computer Vision (ICCV)*, pp. 1836–1839, Seoul, Korea, October 2019.
- [6] M. Yousefi and J. H. L. Hansen, "Block-based high performance CNN architectures for frame-level overlapping speech detection," *IEEE/ACM Transactions on Audio, Speech, and Language Processing*, vol. 29, pp. 28–40, 2021.
- [7] X. Du, T. Kurmann, P.-L. Chang et al., "Articulated multi-instrument 2-D pose estimation using fully convolutional networks," *IEEE Transactions on Medical Imaging*, vol. 37, no. 5, pp. 1276–1287, 2018.
- [8] S. Akçay, M. E. Kundegorski, M. Devereux, and T. P. Breckon, "Transfer learning using convolutional neural networks for object classification within X-ray baggage security imagery," in *Proceedings of the 2016 IEEE International Conference on Image Processing (ICIP)*, pp. 1057–1061, Phoenix, AZ, USA, September 2016.
- [9] S. Akçay and T. P. Breckon, "An evaluation of region based object detection strategies within X-ray baggage security imagery," in *Proceedings of the 2017 IEEE International Conference on Image Processing (ICIP)*, pp. 1337–1341, Beijing, China, September 2017.
- [10] S. Akçay, M. E. Kundegorski, C. G. Willcocks, and T. P. Breckon, "Using deep convolutional neural network architectures for object classification and detection within X-ray baggage security imagery," *IEEE Transactions on Information Forensics and Security*, vol. 13, no. 9, pp. 2203–2215, 2018.
- [11] Y. Wei, Z. Zhu, H. Yu, and W. Zhang, "A real-time Threat Image Projection (TIP) model base on deep learning for X-ray baggage inspection," *Physics Letters A*, vol. 400, 2021.
- [12] D. Mery, E. Svec, M. Arias, V. Rizzo, J. M. Saavedra, and S. Banerjee, "Modern computer vision techniques for X-ray testing in baggage inspection," *IEEE Transactions on Systems, Man, and Cybernetics: Systems*, vol. 47, no. 4, pp. 682–692, 2017.
- [13] R. Gao, Z. Sun, J. Huan et al., "Small foreign metal objects detection in X-ray images of clothing products using faster R-CNN and feature pyramid network," *IEEE Transactions on Instrumentation and Measurement*, vol. 70, pp. 1–11, 2021.
- [14] Y. F. A. Gaus, N. Bhowmik, S. Akçay, P. M. Guillén-García, J. W. Barker, and T. P. Breckon, "Evaluation of a dual convolutional neural network architecture for object-wise anomaly detection in cluttered X-ray security imagery," in *Proceedings of the 2019 International Joint Conference on Neural Networks (IJCNN)*, pp. 1–8, Budapest, Hungary, July 2019.
- [15] J. Redmon, S. Divvala, R. Girshick, and A. Farhadi, "You only look once: unified, real-time object detection," in *Proceedings of the IEEE Conference on Computer Vision and Pattern Recognition*, pp. 779–788, Las Vegas, NV, USA, June 2016.
- [16] W. Liu, D. Anguelov, D. Erhan, C. Szegedy, and S. Reed, "SSD: single shot multibox detector," in *Proceedings of the European Conference on Computer Vision (ECCV)*, pp. 21–37, Amsterdam, Netherlands, October 2016.
- [17] L. Barba-Guamán, J. E. Naranjo, A. Ortiz, and J. G. P. Gonzalez, "Object detection in rural roads through

- SSD and YOLO framework,” *Advances in Intelligent Systems and Computing*, vol. 1, pp. 176–185, 2021.
- [18] S. Narejo, B. Pandey, D. E. Vargas, M. Ciro Rodriguez, and R. Anjum, “Weapon detection using YOLO V3 for smart surveillance system,” *Mathematical Problems in Engineering*, vol. 2021, Article ID 9975700, 9 pages, 2021.
- [19] L. Pang, H. Liu, Y. Chen, and J. Miao, “Real-time concealed object detection from passive millimeter wave images based on the YOLOv3 algorithm,” *Sensors*, vol. 20, no. 6, p. 1678, 2020.
- [20] A. Warsi, M. Abdullah, M. N. Husen, M. Yahya, S. Khan, and N. Jawaid, “Gun detection system using YOLOv3,” in *Proceedings of the 2019 IEEE International Conference on Smart Instrumentation, Measurement and Application (ICSIMA)*, pp. 1–4, IEEE, Kuala Lumpur, Malaysia, August 2019.
- [21] H. Huang, D. Sun, R. Wang, C. Zhu, and B. Liu, “Ship target detection based on improved YOLO network,” *Mathematical Problems in Engineering*, vol. 2020, Article ID 6402149, 10 pages, 2020.
- [22] R. Girshick, J. Donahue, T. Darrell, and J. Malik, “Rich feature hierarchies for accurate object detection and semantic segmentation,” *IEEE Conference on Computer Vision and Pattern Recognition (CVPR)*, pp. 580–587, 2014.
- [23] R. Girshick, “Fast R-CNN,” in *Proceedings of the IEEE Conference on Computer Vision and Pattern Recognition (CVPR)*, pp. 1440–1448, Honolulu, HI, USA, July 2015.
- [24] S. Ren, K. He, R. Girshick, and J. Sun, “Faster R-CNN: towards real-time object detection with region proposal networks,” *IEEE Transactions on Pattern Analysis and Machine Intelligence*, vol. 39, no. 6, pp. 1137–1149, 2017.
- [25] K. He, G. Gkioxari, P. Dollár, and R. Girshick, “Mask R-CNN,” in *Proceedings of the IEEE International Conference on Computer Vision (ICCV)*, pp. 2961–2969, Santiago, Chile, December 2017.
- [26] H. Nguyen, “Improving faster R-CNN framework for fast vehicle detection,” *Mathematical Problems in Engineering*, vol. 2019, Article ID 3808064, 11 pages, 2019.
- [27] X. Dai, J. Hu, H. Zhang et al., “Multi-task faster R-CNN for nighttime pedestrian detection and distance estimation,” *Infrared Physics & Technology*, vol. 115, no. 4, 2021.
- [28] Y. Liu, “An improved faster R-CNN for object detection,” in *Proceedings of the 2018 11th International Symposium on Computational Intelligence and Design (ISCID)*, pp. 119–123, Hangzhou, China, December 2018.
- [29] X. Han, “Modified cascade RCNN based on contextual information for vehicle detection,” *Sensing and Imaging*, vol. 22, no. 1, pp. 1–19, 2021.
- [30] B. Liu, J. Luo, and H. Huang, “Toward automatic quantification of knee osteoarthritis severity using improved Faster R-CNN,” *International Journal of Computer Assisted Radiology and Surgery*, vol. 15, no. 3, pp. 457–466, 2020.
- [31] F. Y. Hu, L. Y. Li, and X. R. Shang, “A review of object detection algorithms based on convolutional neural networks,” *Journal of Suzhou University of Science and Technology (Natural Science Edition)*, vol. 37, no. 2, pp. 1–10, 2020.
- [32] K. He, X. Zhang, S. Ren, and J. Sun, “Deep residual learning for image recognition,” in *Proceedings of the IEEE Conference on Computer Vision and Pattern Recognition (CVPR)*, pp. 770–778, Salt Lake City, UT, USA, June 2016.
- [33] T. Y. Lin, “Feature pyramid networks for object detection,” in *Proceedings of the IEEE Conference on Computer Vision and Pattern Recognition (CVPR)*, pp. 2117–2125, Honolulu, HI, USA, July 2017.
- [34] X. Fu, J. Wang, Z. Hu, Y. Guo, and R. Wang, “Automated segmentation for whole human eye OCT image using RM multistage Mask R-CNN,” *Applied Optics*, vol. 60, no. 9, pp. 2518–2529, 2021.
- [35] Y. Liu, “A survey of research and application of small object detection based on deep learning,” *Acta Electronica Sinica*, vol. 48, no. 3, p. 590, 2020.
- [36] S. Xie, R. Girshick, P. Dollár, Z. Tu, and K. He, “Aggregated residual transformations for deep neural networks,” in *Proceedings of the IEEE Conference on Computer Vision and Pattern Recognition (CVPR)*, pp. 1492–1500, Boston, MA, USA, June 2017.
- [37] T. Lin, P. Dollár, R. Girshick, K. He, B. Hariharan, and S. Belongie, “Feature pyramid networks for object detection,” in *Proceedings of the IEEE Conference on Computer Vision and Pattern Recognition (CVPR)*, pp. 2117–2125, 2017.
- [38] Z. Fang, Z. Cao, Y. Xiao, K. Gong, and J. Yuan, “MAT: Multianchor visual tracking with selective Search region,” *IEEE Transactions on Cybernetics*, vol. 2020, Article ID 3039341, 15 pages, 2020.
- [39] A. Neubeck and L. Van Gool, “Efficient non-maximum suppression,” in *Proceedings of the 18th International Conference on Pattern Recognition (ICPR’06)*, pp. 850–855, 2006.
- [40] J. Long, E. Shelhamer, and T. Darrell, “Fully convolutional networks for semantic segmentation,” in *Proceedings of the IEEE Conference on Computer Vision and Pattern Recognition (CVPR)*, pp. 3431–3440, Salt Lake City, UT, USA, June 2015.
- [41] S. Liu, L. Qi, H. Qin, J. Shi, and J. Jia, “Path aggregation network for instance segmentation,” in *Proceedings of the IEEE Conference on Computer Vision and Pattern Recognition (CVPR)*, pp. 8759–8768, Salt Lake City, UT, USA, June 2018.
- [42] A. Shrivastava, A. Gupta, and R. Girshick, “Training region-based object detectors with online hard example mining,” in *Proceedings of the IEEE Conference on Computer Vision and Pattern Recognition (CVPR)*, pp. 761–769, Las Vegas, NV, USA, June 2016.
- [43] R.-G. Zhou and D.-Q. Liu, “Quantum image edge extraction based on improved Sobel operator,” *International Journal of Theoretical Physics*, vol. 58, no. 9, pp. 2969–2985, 2019.
- [44] Z. Zheng, P. Wang, W. Liu, J. Li, R. Ye, and D. Ren, “Distance-IoU loss: faster and better learning for bounding box regression,” *Proceedings of the AAAI Conference on Artificial Intelligence*, vol. 34, no. 7, pp. 12993–13000, 2020.
- [45] L. Bottou, “Stochastic gradient descent tricks,” *Lecture Notes in Computer Science*, vol. 7700, pp. 421–436, 2012.
- [46] N. Bodla, B. Singh, R. Chellappa, and S. Larry, “Davis. “Soft-NMS -- improving object detection with one line of code,” in *Proceedings of the IEEE International Conference on Computer Vision (ICCV)*, pp. 5561–5569, Venice, Italy, October 2017.
- [47] C. Miao, L. Xie, F. Wan et al., “SIXray: a large-scale security inspection x-ray benchmark for prohibited item discovery in overlapping images,” in *Proceedings of the IEEE/CVF Conference on Computer Vision and Pattern Recognition*, pp. 2119–2128, Long Beach, CA, USA, June 2019.

Research Article

The Local and Parallel Finite Element Scheme for Electric Structure Eigenvalue Problems

Fubiao Lin ¹, Junying Cao ², and Zhixin Liu ^{1,3}

¹School of Mathematics and Statistics, Guizhou University of Finance and Economics, Guiyang 550025, China

²School of Data Science and Information Engineering, Guizhou Minzu University, Guiyang 550025, China

³Guizhou Key Laboratory of Big Data Statistical Analysis, Guizhou University of Finance and Economics, Guiyang, Guizhou 550025, China

Correspondence should be addressed to Zhixin Liu; xinxin905@126.com

Received 30 April 2021; Revised 26 June 2021; Accepted 25 July 2021; Published 20 August 2021

Academic Editor: Qiang Guo

Copyright © 2021 Fubiao Lin et al. This is an open access article distributed under the Creative Commons Attribution License, which permits unrestricted use, distribution, and reproduction in any medium, provided the original work is properly cited.

In this paper, an efficient multiscale finite element method via local defect-correction technique is developed. This method is used to solve the Schrödinger eigenvalue problem with three-dimensional domain. First, this paper considers a three-dimensional bounded spherical region, which is the truncation of a three-dimensional unbounded region. Using polar coordinate transformation, we successfully transform the three-dimensional problem into a series of one-dimensional eigenvalue problems. These one-dimensional eigenvalue problems also bring singularity. Second, using local refinement technique, we establish a new multiscale finite element discretization method. The scheme can correct the defects repeatedly on the local refinement grid, which can solve the singularity problem efficiently. Finally, the error estimates of eigenvalues and eigenfunctions are also proved. Numerical examples show that our numerical method can significantly improve the accuracy of eigenvalues.

1. Introduction

As an important equation in quantum mechanics, Schrödinger eigenvalue problems have important physical background modern electronic structure computations [1, 2]. Thus, finite element methods for solving this problem become an important topic which has attracted the attention of mathematical and physical fields: a priori error estimate is discussed in [3], some posteriori error estimates and adaptive algorithms have been studied in [4–7], and, in addition, it also includes two-scale method [8–12] and the extrapolation methods [13–16].

It is worth noting that some researchers [5, 6, 17] constructed a series of efficient algorithms to solve PDE eigenvalue problems with angular singularity. For elliptic boundary value problem, Xu and Zhou [18] combined two-grid finite element discretization scheme with the local defect correction to propose a general and powerful parallel-computing technique. This technique has been used and developed by many scholars, for instance, it can be used to solve Stokes equation (see [19, 20]), Especially, Xu and Zhou [21], Dai and Zhou [22], and Bi et al. [23–25] developed this method and established local

and parallel three-scale finite element discretizations for symmetric elliptic singular eigenvalue problems.

As a matter of fact, due to the influence of Coulomb potentials, the convergence order of three-dimensional numerical methods and the computational efficiency of numerical methods will further deteriorate [26]. Therefore, one of the most direct and effective methods is to transform the three-dimensional problem into one-dimensional problem. Inspired by [27–29] and others references, it is necessary to further study the high-precision numerical method for singular problems. Therefore, in this paper, we turn to discuss finite element multiscale discretization based on local defect correction. We further apply local defect-correction technique proposed by Xu and Zhou to Schrödinger eigenvalue problems, and our work has the following features. (1) We first extend local and parallel three-scale finite element discretizations for symmetric eigenvalue problems established by Dai and Zhou [22] to solve Schrödinger eigenvalue problem. (2) Based on [23], we establish a new multiscale finite element discretization method by local refinement, and this scheme repeatedly

makes defect correction on finer and finer local meshes to make up for accuracy loss caused by abrupt changes of local mesh size in three-scale scheme. (3) For the two-scale algorithms in [8, 10], we prove the local error estimates of eigenfunctions. (4) Our scheme is simple and easy to carry out, and theoretical analysis and numerical experiment verify its efficiency to solve the singular Schrödinger eigenvalue problem.

The rest of this paper is organized in the following way. In Section 2, we will briefly introduce Schrödinger eigenvalue problem and the associated dimension reduction scheme. In Section 3, we will establish the multiscale finite element method. The error estimates of eigenvalues and eigenfunctions will be studied in Section 4. Several numerical experiments are presented in Section 5 to demonstrate the accuracy and efficiency of our algorithm. Some concluding remarks are given in Section 6.

2. Dimension Reduction Scheme

Consider the Schrödinger eigenvalue problem:

$$-\frac{1}{2}\partial_t((t+1)^2\partial_t u_k) + \frac{k(k+1)}{2}u_k + \frac{R^2}{4}(t+1)^2V_0(r)u_k = \lambda_k \frac{R^2}{4}(t+1)^2u_k, \quad (4)$$

$$u_k(1) = 0. \quad (5)$$

This problem has singularities towards $t = -1$.

Next, we introduce the weighted Sobolev spaces on $\Omega := (-1, 1)$:

$$\begin{aligned} L_\omega^2(\Omega) &:= \left\{ v: \int_\Omega \omega v^2 dt < \infty \right\}, \\ H_{\omega,k}^1(\Omega) &:= \left\{ v: \partial_t^m v \in L_\omega^2(\Omega) \text{ if } k=0, \partial_t^m v \in L_{\omega^m}^2(\Omega) \text{ if } k \geq 1, m=0, 1, v(1)=0 \right\}, \end{aligned} \quad (6)$$

with $\omega(t) := (t+1)^2$. For simplicity of notations in the reminder, we omit the subscript k in u_k and λ_k and denote $H_{\omega,k}^1(\Omega)$ by $H_\omega^1(\Omega)$ for short.

The variational form of (4) and (5) is to find $\lambda \in \mathbb{R}$ and nonzero $u \in H_\omega^1(\Omega)$, satisfying

$$a(u, v) = \lambda b(u, v), \quad \forall v \in H_\omega^1(\Omega), \quad (7)$$

where

$$\begin{aligned} a(u, v) &= \int_\Omega \frac{1}{2}(t+1)^2 u' v' + \frac{k(k+1)}{2} uv + \frac{R^2}{4}(t+1)^2 \\ &\quad (V_0(r) + \mu) uv dt, \\ b(u, v) &= \int_\Omega \frac{R^2}{4}(t+1)^2 uv dt, \end{aligned} \quad (8)$$

$$-\frac{1}{2}\Delta\psi + V\psi = \lambda\psi, \quad \text{in } \mathbb{R}^3, \quad (1)$$

$$\lim_{|x| \rightarrow \infty} \psi = 0, \quad (2)$$

where V is the effective potential and $x = (x_1, x_2, x_3) \in \mathbb{R}^3$.

Applying a truncation from a unbounded domain \mathbb{R}^3 to a bounded spherical domain $\mathbb{B}^3 := \{x \in \mathbb{R}^3: |x| < R\}$, we find

$$\begin{aligned} -\frac{1}{2}\Delta\psi + V\psi &= \lambda\psi, \quad \text{in } \mathbb{B}^3, \\ \psi &= 0, \quad \text{on } \partial\mathbb{B}^3. \end{aligned} \quad (3)$$

Using the spherical coordinate transformation [27], problems (1) and (2) are equivalent to

with $\mu > 0$. According to Theorem 1 in [27], $a(\cdot, \cdot)$ and $b(\cdot, \cdot)$ define the inner product in $H_\omega^1(\Omega)$ and $L_\omega^2(\Omega)$, respectively. Let $\|\cdot\|_a$ and $\|\cdot\|_b$ be the norm induced by the inner products $a(\cdot, \cdot)$ and $b(\cdot, \cdot)$. Let $\|\cdot\|_a$ and $\|\cdot\|_b$.

For $D \subset \Omega_0 \subset \Omega$, we use $D \subset\subset \Omega_0$ to mean that $\text{dist}(\partial D \setminus \partial\Omega, \partial\Omega_0 \setminus \partial\Omega) > 0$.

Assume that $\pi_h(\Omega) = \{\tau\}$ is a mesh of Ω with mesh-size function $h(x)$ whose value is the diameter h_τ of the element τ containing x , and $h(\Omega) = \max_{x \in \Omega} h(x)$ is the mesh diameter of $\pi_h(\Omega)$. We write $h(\Omega)$ as h for simplicity. Let $V_h(\Omega) \subset C(\overline{\Omega})$, defined on $\pi_h(\Omega)$, be a space of piecewise polynomials, and $V_h^0(\Omega) = V_h(\Omega) \cap H_\omega^1(\Omega)$. Given $G \subset \Omega$, we define $\pi_h(G)$ and $V_h(G)$ to be the restriction of $\pi_h(\Omega)$ and $V_h(\Omega)$ to G , respectively, and

$$\begin{aligned} V_h^0(G) &= \{v \in V_h^0(\Omega): v|_{\partial G \setminus \partial\Omega} = 0\}, \\ V_h^0(G) &= \{v \in V_h^0(\Omega): \text{supp } v \setminus \partial\Omega \subset\subset G\}. \end{aligned} \quad (9)$$

For any $G \subset \Omega$ mentioned in this paper, we assume that it aligns with $\pi_h(\Omega)$ when necessary.

In this part, C denotes a positive constant independent of h , which may not be the same constant in different places. For simplicity, we use the symbol $x \leq y$ to mean that $x \leq Cy$.

We adopt the following assumptions similar as in [18] for meshes and finite element space.

(A0) There exists $\nu \geq 1$ such that $h(\Omega)^\nu \leq h(x), \forall x \in \Omega$.

(A1) There exists $r \geq 1$ such that, for $w \in H_\omega^1(\Omega) \cap H^{1+t}(\Omega)$,

$$\inf_{v \in V_h^0(\Omega)} \left(\|h^{-1}(w-v)\|_b + \|w-v\|_a \right) \leq h^t \|w\|_{1+t}, \quad 0 \leq t \leq r. \quad (10)$$

(A2) *Inverse Estimate.* For any $v \in V_h(\Omega_1)$, $\|v\|_{a,\Omega_1} \leq \|h^{-1}v\|_{b,\Omega_1}$.

(A3) *Superapproximation.* For $G \subset \Omega_1$, let $\tilde{\omega} \in C^\infty(\overline{\Omega})$ with $\text{supp } \tilde{\omega} \setminus \partial\Omega \subset \subset G$. Then, for any $w \in V_h(G)$, there exists $v \in V_h^0(G)$ such that $\|h^{-1}(\tilde{\omega}w - v)\|_{a,G} \leq \|w\|_{a,G}$.

The finite element approximation of (7) is given; find $\lambda_h \in \mathbb{C}$ and $u_h \in V_h^0(\Omega)$, $\|u_h\|_a = 1$, satisfying

$$a(u_h, v) = \lambda_h b(u_h, v), \quad \forall v \in V_h^0(\Omega). \quad (11)$$

Define the solution operator $T: L_\omega^2(\Omega) \rightarrow H_\omega^1(\Omega)$ and $T_h: L_\omega^2(\Omega) \rightarrow V_h^0(\Omega)$ as follows:

$$a(Tg, v) = b(g, v), \quad \forall v \in H_\omega^1(\Omega), \quad (12)$$

$$a(T_h g, v) = b(g, v), \quad \forall v \in V_h^0(\Omega). \quad (13)$$

Problems (7) and (11) have the equivalent operator forms (14) and (15), respectively:

$$Tu = \lambda^{-1}u, \quad (14)$$

$$T_h u_h = \lambda_h^{-1}u_h. \quad (15)$$

The following regularity assumption is needed in theoretical analysis. For any $f \in L_\omega^2(\Omega)$, $Tf \in H_\omega^1(\Omega) \cap H^{1+\gamma}(\Omega)$ satisfies

$$\|Tf\|_{1+\gamma} \leq C_\Omega \|f\|_b. \quad (16)$$

According to [30] and Section 5.5 in [31], the above assumption is reasonable.

For some $G \subset \Omega$, we need the following local regularity assumption.

R(G): for any $f \in L_\omega^2(G)$, there exists a $\phi \in H_\omega^1(G) \cap H^{1+\gamma}(G)$ satisfying

$$\begin{aligned} a(\phi, v) &= b(f, v), \quad \forall v \in H_\omega^1(G), \\ \|\phi\|_{1+\gamma, G} &\leq C_G \|f\|_{b, G}, \end{aligned} \quad (17)$$

where C_Ω and C_G are two priori constants.

Define the Ritz projection $P_h: H_\omega^1(\Omega) \rightarrow V_h^0(\Omega)$ by

$$a(u - P_h u, v) = 0, \quad \forall v \in V_h^0(\Omega). \quad (18)$$

Then, $T_h = P_h T$ (see [32]).

Let $M(\lambda)$ be the space spanned by all generalized eigenfunctions corresponding to λ of T , $M_h(\lambda)$ be the space spanned by all generalized eigenfunctions corresponding to all eigenvalues of T_h that converge to λ .

We also need the lemma as follows (see [8, 10]).

Lemma 1. Let (λ, u) be an eigenpair of (7). Then, for all $w \in H_0^1(\Omega)$, $w \neq 0$,

$$\frac{a(w, w)}{b(w, w)} - \lambda = \frac{a(w-u, w-u)}{b(w, w)} - \lambda \frac{b(w-u, w-u)}{b(w, w)}. \quad (19)$$

The a priori error estimates of the finite element approximations (11) can be found in [3, 32].

Lemma 2. Assume that $M(\lambda) \subset H^{r+s}(\Omega)$ ($0 < s < 1$). Then,

$$|\lambda_h - \lambda| \leq h^{2r+2s-2}, \quad (20)$$

and let $u_h \in M_h(\lambda)$ with $\|u_h\|_b = 1$; then, there is $u \in M(\lambda)$ such that

$$\begin{aligned} \|u_h - u\|_a &\leq h^{r+s-1}, \\ \|u_h - u\|_b &\leq h^{r+s-1+\gamma}. \end{aligned} \quad (21)$$

The authors in [18, 33] studied the local behavior of finite element. The following results are given in [18].

Lemma 3. Suppose that $f \in L_\omega^2(\Omega)$ and $G \subset \subset \Omega_0 \subset \Omega$. If $w \in V_h(\Omega_0)$ satisfies

$$a(w, v) = b(f, v), \quad \forall v \in V_0^h(\Omega_0), \quad (22)$$

then

$$\|w\|_{a, G} \leq \|w\|_{b, \Omega_0} + \|f\|_{b, \Omega_0}. \quad (23)$$

Proof. Let $p \geq 2\gamma - 1$ be an integer, and let

$$D \subset \subset \Omega_p \subset \subset \Omega_{p-1} \subset \subset \dots \subset \subset \Omega_1 \subset \subset \Omega_0. \quad (24)$$

Choose $D_1 \subset \Omega$ satisfying $D \subset \subset D_1 \subset \subset \Omega_p$ and $\tilde{\omega} \in C^\infty(\overline{\Omega})$ such that $\text{supp } \tilde{\omega} \subset \subset \Omega_p$ and $\tilde{\omega} \equiv 1$ on $\overline{D_1}$. Then, from (A3), there exists $v \in V_0^h(\Omega_p)$ such that

$$\|\tilde{\omega}^2 w - v\|_{a, \Omega_p} \leq h_{\Omega_0} \|w\|_{a, \Omega_p}, \quad (25)$$

so we have

$$a(w, \tilde{\omega}^2 w - v) \leq h_{\Omega_0} \|w\|_{a, \Omega_p}^2, \quad (26)$$

$$|b(f, v)| \leq \|f\|_{b, \Omega_0} \|v\|_{b, \Omega_p} \leq \|f\|_{b, \Omega_0} \left(h_{\Omega_0} \|w\|_{a, \Omega_p} + \|\tilde{\omega} w\|_{a, \Omega} \right). \quad (27)$$

Since $v \in V_0^h(\Omega_p) \subset V_0^h(\Omega_0)$, the definition w implies

$$a(w, \tilde{\omega}^2 w) = a(w, \tilde{\omega}^2 w - v) + b(f, v). \quad (28)$$

A simple calculation shows that

$$a(\tilde{\omega} w, \tilde{\omega} w) \leq a(w, \tilde{\omega}^2 w) + \|w\|_{b, \Omega_0}^2, \quad \forall w \in H_\omega^1(\Omega). \quad (29)$$

It follows from (26)–(29) that

$$\begin{aligned}
\|\tilde{\omega}w\|_{a,\Omega}^2 &\leq a(w, \tilde{\omega}^2 w) + \|w\|_{b,\Omega_0}^2 \\
&= a(w, \tilde{\omega}^2 w - v) + \|w\|_{b,\Omega_0}^2 + b(f, v) \\
&\leq h_{\Omega_0} \|w\|_{a,\Omega_p}^2 + \|w\|_{b,\Omega_0}^2 + \|f\|_{b,\Omega_0} \left(h_{\Omega_0} \|w\|_{1,\Omega_p} + \|\tilde{\omega}w\|_{a,\Omega} \right),
\end{aligned} \tag{30}$$

and thus,

$$\|w\|_{a,D} \leq h_{\Omega_0}^{1/2} \|w\|_{a,\Omega_p} + \|w\|_{b,\Omega_0} + \|f\|_{b,\Omega_0}. \tag{31}$$

Similarly, we can obtain

$$\|w\|_{a,\Omega_j} \leq h_{\Omega_0}^{1/2} \|w\|_{a,\Omega_{j-1}} + \|w\|_{b,\Omega_0} + \|f\|_{b,\Omega_0}, \quad j = 1, 2, \dots, p. \tag{32}$$

By using (31) and (32), we get from (A0) and (A2) and inverse estimate that

$$\begin{aligned}
\|w\|_{a,D} &\leq h_{\Omega_0}^{(p+1)/2} \|w\|_{a,\Omega_0} + \|w\|_{b,\Omega_0} + \|f\|_{b,\Omega_0} \\
&\leq h_{\Omega_0}^{(p+1)/2} \|h^{-1}w\|_{b,\Omega_0} + \|w\|_{b,\Omega_0} + \|f\|_{b,\Omega_0} \\
&\leq \|w\|_{b,\Omega_0} + \|f\|_{b,\Omega_0}.
\end{aligned} \tag{33}$$

This completes the proof. \square

Lemma 4. Suppose that $G \subset\subset \Omega_0 \subset \Omega$. Then, the following estimates are valid:

$$h^\gamma \|u - P_h u\|_{a,\Omega} + \|u - P_h u\|_{b,\Omega} \leq h^\gamma \inf_{v \in V_h^0(\Omega)} \|u - v\|_{a,\Omega}, \tag{34}$$

$$\|u - P_h u\|_{a,G} \leq \inf_{v \in V_h^0(\Omega)} \|u - v\|_{a,\Omega_0} + h^\gamma \|u - P_h u\|_{a,\Omega}. \tag{35}$$

Proof. By (15), we obtain

$$\|T_h(\lambda_h u_h - \lambda u)\|_a \leq \|\lambda_h u_h - \lambda u\|_b. \tag{36}$$

By the definitions of T , T_h , and P_h , we deduce that

$$\begin{aligned}
\lambda T u &= u, \\
\lambda T_h u &= P_h u.
\end{aligned} \tag{37}$$

Let $P_h^{\Omega_0}$ be the finite element projection onto $V_h^0(\Omega_0)$; then,

$$a(P_h u - P_h^{\Omega_0} u, v) = 0, \quad \forall v \in V_h^0(\Omega_0). \tag{38}$$

According to Lemma 3, we have

$$\|P_h u - P_h^{\Omega_0} u\|_{a,G} \leq \|P_h u - P_h^{\Omega_0} u\|_{b,\Omega_0}. \tag{39}$$

Then, by using (14) and (39), we conclude that

$$\begin{aligned}
\|u - P_h u\|_{a,D} &\leq \|u - P_h^{\Omega_0} u + P_h^{\Omega_0} u - P_h u\|_{a,D} \\
&\leq \inf_{v \in V_h^0(\Omega)} \|u - v\|_{a,\Omega_0} + \|u - P_h u\|_{b,\Omega}.
\end{aligned} \tag{40}$$

Thus, we derive (35) from (39). \square

3. Multiscale Discretizations Based on Local Defect Correction

Consider the eigenvalue problem (7) which has an isolated singular point $t = -1$ (e.g., see Figure 1).

Let $D \subset\subset \Omega$ be a given subdomain containing the singular point z , and we introduce domains:

$$\Omega \supset \Omega_1 \supset \Omega_2 \supset \dots \supset \Omega_l \supset \supset D. \tag{41}$$

Let $\pi_H(\Omega)$ be a shape-regular grid, which is made up of simplices, with size $H \in (0, 1)$, $\pi_w(\Omega)$ be a refined mesoscopic shape-regular grid (from $\pi_H(\Omega)$), and $\pi_{h_i}(\Omega_i)$ be a locally refined grid (from $\pi_{h_{i-1}}(\Omega_{i-1})$) that satisfies $h_{-1} = H$, $h_0 = w$, $h_i \ll h_{i-1}$ ($i = 0, 1, \dots, l$) (Figure 1 shows $\pi_H(\Omega)$, $\pi_w(\Omega)$, and $\pi_{h_1}(\Omega_1)$). Let $V_H^0(\Omega)$, $V_w^0(\Omega)$, and $\{V_{h_i}^0(\Omega_i)\}_1^l$ be finite element spaces of degree less than or equal to r defined on $\pi_H(\Omega)$, $\pi_w(\Omega)$, and $\{\pi_{h_i}(\Omega_i)\}_1^l$, respectively.

Based on algorithm B_0 in [22], we establish the following three-scale discretization scheme.

Scheme 1. (three-scale discretizations based on local defect correction).

Step 1: solve (7) on a globally coarse grid $\pi_H(\Omega)$; find $\lambda_H \in \mathcal{E}$, $u_H \in V_H^0(\Omega)$ such that $\|u_H\|_0 = 1$ and

$$a(u_H, v) = \lambda_H b(u_H, v), \quad \forall v \in V_H^0(\Omega). \tag{42}$$

Step 2: solve two linear boundary value problems on a globally mesoscopic grid $\pi_w(\Omega)$; find $u^w \in V_w^0(\Omega)$ such that

$$a(u^w, v) = \lambda_H b(u_H, v), \quad \forall v \in V_w^0(\Omega), \tag{43}$$

and then, compute the Rayleigh quotient $\lambda^w = a(u^w, u^w)/b(u^w, u^w)$.

Step 3: solve two linear boundary value problems on a locally fine grid $\pi_{h_1}(\Omega_1)$; find $e^{h_1} \in V_{h_1}^0(\Omega_1)$ such that

$$a(e^{h_1}, v) = \lambda^w b(u^w, v) - a(u^w, v), \quad \forall v \in V_{h_1}^0(\Omega_1). \tag{44}$$

Step 4: set

$$u^{w,h_1} = \begin{cases} u^w + e^{h_1}, & \text{on } \bar{\Omega}_1, \\ u^w, & \text{in } \Omega \setminus \bar{\Omega}_1, \end{cases} \tag{45}$$

and compute the Rayleigh quotient:

$$\lambda^{w,h_1} = \frac{a(u^{w,h_1}, u^{w,h_1})}{b(u^{w,h_1}, u^{w,h_1})}. \tag{46}$$

We use $(\lambda^{w,h_1}, u^{w,h_1})$ obtained by Scheme 1 as the approximate eigenpair of (7).

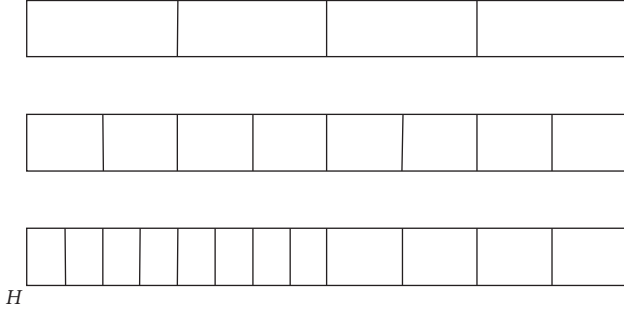


FIGURE 1: Finite element meshes.

It is obvious that (λ^w, u^w) in Scheme 1 can be viewed as approximate eigenpairs obtained by the two-grid discretization scheme in [8, 10] from $\pi_H(\Omega)$ and $\pi_w(\Omega)$.

Using Scheme 1, abrupt changes of mesh size will appear near $\partial\Omega_1$. Influenced by the technique on the transition layer proposed by [23], we repeatedly use the local defect-correction technique to establish the following multiscale discretization scheme.

Scheme 2. (multiscale discretizations based on local defect correction).

Step 1: the same as that of Step 1 of Scheme 1.

Step 2: the same as that of Step 2 of Scheme 1.

Step 3: $u^{w,h_0} \leftarrow u^w$ and $\lambda^{w,h_0} \leftarrow \lambda^w$.

Step 4: for $i = 1, 2, \dots, l$, execute Step 5 and Step 6.

Step 5: solve linear boundary value problems on locally fine grid $\pi_{h_i}(\Omega_i)$; find $e^{h_i} \in V_{h_i}^0(\Omega_i)$ such that

$$a(e^{h_i}, v) = \lambda^{w,h_{i-1}} b(u^{w,h_{i-1}}, v) - a(u^{w,h_{i-1}}, v), \quad \forall v \in V_{h_i}^0(\Omega_i). \quad (47)$$

Step 6: set

$$u^{w,h_i} = \begin{cases} u^{w,h_{i-1}} + e^{h_i}, & \text{on } \bar{\Omega}_i, \\ u^{w,h_{i-1}}, & \text{in } \Omega \setminus \bar{\Omega}_i, \end{cases} \quad (48)$$

and compute

$$\lambda^{w,h_i} = \frac{a(u^{w,h_i}, u^{w,h_i})}{b(u^{w,h_i}, u^{w,h_i})}. \quad (49)$$

We use $(\lambda^{w,h_i}, u^{w,h_i})$ obtained by Scheme 2 as the approximate eigenpair of (7).

4. Theoretical Analysis

Next, we shall discuss the error estimates of Schemes 1 and 2. In our analysis, we introduce an auxiliary grid $\pi_{h_i}(\Omega)$ which is defined globally and denote the corresponding finite element space of degree $\leq r$ by $V_{h_i}^0(\Omega)$ ($i = 1, 2, \dots, l$). We also assume that $\pi_{h_i}(\Omega_i)$ and $V_{h_i}^0(\Omega_i)$ are the restrictions of $\pi_{h_i}(\Omega)$ and a subspace of $V_{h_i}^0(\Omega)$ to Ω_i , respectively, and

$$V_H^0(\Omega) \subset V_w^0(\Omega) \subset V_{h_1}^0(\Omega) \subset V_{h_2}^0(\Omega) \subset \dots \subset V_{h_l}^0(\Omega). \quad (50)$$

For D and Ω_i stated at the beginning of Section 3, let $G_i \subset \Omega$ and $F \subset \Omega$ satisfy $D \subset\subset F \subset\subset G_i \subset\subset \Omega_i$ ($i = 1, 2, \dots, l$).

Theorem 1. Assume that $M(\lambda) \subset H^{r+s}(\Omega) \cap H^{r+1}(\Omega/\bar{D})$ and $(1 < r + s, 0 \leq s < 1)$, and H is properly small. Then, there exists $u \in M(\lambda)$ such that

$$\|u^w - u\|_a \leq H^{r+s-1+\gamma} + w^{r+s-1}, \quad (51)$$

$$\|u^w - u\|_b \leq H^{r+s-1+\gamma}, \quad (52)$$

$$\|u^w - u\|_{a,\Omega \setminus \bar{F}} \leq H^{r+s-1+\gamma} + w^r, \quad (53)$$

$$|\lambda^w - \lambda| \leq H^{2r+2s-2+2\gamma} + w^{2r+2s-2}. \quad (54)$$

Proof. Let $u \in M(\lambda)$ such that $u - u_H$ satisfies Lemma 2. From (12) and (13), Step 2 of Scheme 1, (14), and Lemmas 2 and 4, we derive that

$$\begin{aligned} \|u^w - u\|_a &= \|\lambda_H T_w u_H - \lambda T u\|_a \\ &\leq \|\lambda_H T_w u_H - \lambda T_w u\|_a + \|\lambda T_w u - \lambda T u\|_a \\ &\leq \|\lambda_H u_H - \lambda u\|_b + \lambda \|P_w T u - T u\|_a \\ &\leq H^{r+s-1+\gamma} + w^{r+s-1}, \end{aligned} \quad (55)$$

and then, (51) follows. By Lemmas 2 and 4,

$$\|u^w - u\|_{a,\Omega/\bar{D}} \leq \|\lambda_H u_H - \lambda u\|_b + \lambda \|P_w T u - T u\|_{a,\Omega/\bar{D}} \leq H^{r+s-1+\gamma} + w^r, \quad (56)$$

and then, (53) follows. By calculation,

$$\begin{aligned} \|u^w - u\|_b &= \|\lambda_H T_w u_H - \lambda T u\|_b \\ &\leq \|\lambda_H T_w u_H - \lambda T_w u\|_b + \|\lambda T_w u - \lambda T u\|_b \\ &\leq \|\lambda_H u_H - \lambda u\|_b + \lambda \|P_w T u - T u\|_b \\ &\leq H^{r+s-1+\gamma} + w^{r+s-1+\gamma} \\ &\leq H^{r+s-1+\gamma}, \end{aligned} \quad (57)$$

and then, (52) follows. From (19), we have

$$\lambda^w - \lambda = \frac{a(u^w - u, u^w - u)}{b(u^w, u^w)} - \lambda \frac{b(u^w - u, u^w - u)}{b(u^w, u^w)}. \quad (58)$$

Note that u_H and u^w just approximate the same eigenfunction u . The combination of (51), (52), and (58) yields (54).

Theorem 2 is a critical result in this paper, which develops the results of Theorem 3.3 in [22]. \square

Theorem 2. Assume that $R(\Omega_i)$ holds ($i = 1, 2, \dots, l$), $u \in M(\lambda)$. Then,

$$\begin{aligned}
\|u^{w,h_l} - P_{h_l}u\|_a &\leq \|u - P_{h_l}u\|_{b,\Omega_l} + h_{l-1}^\gamma \|P_{h_l}u - u^{w,h_{l-1}}\|_{a,\Omega_l} \\
&\quad + \|\lambda u - \lambda^{w,h_{l-2}}u^{w,h_{l-2}}\|_{b,\Omega_l} + \|\lambda^{w,h_{l-1}}u^{w,h_{l-1}} - \lambda u\|_b \\
&\quad + \|u^{w,h_{l-1}} - P_{h_l}u\|_{a,\Omega \setminus \overline{G_l}} + \|u^{w,h_{l-1}} - u\|_{a,\Omega \setminus \overline{F}} \quad l \geq 1.
\end{aligned} \tag{59}$$

Proof. Due to the inequality

$$\begin{aligned}
\|u^{w,h_l} - P_{h_l}u\|_{a,\Omega} &\leq \|u^{w,h_l} - P_{h_l}u\|_{a,D} + \|u^{w,h_l} - P_{h_l}u\|_{a,G_l \setminus \overline{D}} \\
&\quad + \|u^{w,h_l} - P_{h_l}u\|_{a,\Omega \setminus \overline{G_l}}
\end{aligned} \tag{60}$$

we shall estimate $\|u^{w,h_l} - P_{h_l}u\|_{a,D}$, $\|u^{w,h_l} - P_{h_l}u\|_{a,G_l \setminus \overline{D}}$ and $\|u^{w,h_l} - P_{h_l}u\|_{a,\Omega \setminus \overline{G_l}}$, respectively.

First, we proceed to estimate $\|u^{w,h_l} - P_{h_l}u\|_{a,D}$. From (18), (47), and (48), we derive

$$\begin{aligned}
a(u^{w,h_l} - P_{h_l}u, v) &= a(u^{w,h_l}, v) - a(P_{h_l}u, v) \\
&= a(u^{w,h_{l-1}} + e^{h_l}, v) - a(u, v) \\
&= \lambda^{w,h_{l-1}}b(u^{w,h_{l-1}}, v) - \lambda b(u, v), \quad \forall v \in V_{h_l}^0(\Omega_l).
\end{aligned} \tag{61}$$

It is obvious that

$$\begin{aligned}
&\lambda^{w,h_{l-1}}b(u^{w,h_{l-1}}, v) - \lambda b(u, v) \\
&= (\lambda^{w,h_{l-1}} - \lambda)b(u, v) + \lambda^{w,h_{l-1}}b(u^{w,h_{l-1}} - u, v), \quad \forall v \in H_0^1(\Omega),
\end{aligned} \tag{62}$$

which together with (61) yields

$$\begin{aligned}
a(u^{w,h_l} - P_{h_l}u, v) &= (\lambda^{w,h_{l-1}} - \lambda)b(u, v) \\
&\quad + \lambda^{w,h_{l-1}}b(u^{w,h_{l-1}} - u, v), \quad \forall v \in V_{h_l}^0(\Omega_l).
\end{aligned} \tag{63}$$

Since $(u^{w,h_l} - P_{h_l}u)|_{\Omega_l} \in V_{h_l}(\Omega_l)$ and $V_{h_l}(\Omega_l) \subset V_{h_l}^0(\Omega_l)$, from the above formula and Lemma 3, we deduce that

$$\|u^{w,h_l} - P_{h_l}u\|_{a,D} \leq \|u^{w,h_l} - P_{h_l}u\|_{b,\Omega_l} + |\lambda^{w,h_{l-1}} - \lambda| + \|u^{w,h_l} - u\|_{b,\Omega_l}. \tag{64}$$

By calculation, we have

$$\begin{aligned}
\|u^{w,h_l} - P_{h_l}u\|_{b,\Omega_l} &\leq \|u^{w,h_{l-1}} - P_{h_l}u\|_{b,\Omega_l} + \|e^{h_l}\|_{b,\Omega_l} \\
&\leq \|u - P_{h_l}u\|_{b,\Omega_l} + \|u - u^{w,h_{l-1}}\|_{b,\Omega_l} + \|e^{h_l}\|_{b,\Omega_l}.
\end{aligned} \tag{65}$$

Substituting the above relation in (64), we obtain

$$\begin{aligned}
\|u^{w,h_l} - P_{h_l}u\|_{a,D} &\leq |\lambda^{w,h_{l-1}} - \lambda| + \|u^{w,h_{l-1}} - u\|_{b,\Omega_l} \\
&\quad + \|u - P_{h_l}u\|_{b,\Omega_l} + \|e^{h_l}\|_{b,\Omega_l},
\end{aligned} \tag{66}$$

To estimate $\|e^{h_l}\|_{b,\Omega_l}$, we use the Aubin–Nitsche duality argument. For any given $f \in L_2(\Omega_l)$, consider the boundary

value problem; find $\varphi \in H_\Gamma^1(\Omega_l) = \{v \in H_\omega^1(\Omega_l): v|_{\partial\Omega_l \setminus \{-1\}} = 0\}$ such that

$$a(\varphi, v) = b(f, v), \quad \forall v \in H_\Gamma^1(\Omega_l). \tag{67}$$

Let φ be the generalized solution of (67) and φ_{h_l} and $\varphi_{h_{l-1}}$ be finite element solutions of (67) in $V_{h_l}^0(\Omega_l)$ and $V_{h_{l-1}}^0(\Omega_l)$, respectively. Then,

$$\begin{aligned}
\|\varphi - \varphi_{h_l}\|_{a,\Omega_l} &\leq h_l^\gamma \|f\|_{b,\Omega_l}, \\
\|\varphi - \varphi_{h_{l-1}}\|_{a,\Omega_l} &\leq h_{l-1}^\gamma \|f\|_{b,\Omega_l}.
\end{aligned} \tag{68}$$

From (47) and (48), we obtain

$$a(u^{w,h_l}, \varphi_{h_l}) = \lambda^{w,h_{l-1}}b(u^{w,h_{l-1}}, \varphi_{h_l}). \tag{69}$$

Then, by the definitions of φ , φ_{h_l} , and e^{h_l} , we deduce that

$$\begin{aligned}
b(e^{h_l}, f) &= a(e^{h_l}, \varphi) = a(e^{h_l}, \varphi_{h_l}) = a(u^{w,h_l} - u^{w,h_{l-1}}, \varphi_{h_l}) \\
&= a(P_{h_l}u - u^{w,h_{l-1}}, \varphi_{h_l}) + a(u^{w,h_l}, \varphi_{h_l}) - a(P_{h_l}u, \varphi_{h_l}) \\
&= a(P_{h_l}u - u^{w,h_{l-1}}, \varphi_{h_l}) + \lambda^{w,h_{l-1}}b(u^{w,h_{l-1}}, \varphi_{h_l}) \\
&\quad - \lambda b(u, \varphi_{h_l}) \\
&= a(P_{h_l}u - u^{w,h_{l-1}}, \varphi_{h_l} - \varphi) + a(P_{h_l}u - u^{w,h_{l-1}}, \varphi - \varphi_{h_{l-1}}) \\
&\quad + a(P_{h_l}u - u^{w,h_{l-1}}, \varphi_{h_{l-1}}) + \lambda^{w,h_{l-1}}b(u^{w,h_{l-1}}, \varphi_{h_l}) \\
&\quad - \lambda b(u, \varphi_{h_l}) \\
&\leq h_{l-1}^\gamma \|P_{h_l}u - u^{w,h_{l-1}}\|_{a,\Omega_l} \|f\|_{b,\Omega_l} + a(P_{h_l}u - u^{w,h_{l-1}}, \varphi_{h_{l-1}}) \\
&\quad + \lambda^{w,h_{l-1}}b(u^{w,h_{l-1}}, \varphi_{h_l}) - \lambda b(u, \varphi_{h_l}).
\end{aligned} \tag{70}$$

Step 2 of Scheme 2 shows that

$$a(u^{w,h_0}, \varphi_{h_0}) = \lambda^{w,h_{-1}}b(u^{w,h_{-1}}, \varphi_{h_0}), \tag{71}$$

namely, for $l = 1$,

$$a(u^{w,h_{l-1}}, \varphi_{h_{l-1}}) = \lambda^{w,h_{l-2}}b(u^{w,h_{l-2}}, \varphi_{h_{l-1}}), \tag{72}$$

for $l > 1$, the above formula follows from (47) and (48). Therefore,

$$\begin{aligned}
a(P_{h_l}u - u^{w,h_{l-1}}, \varphi_{h_{l-1}}) &= a(u - u^{w,h_{l-1}}, \varphi_{h_{l-1}}) \\
&= \lambda b(u, \varphi_{h_{l-1}}) - a(u^{w,h_{l-1}}, \varphi_{h_{l-1}}) \\
&= \lambda b(u, \varphi_{h_{l-1}}) - \lambda^{w,h_{l-2}}b(u^{w,h_{l-2}}, \varphi_{h_{l-1}}) \\
&\leq \|\lambda u - \lambda^{w,h_{l-2}}u^{w,h_{l-2}}\|_{b,\Omega_l} \|f\|_{b,\Omega_l},
\end{aligned} \tag{73}$$

It is clear that

$$\begin{aligned}
|\lambda^{w,h_{l-1}}b(u^{w,h_{l-1}}, \varphi_{h_l}) - \lambda b(u, \varphi_{h_l})| &\leq \|\lambda^{w,h_{l-1}}u^{w,h_{l-1}} - \lambda u\|_{b,\Omega_l} \\
&\quad \|f\|_{b,\Omega_l}.
\end{aligned} \tag{74}$$

Substituting the above two formulae in (70), we derive

$$|b(e^{h_l}, f)| \leq \left(h_{l-1}^\gamma \|P_{h_l} u - u^{w, h_{l-1}}\|_{a, \Omega_l} + \|\lambda u - \lambda^{w, h_{l-2}} u^{w, h_{l-2}}\|_{b, \Omega_l} + \|\lambda^{w, h_{l-1}} u^{w, h_{l-1}} - \lambda u\|_b \right) \|f\|_{b, \Omega_l}. \quad (75)$$

Thus, we obtain

$$\|e^{h_l}\|_{a, \Omega_l} \leq h_{l-1}^\gamma \|P_{h_l} u - u^{w, h_{l-1}}\|_{a, \Omega_l} + \|\lambda u - \lambda^{w, h_{l-2}} u^{w, h_{l-2}}\|_{b, \Omega_l} + \|\lambda^{w, h_{l-1}} u^{w, h_{l-1}} - \lambda u\|_b. \quad (76)$$

Substituting (76) in (66), we obtain

$$\|u^{w, h_l} - P_{h_l} u\|_{a, D} \leq \|u - P_{h_l} u\|_{b, \Omega_l} + h_{l-1}^\gamma \|P_{h_l} u - u^{w, h_{l-1}}\|_{a, \Omega_l} + \|\lambda u - \lambda^{w, h_{l-2}} u^{w, h_{l-2}}\|_{b, \Omega_l} + |\lambda^{w, h_{l-1}} - \lambda| \|u^{w, h_{l-1}} - u\|_b. \quad (77)$$

Similarly, since $(G_l/\bar{D}) \subset\subset \Omega_l$, we deduce

$$\|u^{w, h_l} - P_{h_l} u\|_{a, D} \leq \|u - P_{h_l} u\|_{b, \Omega_l} + h_{l-1}^\gamma \|P_{h_l} u - u^{w, h_{l-1}}\|_{a, \Omega_l} + \|\lambda u - \lambda^{w, h_{l-2}} u^{w, h_{l-2}}\|_{b, \Omega_l} + |\lambda^{w, h_{l-1}} - \lambda| \|u^{w, h_{l-1}} - u\|_b. \quad (78)$$

The remainder is to analyze $\|u^{w, h_l} - P_{h_l} u\|_{a, \Omega/\bar{G}_l}$. From (48), we see that

$$\|u^{w, h_l} - P_{h_l} u\|_{a, \Omega/\bar{\Omega}_l} = \|u^{w, h_{l-1}} - P_{h_l} u\|_{a, \Omega/\bar{\Omega}_l}, \quad (79)$$

which leads to

$$\begin{aligned} & \|u^{w, h_l} - P_{h_l} u\|_{a, \Omega/\bar{G}_l} \\ & \leq \|u^{w, h_l} - P_{h_l} u\|_{a, \Omega/\bar{\Omega}_l} + \|u^{w, h_{l-1}} - P_{h_l} u\|_{a, \Omega/\bar{G}_l} + \|e^{h_l}\|_{a, \Omega/\bar{G}_l} \\ & \leq \|u^{w, h_{l-1}} - P_{h_l} u\|_{a, \Omega/\bar{G}_l} + \|e^{h_l}\|_{a, \Omega/\bar{G}_l}. \end{aligned} \quad (80)$$

It follows from (7), (47), and (62) that

$$\begin{aligned} a(e^{h_l}, v) &= \lambda^{w, h_{l-1}} b(u^{w, h_{l-1}}, v) - a(u^{w, h_{l-1}}, v) - \lambda b(u, v) + a(u, v) \\ &= (\lambda^{w, h_{l-1}} - \lambda) b(u, v) + \lambda^{w, h_{l-1}} b(u^{w, h_{l-1}} - u, v) \\ &\quad - a(u^{w, h_{l-1}} - u, v), \quad \forall v \in V_h^0(\Omega_l). \end{aligned} \quad (81)$$

Then, by Lemma 3, we have

$$\|e^{h_l}\|_{a, \Omega_l/\bar{G}_l} \leq \|e^{h_l}\|_{b, \Omega_l/\bar{F}} + |\lambda^{w, h_{l-1}} - \lambda| + \|u^{w, h_{l-1}} - u\|_{a, \Omega_l/\bar{F}} \quad (82)$$

where $F \subset \Omega$ satisfies $D \subset\subset F \subset\subset G_l$. Substituting (82) in (80), we obtain

$$\begin{aligned} \|u^{w, h_l} - P_{h_l} u\|_{a, \Omega/\bar{G}_l} &\leq \|u^{w, h_{l-1}} - P_{h_l} u\|_{a, \Omega/\bar{G}_l} + \|e^{h_l}\|_{b, \Omega/\bar{F}} \\ &\quad + |\lambda^{w, h_{l-1}} - \lambda| + \|u^{w, h_{l-1}} - u\|_{a, \Omega/\bar{F}}. \end{aligned} \quad (83)$$

It follows from substituting (76) in the above inequality that

$$\begin{aligned} \|u^{w, h_l} - P_{h_l} u\|_{a, \Omega/\bar{G}_l} &\leq \|u^{w, h_{l-1}} - P_{h_l} u\|_{a, \Omega/\bar{G}_l} + h_{l-1}^\gamma \|P_{h_l} u - u^{w, h_{l-1}}\|_{a, \Omega_l} \\ &\quad + \|\lambda u - \lambda^{w, h_{l-2}} u^{w, h_{l-2}}\|_{b, \Omega_l} + \|\lambda^{w, h_{l-1}} u^{w, h_{l-1}} - \lambda u\|_b \\ &\quad + |\lambda^{w, h_{l-1}} - \lambda| + \|u^{w, h_{l-1}} - u\|_{b, \Omega/\bar{F}}. \end{aligned} \quad (84)$$

Combining (60), (77), (78), and (84), finally, we obtain (59). \square

Theorem 3. Assume that the conditions of Theorem 1 hold. Then, there exists $u \in M(\lambda)$ such that

$$\|u^{w, h_1} - u\|_{a, \Omega} \leq h_1^{r+s-1} + w^r + H^{r+s-1+\gamma}, \quad (85)$$

$$\|u^{w, h_1} - u\|_{b, \Omega} \leq w^r + H^{r+s-1+\gamma}, \quad (86)$$

$$\|u^{w, h_1} - u\|_{a, \Omega/\bar{F}} \leq w^r + H^{r+s-1+\gamma}, \quad (87)$$

$$|\lambda^{w, h_1} - \lambda| \leq h_1^{2r+2s-2} + w^{2r} + H^{2r+2s-2+2\gamma}. \quad (88)$$

Proof. Let $u \in M(\lambda)$ such that $u - u_H$ satisfies Lemma 2. From Theorem 2, we know $l = 1$, $h_{-1} = H$, $h_0 = u$, $u^{w, h_0} = u^w$, $\lambda^{w, h_0} = \lambda^w$, $u^{w, h_{-1}} = u_H$, and $\lambda^{w, h_{-1}} = \lambda_H$; thus, we obtain

$$\begin{aligned} \|u^{w, h_1} - P_{h_1} u\|_{a, \Omega} &\leq \|u - P_{h_1} u\|_{0, \Omega_1} + w^\gamma \|P_{h_1} u - u^w\|_{a, \Omega_1} \\ &\quad + \|\lambda u - \lambda_H u_H\|_{b, \Omega_1} + \|\lambda^w u^w - \lambda u\|_b \\ &\quad + \|u^w - P_{h_1} u\|_{a, \Omega/\bar{G}_1} + \|u^w - u\|_{a, \Omega_1/\bar{F}}. \end{aligned} \quad (89)$$

Using Lemma 4, Theorem 1, and Lemma 2 to estimate the terms at the right-hand side of the above formula gives

$$\begin{aligned} \|u^{w, h_1} - P_{h_1} u\|_{a, \Omega} &\leq h_1^{r+s-1+\gamma} + w^\gamma w^{r+s-1} + H^{r+s-1+\gamma} + w^{r+s-1+\gamma} \\ &\quad + (w^{r+s-1+\gamma} + w^r) + (w^{r+s-1+\gamma} + w^r) \\ &\leq H^{r+s-1+\gamma} + w^r. \end{aligned} \quad (90)$$

Combining (35) and (39) yields (85), (86), and (87). From (19), we have

$$\lambda^{w, h_1} - \lambda = \frac{a(u^{w, h_1} - u, u^{w, h_1} - u)}{b(u^{w, h_1}, u^{w, h_1})} - \lambda \frac{b(u^{w, h_1} - u, u^{w, h_1} - u)}{b(u^{w, h_1}, u^{w, h_1})}. \quad (91)$$

TABLE 1: $V = -(1/r)$.

DOF _H	DOF _w	λ_H	λ^w	λ^{w,h_1}	λ^{w,h_2}	λ^{w,h_3}	λ^{w,h_4}
4	16	-0.3558419	-0.4662707	-0.4903221	-0.4963517	-0.4975584	-0.4976819
8	64	-0.4320788	-0.4974509	-0.4993601	-0.4997939	-0.4998737	-0.4998816
16	256	-0.4735824	-0.4998515	-0.4999630	-0.4999897	-0.4999946	-0.4999951
32	1024	-0.4918086	-0.4999910	-0.4999978	-0.4999994	-0.4999997	-0.4999997
4	16	-0.10798797	-0.12015585	-0.12343262	-0.12435602	-0.12457107	-0.12462204
8	64	-0.11060517	-0.12445755	-0.12476411	-0.12484341	-0.12486019	-0.12486334
16	256	-0.12023285	-0.12497717	-0.12499349	-0.12499748	-0.12499831	-0.12499849
32	1024	-0.12372913	-0.12499867	-0.12499966	-0.12499990	-0.12499995	-0.12499996

TABLE 2: $V = (r^2/2)$.

DOF _H	DOF _w	λ_H	λ^w	λ^{w,h_1}	λ^{w,h_2}	λ^{w,h_3}	λ^{w,h_4}
4	16	2.3568087	1.7807519	1.5673755	1.5176295	1.5145651	1.5142457
8	64	1.6871072	1.5041081	1.5010234	1.5002569	1.5001762	1.5001727
16	256	1.5588758	1.5002540	1.5000634	1.5000159	1.5000109	1.5000107
32	1024	1.5155354	1.5000157	1.5000039	1.5000010	1.5000007	1.5000007
4	16	3.0744959	2.6046912	2.5284162	2.5069841	2.5039841	2.5036625
8	64	3.0722770	2.5418424	2.5142338	2.5054025	2.5045811	2.5045358
16	256	2.5890816	2.5004065	2.5001018	2.5000260	2.5000149	2.5000137
32	1024	2.5245263	2.5000247	2.5000062	2.5000016	2.5000009	2.5000008

Combining (85), (86), and (91) yields (88). \square

Theorem 4. Under the conditions of Theorem 1, we further assume that $R(\Omega_i)$ holds ($i = 1, 2, \dots, l$), and

$$\begin{aligned} w^r &= \mathcal{O}(H^{r+s-1+\gamma}), \\ h_l^{r+s-1} &\geq H^{r+s-1+\gamma}. \end{aligned} \quad (92)$$

Then, there exists $u \in M(\lambda)$ such that

$$\|u^{w,h_l} - u\|_{a,\Omega} \leq h_l^{r+s-1}, \quad (93)$$

$$\|u^{w,h_l} - u\|_{b,\Omega} \leq H^{r+s-1+\gamma}, \quad (94)$$

$$\|u^{w,h_l} - u\|_{a,\Omega \setminus \bar{F}} \leq H^{r+s-1+\gamma}, \quad (95)$$

$$|\lambda^{w,h_l} - \lambda| \leq h_l^{2r+s+s-2}. \quad (96)$$

Proof. Let $u \in M(\lambda)$ such that $u - u_H$ satisfies Lemma 2. The proof of (93)–(96) is completed by induction. When $l = 1$, Scheme 2 is actually Scheme 1. Hence, from Theorems 1 and 3 and (92), we know that (93)–(96) hold for $l = 0, 1$.

Suppose (93)–(96) hold for $l - 2$ and $l - 1$, i.e.,

$$\begin{aligned} \|u^{w,h_{l-2}} - u\|_{a,\Omega} &\leq h_{l-2}^{r+s-1}, \\ \|u^{w,h_{l-2}} - u\|_{b,\Omega} &\leq H^{r+s-1+\gamma}, \\ \|u^{w,h_{l-2}} - u\|_{a,\Omega \setminus \bar{F}} &\leq H^{r+s-1+\gamma}, \\ |\lambda^{w,h_{l-2}} - \lambda| &\leq h_{l-2}^{2r+s+s-2}, \\ \|u^{w,h_{l-1}} - u\|_{a,\Omega} &\leq h_{l-1}^{r+s-1}, \\ \|u^{w,h_{l-1}} - u\|_{b,\Omega} &\leq H^{r+s-1+\gamma}, \\ \|u^{w,h_{l-1}} - u\|_{a,\Omega \setminus \bar{F}} &\leq H^{r+s-1+\gamma}, \\ |\lambda^{w,h_{l-1}} - \lambda| &\leq h_{l-1}^{2r+s+s-2}. \end{aligned} \quad (97)$$

Next, we shall prove that (93)–(96) hold for l . Using the above formula and Lemma 4 to estimate the terms at the right-hand side of (59) gives

$$\begin{aligned} \|u^{w,h_l} - P_{h_l} u\|_{a,\Omega} &\leq h_l^{r+s-1+\gamma} + h_{l-1}^\gamma (h_l^{r+s-1} + h_{l-1}^{r+s-1}) + H^{r+s-1+\gamma} \\ &\quad + H^{r+s-1+\gamma} + (H^{r+s-1+\gamma} + h_l^r) + H^{r+s-1+\gamma} \\ &\leq H^{r+s-1+\gamma}. \end{aligned} \quad (98)$$

The combination of (35), (39), and (98) yields (93), (94), and (95). From (19), we have

TABLE 3: $V = r$.

DOF_H	DOF_w	λ_H	λ^w	λ^{w,h_1}	λ^{w,h_2}	λ^{w,h_3}	λ^{w,h_4}
4	16	2.2305059	1.9209211	1.8729501	1.8611124	1.8601497	1.8600937
8	64	1.9785415	1.8584870	1.8564450	1.8559369	1.8558894	1.8558874
16	256	1.8939159	1.8559226	1.8557987	1.8557678	1.8557648	1.8557646
32	1024	1.8658088	1.8557673	1.8557596	1.8557577	1.8557575	1.8557575
4	16	2.9297073	2.7099046	2.6801814	2.6714983	2.6700907	2.6699643
8	64	2.8582383	2.6735285	2.6699339	2.6688537	2.6686711	2.6686594
16	256	2.7093909	2.6680156	2.6678766	2.6678430	2.6678375	2.6678370
32	1024	2.6792284	2.6678409	2.6678323	2.6678303	2.6678299	2.6678299

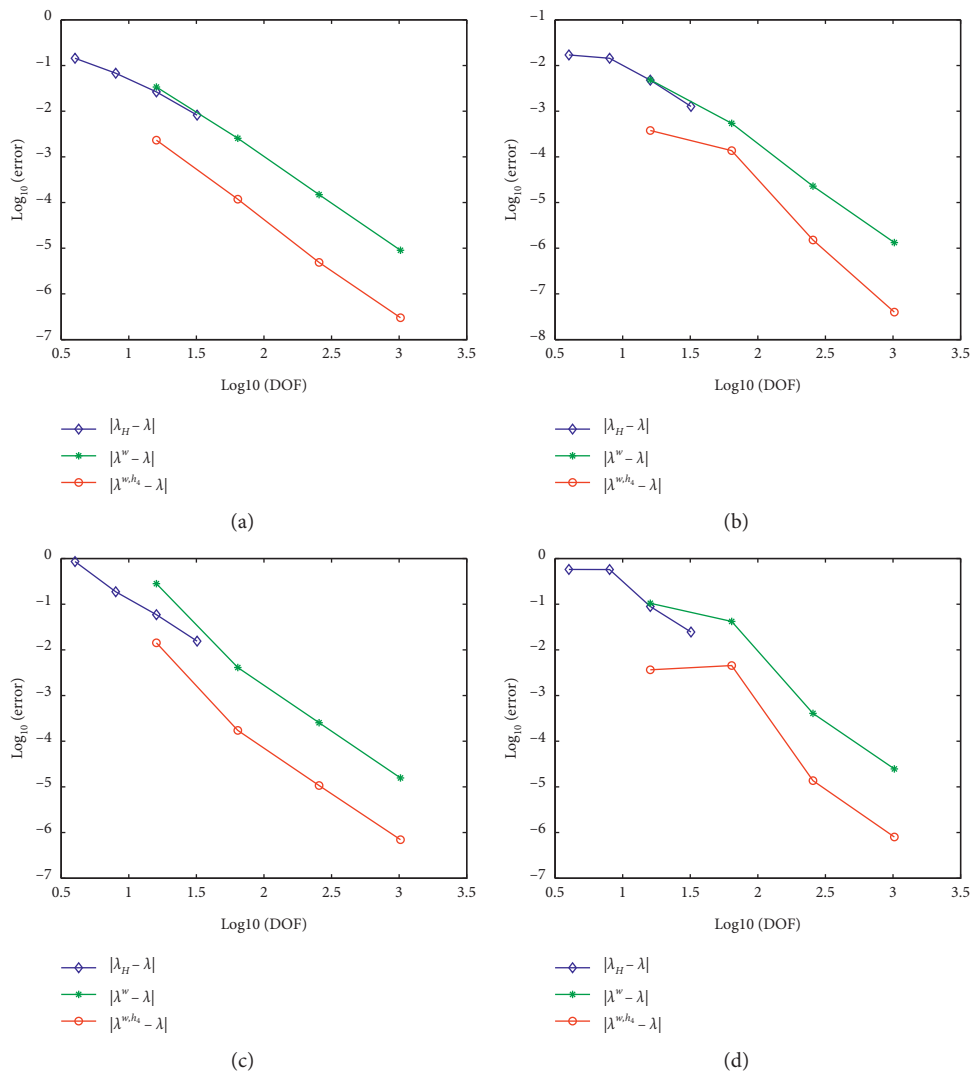


FIGURE 2: Continued.

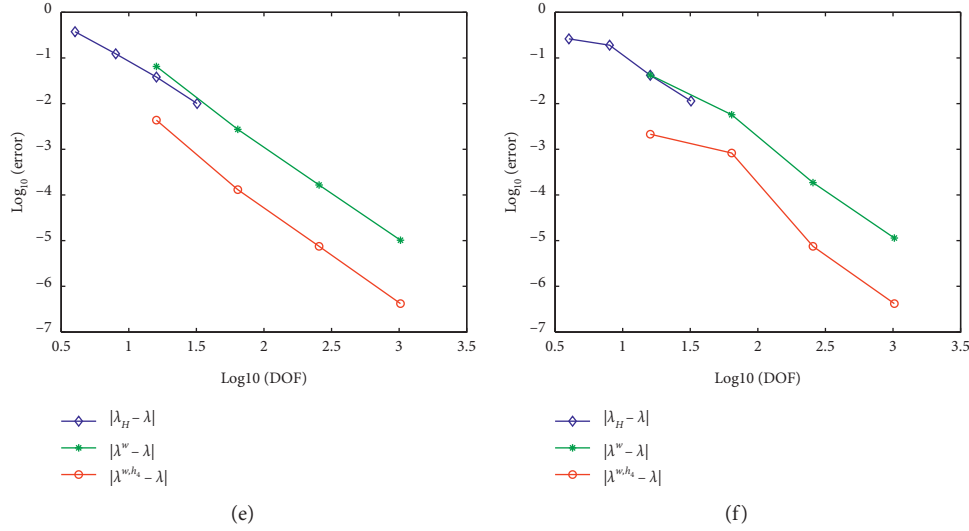


FIGURE 2: Error curve of numerical eigenvalues obtained by multiscale Scheme 2. (a) $V = -(1/r)$, $\lambda = -0.5$. (b) $V = -(1/r)$, $\lambda = -0.125$. (c) $V = -(r^2/2)$, $\lambda = 1.5$. (d) $V = (r^2/2)$, $\lambda = 2.5$. (e) $V = r$, $\lambda = 1.855757081489$. (f) $V = r$, $\lambda = 2.667829482852$.

$$\lambda^{w,h_i} - \lambda = \frac{a(u^{w,h_i} - u, u^{w,h_i} - u)}{b(u^{w,h_i}, u^{w,h_i})} - \lambda \frac{b(u^{w,h_i} - u, u^{w,h_i} - u)}{b(u^{w,h_i}, u^{w,h_i})}. \quad (99)$$

The combination of (93), (94), and (99) yields (96). \square

5. Numerical Experiments

We will report some numerical experiments by using linear finite element and quadratic spectral element on uniform meshes. In our numerical experiments, we use Scheme 2 to solve the problem such that $\Omega_i = (-1, -1 + (1/2^i) \times (3/2))$, $i = 0, 1, 2, \dots$, and locally fine grids have the same degree of freedom as that of globally mesoscopic grid (see Tables 1–3).

In our experiments, the parameter μ is taken to be 1. We set $R = 40$ for the eigenvalue problem with $V = -(1/r)$ and $l = 1$ and $R = 15$ for the other cases. The coarse mesh size and the mesoscopic mesh size satisfy $\omega = H^2$ which means $\text{DOF}_w = \text{DOF}_H^2$.

We use MATLAB 2011b under the package of Chen (see [34]) to solve the problem, and the numerical results are shown in Tables 1–3. This tables corresponds to the results of different potential energy V . From these tables, we can see that, without increasing degree of freedom on locally fine grids, the first local defect correction can largely improve the accuracy of the eigenvalue, and the local defect corrections that follows can gradually improve the accuracy of the eigenvalue by overcoming the singularity at the origin. Here, we set

$$\text{DOF}_w = \text{DOF}_{\Omega_i}, \quad i = 1, 2, \dots \quad (100)$$

In Figure 2, we also plot the error curve of numerical eigenvalues obtained by multiscale Scheme 2. It can be seen that using coarse finite element space with the mesh size H , the error of the finite element eigenvalues is around poor accuracy 10^{-2} . After performing the two-grid iteration, the

error of the finite element eigenvalues can be increased from 10^{-2} to 10^{-5} . The final multiscale iteration can improve the error up to $10^{-6} \sim 10^{-7}$. These figures show the accuracy and effectiveness of our numerical scheme.

6. Conclusion

In this paper, we developed a efficient multiscale finite element method for solving the Schrödinger eigenvalue problem with three-dimensional domain. Our scheme can correct the defects repeatedly on the local refinement grid, which can solve the singularity problem efficiently. The error estimates of eigenvalues and eigenfunctions are proved. Some numerical examples are presented to verify the effectiveness of our numerical method.

Data Availability

The data used to support the findings of this study are included within the article.

Conflicts of Interest

The authors declare that they have no conflicts of interest.

Acknowledgments

The research was supported by NSFC (nos. 62062018, 11901135, and 11961009), Guizhou Province University Science and Technology top talents project (no. KY[2018]047), Guizhou Key Laboratory of Big Data Statistics Analysis (no. BDSA20200102), and foundation of Guizhou Science and Technology Department (no. [2020]1Y015).

References

- [1] D. B. Cook, *Handbook of Computational Quantum Chemistry*, Courier Dover Publications, New York, NY, USA, 2012.

- [2] Y. Saad, J. R. Chelikowsky, and S. M. Shontz, "Numerical methods for electronic structure calculations of materials," *SIAM Review*, vol. 52, no. 1, pp. 3–54, 2020.
- [3] J. H. Bramble and J. E. Osborn, "Rate of convergence estimates for nonselfadjoint eigenvalue approximations," *Mathematics of Computation*, vol. 27, no. 123, p. 525, 1973.
- [4] J. Han and Y. Yang, "A class of spectral element methods and its A priori/A posteriori error estimates for 2nd-order elliptic eigenvalue problems," *Abstract and Applied Analysis*, vol. 2013, Article ID 262010, 14 pages, 2013.
- [5] V. Heuveline and R. Rannacher, "A posteriori error control for finite element approximations of elliptic eigenvalue problems," *Advances in Computational Mathematics*, vol. 15, no. 1/4, pp. 107–138, 2001.
- [6] V. Heuveline and R. Rannacher, "Adaptive FE eigenvalue approximation with application to hydrodynamic stability analysis," in *Proceedings of the international conference on Advances in Numerical Mathematics*, Moscow, Russia, September 2005.
- [7] H. Bi, Y. Zhang, and Y. Yang, "Two-grid discretizations and a local finite element scheme for a non-selfadjoint Stekloff eigenvalue problem," *Computers & Mathematics with Applications*, vol. 79, no. 7, pp. 1895–1913, 2020.
- [8] K. Kolman, "A two-level method for nonsymmetric eigenvalue problems," *Acta Mathematicae Applicatae Sinica, English Series*, vol. 21, no. 1, pp. 1–12, 2005.
- [9] J. Zhang and X. Yang, "Decoupled, non-iterative, and unconditionally energy stable large time stepping method for the three-phase Cahn-Hilliard phase-field model," *Journal of Computational Physics*, vol. 404, Article ID 109115, 2020.
- [10] Y. Yang and X. Fan, "Generalized Rayleigh quotient and finite element two-grid discretization schemes," *Science in China Series A: Mathematics*, vol. 52, no. 9, pp. 1955–1972, 2009.
- [11] Y. Yang, "H²-Conforming methods and two-grid discretizations for the elastic transmission eigenvalue problem," *Communications in Computational Physics*, vol. 28, no. 4, pp. 1366–1388, 2020.
- [12] Q. Li and G. Du, "Local and parallel finite element methods based on two-grid discretizations for the nonstationary Navier-Stokes equations," *Numerical Algorithms*, pp. 1–22, 2021.
- [13] T. Lü and Y. Feng, "Splitting extrapolation based on domain decomposition for finite element approximations," *Science in China Series E: Technological Sciences*, vol. 40, no. 2, pp. 144–155, 1997.
- [14] J. Zhang and X. Yang, "Unconditionally energy stable large time stepping method for the L2-gradient flow based ternary phase-field model with precise nonlocal volume conservation," *Computer Methods in Applied Mechanics and Engineering*, vol. 361, Article ID 112743, 2020.
- [15] Y. Yang, H. Bi, and S. Li, "The extrapolation of numerical eigenvalues by finite elements for differential operators," *Applied Numerical Mathematics*, vol. 69, pp. 59–72, 2013.
- [16] J. Zhang and X. Yang, "A fully decoupled, linear and unconditionally energy stable numerical Scheme for a melt-convective phase-field dendritic solidification model," *Computer Methods in Applied Mechanics and Engineering*, vol. 363, Article ID 112779, 2020.
- [17] J. Zhang, C. Chen, X. Yang, Y. Chu, and Z. Xia, "Efficient, Non-iterative, and second-order accurate numerical algorithms for the anisotropic Allen-Cahn Equation with precise nonlocal mass conservation," *Journal of Computational and Applied Mathematics*, vol. 363, pp. 444–463, 2020.
- [18] J. C. Xu and A. H. Zhou, "Local and parallel finite element algorithms based on two-grid discretizations," *Mathematics of Computation*, vol. 69, pp. 881–909, 2000.
- [19] Y. He, J. Xu, A. Zhou, and J. Li, "Local and parallel finite element algorithms for the Stokes problem," *Numerische Mathematik*, vol. 109, no. 3, pp. 415–434, 2008.
- [20] Y. He, L. Mei, Y. Shang, and J. Cui, "Newton iterative parallel finite element algorithm for the steady Navier-Stokes equations," *Journal of Scientific Computing*, vol. 44, no. 1, pp. 92–106, 2010.
- [21] J. Xu and A. Zhou, "Local and parallel finite element algorithms for eigenvalue problems," *Acta Mathematicae Applicatae Sinica, English Series*, vol. 18, no. 2, pp. 185–200, 2002.
- [22] X. Dai and A. Zhou, "Three-scale finite element discretizations for quantum eigenvalue problems," *SIAM Journal on Numerical Analysis*, vol. 46, no. 1, pp. 295–324, 2008.
- [23] H. Bi, Y. Yang, and H. Li, "Local and parallel finite element discretizations for eigenvalue problems," *SIAM Journal on Scientific Computing*, vol. 35, no. 6, pp. A2575–A2597, 2013.
- [24] Y. Yang and H. Bi, "Two-grid finite element discretization schemes based on shifted-inverse power method for elliptic eigenvalue problems," *SIAM Journal on Numerical Analysis*, vol. 49, no. 4, pp. 1602–1624, 2011.
- [25] Y. Yang and J. Han, "Multilevel finite element discretizations based on local defect correction for nonsymmetric eigenvalue problems," *Computers & Mathematics with Applications*, vol. 70, no. 8, pp. 1799–1816, 2015.
- [26] A. Gordon, C. Jirauschek, and F. X. KRtner, "Numerical solver of the time-dependent Schrödinger equation with Coulomb singularities," *Physical Review A*, vol. 73, no. 4, p. 838, 2006.
- [27] J. Zhang, F. Lin, and J. Wang, "An efficient spectral-Galerkin method based on a dimension reduction scheme for eigenvalue problems of Schrödinger equations," *Mathematical Methods in the Applied Sciences*, vol. 42, no. 6, pp. 2069–2082, 2019.
- [28] J. Zhang and X. Fan, "An efficient spectral method for the helmholtz transmission eigenvalues in polar geometries," *Discrete and Continuous Dynamical Systems*, vol. 24, no. 9, pp. 4799–4813, 2019.
- [29] J. An, "A Legendre-Galerkin spectral approximation and estimation of the index of refraction for transmission eigenvalues," *Applied Numerical Mathematics*, vol. 108, pp. 171–184, 2016.
- [30] P. Grisvard, *Elliptic Problems in Nonsmooth Domains*, Pitman, London, UK, 1985.
- [31] S. C. Brenner and L. R. Scott, *The Mathematical Theory of Finite Element Methods*, Springer-Verlag, New York, NY, USA, 2nd edition, 2002.
- [32] I. Babuska and J. E. Osborn, "Eigenvalue problems," in *Finite Element Methods (Part 1), Handbook of Numerical Analysis*, P. G. Ciarlet and J. L. Lions, Eds., pp. 640–787, Elsevier Science Publishers, North-Holland, Netherlands, 1991.
- [33] L. B. Wahlbin, "Local behavior in finite element methods," in *Finite Element Methods (Part1), Handbook of Numerical Analysis*, P. G. Ciarlet and J. L. Lions, Eds., Elsevier Science Publishers, North-Holland, Netherlands, pp. 355–522, 1991.
- [34] L. Chen, *IFEM: An Innovative Finite Element Methods Package in MATLAB*, International Federation for Emergency Medicine, Bengaluru, India, 2008.

Research Article

Prediction of Frequency Response Function for Cylindrical Thin-Walled Workpiece with Fixture Support Constraints

Jinjie Jia , Yuwen Sun , and Jinbo Niu 

Key Laboratory for Precision and Non-Traditional Machining Technology of Ministry of Education, School of Mechanical Engineering, Dalian University of Technology, Dalian 116024, China

Correspondence should be addressed to Jinbo Niu; niujinbo@hotmail.com

Received 14 March 2021; Revised 20 April 2021; Accepted 30 July 2021; Published 14 August 2021

Academic Editor: Alberto Campagnolo

Copyright © 2021 Jinjie Jia et al. This is an open access article distributed under the Creative Commons Attribution License, which permits unrestricted use, distribution, and reproduction in any medium, provided the original work is properly cited.

Auxiliary fixtures are widely used to enhance the rigidity of cylindrical thin-walled workpieces (CTWWs) in the machining process. Nevertheless, the accurate and efficient prediction of frequency response function (FRF) for the workpiece-fixture system remains challenging due to the complicated contact constraints between workpiece and fixture. This paper proposes an analytical solution for the comprehensive FRF analysis of the CTWW-fixture system. Firstly, based on the vector mechanics, the mode shape functions of the workpiece are presented using the classical theory of thin shell. The variable separation method is utilized to deal with the inter-mode coupling of the workpiece. Secondly, the motion equation of the CTWW with fixture constraints is established using analytical mechanics from the viewpoint of energy balance. Finally, the FRFs of the CTWW-fixture system are derived by means of modal superposition. Experimental modal tests verify that the predicted FRFs are in good agreement with the measured curves.

1. Introduction

Cylindrical thin-walled parts such as engine casings are widely used in aerospace industries. Due to the low rigidity of thin-walled workpiece, it is prone to produce large-amplitude vibrations and even regenerative chatter during the machining process [1, 2], which consequently affect the final part quality [3, 4]. In order to enhance the rigidity of the machining system, auxiliary fixtures have been widely designed and used to enhance the rigidity of thin-walled parts [5].

Positioning error and clamping stability under static or quasistatic loads are primary concerns with regard to fixture design. There are two main sources of positioning errors: the contact compliance between the workpiece and the fixture [6] and the geometric errors of the locators [7, 8]. The positioning accuracy is affected by many factors including dimensional error [9, 10], clamping force [11], clamping sequence [12], and so on. The clamping stability is affected not only by the contact compliance but also by the rigidity of the fixture components [13]. To determine the stability, the

screw theory [14] is widely used, where the applied load is equivalently regarded as a rotation and a translation along the same axis.

For flexible workpieces, the compliance cannot be neglected when analyzing the contact status between workpiece and fixture. As far as the positioning error is concerned, it is mainly affected by the local deformation of the workpiece-fixture contact area. Also, the deformation contribution caused by the workpiece-fixture contact compliance is much smaller than the workpiece deformation. Thus, the workpiece-fixture contact could be regarded as rigid compared to the compliance of the workpiece [15]. Moreover, for analyzing the system stability, the difference between rigid workpieces and flexible workpieces lies in the influence of workpiece compliance on clamping force and contact. Among them, the minimum clamping force [16] needs to be determined to prevent slippage of the workpiece, and a reasonable contact area [17] needs to be identified to meet the form-closure condition. From the above analysis, the compliance of the workpiece should be taken into account, which significantly affects the quality of machined surfaces [18].

The above works regard the workpiece-fixture system as static or quasistatic and ignore the dynamic characteristics. Nevertheless, the interrupted milling forces have high-frequency components, especially for thin-walled workpieces [3]. Therefore, the performance of fixture should be evaluated under dynamic loads. Rigid body dynamics [19], as the basis of the dynamics research of the workpiece-fixture system, is widely used. Among them, the research studies of workpiece-fixture contact including contact modeling [20] and contact analysis [21] are very critical. Contact modeling is mainly studied by means of analytical methods [22–24] and finite element methods [25, 26]. For contact analysis, many factors such as nonlinear behavior [27], stiffness [28], friction damping [29], and so on should be considered, which have great influence on the dynamics of rigid bodies. In this way, the fixturing stability of the system [30] and the optimal design of the fixture [19] can be effectively analyzed.

Regarding the influence of fixtures on the dynamics of flexible workpieces, however, the relevant research is very limited. Due to the weak rigidity of flexible workpieces, adding support [31, 32], which has a great impact on the dynamic characteristics of the workpiece, in the fixture design is an effective way. In order to study it, the frequency response function (FRF) [33] is often used for analysis. In the analysis process, the finite element method (FEM) [34, 35] is an excellent numerical tool used to obtain relevant detailed information. When using this method, it was necessary to divide very fine grids and set complex equivalent boundary conditions to ensure the accuracy of the results, which would cause a significant reduction in calculation efficiency [36]. To solve this problem, the analytical method focusing on thin-walled plate or frame structures [37, 38] is widely used to analyze the effects of fixture on the dynamic characteristics of the workpiece.

Nevertheless, to the authors' knowledge, few research concentrates on the effects of fixtures on cylindrical thin-walled structures, especially from the perspective of dynamics. Under the motivation, the main objective of this paper is to develop a comprehensive analytical solution to predict the FRFs of the system so as to investigate the effects of fixture support on the dynamic characteristics of CTWW. The outline of this paper is organized as follows. Section 2 establishes the motion equation of the workpiece-fixture system. The frequency response functions of the workpiece-fixture system are predicted in Section 3. Section 4 verifies the feasibility and accuracy of the proposed method. Some important conclusions are listed in Section 5.

2. Motion Equation of the Workpiece-Fixture System

Adding fixture support can effectively improve the rigidity of the CTWWs, which makes the modeling and analysis of the system more complicated. Therefore, it is necessary to focus on the establishment of the motion equation of the workpiece-fixture system, which is the basis for investigating the effects of fixture support on workpiece dynamic characteristics. Without losing generality, a typical thin-walled cylindrical structure with fixture constraints is taken to

explore the mechanism, as shown in Figure 1. The outside surface of the cylindrical workpiece is required to be further milled from the free end to the fixed end for lightweight purposes. In this paper, the boundary conditions are determined according to the actual machining situation. The base of the workpiece is clamped, i.e., the slope and displacement are equal to zero. The top edge of the workpiece is free, i.e., the moments and shear forces are equal to zero.

2.1. Mode Shape Functions of the CTWW. In this section, the dynamic balance equation of the CTWW is established using the vector mechanics method. The mode shape functions can be obtained. The 3D model of this part can be equivalently represented using a continuous, homogeneous, and isotropic cylindrical shell, as shown in Figure 2.

The workpiece has an axial length L , a middle surface radius R , and a constant thickness H . A cylindrical coordinate system (o, z, θ, r) is used to take advantage of the axis symmetry of the structure, and the origin is set to the center of the fixed end ($z=0$) of the workpiece. The displacements on the middle surface with respect to the coordinate system are represented by $u(z, \theta, t)$, $v(z, \theta, t)$, and $w(z, \theta, t)$ in the tangential, radial, and axial directions, respectively. The CTWW is clamped at the bottom ($z=0$), and the other end is free ($z=L$). Since the thickness of the workpiece is much smaller than other dimensions, a thin-walled cylindrical shell assumption is considered. In addition, the straight line perpendicular to the middle surface of the workpiece remains unchanged before and after deformation [39].

In the modeling process, a series of cylindrical shell elements are used to simulate the middle surface. An arbitrary element is expressed in Figure 3. We take this element as an example to illustrate the modeling process. Each shell is constructed by an arc $Rd\theta$ and a line segment dz , respectively. The forces including external forces p_e ($e = r, \theta, z$) and inertial forces $\rho H (\partial^2 \text{in}^2 / \partial t^2)$ ($\text{in} = u, v, w$) are shown in Figure 3(a), and the internal forces and internal moments are shown in Figures 3(b) and 3(c). By multiplying all internal forces by the arc length of the side, multiplying all external force components and inertial forces by the element area, and then projecting the product in three directions, the free vibration differential equations of the CTWW can be established as follows [40]:

$$\begin{cases} \frac{1}{R} \frac{\partial N_\theta}{\partial \theta} + \frac{\partial N_{z\theta}}{\partial z} + \frac{Q_\theta}{R} - \rho H \frac{\partial^2 u}{\partial t^2} = 0, \\ \frac{\partial Q_z}{\partial z} + \frac{\partial Q_\theta}{R \partial \theta} - \frac{N_\theta}{R} - \rho H \frac{\partial^2 v}{\partial t^2} = 0, \\ \frac{\partial N_z}{\partial z} + \frac{1}{R} \frac{\partial N_{z\theta}}{\partial \theta} - \rho H \frac{\partial^2 w}{\partial t^2} = 0, \end{cases} \quad (1)$$

where ρ is the density of the workpiece, N_θ , $N_{z\theta}$, N_z and Q_θ , Q_z are the internal forces and transverse shear forces per unit length on the middle surface, and their specific expressions are given by

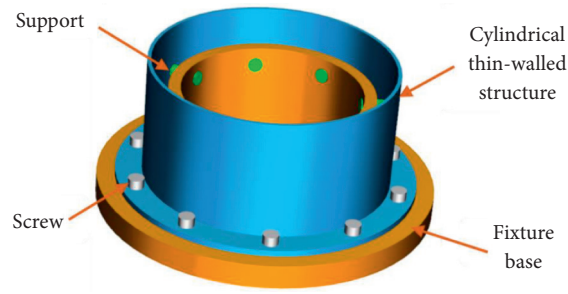


FIGURE 1: Schematic illustration of a typical cylindrical thin-walled structure with fixture constraints.

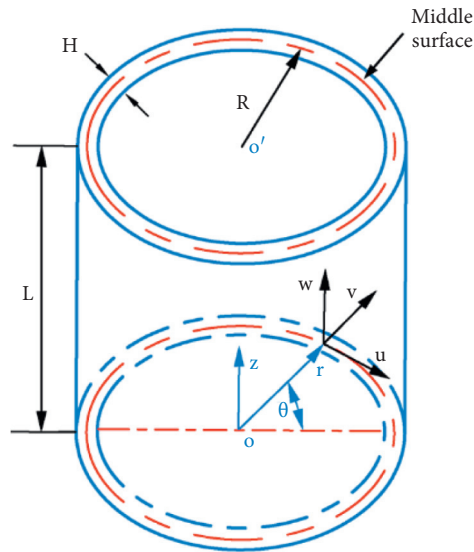


FIGURE 2: Coordinate system and dimensions for a cylindrical shell.

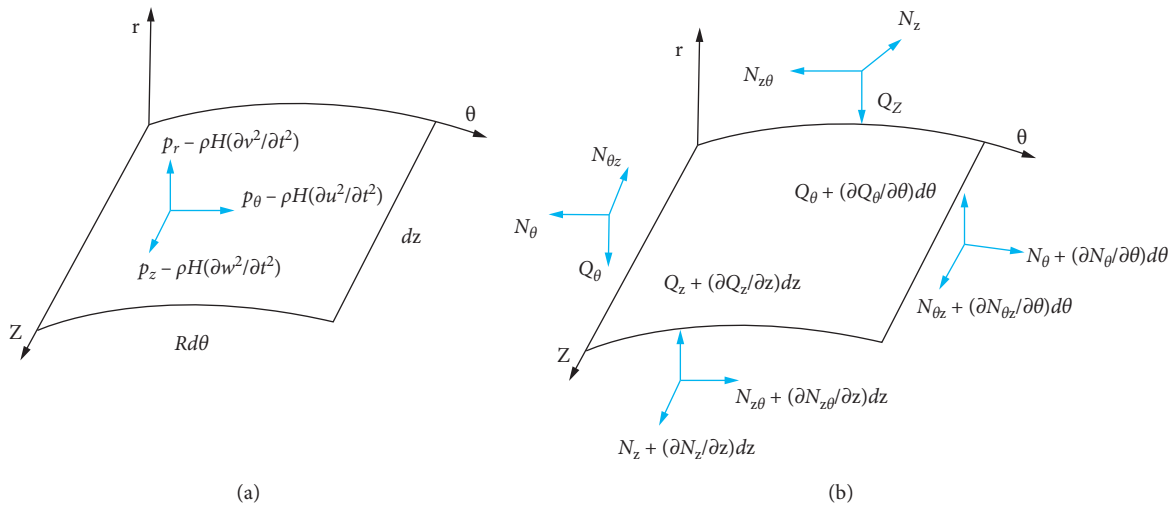


FIGURE 3: Continued.

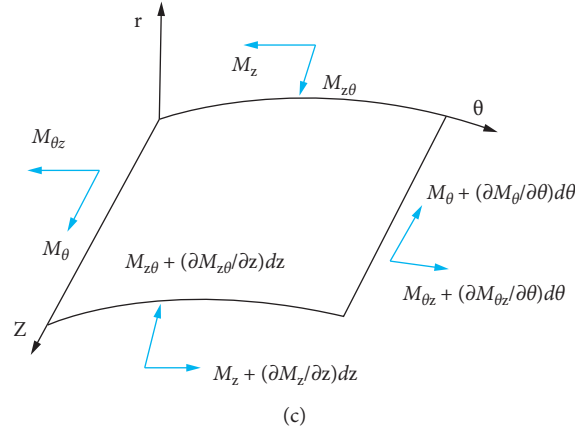


FIGURE 3: Forces and moments acting on a cylindrical shell element. (a) External forces and inertial forces. (b) Internal forces. (c) Internal moments.

$$\left\{ \begin{array}{l} N_\theta = K \left[\frac{1}{R} \left(\frac{\partial u}{\partial \theta} + v \right) + \mu \frac{\partial w}{\partial z} \right], \\ N_{z\theta} = K \frac{1-\mu}{2} \left(\frac{\partial u}{\partial z} + \frac{1}{R} \frac{\partial w}{\partial \theta} \right), \\ N_z = K \left[\frac{\partial w}{\partial z} + \frac{\mu}{R} \left(\frac{\partial u}{\partial \theta} + v \right) \right], \\ M_z = D \left[-\frac{\partial^2 v}{\partial z^2} + \frac{\mu}{R^2} \left(\frac{\partial u}{\partial \theta} - \frac{\partial^2 v}{\partial \theta^2} \right) \right], \\ M_\theta = D \left[\frac{1}{R^2} \left(\frac{\partial u}{\partial \theta} - \frac{\partial^2 v}{\partial \theta^2} \right) - \mu \frac{\partial^2 v}{\partial z^2} \right], \\ M_{z\theta} = D \frac{1-\mu}{2R} \left(\frac{\partial u}{\partial z} - 2 \frac{\partial^2 v}{\partial z \partial \theta} \right), \\ Q_z = \frac{\partial M_z}{\partial z} + \frac{\partial M_{z\theta}}{R \partial \theta}, \\ Q_\theta = \frac{\partial M_{z\theta}}{\partial z} + \frac{\partial M_\theta}{R \partial \theta} \end{array} \right. \quad (2)$$

$$\begin{bmatrix} L_{11} & L_{12} & L_{13} \\ L_{21} & L_{22} & L_{23} \\ L_{31} & L_{32} & L_{33} \end{bmatrix} \begin{Bmatrix} u \\ v \\ w \end{Bmatrix} = \begin{Bmatrix} 0 \\ 0 \\ 0 \end{Bmatrix}, \quad (3)$$

where $L_{i_d j_d} = (i_d, j_d = 1, 2, 3)$ are differential operators with respect to z and θ , and the specific expressions are given in Appendix A.

To solve equation (3), a synchronous motion is considered, i.e., natural modes of vibration [41]:

$$\begin{cases} u(x, \theta, t) = U(x, \theta)q(t), \\ v(x, \theta, t) = V(x, \theta)q(t), \\ w(x, \theta, t) = W(x, \theta)q(t), \end{cases} \quad (4)$$

where $U(x, \theta)$, $V(x, \theta)$, and $W(x, \theta)$ are the mode shapes and $q(t)$ is the generalized coordinate.

The vibration forms of CTWW include axial and circumferential vibrations, as shown in Figure 4. The axial vibration form in Figure 4(a) is composed of m half-waves. The circumferential vibration form in Figure 4(b) consists of radial and tangential vibration, where n is the number of circumferential waves. Therefore, the modal shape of the cylindrical shell can be determined by any combination of the axial half-wave number m and the circumferential wave number n .

Considering the inter-mode coupling, a variable separation method is employed to separate the spatial dependence of modal shapes between axial and circumferential directions. The modal shape of the thin-walled cylindrical shell is expanded in a double series in terms of beam function in the axial direction and Fourier series in the circumferential direction. This method can use simple functions to decouple the complex coupled dynamics system and avoid the tedious mathematical calculation process. Therefore, the tangential, radial, and axial displacements of the workpiece vary according to [42]

where M_z , M_θ , and $M_{z\theta}$ are the internal moments on the middle surface, $K = EH/(1 - \mu^2)$ is the tensile stiffness of the cylinder shell, $D = EH^3/12(1 - \mu^2)$ is the flexural rigidity of the cylindrical shell, E is Young's modulus, and μ is Poisson's ratio.

By substituting equation (2) into (1), the governing equations expressed by displacements u , v , and w can be obtained as

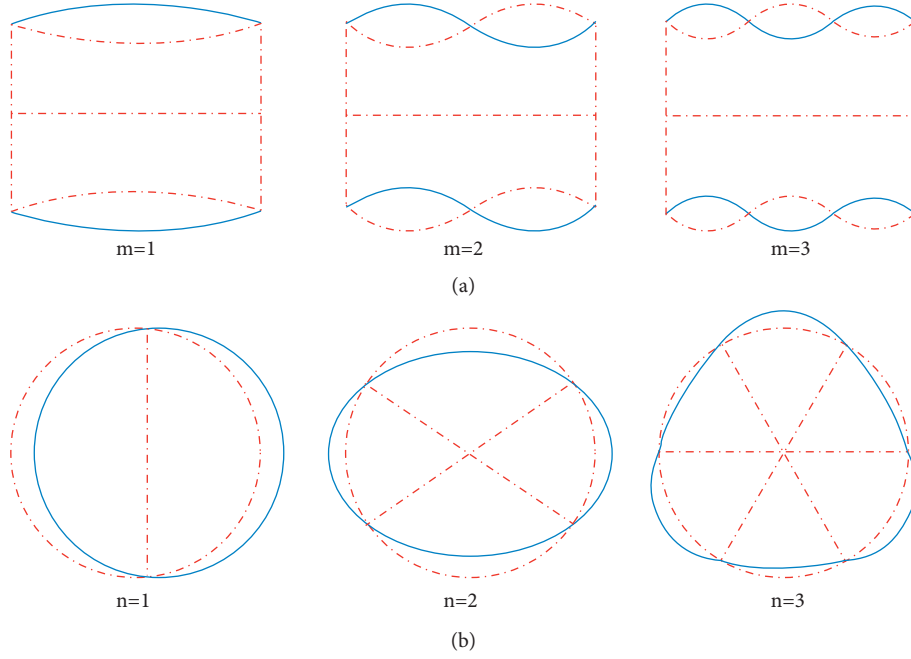


FIGURE 4: Vibration forms of the CTWW. (a) Axial vibration forms. (b) Circumferential vibration forms.

$$\left\{ \begin{array}{l} u(z, \theta, t) = \sum_{m=0}^{\infty} \sum_{n=0}^{\infty} A_{mn} \phi_m(z) \sin(n\theta) q(t), \\ v(z, \theta, t) = \sum_{m=0}^{\infty} \sum_{n=0}^{\infty} B_{mn} \phi_m(z) \cos(n\theta) q(t), \\ w(z, \theta, t) = \sum_{m=0}^{\infty} \sum_{n=0}^{\infty} C_{mn} \frac{d\phi_m(z)}{d(z/L)} \cos(n\theta) q(t), \end{array} \right. \quad (5)$$

$$\left\{ \begin{array}{l} \cosh \lambda_m \cos \lambda_m = -1, \\ \sigma_m = \frac{\sinh \lambda_m - \sin \lambda_m}{\cosh \lambda_m + \cos \lambda_m}, \\ a_1 = a_3 = 1, \\ a_2 = a_4 = -1. \end{array} \right. \quad (7)$$

where A_{mn} , B_{mn} , and C_{mn} are the (m, n) -th modal amplitudes in the tangential, radial, and axial directions, respectively, and $\phi_m(z)$ is the axial mode shape function that is defined as a beam mode shape function corresponding to the boundary conditions at both ends, which can be expressed as [43]

$$\begin{aligned} \phi_m(z) = & a_1 \cos h\left(\frac{\lambda_m z}{L}\right) + a_2 \cos\left(\frac{\lambda_m z}{L}\right) \\ & - \sigma_m \left[a_3 \sin h\left(\frac{\lambda_m z}{L}\right) + a_4 \sin\left(\frac{\lambda_m z}{L}\right) \right], \end{aligned} \quad (6)$$

where the values of a_{i_z} ($i_z = 1, 2, 3, 4$), λ_m , and σ_m can be determined according to the boundary conditions of the beam. In this paper, the clamped-free boundary condition is considered, and the parameters of the beam function satisfy the following relationships:

By substituting equation (5) into (3) and performing Galerkin discretization, a set of ordinary differential equations can be obtained as follows:

$$\left\{ \begin{array}{l} \int_0^L \int_0^{2\pi} (L_{11}u + L_{12}v + L_{13}w) \phi_m(z) \sin(n\theta) R d\theta dz = 0, \\ \int_0^L \int_0^{2\pi} (L_{21}u + L_{22}v + L_{23}w) \phi_m(z) \cos(n\theta) R d\theta dz = 0, \\ \int_0^L \int_0^{2\pi} (L_{31}u + L_{32}v + L_{33}w) \frac{d\phi_m(z)}{d(z/L)} \cos(n\theta) R d\theta dz = 0. \end{array} \right. \quad (8)$$

Further integrating equation (8), the frequency characteristic equation of the workpiece can be obtained as follows:

$$\begin{bmatrix} c_{11} & c_{12} & c_{13} \\ c_{21} & c_{22} & c_{23} \\ c_{31} & c_{32} & c_{33} \end{bmatrix} \begin{Bmatrix} A_{mn} \\ B_{mn} \\ C_{mn} \end{Bmatrix} = 0, \quad (9)$$

where $c_{i_c j_c}$ ($i_c, j_c = 1, 2, 3$) are the undetermined coefficients as given in Appendix B, which are related to the natural frequency, geometric parameters, and material parameters of the workpiece.

Since equation (9) has nontrivial solutions, the determinant of the coefficient matrix must be zero, i.e.,

$$\begin{cases} \gamma_1 = -c_{13} - c_{21} - c_{32}, \\ \gamma_2 = c_{13}c_{21} + c_{13}c_{32} + c_{21}c_{32} - c_{11}c_{23} - c_{12}c_{33} - c_{22}c_{31}, \\ \gamma_3 = c_{13}c_{22}c_{31} + c_{11}c_{23}c_{32} + c_{12}c_{21}c_{33} - c_{11}c_{22}c_{33} - c_{12}c_{23}c_{33} - c_{13}c_{21}c_{32}. \end{cases} \quad (12)$$

Based on equation (11), three natural frequency solutions are obtained and substituted into equation (9). As a result, ratios of modal amplitudes can be expressed as

$$\begin{cases} \frac{A_{mn}}{B_{mn}} = \frac{c_{22}(\omega_{mn}^2 - c_{13}) + c_{12}c_{23}}{c_{11}c_{23} - (\omega_{mn}^2 - c_{13})(\omega_{mn}^2 - c_{21})}, \\ \frac{B_{mn}}{C_{mn}} = \frac{(\omega_{mn}^2 - c_{13})(\omega_{mn}^2 - c_{21}) - c_{11}c_{23}}{c_{12}(\omega_{mn}^2 - c_{21}) + c_{22}c_{11}}. \end{cases} \quad (13)$$

The above formulae reveal that there are three natural frequencies with regard to each combination (m, n), and each frequency is related to one vibration direction. Among them, the lowest frequency value corresponds to the most flexural vibration direction, and the other two correspond to the in-plane vibrations. In this way, the calculated natural frequencies and mode shape functions of the CTWW will be used to establish the motion equation for the workpiece-fixtured system in next section.

2.2. Motion Equation of the CTWW with Fixture Support Constraints. For the workpiece-fixtured system, an analytical mechanics method will be introduced to establish the motion equation. The generalized coordinates are used to determine the position of the system. The scalar functions such as kinetic energy, elastic strain energy, potential energy, dissipated energy, and the work done by external forces are used to describe the amount of motion. The Lagrange equation is used to obtain the relationships between multiple energies. And the specific modeling process will be described in detail as follows.

According to the research in [44], the displacement expression of the workpiece without support is still applicable for cases with support. Therefore, based on equation

$$\det([c_{i_c j_c}]) = 0, \quad (i_c, j_c = 1, 2, 3). \quad (10)$$

A characteristic equation of the workpiece can be obtained from equation (10) as

$$(\omega_{mn}^2)^3 + \gamma_1(\omega_{mn}^2)^2 + \gamma_2\omega_{mn}^2 + \gamma_3 = 0, \quad (11)$$

where ω_{mn} is the natural frequency corresponding to the (m, n)-th mode and γ_{i_r} ($i_r = 1, 2, 3$) are the coefficients which can be written as

(5), the kinetic energy T of the CTWW under external forces can be expressed as

$$\begin{aligned} T = \frac{\rho H}{2} \int_0^L \int_0^{2\pi} & \left(\left(\frac{\partial u(z, \theta, t)}{\partial t} \right)^2 + \left(\frac{\partial v(z, \theta, t)}{\partial t} \right)^2 \right. \\ & \left. + \left(\frac{\partial w(z, \theta, t)}{\partial t} \right)^2 \right) R d\theta dx = \frac{1}{2} m_p \dot{\mathbf{q}} \mathbf{M} \dot{\mathbf{q}}^T, \end{aligned} \quad (14)$$

where m_p represents the mass per unit area of the cylindrical shell and $\dot{\mathbf{q}}$ is a $1 \times (3M \cdot N)$ matrix, and it can be expressed as $\dot{\mathbf{q}} \in R^{1 \times 3MN}$, where M and N represent the number of related subitems corresponding to m and n in equation (5), respectively. Each of the generalized coordinate velocity matrix element is $\dot{q} = \partial q / \partial t$. The mass matrix \mathbf{M} can be expressed as

$$\mathbf{M} = \begin{bmatrix} \mathbf{M}_1 & & & 0 \\ & \mathbf{M}_2 & & \\ & & \ddots & \\ \text{sym} & & & \mathbf{M}_{MN} \end{bmatrix}_{3MN \times 3MN}, \quad (15)$$

where the submatrix \mathbf{M}_{i_m} ($i_m = 1, 2, \dots, MN$) stands for the mass elements in the three directions corresponding to the i_m -th degree of freedom, each submatrix is a 3×3 matrix, and each element in the submatrix is given in Appendix C. These elements are related to the mode shape functions of the CTWW. The symbol "sym" in the matrix \mathbf{M} is short for symmetry.

Deformation generates internal strain and stress and therefore creates elastic strain energy. Based on the classical thin shell theory, the elastic strain energy U of the workpiece can be obtained as [45]

$$U = \int_0^L \int_0^{2\pi} \frac{EH}{2(1-\mu^2)} \left\{ \begin{aligned} & \left[\frac{\partial w}{\partial z} + \frac{1}{R} \left(\frac{\partial u}{\partial \theta} + v \right) \right]^2 - \frac{2(1-\mu)}{R} \left[\frac{\partial w}{\partial z} \left(\frac{\partial u}{\partial \theta} + v \right) \right] + \frac{1-\mu}{2} \left(\frac{1}{R} \frac{\partial w}{\partial \theta} + \frac{\partial u}{\partial z} \right)^2 \\ & + \frac{H^2}{12} \left[\frac{\partial^2 v}{\partial z^2} + \frac{1}{R^2} \left(\frac{\partial^2 v}{\partial \theta^2} - \frac{\partial u}{\partial \theta} \right) \right]^2 - \frac{H^2(1-\mu)}{6R^2} \left[\frac{\partial^2 v}{\partial z^2} \left(\frac{\partial^2 v}{\partial \theta^2} - \frac{\partial u}{\partial \theta} \right) \right] + \frac{H^2(1-\mu)}{6R^2} \left(\frac{\partial^2 v}{\partial z \partial \theta} - \frac{\partial u}{2 \partial z} \right)^2 \end{aligned} \right\} R d\theta dz$$

$$= \frac{1}{2} D \mathbf{q} \mathbf{K}_w \mathbf{q}^T, \quad (16)$$

where \mathbf{K}_w is the stiffness matrix, which has the same dimension with the mass matrix \mathbf{M} , and the element in each submatrix is given in Appendix D.

Each fixture support can be modeled as a spring and a damping element, as shown in Figure 5. Under the excitation of external forces, the fixture support outputs normal force and tangential forces on the workpiece within the support area.

Assuming that the fixture support a is located at (z_a, θ_a) , the potential energy P of all fixture supports can be written as

$$P = \frac{1}{2} \sum_{a=1}^{p_a} \left[k_{\theta a} u^2(z_a, \theta_a) + k_{r a} v^2(z_a, \theta_a) + k_{z a} w^2(z_a, \theta_a) \right]$$

$$= \frac{1}{2} \sum_{a=1}^{p_a} \mathbf{q} \mathbf{K}_s \mathbf{q}^T, \quad (17)$$

$$\mathbf{K}_{i_s, j_s} = \begin{bmatrix} k_{\theta a} (\Phi_{mn}^u(z_a, \theta_a))^2 & & 0 \\ & k_{r a} (\Phi_{mn}^v(z_a, \theta_a))^2 & \\ & \text{sym} & k_{z a} (\Phi_{mn}^w(z_a, \theta_a))^2 \end{bmatrix}, \quad (i_s, j_s = 1, 2, \dots, MN), \quad (18)$$

where $\Phi_{mn}^u(z_a, \theta_a)$, $\Phi_{mn}^v(z_a, \theta_a)$, and $\Phi_{mn}^w(z_a, \theta_a)$ are the mode shape functions in three directions, which are functions of the support positions and can be obtained from Appendix C.

Since the workpiece-fixture system is an energy dissipative system, the damping effect cannot be ignored. To describe the energy dissipation of the system, it is necessary

to comprehensively consider the damping characteristics of the workpiece and fixture supports. In the modeling process, the nonconservative damping forces are assumed to be viscous damping forces, and the Rayleigh dissipation function is used to express the dissipated energy R_d of the system, which can be given as

$$R_d = \frac{c_w}{2} \int_0^L \int_0^{2\pi} \left(\left(\frac{\partial u(z, \theta, t)}{\partial t} \right)^2 + \left(\frac{\partial v(z, \theta, t)}{\partial t} \right)^2 + \left(\frac{\partial w(z, \theta, t)}{\partial t} \right)^2 \right) R d\theta dx$$

$$+ \frac{1}{2} \sum_{a=1}^{p_a} c_s \left(\left(\frac{\partial u(z, \theta, t)}{\partial t} \right)^2 + \left(\frac{\partial v(z, \theta, t)}{\partial t} \right)^2 + \left(\frac{\partial w(z, \theta, t)}{\partial t} \right)^2 \right) \quad (19)$$

$$= \frac{c_w}{2} \dot{\mathbf{q}} \mathbf{C}_w \dot{\mathbf{q}}^T + \frac{c_s}{2} \sum_{a=1}^{p_a} \dot{\mathbf{q}} \mathbf{C}_s \dot{\mathbf{q}}^T,$$

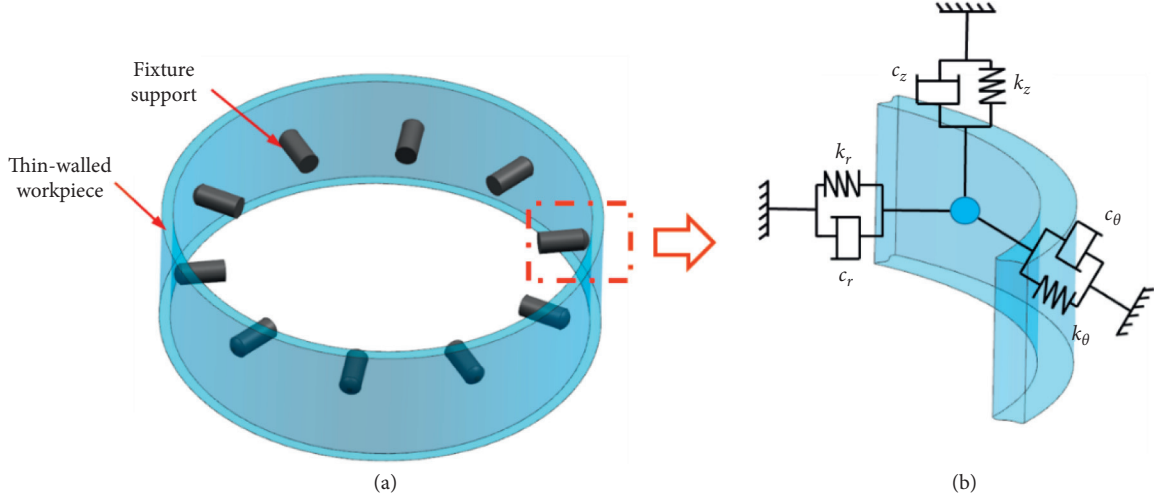


FIGURE 5: Illustration of the workpiece-fixture system. (a) CTWW with fixture support constraints. (b) Equivalent model of the fixture support.

where c_w and c_s are the damping coefficients of the workpiece and fixture support, respectively, and C_w and C_s are the damping matrices corresponding to the workpiece and fixture support, respectively.

Supposing that the workpiece is subjected to an external force F_e , the work W done by F_e can be obtained as

$$W = F_{e,u}u + F_{e,v}v + F_{e,w}w = \mathbf{F}_e \Phi \mathbf{q}^T, \quad (20)$$

where $F_{e,u}$, $F_{e,v}$, and $F_{e,w}$ are the tangential, radial, and axial force components acting on the CTWW, respectively, and $\mathbf{F}_e \in R^{1 \times 3MN}$ and $\Phi \in R^{3MN \times 3MN}$ are the external force

matrix and mode shape matrix, respectively, which can be written as

$$\begin{cases} \mathbf{F}_e = [\mathbf{F}_{e,1} \ \mathbf{F}_{e,2} \ \cdots \ \mathbf{F}_{e,MN}]_{1 \times 3MN}, \\ \Phi = \begin{bmatrix} \Phi_1 & & 0 \\ & \Phi_2 & \\ & & \ddots \\ \text{sym} & & & \Phi_{MN} \end{bmatrix}_{3MN \times 3MN}. \end{cases} \quad (21)$$

The submatrices in the above matrices can be expressed as

$$\begin{cases} \mathbf{F}_{e,i_e} = [F_{e,i_e,u} \ F_{e,i_e,v} \ F_{e,i_e,w}], & (i_e = 1, 2, \dots, MN), \\ \Phi_{i_m} = \begin{bmatrix} \Phi_{i_m,mn}^u(z, \theta) & & 0 \\ & \Phi_{i_m,mn}^v(z, \theta) & \\ \text{sym} & & \Phi_{i_m,mn}^w(z, \theta) \end{bmatrix}, & (i_m = 1, 2, \dots, MN). \end{cases} \quad (22)$$

According to the above derivations, the scalar functions of the system such as kinetic energy, elastic strain energy, potential energy, dissipated energy, and work have been given, which are used to describe the amount of motion of the system, and their relationship can be obtained based on the Lagrange equation as [46]

$$\frac{d}{dt} \left(\frac{\partial T}{\partial \dot{q}} \right) - \frac{\partial T}{\partial q} + \frac{\partial R_d}{\partial \dot{q}} + \frac{\partial (U + P)}{\partial q} = \frac{\partial W}{\partial q}. \quad (23)$$

By substituting equations (14), (16), (17), (19), and (20) into (23), the motion equation of the workpiece-fixture

system can be expressed in terms of generalized coordinates and mode shapes as follows:

$$m_p \mathbf{M} \ddot{\mathbf{q}} + (c_w \mathbf{C}_w + c_s \mathbf{C}_s) \dot{\mathbf{q}} + \left(D \mathbf{K}_w + \sum_{a=1}^{P_a} \mathbf{K}_s \right) \mathbf{q} = \mathbf{F}_e \Phi. \quad (24)$$

Considering the complexity of the system damping, it is approximated by Rayleigh damping. The motion equation of the system can be written as

$$\mathbf{M} \ddot{\mathbf{q}} + \mathbf{C} \dot{\mathbf{q}} + \mathbf{K} \mathbf{q} = \mathbf{F}, \quad (25)$$

where

$$\begin{cases} \mathbf{C} = \alpha \mathbf{M} + \frac{\beta (D\mathbf{K}_w + \sum_{a=1}^{P_a} \mathbf{K}_s)}{m_p}, \\ \mathbf{K} = \frac{(D\mathbf{K}_w + \sum_{a=1}^{P_a} \mathbf{K}_s)}{m_p}, \\ \mathbf{F} = \frac{\mathbf{F}_e \Phi}{m_p}, \end{cases} \quad (26)$$

where α and β are constants.

In this way, the motion equation of the workpiece-fixture system is established. It can be seen that the proposed method can considerably reduce the computational complexity of the vector relationship by using the scalar functions, thereby making the modeling of the complex system easier and facilitating the prediction of the FRFs for the workpiece-fixture system in next section.

3. Frequency Response Function of the Workpiece-Fixture System

Fixture support increases the rigidity of the CTWW and also changes its dynamic characteristics. In this section, the workpiece-fixture system is regarded as a linear time-invariant (LTI) system, and the FRF is predicted.

By taking Fourier transform on equation (25), it becomes

$$(\mathbf{K} - \omega^2 \mathbf{M} + j\omega \mathbf{C}) \mathbf{q}(\omega) = \mathbf{F}(\omega). \quad (27)$$

Based on equation (27), the motion equation of the undamped free vibration system is given by

$$(\mathbf{K} - \omega^2 \mathbf{M}) \mathbf{q}(\omega) = 0. \quad (28)$$

From equation (28), the natural frequencies can be calculated for each set of (m, n) . Among the three frequencies in axial, radial, and tangential directions, the minimum value corresponds to the radial natural frequency, which will be analyzed in detail.

For the LTI system, the system response can be represented using the mode superposition method [47]. Thus, the response vector \mathbf{q} can be written as

$$\mathbf{q}(\omega) = \Psi \mathbf{p}(\omega), \quad (29)$$

where $\Psi = [\Psi_1 \ \Psi_2 \ \cdots \ \Psi_{N_d}]$ is a new mode shape matrix, Ψ_r ($r = 1, 2, \dots, N_d$) is the r -th order mode shape vector, $\mathbf{p} = [p_1(\omega) \ p_2(\omega) \ \cdots \ p_{N_d}(\omega)]^T$ is the modal coordinate vector, and N_d is the number of modes.

Substituting equation (29) into (27) and premultiplying it by Ψ^T , the r -th order modal equation of the system can be obtained on the basis of the orthogonality of the mode shapes:

$$(K_r - \omega^2 M_r + j\omega C_r) p_r = F_r, \quad (30)$$

where F_r is the r -th order modal force and K_r , M_r , and C_r are the r -th order modal stiffness, modal mass, and modal damping, respectively.

According to the above equation, the r -th order modal coordinate can be obtained as

$$p_r = \frac{F_r}{K_r - \omega^2 M_r + j\omega C_r}, \quad (31)$$

where $F_r = \Psi_r^T \mathbf{F}(\omega) = \sum_{l=1}^{p_n} \varphi_{lr} f_{j_r}(\omega)$, ($j_r = 1, 2, \dots, p_n$), φ_{lr} is the mode shape of the r -th order mode at the measurement point l , and p_n is the number of measurement points.

In this section, single point excitation is considered. Supposing that the exciting force is applied to point s , the force vector can be written as

$$\mathbf{F}(\omega) = [0 \ \cdots \ 0 \ \cdots \ f_s(\omega) \ \cdots \ 0]^T, \quad (32)$$

and the r -th order modal force becomes

$$F_r = \varphi_{sr} f_s(\omega). \quad (33)$$

Since the workpiece-fixture system is regarded as a LTI system, the response at any point l can be expressed as

$$q_l(\omega) = \varphi_{l1} p_1(\omega) + \varphi_{l2} p_2(\omega) + \cdots + \varphi_{lN} p_N(\omega) = \sum_{r=1}^{N_d} \varphi_{lr} p_r(\omega). \quad (34)$$

By substituting equations (31) and (33) into (34), the frequency response function between the measurement point l and the excitation point s can be given by

$$\frac{q_l(\omega)}{f_s(\omega)} = H_{ls}(\omega) = \sum_{r=1}^{N_d} \frac{\varphi_{lr} \varphi_{sr}}{K_r - \omega^2 M_r + j\omega C_r}, \quad (35)$$

i.e.,

$$H_{ls}(\omega) = \sum_{r=1}^{N_d} \frac{1}{K_{er} [(1 - \bar{\omega}_r^2 + 2j\xi_r \bar{\omega}_r)]}, \quad (36)$$

where $K_{er} = (K_r / \varphi_{lr} \varphi_{sr})$ in unit N/m, $\bar{\omega}_r = (\omega / \omega_r)$, $\xi_r = (C_r / 2M_r \omega_r)$, and ω_r is the r -th order natural frequency of the system in unit rad/s.

Through the above analysis, the FRFs of the workpiece-fixture system are obtained, in which a complete mode set is used, that is, all modes are superimposed. However, in actual analysis, the modal truncation method is widely used to reduce the computational burden. The dynamic characteristics of the system are investigated by selecting the first several modes, which will be applied in subsequent verification of the proposed method.

4. Verification

To verify the feasibility of the proposed method, a series of numerical calculation and experimental modal tests are carried out on a specifically designed workpiece-fixture system.

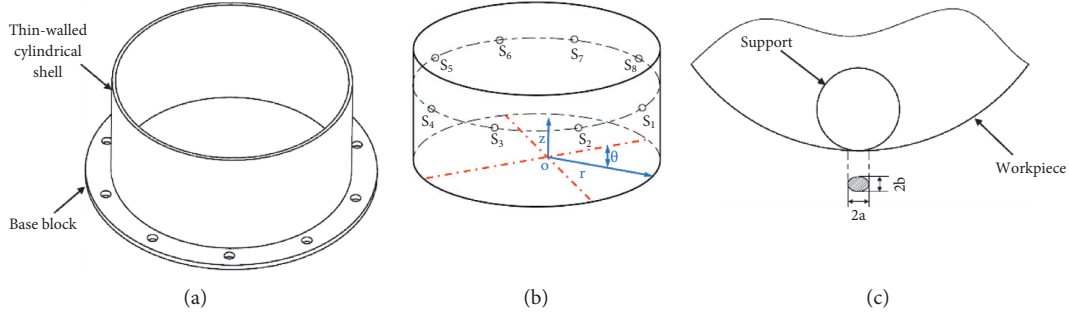


FIGURE 6: The designed CTWW for verification. (a) Schematic illustration of CTWW. (b) Fixture support layout scheme. (c) Ball head support and workpiece.

4.1. Workpiece and Fixture Support. A specific CTWW and fixture support layout are designed to validate the proposed method, as shown in Figure 6. The workpiece in Figure 6(a) is composed of two parts: the base block and the thin-walled cylindrical shell. For the base block, its outer diameter is 250 mm and inner diameter is 200 mm. To achieve the clamped boundary conditions at the bottom of the workpiece, the base block is designed to have ten cylindrical holes that are used to bolt the workpiece to the fixture base. For the thin-walled cylindrical shell, the outer diameter is 206 mm, inner diameter is 200 mm, and the height is 100 mm. Furthermore, the material of the workpiece is aluminum alloy 6061, which has the following physical parameters [44], as listed in Table 1. Without loss of generality, a support layout strategy used in actual on-site processing is presented, as shown in Figure 6(b). The specific locations of the fixture supports are listed in Table 2.

In this section, the support is designed with a ball head, which can ensure full contact with the inner wall of the workpiece. Under the action of the supporting force, the contact area between the support and the workpiece is elliptical, as shown in Figure 6(c). Since the rigidity of the workpiece in the radial direction is the weakest, only the supporting effect in this direction is considered in the study. Thus, the contact stiffness between the support and the workpiece is

$$k_s = \frac{dF_s}{d\delta_s}, \quad (37)$$

where F_s is the radial support force and δ_s is the elastic deformation, which can be obtained based on Hertz contact, and it is [48]

$$\delta_s = \delta^* \left[\frac{3F_s}{2 \sum \rho_t} \left(\frac{1 - \nu_f^2}{E_f} + \frac{1 - \nu_w^2}{E_w} \right) \right]^{2/3} \frac{\sum \rho_t}{2}, \quad (38)$$

where δ^* is a dimensionless parameter (the specific expression is given in Appendix E), ν_f and ν_w are Poisson's ratios of the support and the workpiece, respectively, E_f and E_w are the elastic moduli of the support and the workpiece, respectively, and $\sum \rho_t$ is the sum of curvature of the contact part of the workpiece and the support.

TABLE 1: Physical parameters of the aluminum alloy 6061.

Young's modulus (Pa)	Poisson's ratio	Density (kg/m ³)
68.9×10^9	0.33	2800

TABLE 2: Fixture support layout as shown in Figure 6(b).

Supports	Positions (z, θ , r)
S1	(60, 45, 100)
S2	(60, 90, 100)
S3	(60, 135, 100)
S4	(60, 180, 100)
S5	(60, 225, 100)
S6	(60, 270, 100)
S7	(60, 325, 100)
S8	(60, 360, 100)

After the workpiece and fixture support layout are determined, a series of numerical calculation and hammer tests can be carried out to verify the proposed method.

4.2. Numerical Calculation and Hammer Tests. Since the low-order modes have a great influence on the workpiece, the first two modes are considered in this paper. According to equation (36), the FRFs of the workpiece-fixture system can be obtained. To investigate the effects of fixture support on workpiece dynamic characteristics, the point with weak local stiffness is a good choice for comparison. Here, points along the circumferential path at the axial coordinate of 95 mm are selected to calculate the FRFs, and the predicted results of the workpiece with and without fixture support are shown in Figure 7. In the calculation process, the damping coefficients of the workpiece-fixture system are decided by means of impact test, where the damping ratio can be obtained. In addition, for the case of support, the diameter of the support ball head is 7 mm, and the support force is 15 N. It can be seen that after the fixture support is added to the workpiece, the FRF has the phenomenon of natural frequency value shift and amplitude reduction.

To verify the accuracy of the predicted FRFs, hammer tests are performed, as shown in Figure 8. Among them, the size of the experimental workpiece is the same as that of the designed structure, as shown in Figure 6(a), and the specific fixture support layout is consistent with that in Figure 6(b).

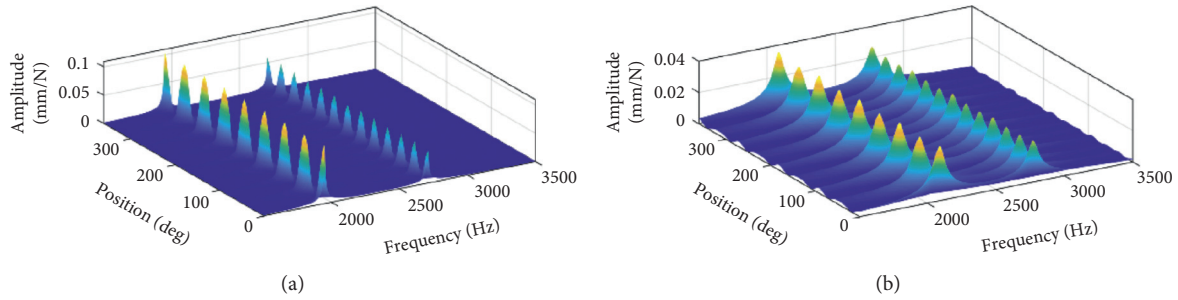


FIGURE 7: Comparisons of the predicted FRFs of workpiece. (a) Without support. (b) With support.

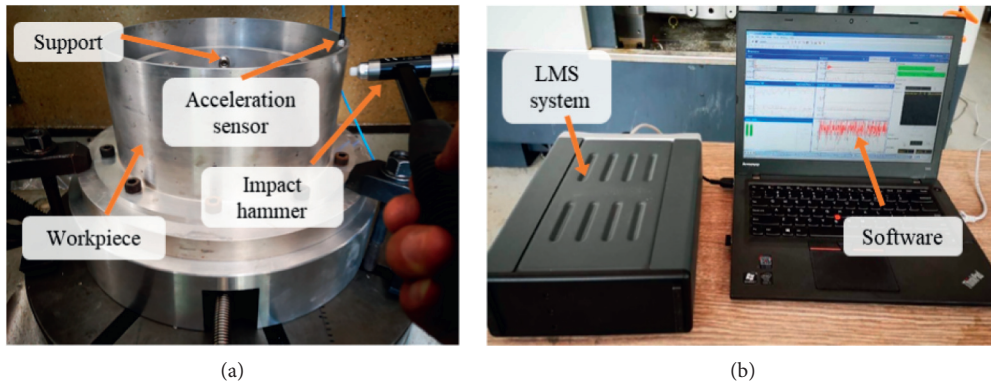


FIGURE 8: Experimental setup for hammer tests.

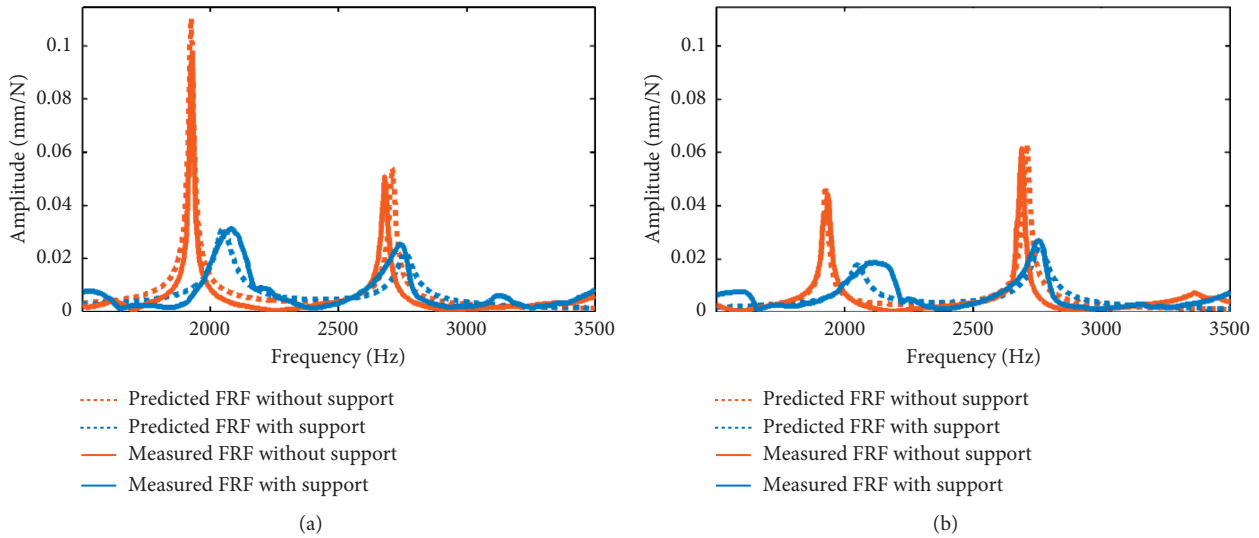


FIGURE 9: Comparisons of the FRFs of the workpiece with and without fixture support. (a) Point 1. (b) Point 2.

Moreover, the diameter of the support ball head and the support force are also in accord with those in the prediction. During the test, an impact hammer PCB 086C01 is selected as the excitation source and an acceleration sensor PCB 356A01 is used to obtain the vibration response of the workpiece. The transfer function between the excitation point and the response point can be obtained by the ratio of acceleration to force, and then it can be integrated to obtain

the ratio of displacement to force in the LMS data acquisition system SCADAS SCM202.

With the help of the above experimental setup, the FRFs of the workpiece with and without fixture support can be obtained. In order to analyze the effects of fixture support on the dynamic characteristics of the workpiece, two points P1 (95, 3, 103) and P2 (95, 33, 103) on the workpiece are selected, for which the measured FRFs are shown in Figure 9.

TABLE 3: Comparison of the predicted and measured natural frequency values.

Support layout	Modes	Predicted (Hz)	Measured (Hz)
Without support	1	1926	1930
	2	2710	2685
With support	1	2052	2081
	2	2761	2743

At the same time, the predicted FRFs of the two points are also included for comparison. It can be observed that the measured results are basically consistent with the predicted results.

In order to further observe the changes in the dynamic characteristics of the workpiece after adding support, the natural frequency values and amplitudes of the FRFs are compared and analyzed, respectively. The natural frequency values of the workpiece with and without fixture support are listed in Table 3. It can be seen that the predicted natural frequency values agree well with the experimental values, and the errors are within 5%. Moreover, it can be noted that the support has a greater influence on the natural frequency value of the low-order mode of the workpiece. Specifically, the frequency change of the first-order mode is much larger than that of the second-order mode.

As shown in Figure 9, the amplitudes are effectively reduced after adding fixture supports. The amplitude of each mode also changes with the measured position, which is attributed to the influence of mode shape of the workpiece. Experimental modal tests reveal that the amplitude changes of the two points are in line with the predicted results. The slight discrepancies between the predicted results and the test results may be caused by the measurement error in the test process or the simplification error of the complex interaction between workpiece and fixture support, which deserves further exploration in the future.

5. Conclusions

In this paper, a comprehensive analytical solution is proposed to investigate effects of fixture supports on the dynamic characteristics of CTWWs. During the modeling process, a number of methods are used, such as the vector mechanics method, the analytical mechanics method, the variable separation method, the modal superposition method, and the modal truncation method. These methods can simplify the analysis of the complex multi-degree-of-freedom system and avoid tedious mathematical calculation. According to the developed model, effects of fixture support on workpiece dynamic characteristics can be analyzed effectively. The feasibility of the proposed method is verified on a specifically designed workpiece-fixture system by means of numerical calculation and experimental hammer tests. The FRFs of different points on the workpiece with and without support are compared and analyzed, and some important conclusions are drawn as follows:

- (1) The FRFs of the CTWW with fixture support constraints can be accurately predicted by using the

proposed method, which are in good agreement with the experimental results.

- (2) The dynamics of the CTWW can be improved by adding fixture support, where the FRFs of the system have changed a lot. Specifically, the natural frequency value increases and the amplitude decreases, especially for low-order modes.
- (3) The influence of the fixture support on the dynamics of the CTWW can be explained clearly from the mechanism, that is, the stiffness of the support can affect the natural frequency value of the FRF, and the damping of the support can affect the amplitude of the FRF.
- (4) In the design of fixtures for thin-walled workpieces, adding auxiliary supports is an effective method, which can increase the rigidity of the system and reduce the vibration of the system.

The main work of this paper is to investigate effects of fixture support on the dynamic characteristics of CTWW. Further, there are some other problems that need to be considered in the future, such as the effects of different support types and number of supports on the dynamic characteristics of thin-walled workpiece. In addition, the complex interaction between the support and the workpiece is an important factor that affects the accuracy of the prediction, which also needs to be explored in the future.

Appendix

A. Differential Operators in Equation (3)

The differential operators of thin-walled workpiece in equation (3) are

$$\begin{aligned}
 L_{11} &= K \frac{1+\mu}{2R} \frac{\partial^2}{\partial\theta\partial z}, \\
 L_{12} &= K \frac{\mu}{R} \frac{\partial}{\partial z}, \\
 L_{13} &= K \frac{\partial^2}{\partial z^2} + K \frac{1-\mu}{2R^2} \frac{\partial^2}{\partial\theta^2}, \\
 L_{21} &= K \frac{1-\mu}{2} \frac{\partial^2}{\partial z^2} + K \frac{1}{R^2} \frac{\partial^2}{\partial\theta^2} + D \frac{1-\mu}{2R^2} \frac{\partial^2}{\partial z^2} + D \frac{1}{R^4} \frac{\partial^2}{\partial\theta^2}, \\
 L_{22} &= K \frac{1}{R^2} \frac{\partial}{\partial\theta} - D \frac{1}{R^4} \frac{\partial^3}{\partial\theta^3} - D \frac{1}{R^2} \frac{\partial^3}{\partial z^2\partial\theta}, \\
 L_{23} &= K \frac{1+\mu}{2R} \frac{\partial^2}{\partial\theta\partial z}, \\
 L_{31} &= K \frac{1}{R^2} \frac{\partial}{\partial\theta} - D \frac{1}{R^4} \frac{\partial^3}{\partial\theta^3} - D \frac{1}{R^2} \frac{\partial^3}{\partial z^2\partial\theta}, \\
 L_{32} &= K \frac{1}{R^2} + D \frac{\partial^4}{\partial z^4} + D \frac{1}{R^4} \frac{\partial^4}{\partial\theta^4} + D \frac{2}{R^2} \frac{\partial^4}{\partial z^2\partial\theta^2}, \\
 L_{33} &= K \frac{\mu}{R} \frac{\partial}{\partial z}.
 \end{aligned}$$

(A.1)

B. Undetermined Coefficients in Equation (9)

The expressions of the undetermined coefficients c_{i,j_c} in equation (9) are given as follows:

$$\begin{aligned}
 c_{11} &= K \frac{n(1+\mu)}{2\rho HR} \frac{\int_0^L \phi'_m(z) \phi'''_m(z) dz}{\int_0^L \phi'_m(z) \phi'_m(z) dz}, \\
 c_{12} &= K \frac{\mu}{\rho HR} \frac{\int_0^L \phi'_m(z) \phi'''_m(z) dz}{\int_0^L \phi'_m(z) \phi'_m(z) dz}, \\
 c_{13} &= \omega_{mn}^2 + \frac{K}{\rho H} \left[\frac{\int_0^L \phi_m(z) \phi''_m(z) dz}{\int_0^L \phi_m(z) \phi_m(z) dz} - \frac{n^2(1-\mu)}{2R^2} \right], \\
 c_{21} &= \omega_{mn}^2 + \frac{(KR^2 + D)}{\rho HR^2} \left(\frac{1-\mu}{2} \frac{\int_0^L \phi_m(z) \phi''_m(z) dz}{\int_0^L \phi_m(z) \phi_m(z) dz} - \frac{n^2}{R^2} \right), \\
 c_{22} &= \frac{Dn}{\rho HR^2} \left(\frac{\int_0^L \phi_m(z) \phi''_m(z) dz}{\int_0^L \phi_m(z) \phi_m(z) dz} - \frac{n^2}{R^2} \right) + \frac{Kn}{\rho HR^2}, \\
 c_{23} &= -K \frac{n(1+\mu)}{2\rho HR} \frac{\int_0^L \phi'_m(z) \phi'''_m(z) dz}{\int_0^L \phi'_m(z) \phi'_m(z) dz}, \\
 c_{31} &= \frac{Dn}{\rho HR^2} \left(\frac{\int_0^L \phi_m(z) \phi''_m(z) dz}{\int_0^L \phi_m(z) \phi_m(z) dz} - \frac{n^2}{R^2} \right) - \frac{Kn}{\rho HR^2}, \\
 c_{32} &= \omega_{mn}^2 + D \frac{n^2}{\rho HR^2} \left(2 \frac{\int_0^L \phi_m(z) \phi''_m(z) dz}{\int_0^L \phi_m(z) \phi_m(z) dz} - \frac{n^2}{R^2} \right) + \frac{K}{\rho HR^2} + \frac{D}{\rho H} \frac{\int_0^L \phi_m(z) \phi'''_m(z) dz}{\int_0^L \phi_m(z) \phi_m(z) dz}, \\
 c_{33} &= -K \frac{\mu}{\rho HR} \frac{\int_0^L \phi'_m(z) \phi''_m(z) dz}{\int_0^L \phi'_m(z) \phi'_m(z) dz},
 \end{aligned} \tag{B.1}$$

where the superscripts of $\phi'_m(z)$, $\phi''_m(z)$, $\phi'''_m(z)$, and $\phi''''_m(z)$ represent the corresponding derivative order.

C. Element Expression in Equation (15)

The expression of each element in the submatrix in equation (15) is

$$\begin{aligned}
 M_{11} &= \rho H \int_0^L \int_0^{2\pi} \Phi_{mn}^u(z, \theta) \Phi_{mn}^u(z, \theta) R d\theta dz, \\
 M_{22} &= \rho H \int_0^L \int_0^{2\pi} \Phi_{mn}^v(z, \theta) \Phi_{mn}^v(z, \theta) R d\theta dz, \\
 M_{33} &= \rho H \int_0^L \int_0^{2\pi} \Phi_{mn}^w(z, \theta) \Phi_{mn}^w(z, \theta) R d\theta dz, \\
 M_{12} &= M_{13} = M_{21} = M_{23} = M_{31} = M_{32} = 0,
 \end{aligned} \tag{C.1}$$

where $\Phi_{mn}^u(z, \theta)$, $\Phi_{mn}^v(z, \theta)$, and $\Phi_{mn}^w(z, \theta)$ are the mode shape functions in three directions, and they can be expressed as

$$\begin{aligned}
 \Phi_{mn}^u(z, \theta) &= A_{mn} \phi_m(z) \sin(n\theta), \\
 \Phi_{mn}^v(z, \theta) &= B_{mn} \phi_m(z) \cos(n\theta), \\
 \Phi_{mn}^w(z, \theta) &= C_{mn} \frac{d\phi_m(z)}{d(z/L)} \cos(n\theta).
 \end{aligned} \tag{C.2}$$

D. Element Expression in Equation (16)

The expression of each element in the submatrix in equation (16) is

$$\begin{aligned}
K_{11} &= \frac{EH}{1-\mu^2} \int_0^L \int_0^{2\pi} \left[\left(\frac{\partial \Phi_{mn}^w(z, \theta)}{\partial z} \right)^2 + \frac{1-\mu}{2R^2} \left(\frac{\partial \Phi_{mn}^w(z, \theta)}{\partial \theta} \right)^2 \right] R d\theta dz, \\
K_{12} = K_{21} &= \frac{EH}{2(1-\mu^2)} \int_0^L \int_0^{2\pi} \left(\frac{2\mu}{R} \frac{\partial \Phi_{mn}^w(z, \theta)}{\partial z} \frac{\partial \Phi_{mn}^u(z, \theta)}{\partial \theta} + \frac{1-\mu}{R} \frac{\partial \Phi_{mn}^w(z, \theta)}{\partial \theta} \frac{\partial \Phi_{mn}^u(z, \theta)}{\partial z} \right) R d\theta dz, \\
K_{13} = K_{31} &= \frac{EH}{2(1-\mu^2)} \int_0^L \int_0^{2\pi} \left(\frac{2\mu}{R} \frac{\partial \Phi_{mn}^w(z, \theta)}{\partial z} \Phi_{mn}^v(z, \theta) \right) R d\theta dz, \\
K_{22} &= \frac{EH}{1-\mu^2} \int_0^L \int_0^{2\pi} \left[\left(\frac{1}{R^2} + \frac{H^2}{12R^4} \right) \left(\frac{\partial \Phi_{mn}^u(z, \theta)}{\partial \theta} \right)^2 + \left(\frac{H^2}{24R^2} + \frac{1}{2} \right) (1-\mu) \left(\frac{\partial \Phi_{mn}^u(z, \theta)}{\partial z} \right)^2 \right] R d\theta dz, \\
K_{23} = K_{32} &= \frac{EH}{2(1-\mu^2)} \int_0^L \int_0^{2\pi} \left[\begin{aligned} &\frac{2}{R^2} \frac{\partial \Phi_{mn}^u(z, \theta)}{\partial \theta} \Phi_{mn}^v(z, \theta) - \frac{\mu H^2}{6R^2} \frac{\partial \Phi_{mn}^u(z, \theta)}{\partial \theta} \frac{\partial^2 \Phi_{mn}^v(z, \theta)}{\partial z^2} \\ &\frac{H^2}{6R^4} \frac{\partial \Phi_{mn}^u(z, \theta)}{\partial \theta} \frac{\partial^2 \Phi_{mn}^v(z, \theta)}{\partial \theta^2} - \frac{H^2(1-\mu)}{6R^2} \frac{\partial \Phi_{mn}^u(z, \theta)}{\partial z} \frac{\partial^2 \Phi_{mn}^v(z, \theta)}{\partial z \partial \theta} \end{aligned} \right] R d\theta dz, \\
K_{33} &= \frac{EH}{1-\mu^2} \int_0^L \int_0^{2\pi} \left[\begin{aligned} &\left(\frac{\partial \Phi_{mn}^v(z, \theta)}{R} \right)^2 + \frac{H^2}{12R^4} \left(\frac{\partial^2 \Phi_{mn}^v(z, \theta)}{\partial \theta^2} \right)^2 + \frac{\mu H^2}{6R^2} \frac{\partial^2 \Phi_{mn}^v(z, \theta)}{\partial z^2} \frac{\partial^2 \Phi_{mn}^v(z, \theta)}{\partial \theta^2} \\ &+ \frac{H^2}{12} \left(\frac{\partial^2 \Phi_{mn}^v(z, \theta)}{\partial z^2} \right)^2 + \frac{H^2(1-\mu)}{6R^2} \left(\frac{\partial^2 \Phi_{mn}^v(z, \theta)}{\partial z \partial \theta} \right)^2 \end{aligned} \right] R d\theta dz.
\end{aligned} \tag{D.1}$$

E. Dimensionless Parameter in Equation (38)

The expression of dimensionless parameter δ^* in equation (38) is

$$\delta^* = \frac{2\Gamma}{\pi} \left(\frac{\pi}{2k_{ab}^2 \Sigma} \right)^{1/3}, \tag{E.1}$$

where

$$k_{ab} = \frac{a}{b},$$

$$\Gamma = \int_0^{2\pi} \left[1 - \left(1 - \frac{1}{k_{ab}^2} \right) \sin^2 \varphi^2 \right]^{-1/2} d\varphi, \tag{E.2}$$

$$\Sigma = \int_0^{2\pi} \left[1 - \left(1 - \frac{1}{k_{ab}^2} \right) \sin^2 \varphi^2 \right]^{1/2} d\varphi,$$

where k_{ab} is the ellipticity of the contact ellipse and Γ and Σ are the complete elliptic integrals of the first and second types, respectively, and they can be obtained according to the related formulae of [49].

Data Availability

The data used to support the findings of this study are included within the article and are available from the corresponding author upon request.

Conflicts of Interest

The authors declare that there are no conflicts of interest regarding the publication of this paper.

Acknowledgments

This study was supported by the NKRDPC (grant no. 2018YFA0704603) and the National Natural Science Foundation of China (grant no. 51905076).

References

- [1] Y. Sun and S. Jiang, "Predictive modeling of chatter stability considering force-induced deformation effect in milling thin-walled parts," *International Journal of Machine Tools and Manufacture*, vol. 135, pp. 38–52, 2018.
- [2] S. Jiang and Y. Sun, "Stability analysis for a milling system considering multi-point-contact cross-axis mode coupling and cutter run-out effects," *The Mechanical Systems and Signal Processing*, vol. 141, p. 106452, 2020.
- [3] J. Niu, J. Xu, F. Ren, Y. Sun, and D. Guo, "A short review on milling dynamics in low-stiffness cutting conditions: modeling and analysis," *Journal of Advanced Manufacturing Science and Technology*, vol. 1, no. 1, p. 2020004, 2021.
- [4] Y. Sun, J. Jia, J. Xu, M. Chen, and J. Niu, "Path, feedrate and trajectory planning for free-form surface machining: a state-of-the-art review," *Chinese Journal of Aeronautics*, 2021.
- [5] A. Gameros, S. Lowth, D. Axinte, A. Nagy-Sochacki, O. Craig, and H. R. Siller, "State-of-the-art in fixture systems for the manufacture and assembly of rigid components: a review,"

- International Journal of Machine Tools and Manufacture*, vol. 123, pp. 1–21, 2017.
- [6] B. Li and S. N. Melkote, “Fixture clamping force optimisation and its impact on workpiece location accuracy,” *The International Journal of Advanced Manufacturing Technology*, vol. 17, no. 2, pp. 104–113, 2001.
 - [7] G. H. Qin, W. H. Zhang, and M. Wan, “A mathematical approach to analysis and optimal design of a fixture locating scheme,” *International Journal of Advanced Manufacturing Technology*, vol. 29, no. 3–4, pp. 349–359, 2006.
 - [8] M. Sága, M. Blatnická, M. Blatnický, J. Dižo, and J. Gerlici, “Research of the fatigue life of welded joints of high strength steel S960 Q1 created using laser and electron beams,” *Materials*, vol. 13, no. 11, p. 2539, 2020.
 - [9] M. Estrems, H. T. Sanchez, and F. Faura, “Influence of fixtures on dimensional accuracy in machining processes,” *The International Journal of Advanced Manufacturing Technology*, vol. 21, no. 5, pp. 384–390, 2003.
 - [10] M. Blatnický, D. Jan, M. Sága, J. Gerlici, and E. Kuba, “Design of a mechanical part of an automated platform for oblique manipulation,” *Applied Sciences-Basel*, vol. 10, no. 23, p. 8467, 2020.
 - [11] S. P. Siebenaler and S. N. Melkote, “Prediction of workpiece deformation in a fixture system using the finite element method,” *International Journal of Machine Tools and Manufacture*, vol. 46, no. 1, pp. 51–58, 2006.
 - [12] A. Raghu and S. N. Melkote, “Analysis of the effects of fixture clamping sequence on part location errors,” *International Journal of Machine Tools and Manufacture*, vol. 44, no. 4, pp. 373–382, 2004.
 - [13] L. Nagendran, K. Srinivasan, and V. Ranjeev, “Analytical and experimental studies on fixtured work pieces,” *AIP Conference Proceedings*, vol. 712, pp. 690–694, 2004.
 - [14] M. J. Nategh and H. Parvaz, “Development of computer aided clamping system design for workpieces with freeform surfaces,” *Computer-Aided Design*, vol. 95, pp. 52–61, 2018.
 - [15] R. Haymanali, E. C. De Meter, and M. W. Trethewey, “Development of a compliance tester for assessing and reducing the static compliance of fixture-workpiece systems,” *Journal of Manufacturing Systems*, vol. 19, no. 2, pp. 108–120, 2000.
 - [16] E. C. De Meter, W. Xie, S. Choudhuri, S. Vallapuzha, and M. W. Trethewey, “A model to predict minimum required clamp pre-loads in light of fixture-workpiece compliance,” *International Journal of Machine Tools and Manufacture*, vol. 41, no. 7, pp. 1031–1054, 2001.
 - [17] H. T. Sánchez, M. Estrems, and F. Faura, “Fixturing analysis methods for calculating the contact load distribution and the valid clamping regions in machining processes,” *The International Journal of Advanced Manufacturing Technology*, vol. 29, no. 5, pp. 426–435, 2006.
 - [18] S. Ratchev, K. Phuah, and S. Liu, “Fea-based methodology for the prediction of part-fixture behaviour and its applications,” *Journal of Materials Processing Technology*, vol. 191, no. 1–3, pp. 260–264, 2007.
 - [19] B. Li and S. N. Melkote, “Optimal fixture design accounting for the effect of workpiece dynamics,” *International Journal of Advanced Manufacturing Technology*, vol. 18, no. 10, pp. 701–707, 2001.
 - [20] S. Satyanarayana and S. N. Melkote, “Finite element modeling of fixture-workpiece contacts: single contact modeling and experimental verification,” *International Journal of Machine Tools and Manufacture*, vol. 44, no. 9, pp. 903–913, 2004.
 - [21] G. Chen, X. Shu, J. Liu, B. Zhang, and J. Feng, “A new method for distortion calculations in additive manufacturing: contact analysis between a workpiece and clamps,” *International Journal of Mechanical Sciences*, vol. 171, p. 105362, 2020.
 - [22] A. P. Christoforou, A. S. Yigit, and M. Majeed, “Low-velocity impact response of structures with local plastic deformation: characterization and scaling,” *Journal of Computational and Nonlinear Dynamics*, vol. 8, p. 0110121, 2013.
 - [23] H. Ghaednia, D. B. Marghitu, and R. L. Jackson, “Predicting the permanent deformation after the impact of a rod with a flat surface,” *Journal of Tribology-Transactions of the ASME*, vol. 137, p. 0114031, 2015.
 - [24] D. Rathbone, M. Marigo, D. Dini, and B. van Wachem, “An accurate force-displacement law for the modelling of elastic-plastic contacts in discrete element simulations,” *Powder Technology*, vol. 282, no. SI, pp. 2–9, 2015.
 - [25] J.-R. Riba, A.-G. Mancini, C. Abomailek, and F. Capelli, “A 3D-fem-based model to predict the electrical constriction resistance of compressed contacts,” *Measurement*, vol. 114, pp. 44–50, 2018.
 - [26] A. R. Khoei and M. Nikbakht, “Contact friction modeling with the extended finite element method (X-Fem),” *Journal of Materials Processing Technology*, vol. 177, no. 1–3, pp. 58–62, 2006.
 - [27] B. Wiegert, H. Hetzler, and W. Seemann, “A simplified elastohydrodynamic contact model capturing the nonlinear vibration behaviour,” *Tribology International*, vol. 59, pp. 79–89, 2013.
 - [28] B. Hu, C. Zhou, and S. Chen, “Elastic dynamics modelling and analysis for a valve train including oil film stiffness and dry contact stiffness,” *Mechanism and Machine Theory*, vol. 131, pp. 33–47, 2019.
 - [29] X. D. Lu, J. Zhao, J. L. Mo, Q. Zhang, X. Zhang, and Z. R. Zhou, “Improvement of dynamical and tribological properties of friction systems by introducing parallel-grooved structures in elastic damping components,” *Composite Structures*, vol. 192, pp. 8–19, 2018.
 - [30] Y. J. G. Liao and S. J. Hu, “Flexible multibody dynamics based fixture-workpiece analysis model for fixturing stability,” *International Journal of Machine Tools and Manufacture*, vol. 40, no. 3, pp. 343–362, 2000.
 - [31] A. Matsubara, Y. Taniyama, J. Wang, and D. Kono, “Design of a support system with a pivot mechanism for suppressing vibrations in thin-wall milling,” *CIRP Annals*, vol. 66, no. 1, pp. 381–384, 2017.
 - [32] J. Fei, B. Lin, J. Xiao et al., “Investigation of moving fixture on deformation suppression during milling process of thin-walled structures,” *Journal of Manufacturing Processes*, vol. 32, pp. 403–411, 2018.
 - [33] J. Ma, D. Zhang, B. Wu, M. Luo, and Y. Liu, “Stability improvement and vibration suppression of the thin-walled workpiece in milling process via magnetorheological fluid flexible fixture,” *International Journal of Advanced Manufacturing Technology*, vol. 88, no. 5–8, pp. 1231–1242, 2017.
 - [34] M. Meshreki, H. Attia, and J. Kovecses, “A new analytical formulation for the dynamics of multipocket thin-walled structures considering the fixture constraints,” *Journal of Manufacturing Science and Engineering-Transactions of the ASME*, vol. 133, p. 0210142, 2011.
 - [35] J. Yan and G. Qiang, “Simulation of multi-axis grinding considering runout based on envelope theory,” *Chinese Journal of Aeronautics*, vol. 33, pp. 3526–3534, 2020.
 - [36] X. Xie, H. Zheng, S. Jonckheere, A. van de Walle, B. Plumers, and W. Desmet, “Adaptive model reduction technique for large-scale dynamical systems with frequency-dependent

- damping,” *Computer Methods in Applied Mechanics and Engineering*, vol. 332, pp. 363–381, 2018.
- [37] M. Meshreki, H. Attia, and J. Kovecses, “Development of a new model for the varying dynamics of flexible pocket-structures during machining,” *Journal of Manufacturing Science and Engineering-Transactions of the ASME*, vol. 133, p. 0410024, 2011.
- [38] X.-J. Wan and Y. Zhang, “A novel approach to fixture layout optimization on maximizing dynamic machinability,” *International Journal of Machine Tools and Manufacture*, vol. 70, pp. 32–44, 2013.
- [39] F. Pellicano, “Vibrations of circular cylindrical shells: theory and experiments,” *Journal of Sound and Vibration*, vol. 303, no. 1-2, pp. 154–170, 2007.
- [40] Z. Luo, N. Sun, Y. Wang, K. Zhang, and Q. Han, “Study of vibration characteristics of the short thin cylindrical shells and its experiment,” *Journal of Vibroengineering*, vol. 15, no. 3, pp. 1270–1283, 2013.
- [41] Y. Kurylov and M. Amabili, “Polynomial versus trigonometric expansions for nonlinear vibrations of circular cylindrical shells with different boundary conditions,” *Journal of Sound and Vibration*, vol. 329, no. 9, pp. 1435–1449, 2010.
- [42] W. Soedel, *Vibrations of Shells and Plates*, Marcel Dekker Inc, New York, NY, USA, 2004.
- [43] C. T. Loy, K. Y. Lam, and C. Shu, “Analysis of cylindrical shells using generalized differential quadrature,” *Shock and Vibration*, vol. 4, no. 3, pp. 193–198, 1997.
- [44] X.-J. Wan, Y. Zhang, and X.-D. Huang, “Investigation of influence of fixture layout on dynamic response of thin-wall multi-framed work-piece in machining,” *International Journal of Machine Tools and Manufacture*, vol. 75, pp. 87–99, 2013.
- [45] M. Amabili, *Nonlinear Vibrations and Stability of Shells and Plates*, Cambridge University Press, New York, NY, USA, 2008.
- [46] J. Ma, D. Zhang, B. Wu, M. Luo, and B. Chen, “Vibration suppression of thin-walled workpiece machining considering external damping properties based on magnetorheological fluids flexible fixture,” *Chinese Journal of Aeronautics*, vol. 29, no. 4, pp. 1074–1083, 2016.
- [47] D. J. Ewins, *Modal Testing: Theory, Practice and Application*, Imperial College of Science, Technology and Medicine, London, UK, 2000.
- [48] T. A. Harris and M. N. Kotzalas, *Essential Concepts of Bearing Technology*, Taylor & Francis, Oxfordshire, UK, 2006.
- [49] D. E. Brewe and B. J. Hamrock, “Simplified solution for elliptical-contact deformation between two elastic solids,” *Journal of Lubrication Technology*, vol. 99, no. 4, pp. 485–487, 1977.

Research Article

Design and Error Compensation Performance of a Precision Micro-Drive Rotary System

Manzhi Yang ¹, Gang Jing ¹, Zhenyang Lv,¹ Wei Guo,¹ Yumei Huang,² Kaiyang Wei ¹,
Linyue Li ¹, Bin Feng,¹ Hongyu Ge,¹ and Shuaitian Li¹

¹College of Mechanical Engineering, Xi'an University of Science and Technology, No. 58 Yanta Middle Road, Xi'an, Shaanxi 710054, China

²School of Mechanical and Precision Instrumental Engineering, Xi'an University of Technology, No. 8 Jinhua South Road, Xi'an, Shaanxi 710048, China

Correspondence should be addressed to Manzhi Yang; xkdymz@xust.edu.cn

Received 23 April 2021; Accepted 17 June 2021; Published 20 July 2021

Academic Editor: Shanglei Jiang

Copyright © 2021 Manzhi Yang et al. This is an open access article distributed under the Creative Commons Attribution License, which permits unrestricted use, distribution, and reproduction in any medium, provided the original work is properly cited.

In order to obtain motion with large travel and high precision, the micro-drive system is used to compensate for the motion error of the macro-drive system in the macro/micro dual-drive system. The research on the micro-drive rotary system lags behind the micro-drive linear system, so it is of great significance to study the designing and error compensation performance of a precision micro-drive rotary system. In this paper, a precision micro-drive rotary system is designed, the error compensation scheme of the system is proposed, and the system feasibility in design and error compensation is tested by FEM simulation analysis and performance experiments. Firstly, a precision micro-drive rotary system is designed to provide high-precision rotary motion, which consists of a micro rotary mechanism and PZT. In the system, the micro rotary mechanism is developed based on the compound motion principle of flexure hinge, which can accurately transform an input of linear motion into an output of rotary motion according to a certain relationship. Secondly, for finishing the error compensation scheme of the system, the maximum compensation modifier θ'_{\max} is proposed based on the analysis of error compensation equations of point-to-point motion and continuous motion. Finally, in order to facilitate the use of engineering, the driven voltage equation of error compensation is derived by the error compensation performance experiment. The simulation and experiment results indicate that both the design and error-compensation-range of the system satisfy the needs of practical application.

1. Introduction

Mechanical equipment manufacturing is the key of the manufacturing industry. Because the precision requirements of mechanical systems in the modern industry continually improve, the machining precision and motion precision requirements of equipment manufacturing mechanical systems continually increase [1–3]. At present, precision and ultra-precision processing technologies are important realization methods of mechanical equipment precision manufacturing [4–10]. The precision feed technology is an important realization method of ultra-precision processing technology [11–13]. In addition, the macro/micro dual-drive system solves the contradiction between large-motion travel

and high motion precision, which can provide motion with large travel and high precision. The macro/micro dual-drive system has been widely used in high-technology fields such as the advanced war industry, biological medicine, and precision electronics [14–19].

In the macro/micro dual-drive system, as macro-actuators (i.e., direct drive motor) have their own defects such as vibration and motion pulse error, the macro-drive system can only provide large-travel displacement, but it cannot provide motion in ultrahigh precision (i.e., nanometer level or sub-arc-second level) even after error compensation. However, a micro-drive system can reach ultra-high precision because of ultra-precision drive by micro-actuators and the good transmission performance of the micro

mechanism. The micro-drive system can compensate for the motion error of the macro-drive system with a higher precision level, so the macro/micro dual-drive system can provide motion with large travel and high precision [20–23]. By providing accurate motion based on the compound motion principle of the flexure hinge, the micro-mechanism is the core part of the micro-drive system [24–27]. Therefore, it is necessary to study the performance of the micro-drive system.

In recent years, many scholars studied the micro-drive system, and they mainly focused on certain research areas, such as mechanical structure design, structure optimization, dynamic analysis, and practical application. A precision MEMS (Micro-electromechanical System) mechanism with six degrees of freedoms was designed, which can be applied to electron transport micro-scopes with the size of $10\ \mu\text{m} \times 20\ \mu\text{m} \times 0.2\ \mu\text{m}$; in addition, the mechanism has realized precision rotary motion in three-dimensional space [28]. A bridge micro-mechanism with three degrees of freedoms was developed, and the Z direction of the mechanism has high stiffness and stability, which can resist large external thrust. The structure of the mechanism was optimized by the sequential quadratic rule, and the experiment results show that the optimization method is very effective [29]. A flexible micro-mechanism with two-directional rotary motion driven by Giant Magnetostrictive Actuator was proposed, and the dynamic model of mechanism parameters was given based on the dynamic model establishment [30]. A new chip-level comb-drive magnifying micro-drive platform with three degrees of freedom (X -, Y -, and Z -directions) was designed, and the platform can achieve large displacements of $25.2\ \mu\text{m}$ in x -direction, $20.4\ \mu\text{m}$ in y -direction, and $58.5\ \mu\text{m}$ in z -direction [31]. A new compliant mechanism constituted by flexure hinges with two-straight circular and multinotched was mentioned, whose structure optimization was accomplished using the topological method; the mechanism performances were analyzed by the finite element method, including the stiffness, rotary precision, and horizontal stress, and the analysis results show that the mechanism performances are excellent [32]. A fully compliant, potentially monolithic, power transmission mechanism, which can rectify a large lateral offset between two parallel rotational axes, was developed; the internal stiffness is removed by static balancing and results in a statically balanced compliant transmission mechanism, that is, with zero actuation stiffness [33].

At present, the research on the micro-drive system mainly concentrates on linear motion, and many studies have been used in production [34–36]. However, research on the micro-drive rotary system is rare, and the positional accuracy is concentrated on the arc-second ($''$) level [37, 38]. Therefore, a new micro-mechanism is badly in need of transforming the linear motion into rotary motion with high-precision, and then we can obtain high-precision rotary motion based on the ultra-high precision of linear motion. In this paper, a micro rotary system is designed which can solve the low-precision problem of the rotary system. In this system, a new micro rotary mechanism is developed based on the compound motion principle of

flexure hinge, and an ultra-high-precision PZT as micro-actuators to drive the micro-mechanism.

Additionally, the error compensation performance of the micro-drive rotary system can directly affect the motion precision of the macro/micro dual-drive rotary system. Therefore, it is significant to design an error compensation analysis for the micro-drive rotary system.

A precision micro rotary system is designed to obtain the rotary motion with high precision. The precision micro rotary system could convert the linear displacement into the rotary displacement accurately, thus solving the problem of low precision of rotary motion and proposing the error compensation scheme of the system.

The driven voltage equation of error compensation is derived by the error compensation performance experiment. The simulation and experiment results show that both the design and error compensation performance of the system satisfy the needs of practical application. This study has reference significance to research on design and error compensation performance of the micro-drive rotary system.

The rest of this paper is organized as follows: Section 2 introduces the design of the micro-drive rotary system. The error compensation scheme of the system is given in Section 3. In Section 4, strength and modal analysis of the system by FEM simulation are finished. Section 5 carries out modal and error compensation performance experiments and analyzes results. The conclusions are drawn in Section 6.

2. Design of the Micro-Drive Rotary System

At the macro/micro dual-drive system, the macro-drive system provides the motion with large travel, and the micro-drive system compensates the position error of the macro-drive system; therefore, the macro/micro dual-drive system has high-precision and large-travel motion. To develop a macro/micro dual-drive rotary system with high precision and large travel, a precision micro-drive rotary system is designed, and the system uses the PZT as a micro-actuator to drive the micro rotary mechanism to obtain high-precision rotary motion. The micro-drive rotary system is shown in Figure 1.

2.1. The Micro Rotary Mechanism. When a flexible material is stressed, the flexure hinge will produce minor deformation, which can realize the transmission motion and guiding motion; this principle is the compound motion principle of the flexure hinge. The transmission motion amplifies or reduces an input motion with a certain ratio, and transmission motion can also sometimes transform motion between linear and rotary with a certain relationship. The guiding motion guides the direction of motion by flexure hinges, which can ensure that there is a displacement of motion only in motion direction, and there is no non-motion direction displacement during motion.

In this paper, a micro rotary mechanism with single-DOF symmetric drive and guiding and transformation is designed based on the compound motion principle of

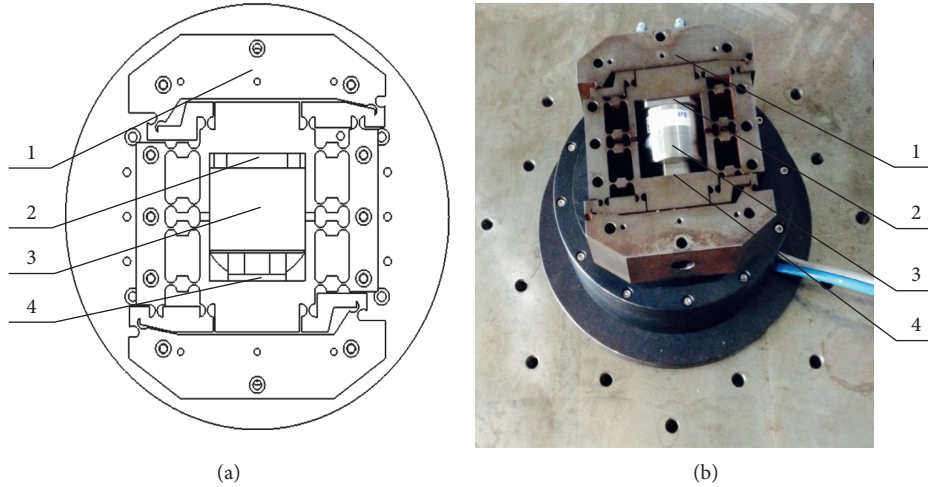


FIGURE 1: The micro-drive rotary system. (a) Schematic diagram of the micro-drive rotary system. (b) Picture of the micro-drive rotary system. (1) The micro rotary mechanism. (2) Gasket. (3) PZT (piezoelectric actuator). (4) Fixing sleeve.

flexure hinge, which can accurately transform the input of linear motion into an output of rotary motion according to a certain relationship (i.e., realize the accurate transformation of Δu to $\Delta\theta$). The micro rotary mechanism is shown in Figure 2, and the stereogram of the mechanism is shown in Figure 2(a). The micro rotary mechanism consists of four parts: *a*, *b*, *c*, and *d*. Part *a* consists of the connecting element between macro-drive and micro-drive, which is the element that connects the motion of the macro-drive with the motion of the micro-drive. Part *b* is the input motion element of the micro-drive, which brings the input linear motion (Δu) of PZT to the micro rotary mechanism. Part *c* is the flexure hinge element, which transforms and guides. Part *d* is the output motion element, which delivers the output rotary motion ($\Delta\theta$) of the micro rotary mechanism to the rotary workbench.

The structure and working principle of the micro rotary mechanism as shown in Figure 2(b); there are 26 flexure hinge elements in the *x-y* plane with symmetrical distribution about center point 0, and the 26 flexure hinge elements having the same size are numbered as shown in Figure 2(b). Because the mechanism has a symmetrical structure, it is feasible only to study the top half of the mechanism when we analyze its working condition. The symmetrical structure parts of *a* contain a_1 (at the left half parts of the mechanism) and a_2 (at the right half parts of the mechanism). Similarly, *b* contains b_1 (at the top half of the mechanism) and b_2 (at the bottom half of the mechanism), and *d* contains d_1 (at the top half of the mechanism) and d_2 (at the bottom half of the mechanism). The pivots of flexure hinges 2, 6, 8, 11, and 13 are connected with *a*. a_1 and a_2 are each fixed by 3 M4 socket head cap screws (the six screws are simplified for simple construction). The pivots of flexure hinges 3 and 5 are connected with d_1 , and d_1 and d_2 are each connected with the rotary workbench by 3 M4 socket head cap screws (the six screws are simplified for simple

construction). The pivots of flexure hinges 1, 4, 7, 9, 10, and 12 are connected with b_1 . The connecting rod 123 (which consists of points 1, 2, and 3; other connecting rods are similarly defined) completes the transform from linear motion to rotary motion. Flexure hinges 6–13 complete the guiding for the mechanism, and the mechanism will have no non-motion direction displacement (the *y*-axis is the motion direction). Flexure hinges 4 and 5 are used to balance the *x*-direction force and moment because flexure hinge 1 moves around the pivot of flexure hinge 2, while the mechanism is working.

We establish the rectangular coordinate system as shown in Figure 2(b). When PZT has a micro-drive displacement Δu along the forward direction of the *y* axle, part b_1 has displacement Δu . Simultaneously, the pivots of flexure hinges 1 and 4 have *x*-axle displacement Δu , and after the motion, the pivot of flexure hinges 1 and 4 will move to $1'$ and $4'$. The pivot of flexure hinges 3 and 5 will move to $3'$ and $5'$; because they are constrained by part d_1 , the distance between $3'$ and center point 0 is equal to the distance from 3 to center point 0 (distance r is constant). As constrained by parts b_1 and d_1 , at connecting rod 123, l_{12} (length from point 1 to point 2) will shorten, l_{23} (length from point 2 to point 3) will elongate, l_{13} (length from point 1 to point 3) = $l_{1'3'}$ (length from point $1'$ to point $3'$), and the location of point $3'$ can be calculated. The included angle is between L_{03} (the connect line from point 0 to point 3) and $L_{03'}$ (the connect line from point 0 to point $3'$), and the angle is the output rotary motion displacement ($\Delta\theta$).

Additionally, because the mechanism has a symmetrical structure, the bottom half of the mechanism has the identical output rotary motion displacement ($\Delta\theta$) driven by PZT with an input linear motion displacement (Δu). This motion process of the mechanism will accurately transform the input linear motion (Δu) to the output rotary motion ($\Delta\theta$). The PZT will not bear the force or torque with non-motion

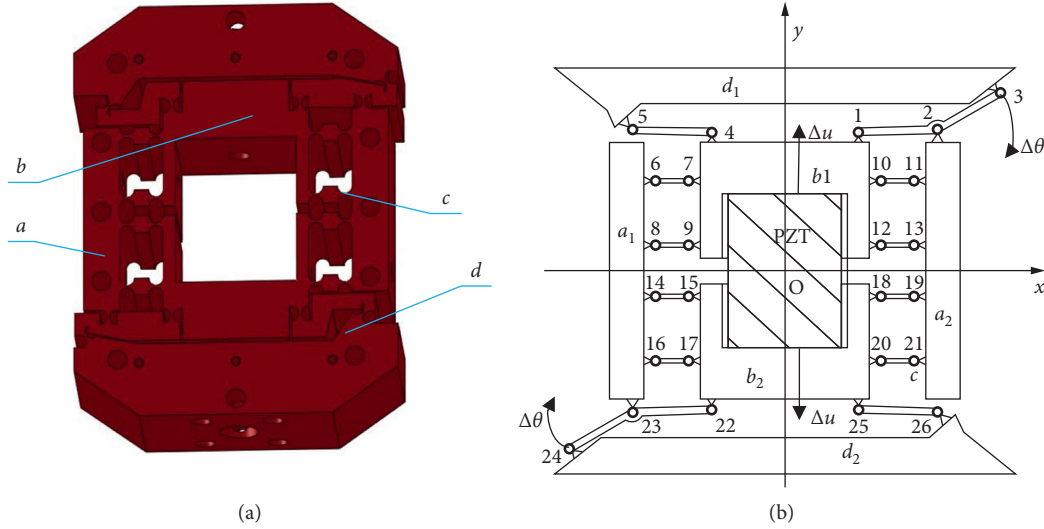


FIGURE 2: The micro rotary mechanism. (a) The stereogram of the mechanism. (b) Working principle of the micro rotary mechanism.

direction, and the mechanism does not have non-motion direction displacement, which can ensure the precision and stationary of the mechanism motion.

2.2. Micro Actuators. Two common micro-actuators are PZT (piezoelectric actuator) and GMA (giant magnetostrictive actuator). The motion accuracy of PZT is higher than that of GMA.

PZT is one kind of the micro-drivers, which works on the principle inverse piezoelectric effect of piezoelectric materials, and PZT can produce displacement of several micrometers to tens of micrometers. Because of advantages such as high precision, rapid response, small size, and large-output-force, PZT has been used widely in fields such as the advanced war industry, biological medicine, precision electronics, intelligent robot, and precision machinery. According to the parameter demand of this system, such as the size of the driver, driving force, and driving displacement, the model of the high-precision PZT is P-235.1S of PI Company; the PZT is shown in Figure 3. The main parameters of the PZT are shown in Table 1, closed-loop travel is $15\ \mu\text{m}$, the closed-loop resolution is $0.3\ \text{nm}$, and the drive frequency is $300\ \text{Hz}$.

The micro rotary mechanism is designed as shown in Section 2.1, and the mechanism is processed by wire-electrode cutting with the spring steel material 60Si2Mn. The micro-drive rotary system is developed as shown in Figure 1, and the fixed part and gasket are designed to connect two ends of the PZT to the micro rotary mechanism.

3. Error Compensation Scheme of the Micro-Drive Rotary System

The error compensation scheme of the micro-drive rotary system can directly affect the motion performance of the

macro/micro dual-drive system, so it is important to study the scheme.

Two motion methods of the macro/micro dual-drive system are point-to-point motion and continuous motion. In the point-to-point motion, the motions of the macro-drive and micro-drive are out-of-sync: the micro-drive system compensates for the motion error of the macro-drive system after the macro-drive system finishes its motion. In continuous motion, the motions of the macro-drive and micro-drive are synchronous: the micro-drive system compensates for the motion error of the macro-drive system when the macro-drive system is moving.

To calculate the motion error of the macro-drive rotary system, we detect n points in the entire circumference within 360 degrees; the angular position and angular error of the i th point are x_i and θ_i ; and the error of the point is (x_i, θ_i) .

Hence, we have the following equation:

$$x_i = (i - 1)P_i + x_0, \quad (1)$$

where x_0 is the angular value of the initial point, x_i is the angular value of the i th detection point, and P_i is the angular distance between the i th and $(i - 1)$ th detection points.

If the i th detection point is detected q times, the detection error θ_i of the detection points is

$$\theta_i = \frac{1}{q} \sum_{j=1}^q \theta_{ij}, \quad (2)$$

where j is the j th time detection in the q times at the i th detection point.

3.1. Point-to-Point Motion. The error compensation equation of the point-to-point motion is

$$\theta + \theta' = 0, \quad (3)$$

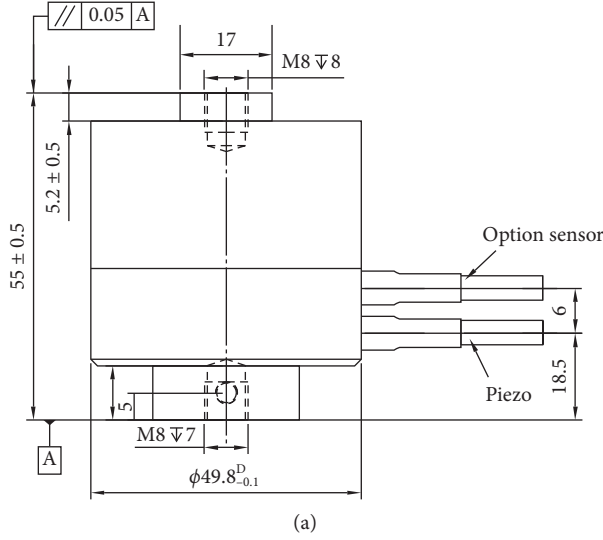


FIGURE 3: PZT model is P235.1S. (a) PZT structure dimension drawing. (b) The picture of the PZT.

TABLE 1: Main parameters of the P235.1S PZT.

Index	Parameter
Length	55 mm
Cylinder diameter	49.8 mm
Closed-loop travel	15 μ m
Resolution	0.3 nm
Linearity	0.2%
Static large-signal stiffness	860 N/m
Operating voltage	0–10 V
Maximum push	30000 N
Maximum pull	3500 N
Shear force limit	707 N
Torque limit	2 Nm
Maximum motion frequency	300 Hz

where θ and θ' are the error matrix and compensation modifier matrix of each point, $\theta = [\theta_0 \ \theta_1 \ \dots \ \theta_i \ \dots \ \theta_n]^T$, $\theta' = [-\theta_0 \ -\theta_1 \ \dots \ -\theta_i \ \dots \ -\theta_n]^T$.

The precision evaluation of error compensation for equation (3) is

$$\sigma^2 = \frac{S}{n-2}, \quad (4)$$

where σ is the residual variance, s is the residual sum of squares, and n is the number of the detection points.

This motion can be compensated by the pitch compensation method and backlash compensation method, and the maximum compensation modifier is

$$\theta'_{\max} = \max\{|\theta_0| \ |\theta_1| \ \dots \ |\theta_i| \ \dots \ |\theta_n|\}. \quad (5)$$

3.2. *Continuous Motion.* The error compensation equation of continuous motion is a curvilinear equation, and the equation between x_i and θ_i is

$$\theta = f(x). \quad (6)$$

If θ_i , which are the errors of each point x_i , are known, then the data array $\theta = f(x)$ ($x = x_0, x_1, \dots, x_n$) is known.

If there is an m -order polynomial of $P_m(x) = \sum_{k=0}^m a_k x^k$ ($m < n$), to minimize $R = \sum_{i=0}^n [f(x_i) - P_m(x_i)]^2$, $P_m(x_i)$ is the fitting polynomial of (x) using the least square method.

Thus, the problem of continuous motion modeling becomes the problem of solving the least square solution about a_k ($k = 0, 1, \dots, m$) in the following equation:

$$\sum_{k=0}^m a_k x_i^k = \theta_i, \quad (i = 0, 1, \dots, n, n > m). \quad (7)$$

If a_k is a variable, equation (7) can be transformed to the following matrix equation:

$$\begin{bmatrix} 1 & x_0 & x_0^2 & \dots & x_0^m \\ 1 & x_1 & x_1^2 & \dots & x_1^m \\ \dots & \dots & \dots & \dots & \dots \\ 1 & x_n & x_n^2 & \dots & x_n^m \end{bmatrix} \begin{bmatrix} a_0 \\ a_1 \\ \vdots \\ a_m \end{bmatrix} = \begin{bmatrix} \theta_0 \\ \theta_1 \\ \vdots \\ \theta_n \end{bmatrix}, \quad (8)$$

which is a hyperpositive definite equation and its corresponding normal equation is

$$\begin{bmatrix} m+1 & \sum_{i=0}^n x_i & \sum_{i=0}^n x_i^2 & \dots & \sum_{i=0}^n x_i^m \\ \sum_{i=0}^n x_i & \sum_{i=0}^n x_i^2 & \sum_{i=0}^n x_i^3 & \dots & \sum_{i=0}^n x_i^{m+1} \\ \dots & \dots & \dots & \dots & \dots \\ \sum_{i=0}^n x_i^m & \sum_{i=0}^n x_i^{m+1} & \sum_{i=0}^n x_i^{m+2} & \dots & \sum_{i=0}^n x_i^{2m} \end{bmatrix} \begin{bmatrix} a_0 \\ a_1 \\ \vdots \\ a_m \end{bmatrix} = \begin{bmatrix} \sum_{i=0}^n \theta_i \\ \sum_{i=0}^n x_i \theta_i \\ \vdots \\ \sum_{i=0}^n x_i^m \theta_i \end{bmatrix}. \quad (9)$$

Then, a_k can be solved using equation (9), and the fitting polynomial of $f(x)$ using the least square method is analyzed as

$$P_m(x) = a_0 + a_1x + a_2x^2 + \dots + a_mx^m, \quad (10)$$

which is the error model of continuous motion. The error compensation equation of continuous motion is

$$\theta'(x) = -P_m(x) = -a_0 - a_1x - a_2x^2 - \dots - a_mx^m. \quad (11)$$

This motion can be compensated by coupling the error compensation equation (11) with the control program of system motion, and the maximum compensation modifier is

$$\theta'_{\max} = |-P_m(x_i)|_{\max}. \quad (12)$$

4. Simulation and Analysis

4.1. Strength Analysis. In the strength analysis of the micro-drive rotary system, because the PZT has sufficiently large stiffness (the PZT can bear a maximum thrust of 3000 N), it just needs to check whether the strength of the micro rotary mechanism satisfies the material requirement under the maximum driving displacement by PZT. In this paper, the strength of the micro rotary mechanism is analyzed by the statics module of FEM software.

By importing the 3D model of the micro rotary mechanism into the finite element software, we obtain that the radius and minimum thickness of the flexure hinges are 3 mm and 1 mm, and the size of the mechanism is 160 mm × 150 mm × 50 mm (length × width × height). We select the parameters of 60Si2Mn as the material properties of the mechanism. To conveniently apply loading to the mechanism, we made an imprint face in the mechanism and fit its structure for the inner surface between the mechanism and the PZT. For meshing, we mesh the entire mechanism using the method of free meshing. Then, we refine the grid cell for 52 cylinders of flexure hinges with 0.5 mm mesh. After meshing, in the meshing model, the number of nodes is 527148; the number is 327190. During loading, we apply a fixed constraint on the 6 threaded hole cylinders of M4 in part *a*. The maximum displacement of the PZT is 15 μm, so the *y*-positive-direction and *y*-negative-direction

displacements with 7.5 μm are loaded at the position of the imprint face, and the preparation of FEM analysis is shown in Figure 4.

The maximum simulation stress of the micro rotary mechanism is shown in Figure 5, and the maximum stress of the mechanism is 30.964 MPa.

The allowable stress of the material is

$$[\sigma] = \frac{\sigma_s}{\lambda}. \quad (13)$$

The yield limit σ of 60Si2Mn is 1176 MPa, and the safety factor λ is 1.5. Substituting the values of σ_s and λ into equation (13), we calculate that the material allowable stress $[\sigma]$ is 784 MPa. The maximum stress of the micromechanism is 30.964 MPa, which is far less than the allowable stress of the material.

According to the finite element analysis of statics, the maximum stress of the micro rotary mechanism during movement is far less than the allowable stress of the material, which indicates that the mechanism structure design is reasonable, and the mechanism satisfies the demand of the material strength check.

4.2. Modal Analysis. To determine whether the mechanism mechanism will cause resonance during motion and find the suitable work frequency range of the mechanism, it is necessary to analyze the inherent frequency of the micro-mechanism in its work environment. In this paper, the modal performance of the mechanism is analyzed by the dynamic modules of the FEM.

The modal analysis of the mechanism using the dynamic module of the FEM software, the modeling, and meshing of the mechanism are similar to the strength analysis (as in Section 4.1), and results as shown in Figure 6, because values of the first 6 orders are close to 0, the 7th–12th orders can be regarded as the first 6 orders, and the first 6 orders of inherent frequency of the mechanism are shown in Figure 6.

The simulation results indicate that the micro-drive rotary system will cause no resonance during motion because the drive frequency of the PZT (drive frequency is 300 Hz) does not coincide with each order of inherent frequency of the mechanism.

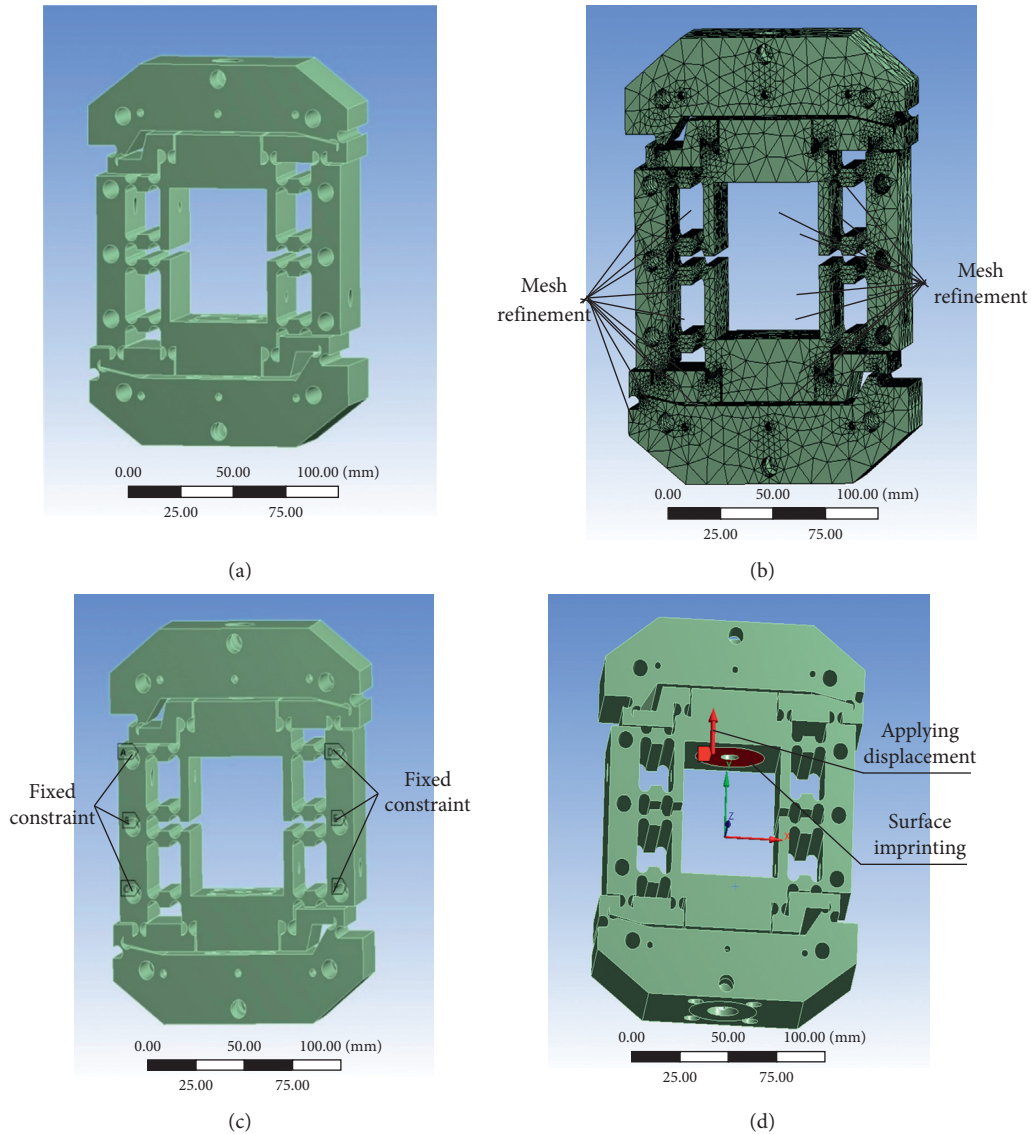


FIGURE 4: The preparation of FEM analysis. (a) Importing model. (b) Meshing. (c) Constraint condition. (d) Loading.

5. Experimental Verification

5.1. Modal Experiment. In the free dynamic experiment of the mechanism, the main experiment test apparatus is the dynamic test control analysis system produced by *M+P* company, and other corollary equipment includes the data collection sensor, high-precision hammer of PCB, and elastic rope. To avoid the effect of the external environment, the dynamic experiment of the mechanism is finished using the free hanging method. In this experiment, the mechanism with free hanging is knocked by a high-precision hammer of PCB, and the test data is recorded by the dynamic test control analysis system. The free dynamic experiment of the mechanism is performed as shown in Figure 7, and the test result of the experiment is shown in Figure 8.

The first six orders of inherent frequency of the mechanism are analyzed by the dynamic modules of the FEM

software (as in Section 4.2) and free dynamic experiment results are shown in Figure 9.

The simulation and experiment results of the mechanism modal show two conclusions can be drawn as follows:

- (1) The maximum error between the two analysis methods is 6.52%, which shows that the simulation and experiment results are similar and accurate, and the system has excellent modal performance because the first-order inherent frequency of the mechanism is approximately 230 Hz.
- (2) The micro-drive system is driven by a PZT of model P-235.1S, which is produced by PI Company, and the drive frequency of the PZT is 300 Hz. The second- and third-order inherent frequencies of the mechanism are 267.19 Hz and 925.00 Hz. Therefore, the micro-drive rotary system will cause no resonance during motion.

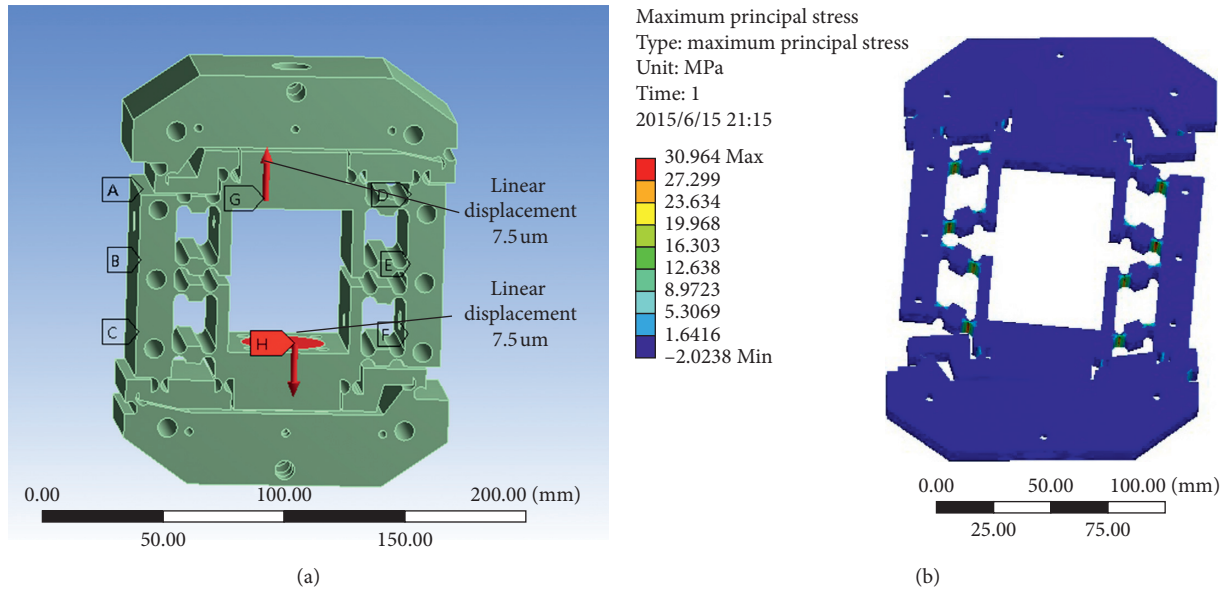


FIGURE 5: The maximum simulation stress of the micro rotary mechanism. (a) Loading displacements. (b) Result of simulation.

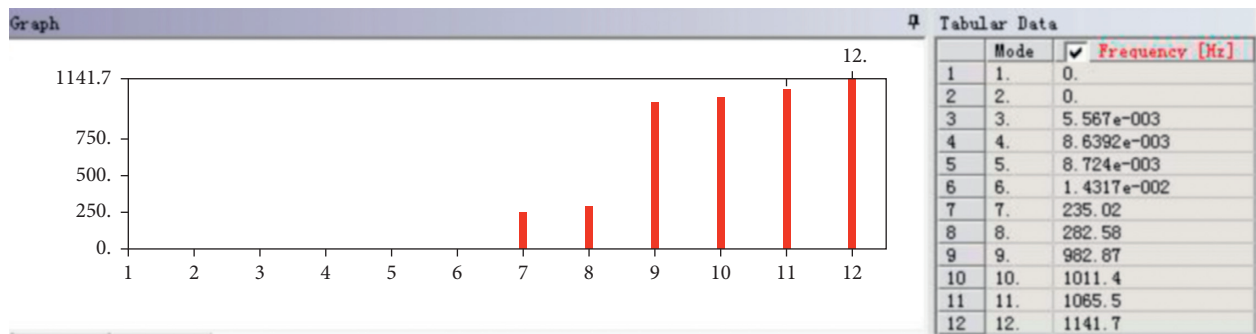


FIGURE 6: The first six-order (7th-12th) inherent frequency of the mechanism.

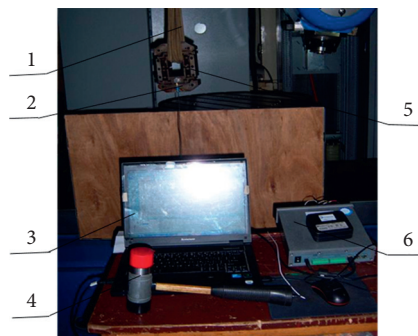


FIGURE 7: Free dynamic experiment of the mechanism. (1) Rubber rope. (2) Data acquisition front end. (3) Computer. (4) PCB high precision hammer. (5) Micro rotation mechanism. (6) The dynamic test control analysis system.

5.2. Error Compensation Performance Experiment. The micro-drive rotary system has different motion performance in the environment of the macro/micro dual-drive system and just micro-drive. To test the error compensation

performance of the micro-drive rotary system, the experiment should be in the environment of the macro/micro dual-drive system. In this experiment, the function between driven voltage U of the PZT and output motion $\Delta\theta$ of the

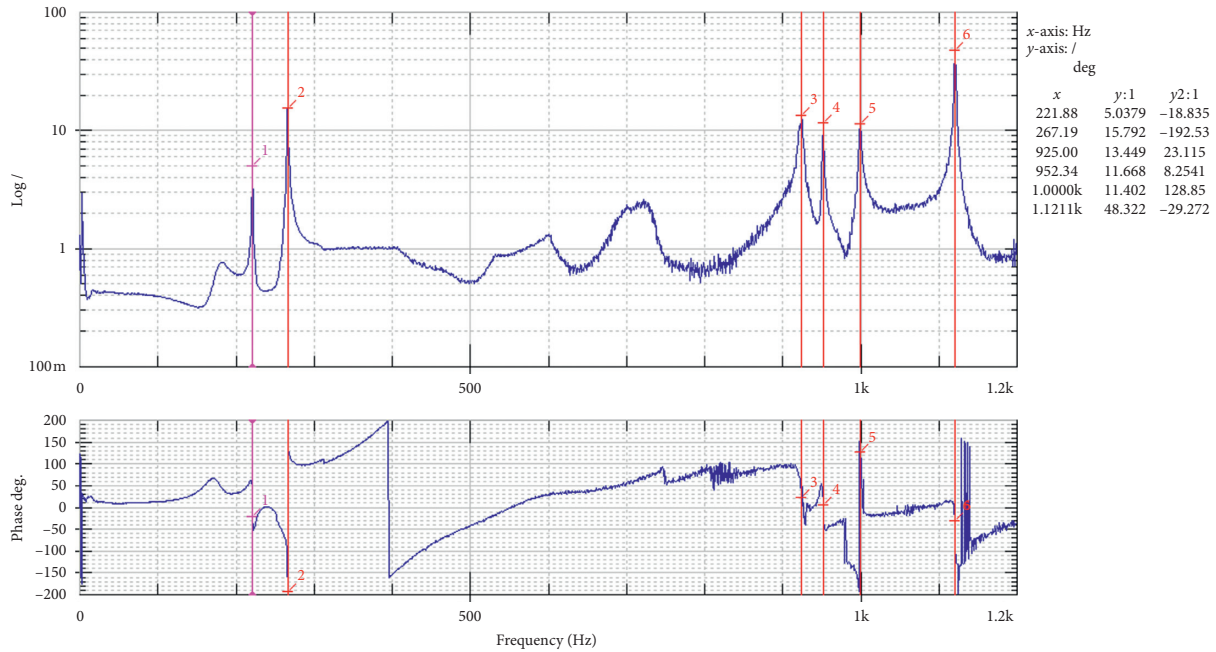


FIGURE 8: Result of the free dynamic experiment.

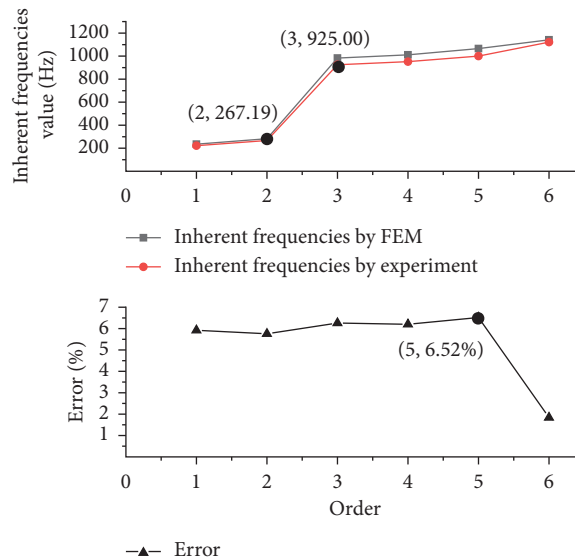


FIGURE 9: The simulation and experiment results of mechanism model.

micro-drive rotary system is analyzed, and driven voltage U matching a known error compensation $\Delta\theta$ can be solved by the function.

To prevent external factors such as vibration and temperature variation from affecting the experiment results, the error compensation experiment is finished at a vibration isolation platform of the thermostatic laboratory.

In the error compensation experiment, the main experiment test apparatus includes the micro rotary mechanism, PZT, dual-frequency laser interferometer (model XL80 of Renishaw Company), control system of PMAC, direct drive motor (model DM1C-004 of Yokogawa Company), and experiment box. The error compensation

experiment is shown in Figure 10. The temperature compensating sensor and humidity compensating sensor are installed on the two sides of the experiment box. In the environment of vibration isolation, constant temperature, and constant humidity, the output motion $\Delta\theta$ of the micro-drive rotary system is detected by the dual-frequency laser interferometer when the system is driven with driven voltage U . The piezoelectric actuator is used for closed-loop feedback. Specifically, the precision displacement sensor inside the piezoelectric actuator is used for closed-loop feedback.

The range of driven voltage U of the PZT is 0–10 V (because the PZT requires a small length to preload before working, and the maximum driven voltage U is 9.8 V as

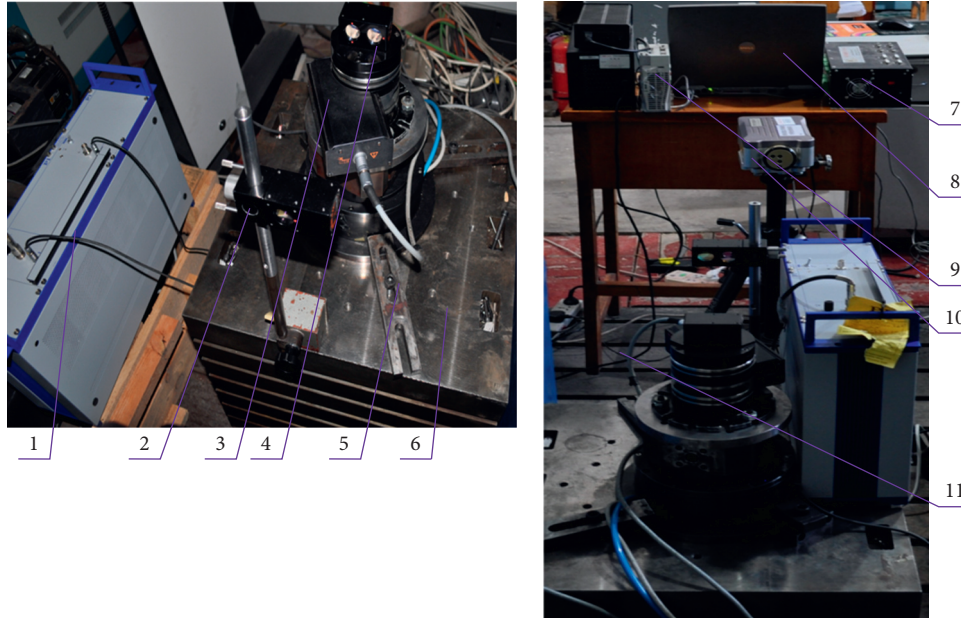


FIGURE 10: Compensation performance test diagram of the fretting rotary system. (1) PZT. (2) MirrorI. (3) Calibration shaft. (4) Mirror II. (5) Fixed clamp. (6) Experiment box. (7) Control system of PMAC. (8) Computer. (9) Diver of direct drive motor. (10) Dual-frequency laser interferometer. (11) Vibration isolation.

tested). To have a similar amount of elongation and shortening of PZT, the initial driven voltage U of the PZT is set to 5 V. The micro-drive rotary system can compensate the macro-drive rotary system with positive error and negative error. In the experiment, the PZT is controlled by closed-loop control, the motor is stopping but under servo status to ensure motion in the environment of the macro/micro dual-drive system. The driven voltage U of the PZT is set to 5 V, and the current position of the calibration axis is set to the initial position (i.e., we define the position of the system with driven voltage U of 5 V as the standard position). Then, we detect the output motion $\Delta\theta$ of the micro-drive rotary system in the ascent stage (driven voltage U is 5–9.8 V) and declining stage (driven voltage U is 5–0 V) using the dual-frequency laser interferometer, and the experiment results are shown in Figure 11.

To conveniently compensate for the errors of the micro-drive rotary system, the motion of the system in the ascent stage and declining stage is linearly fitted according to the experiment result. The fitted equations are the equations of U with error compensation. The linear-fitting of U and $\Delta\theta$ is shown in Figure 12.

The linear fit equation of the micro-drive rotary system in the ascent stage is

$$U = 1.498\Delta\theta + 5.03. \quad (14)$$

The linearity of the linear equation is 0.9985.

The linear fit equation of the micro-drive rotary system in the declining stage is

$$U = 1.596\Delta\theta + 4.82. \quad (15)$$

The linearity of the linear equation is 0.9952.

When the micro-drive rotary system is compensating the errors of the macro-drive rotary system, if the required compensation angle $\Delta\theta$ is positive, the driven voltage U can be calculated by equation (14) to be 5–9.8 V. If the required compensation angle $\Delta\theta$ is negative, the driven voltage U can be calculated by equation (15) to be 5–0 V.

In order to facilitate the use of engineering, according to equations (14) and (15), if the initial driven voltage is a common value of X ($0 \leq X \leq 9.8$), the driven voltage (U) equation of error compensation is

$$U = \begin{cases} 1.498\Delta\theta + X + 0.03 & (0 \leq \Delta\theta \leq 6.1 - 0.62X, \text{ ascent stage}) \\ 1.596\Delta\theta + X - 0.18 & (-0.62X \leq \Delta\theta \leq 0, \text{ declining stage}). \end{cases} \quad (16)$$

In equation (16), the unit of voltage is volt (V), and the unit of error compensation angle $\Delta\theta$ is arc-second ($''$). And when $0 \leq X \leq 9.8$, $-0.62X \leq \Delta\theta \leq 6.1 - 0.62X$.

Equation (16) is the driven voltage (U) equation of error compensation when the initial driven voltage is X .

The error compensation performance experiment results show two conclusions can be drawn as follows:

- (1) The driven voltage equation of error compensation is derived based on the experiment result, and the driven voltage U can be calculated by equation (16) when $0 \leq X \leq 9.8$ (X is the initial driven voltage).
- (2) The micro-drive rotary system can satisfy the error compensation demand of the macro-/micro dual-drive system, and the error compensation performance of the system is excellent. According to equation (16), the maximum error compensation angle ($\Delta\theta_{\max}$) of the micro-drive rotary system is $6.1''$. In the macro/micro dual-drive system, the macro-

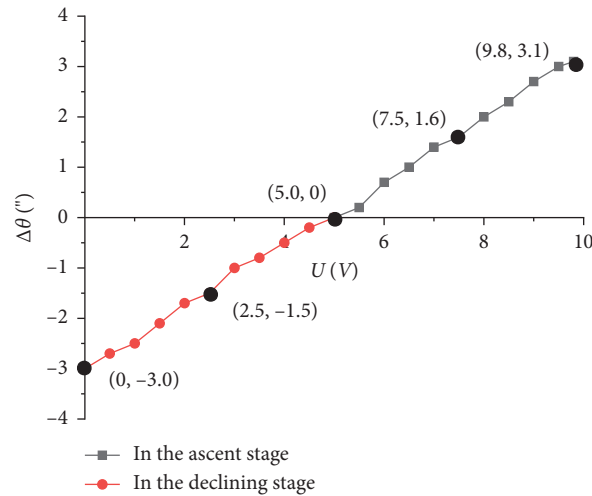


FIGURE 11: Error compensation performance experiment results.

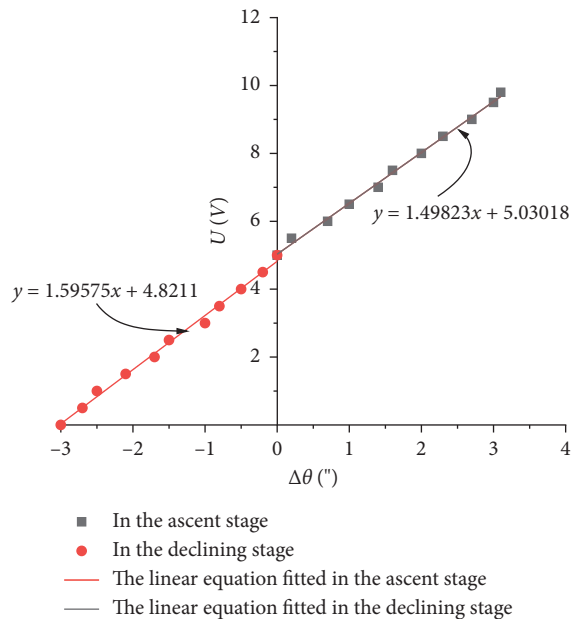


FIGURE 12: The linear-fitting of U and $\Delta\theta$.

drive system is driven by a direct drive motor of model DM1C-004, and the maximum positive and maximum negative errors of the motor are $2.0''$ and $-2.7''$. According to equations (5) and (12), the maximum compensation modifier (θ'_{\max}) is $2.7''$. As $\Delta\theta_{\max} > \theta'_{\max}$, the system can meet the error compensation demand in practical application.

6. Conclusion

In this paper, a new precision micro-drive rotary system is designed in order to obtain a high-precision rotary motion, the error compensation scheme of the system is proposed, and the system design and error compensation performances are verified by FEM simulation and experiments.

In the micro-drive rotary system, the micro rotary mechanism is driven by the PZT (the drive precision of PZT

at 0.1 nm level). The system can accurately transform linear motion into rotary motion; therefore, the low-precision of micro rotary motion can be enhanced. According to simulation and experiments, the maximum stress of the mechanism is far less than the allowable stress (30.964 MPa) of the material, and the micro-drive rotary system will cause no resonance during motion.

The error compensation equations (5) and (12) and the driven voltage equation of error compensation (16) are derived, and they are fit for engineering use. As the maximum error compensation angle ($\Delta\theta_{\max}$) and the maximum compensation modifier (θ'_{\max}) are $6.1''$ and $2.7''$, the micro-drive rotary system can satisfy the error compensation demand of the macro/micro dual-drive system.

This study is beneficial to research on the micro-drive rotary system with high-precision (such as precision in sub-arc-second), and it is helpful to promote the development of the macro/micro dual-drive technology. In addition, the research results about error compensation of the system in this paper are useful for engineering practice.

Data Availability

The data used to support the findings of this study are available from the corresponding author upon request.

Conflicts of Interest

The authors declare no conflicts of interest with respect to the research in this article.

Acknowledgments

The authors would like to thank the support of the National Natural Science Foundation of China (51805428 and 51705417), the Basic Research Project of Natural Science in Shaanxi Province (2018JQ5205 and 2017JM5042), the Key Research and Development Project of Shaanxi Province (2016KTZDGY4-01), the Science and Technology Plan Project of Xi'an City (201805036YD14CG20 (7)), the Special

Scientific Research Project of the Shaanxi Province Department of Education (18JK0528), and the Science and Technology Plan Project of Beilin District (GX2032).

References

- [1] Y. W. Sun, M. S. Chen, J. J. Jia, Y. S. Lee, and D. M. Guo, "Jerk-limited feedrate scheduling and optimization for five-axis machining using new piecewise linear programming approach," *Science China Technological Sciences*, vol. 62, no. 7, pp. 1067–1081, 2019.
- [2] K. Ekholm, A. Moxnes, and K. H. Ulltveitmo, "Manufacturing restructuring and the role of real exchange rate shocks," *Journal of International Economics*, vol. 86, pp. 101–117, 2012.
- [3] F. C. Wang, L. S. Chen, Y. C. Tsai, C. H. Hsieh, and J. Y. Yen, "Robust loop-shaping control for a nano-positioning stage," *Journal of Vibration and Control*, vol. 20, no. 6, pp. 885–900, 2014.
- [4] Y. C. Yang, X. Wang, J. W. Zhang et al., "Automatic phase-locked control of grating tiling," *Optics and Lasers in Engineering*, vol. 50, no. 2, pp. 262–267, 2012.
- [5] S. Y. Zeng and L. Blunt, "Experimental investigation and analytical modeling of the effects of process parameters on material removal rate for bonnet polishing of cobalt chrome alloy," *Precision Engineering*, vol. 38, no. 2, pp. 348–355, 2014.
- [6] S. Zenla, L. B. Ayed, M. Nouari, and A. Delameziere, "Numerical prediction of the chip formation process and induced damage during the machining of carbon/epoxy composites," *International Journal of Mechanical Sciences*, vol. 90, pp. 89–101, 2015.
- [7] H. J. Ahn, "Eddy current damper type reaction force compensation mechanism for linear motor motion stage," *International Journal of Precision Engineering and Manufacturing-Green Technology*, vol. 3, no. 1, pp. 67–74, 2016.
- [8] E. L. Zheng, R. Zhu, S. H. Zhu, and X. J. Lu, "A study on dynamics of flexible multi-link mechanism including joints with clearance and lubrication for ultra-precision presses," *Nonlinear Dynam*, vol. 83, no. 1-2, pp. 137–159, 2016.
- [9] S. L. Jiang and Y. W. Sun, "Stability analysis for a milling system considering multi-point-contact cross-axis mode coupling and cutter run-out effects," *Mechanical Systems and Signal Processing*, vol. 141, Article ID 106452, 2020.
- [10] R. Majumdar and I. Paprotny, "Configurable post-release stress engineering of surface micro-machined MEMS structures," *Journal of Microelectromechanical Systems*, vol. 26, no. 3, pp. 671–678, 2017.
- [11] H. Itagaki and M. Tsutsumi, "Control system design of a linear motor feed drive system using virtual friction," *Precision Engineering*, vol. 38, no. 2, pp. 237–248, 2014.
- [12] J. W. Wu, K. C. Huang, M. L. Chiang, M. Y. Chen, and L. C. Fu, "Modeling and controller design of a precision hybrid scanner for application in large measurement-range atomic force microscopy," *IEEE of Thermal Power Electronics*, vol. 61, no. 7, pp. 3704–3712, 2014.
- [13] S. L. Xu, K. Shimada, M. Mizutani, and T. Kuriyagawa, "Fabrication of hybrid micro/nano-textured surfaces using rotary ultrasonic machining with one-point diamond tool," *International Journal of Machine Tools and Manufacture*, vol. 86, no. 6, pp. 12–17, 2014.
- [14] D. Bassing and A. S. Braeuer, "The lag between micro-and macro-mixing in compressed fluid flows," *Chemical Engineering and Sciences*, vol. 163, pp. 105–113, 2017.
- [15] L. Y. Zhang, J. Gao, X. Chen et al., "Implementation and experiment of an active vibration reduction strategy for macro-micro positioning system," *Precision Engineering*, vol. 51, pp. 319–330, 2018.
- [16] C. You, M. H. Lee, H. J. Lee et al., "The effect of macro/micro combination pore structure of biphasic calcium phosphate scaffold on bioactivity," *Ceramics International*, vol. 43, no. 4, pp. 3540–3546, 2017.
- [17] W. Tang, D. Lin, Y. M. Yu et al., "Bioinspired trimodal macro/micro/nano-porous scaffolds loading rhBMP-2 for complete regeneration of critical size bone defect," *Acta Biomaterialia*, vol. 32, pp. 309–323, 2016.
- [18] X. C. Zhuang, S. M. Ma, and Z. Zhao, "A microstructure-based macro-micro multi-scale fine-blanking simulation of ferrite-cementite steels," *International Journal of Mechanical Sciences*, vol. 128, pp. 14–427, 2017.
- [19] Y. L. Yang, Y. D. Wei, J. Q. Lou, L. Fu, and X. W. Zhao, "Nonlinear dynamic analysis and optimal trajectory planning of a high-speed macro-micro manipulator," *Journal of Sound and Vibration*, vol. 405, pp. 112–132, 2017.
- [20] X. Q. Sun and B. T. Yang, "A new methodology for developing flexure-hinged displacement amplifiers with micro-vibration suppression for a giant magnetostrictive micro-drive system," *Sensors and Actuators A: Physical*, vol. 263, pp. 30–43, 2017.
- [21] M. Lok, E. F. Helbling, X. Zhang, R. Wood, D. Brooks, and G. Y. Wei, "A low mass power electronics unit to drive piezoelectric actuators for flying microrobots," *IEEE of Thermal Power Electronics*, vol. 33, no. 4, pp. 3180–3191, 2017.
- [22] T. Mashimo, "Miniature preload mechanism for a micro ultrasonic motor," *Sensors and Actuators A: Physical*, vol. 257, pp. 106–112, 2017.
- [23] E. Hosseini, P. O. Theillet, and O. N. Pierron, "Temperature and humidity effects on the quality factor of a silicon lateral rotary micro-resonator in atmospheric air," *Sensors and Actuators A: Physical*, vol. 189, pp. 380–389, 2013.
- [24] D. C. Zhu and Y. P. Feng, "Structure design of a 3-DOF UPC type rotational fully spatial compliant parallel manipulator," *International Journal of Advancements in Computing Technology*, vol. 5, no. 8, pp. 70–81, 2013.
- [25] R. Pan, X. J. Zhao, P. T. Liu, and R. M. Ren, "Micro-mechanism of polygonization wear on railroad wheels," *Wear*, vol. 392, pp. 213–220, 2017.
- [26] X. J. Fan, M. M. Sun, Z. H. Lin et al., "Automated noncontact micromanipulation using magnetic swimming microrobots," *IEEE of Thermo Nanotechnology*, vol. 90, 2018.
- [27] M. A. A. Felon and T. Furukawa, "Design of an active flapping wing mechanism and a micro aerial vehicle using a rotary actuator," *Mechanism and Machine Theory*, vol. 45, no. 2, pp. 137–146, 2010.
- [28] D. M. Brouwer, B. R. D. Jong, and H. M. J. R. Soemers, "Design and modeling of a six DOFs MEMS-based precision manipulator," *Precision Engineering*, vol. 34, no. 2, pp. 307–319, 2010.
- [29] K. Kim, D. Ahn, and D. Gweon, "Optimal design of a 1-rotational DOF flexure joint for a 3 DOF H-type stage," *Mechatronics*, vol. 22, pp. 24–32, 2011.
- [30] J. H. Qu, J. Tang, Y. B. Gianchandani, K. R. Oldham, and S. R. Green, "Dynamic modeling of a bidirectional magnetoelastic rotary micro-motor," *Sensors and Actuators A: Physical*, vol. 223, pp. 49–60, 2015.
- [31] G. P. Xue, M. Toda, and T. Ono, "Comb-drive XYZ-micro-stage with large displacements based on chip-level micro-assembly," *Journal of Microelectromechanical and Sciences*, vol. 25, no. 6, pp. 989–998, 2016.

- [32] M. Liu, X. M. Zhang, and S. Fatikow, "Design and analysis of a multi-notched flexure hinge for compliant mechanisms," *Precision Engineering*, vol. 48, pp. 92–304, 2017.
- [33] D. F. Machekposhti, N. Tolou, and J. L. Herder, "A statically balanced fully compliant power transmission mechanism between parallel rotational axes," *Mechanism & Machine Theory*, vol. 119, pp. 51–60, 2018.
- [34] C. Du, Y. Zhang, A. Kong, and Z. Yuan, "High-precision and fast response control for complex mechanical systems-servo performance of dedicated servo recording systems," *IEEE Transactions on Magnetics*, vol. 53, no. 3, pp. 1–5, 2017.
- [35] Z. X. Shao, S. L. Wu, J. G. Wu, and H. Y. Fu, "A novel 5-DOF high-precision compliant parallel mechanism for large-aperture grating tiling," *Mechanical Sciences*, vol. 8, no. 2, pp. 349–358, 2017.
- [36] F. Jiang, J. Chen, H. Bi, L. Y. Li, W. K. Jing, and J. Zhang, "The underlying micro-mechanism of performance enhancement of non-polar n -ZnO/ p -AlGaIn ultraviolet light emitting diode with i -ZnO inserted layer," *Applied Physics Letters*, vol. 112, no. 3, Article ID 033505, 2018.
- [37] Y. X. Peng, S. Ito, Y. Shimizu, and W. Gao, "A micro-stage for linear-rotary positioning," *Key Engineering Materials*, vol. 523, pp. 650–655, 2012.
- [38] W. X. Xu and Y. B. Wu, "Piezoelectric actuator for machining on macro-to-micro cylindrical components by a precision rotary motion control," *Mechanical Systems and Signal Processing*, vol. 114, pp. 439–447, 2019.

Research Article

High-Precision Guide Stiffness Analysis Method for Micromechanism Based on the Boundary Element Method

Manzhi Yang ¹, Zhenyang Lv ¹, Gang Jing ¹, Wei Guo,¹ Yumei Huang,² Linyue Li ¹, Kaiyang Wei ¹, Bin Feng,¹ and Hongyu Ge¹

¹College of Mechanical Engineering, Xi'an University of Science and Technology, No. 58 Yanta Middle Road, Xi'an 710054, Shaanxi, China

²School of Mechanical and Precision Instrumental Engineering, Xi'an University of Technology, No. 8 Jinhua South Road, Xi'an 710048, Shaanxi, China

Correspondence should be addressed to Manzhi Yang; xkdymz@xust.edu.cn

Received 21 April 2021; Accepted 17 June 2021; Published 28 June 2021

Academic Editor: Shanglei Jiang

Copyright © 2021 Manzhi Yang et al. This is an open access article distributed under the Creative Commons Attribution License, which permits unrestricted use, distribution, and reproduction in any medium, provided the original work is properly cited.

The guide stiffness performance directly affects the motion of the micromechanism in accuracy and security. Therefore, it is crucial to analyze the guide stiffness precisely. In this paper, a high-precision guide stiffness analysis method for the micromechanism by the boundary element method (BEM) is proposed. The validity and accuracy of the analysis method are tested by a guide stiffness experiment. In order to ensure the accuracy and safety during the micromechanism motion, a guiding unit of the micromechanism was designed based on the guiding principle. The guiding unit can provide parasitic motion and additional force in the motion of the micromechanism. Then, the stiffness equations of the beam element are derived by the boundary element method. The stiffness equation of straight circular flexure hinge is analyzed by rigid discretization and rigid combination, and the guide stiffness of the mechanism is investigated by rigid combination. Finally, according to the actual situation, the stiffness matrix of the guide rail (K_b) was proposed, and the analytical value of the guide stiffness was calculated to be $22.2 \text{ N}/\mu\text{m}$. The guide stiffness performance experiment was completed, and the experimental value is $22.3 \text{ N}/\mu\text{m}$. Therefore, the error between the analysis method and the experimental results is 0.45%. This study provides a new method for the stiffness analysis of high-precision micromechanisms and presents a reference for the design and stiffness analysis of complex structures. This method is helpful for stiffness analysis of the microrotary mechanism with high accuracy.

1. Introduction

With the rapid development of numerical control technology, advanced manufacturing has called for higher requirements for precision machining technology [1–3]. Macro/micro-dual-drive technology has solved the contradiction of large-motion travel and high-motion precision for a single-drive mechanism system and provided motion for large travel and high precision. The macro/micro-dual-drive system has been widely used in high-technology fields, such as the advanced weapons industry, biological medicine, and precision electronics [4–9]. In the macro/micro-dual-drive system, the microdrive system can compensate the motion error of the macrodrive system and provide high-precision

motion for the macro/micro-dual-drive system [10–13]. As this mechanism can provide accurate motion based on the compound motion principle of a flexure hinge, the micromechanism is a core component of the microdrive system [14–17], and the performance of the micromechanism is directly affected by the performance of the microdrive system [18–21].

Many scholars have conducted research on the motion performance and practical application of the microlinear mechanism [22–25]. Meanwhile, some scholars focus on studying microrotary mechanism [26, 27]. Because of parasitic motion and additional force, the motion accuracy and safety of the micromechanism will be reduced. The parasitic movement in nonmotion directions will affect the accuracy

of the movement in motion direction. Microactuators (i.e., PZT) are generally assembled inside the micromechanism to drive the mechanism, and usually, the stiffness of microactuators in motion direction is very high. The stiffness of microactuators in nonmotion directions is usually very low, and additional force will badly affect the safety of microactuators during motion of a micromechanism. As the guiding motion principle, the guide unit of micromechanism can provide relaxation of parasitic movement and additional force during the motion. Therefore, it is necessary to design a guide unit of micromechanism.

As a significant performance indicator of the micromechanism, the stiffness can affect the motion performance of the mechanism under external load. In recent years, many scholars have conducted research on the stiffness of the micromechanism, and significant achievements have been achieved. Using the relational expression of Castigliano's second theorem to express the displacement and force of the end of the flexure hinge, the relative displacement vector of the flexure hinge was analyzed and calculated, and the stiffness matrix of the system was proposed, and meanwhile, the minimum motion principle was obtained [28]. The stiffness model is based on the way the flexure members are connected in serial or parallel combinations, and the modeling allows one to formulate the functional relationship between stiffness and dimensions as well as the free shape of the FPM in the design process, while the proposed analytical model is validated by the FEM model and experiments [29]. A novel six-strut compliant parallel mechanism based on the development of wide-range flexure hinges is explored, the stiffness equation of an individual flexure hinge is established, and the stiffness of the whole mechanism is modeled by assembling stiffness matrixes and formulating constraint equations, after which the system stiffness influence plots are presented and discussed [30]. A bridge micromechanism with 3 degrees of freedom was designed. The z -direction of the mechanism had higher rigidity and stability, which could resist large external thrust. The structure of the organization is optimized by adopting the sequential quadratic rule. Finally, the experiments show that the optimization method is highly effective [31]. A novel type of flexible mechanism composed of two straight circular flexure hinges with multiple notches was designed. The topology method is used to optimize the mechanism structure, and the finite element method was used to analyze the stiffness, rotation accuracy, and horizontal stress of the mechanism. The analysis results show that the mechanism performances are excellent [32]. A fully compliant, potentially monolithic, and power transmission mechanism that can rectify a large lateral offset between two parallel rotational axes is presented. The transmission stiffness and the actuation stiffness of the designed device are predicted by the theoretical model and finite element modeling [33].

As the guide unit can ensure accuracy and safety during the motion of the micromechanism, it is significant to analyze the guide stiffness of the micromechanism. However, there are rarely relevant papers to explore the guide stiffness of the micromechanism. The stiffness of the guide unit is interpreted by the stiffness formula in most studies. This

method will gain an inevitable error because of the stiffness model error in the analysis of a micromechanism with a complex structure. BEM is a method of dividing discrete elements within a defined range on the boundary, accurately decomposing the research object and then analyzing the boundary problem. BEM has many advantages, such as less preparation work in data, being vital to deal with particular engineering problems, and high accuracy [34, 35]. Moreover, BEM has a significant advantage in solving practical engineering problems with complex structures or complex boundary conditions. It is a particularly prominent advantage of BEM to analyze beams with exact solutions. Therefore, it is appropriate to examine the guide stiffness by BEM.

In this paper, a guide unit of micromechanism is designed for relaxation of parasitic movement and additional force in the micromechanism movement, which can ensure accuracy and safety during its motion, and this research is beneficial to the structural design of the micromechanism. A high-precision guide stiffness analysis method by the boundary element method (BEM) is proposed, and the validity and accuracy of the analysis method are tested by experiment. And, this study provides a new method to analyze the stiffness of micromechanism with high precision.

The rest of this paper is organized as follows. Section 2 introduces the design and guiding motion principle of the guiding unit, which can provide relaxation of parasitic movement and additional force. The high-precision guide stiffness analysis method by the boundary element method (BEM) is given in Section 3. In Section 4, the guide stiffness matrix (K_b) and analytical value are calculated. Section 5 carries out the guide stiffness experiment and analyses results. The conclusions are drawn in Section 6.

2. The Guide Unit of the Micromechanism

When flexible material is stressed, the flexure hinge will produce minor deformation, realizing the transmission motion and guiding motion. In all kinds of flexure hinges, the straight circular flexure hinge is the most widely used because it can meet demand both precision and range of motion.

The equivalent model of straight circular flexure hinge is shown in Figure 1. Point a is the starting point of the hinge, point c is the midpoint of the hinge, and point b is the terminal point of the hinge. Point a' and point b' are the starting point and the terminal point the hinge after motioning. l_i is half the length of the hinge in the x -direction.

The guiding motion principle is a micromechanism motion principle based on symmetrical structure, to ensure micromechanism motion is accurate in the motion direction. The displacement that can provide motion only exists in the motion direction and there is no nonmotion direction during the motion process.

2.1. Design of the Guide Unit. We have designed two kinds of micromechanisms in our research project, as shown in Figure 2. The microlinear mechanism is shown in

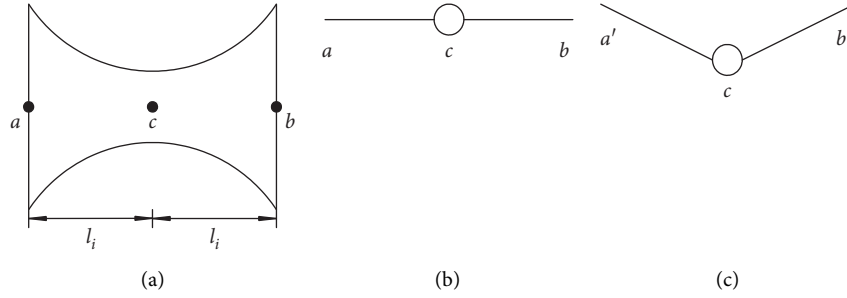


FIGURE 1: The equivalent model of straight circular flexure hinge. (a) Structural diagram of flexure hinge. (b) Structural simplified of flexure hinge. (c) Structural simplified of flexure hinge after motioning.

Figure 2(a), which can realize transmission in the linear motion with different ratios, include amplification and reduction. And, the microrotary mechanism is shown in Figure 2(b), which can transform an input of linear motion into an output of rotary motion according to a particular relationship. For relaxation of parasitic movement and additional force, the guide unit is designed in two kinds of micromechanisms. In Figure 2(a), the mechanism has eight units: 1-2, 3-4, 5-6, 7-8, 9-10, 11-12, 13-14, and 15-16, and they are guide units. Similarly, in Figure 2(b), the mechanism has eight guide units: 6-7, 8-9, 10-11, 12-13, 14-15, 16-17, 18-19, and 20-21.

The motion model of the guide unit is shown in Figure 3. The guide unit consists of flexure hinge I, rod 1, and flexure hinge II. The eight guide units are symmetrically distributed on both sides of b parts. When the b parts move along the y -positive direction or the y -negative direction driven by PZT, the eight guide units can be seen as y -direction motion guide rails of b parts by obtaining the same deformations along with two y -directions. Therefore, b parts will bear the load and produce displacement in y -directions and will not bear or make displacement in nonmotion directions (i.e., x -directions). The above motion process can realize the guiding motion of the micromechanism, ensure the accuracy of the motion with no displacement in nonmotion directions, and ensure the safety of PZT working with no load in nonmotion directions.

2.2. Guiding Motion Principle of the Guide Unit. The guide unit is symmetrically distributed on both sides of PZT, which can realize the guiding effect of the micromechanism, and the guide unit is the same as the linear motion guide. The guiding motion principle of the guide unit is shown in Figure 4, 1 is a fixed station, 2 is moving parts, and four guide units (3, 4, 5, 6) constitute the linear motion guide to guiding the linear motion of 2. Figures 4(a) and 4(b), respectively, show the structure diagram of the balance and motion of the guide unit group under the action of driving load P .

Taking guide unit 5 as an example, the guiding motion principle of guide unit 5 is shown in Figure 5. The rectangular coordinate system is established, as shown in Figure 5, and the left endpoint of the guide unit 5 is the origin of coordinates. The structural diagram of the guide unit in balance is shown in Figure 5(a), and the right side of the

guide unit is fixed. The guide unit consists of flexure hinge I, rod 1 and flexure hinge II. Flexure hinge I is equivalent simplified including revolute pair c and two rods (ac and cb), flexure hinge II is equivalent simplified into revolute pair e and two rods (de and ef); the length of the four rods (ac , cb , de and ef) are l_i , and the length of rod 1 is l_1 .

The structural diagram of the guide unit in motion is shown in Figure 5(b). In the left side of the guide unit, a linear motion displacement as Δu under an external load will occur. As the right side of the guide unit is fixed, the guide unit will produce tensile deformation and bending deformation, which is equivalent as all the rods are extended and all the points are rotated. The left side of the guide unit motion is a displacement of Δu in the direction of the y -axis, which can be regarded as the rotation of the guide unit with the direction of $\Delta\theta$. The equivalent figure of guiding motion is shown in Figure 5(c). The guide unit will rotate an angle $\Delta\theta$ after the left side of the guide unit moving with Δu under an external load.

The guiding motion of the other three guide units (3, 4, and 6) is similar to that of guiding unit 5. Since the four guide units are symmetrically distributed around the fixed working station 1 and the moving parts 2, the guide unit realizes the motion direction of the guiding moving part 2, and each of the guide units (3, 4, 5, and 6) will rotate an angle $\Delta\theta$ after parts 2 moving with Δu .

l is the length of guide unit after motion:

$$l = \sqrt{\Delta u^2 + (l_1 + 4l_i)^2}, \quad (1)$$

$\Delta\theta$ is the included angle between guide unit and x -axis after motion:

$$\Delta\theta = \arctan\left(\frac{\Delta u}{l_1 + 4l_i}\right), \quad (2)$$

y'_k is the displacement in y -directions of every position point at guide unit after motion:

$$y'_k = (l_1 + 4l_i - x_k)\tan(\Delta\theta), \quad (0 < x_k < l_1 + 4l_i), \quad (3)$$

where x_k is coordinate value in x -directions of every position point at guide unit.

And, equation (3) is the mathematical model of guiding motion.

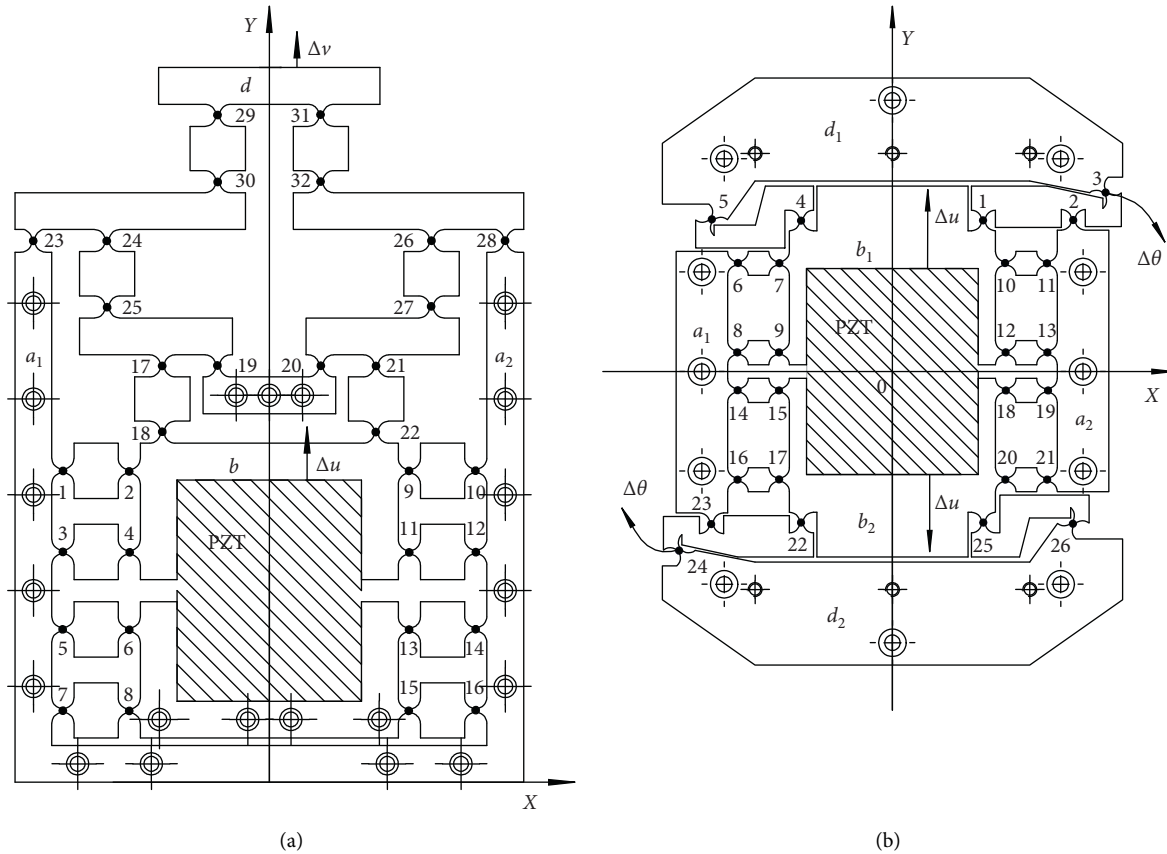


FIGURE 2: Two kinds of micromechanism. (a) The linear micromechanism. (b) The microrotary mechanism.

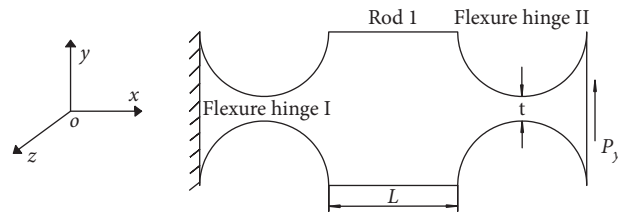


FIGURE 3: Stiffness-analysis model of the guide unit of the micromechanism.

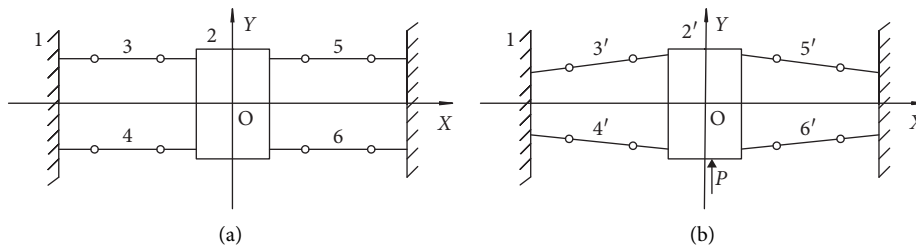


FIGURE 4: Guiding motion principle of the guide unit. (a) Structural diagram of the guide unit group in balance. (b) Structural diagram of the guide unit group in motion.

During the motion of moving parts 2, the guide units will produce force and displacement because of elongation of rods, the forces of the left two guide units (3, 4) can balance the forces of the right two guide units (5, 6). The displacement of the left two guide units (3, 4) can balance the displacements of the right two guide units (5, 6). As the

symmetrical structure, force and displacement between the left two guide units (3, 4) and the right two guide units (5, 6) are counteract. This principle can ensure force and displacement of motion only exist in the motion direction and that there is no nonmotion direction force and displacement during motion.

According to the guiding motion principle, the micro-mechanism has no parasitic motion and additional force in the process of motion, which ensures the accuracy and safety of the movement.

3. The Stiffness Analysis Theory Based on the Boundary Element Method

The guide unit is shown in Figure 3, and it consists of 2 straight circular flexure hinges (i.e., flexure hinge I and flexure hinge II) and a rod (i.e., rod 1), and the structure of the straight circular flexure hinge is more complex than the rod. BEM has advantages such as less preparation work in data, strong capacity to deal with particular engineering problems, and high accuracy, and BEM has a significant advantage in solving practical engineering problems with complex structure and complex boundary

conditions. Thus, it is appropriate to analyze the stiffness of the guide unit by BEM.

3.1. Analysis of Static Bending Including Tension and Compression for Beam Element. The static tension and compression for beam elements in the x - y plane are shown in Figure 6. Points 1 and 2 are the two endpoints of the beam, P is the external load of tension and compression for the beam, L is the length of the beam, and the main parameters of the static tension and compression for the beam are shown in Table 1.

The tension and compression stress condition for the microunit of the beam element is shown in Figure 7.

The boundary equation of tension and compression for the beam element can be deduced as

$$\begin{bmatrix} 1 - F^*(0,0) & F^*(L,0) \\ -F^*(0,L) & 1 + F^*(L,L) \end{bmatrix} \begin{Bmatrix} U(0) \\ U(L) \end{Bmatrix} = \begin{bmatrix} U^*(0,0) & U^*(L,0) \\ U^*(0,L) & U^*(L,L) \end{bmatrix} \begin{Bmatrix} F(0) \\ F(L) \end{Bmatrix} + \sum P_i \begin{Bmatrix} U^*(x_i,0) \\ U^*(x_i,L) \end{Bmatrix}, \quad (4)$$

where U^* is the differential of longitudinal displacement, F^* is the differential of axial force, U is the longitudinal displacement value of the boundary point, and F is the axial force value of the boundary point.

Static bending for the beam element in the x - y plane is shown in Figure 8. Point 1 and point 2 are the two endpoints of the beam, P is the external load of bending for the beam, L

is the length of the beam, and the main parameters of the static bending for the beam are shown in Table 2.

The bending stress condition for the microunit of the beam element is shown in Figure 9.

The boundary equation of bending for the beam element can be deduced as

$$\begin{bmatrix} -1 - Q^*(0,0) & -M^*(0,0) & Q^*(L,0) & M^*(L,0) \\ -Q^*(0,L) & -M^*(0,L) & -1 + Q^*(L,L) & M^*(L,L) \\ 0 & -1 - Q^*(0,0) & 0 & Q^*(L,0) \\ 0 & -Q^*(0,L) & 0 & -1 + Q^*(L,L) \end{bmatrix} \begin{Bmatrix} V(0) \\ T(0) \\ V(L) \\ T(L) \end{Bmatrix} = \begin{bmatrix} T^*(0,0) & V^*(0,0) & T^*(L,0) & V^*(L,0) \\ T^*(0,L) & V^*(0,L) & -T^*(L,L) & V^*(L,L) \\ \frac{-M^*(0,0)}{EI} & -T^*(0,0) & \frac{M^*(L,0)}{EI} & -T^*(L,0) \\ \frac{-M^*(0,L)}{EI} & -T^*(0,L) & \frac{-M^*(L,L)}{EI} & -T^*(L,L) \end{bmatrix} \begin{Bmatrix} M(0) \\ Q(0) \\ M(L) \\ Q(L) \end{Bmatrix} + \sum P_i \begin{Bmatrix} V^*(x_i,0) \\ V^*(x_i,L) \\ -T^*(x_i,0) \\ -T^*(x_i,L) \end{Bmatrix}, \quad (5)$$

where q is distributed load, Q is shear force, M is bending moment, E is the longitudinal modulus of elasticity, I is a moment of inertia, V is bending displacement (i.e., deflection), T is bending angular displacement (i.e., deflection angle), P_i is the i th external load, and x_i is the position of action for P_i .

The boundary stiffness equation of bending, including tension and compression for the beam element, can be deduced from equations (4) and (5) as

$$[\mathbf{H}]\{\mathbf{U}\} = [\mathbf{G}]\{\mathbf{F}\} + \{\mathbf{P}_f\}. \quad (6)$$

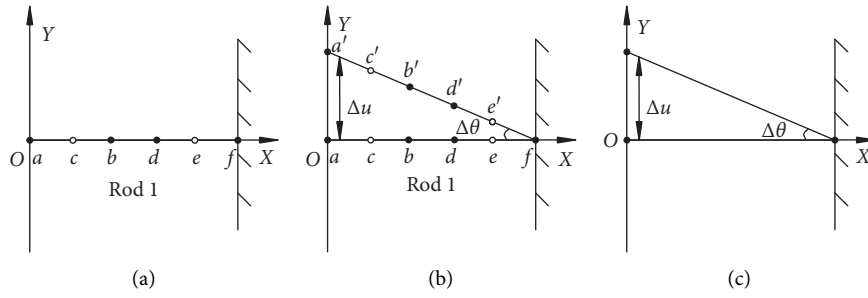


FIGURE 5: Guiding motion principle of the guide unit. (a) Structural diagram of the guide unit in balance. (b) Structural diagram of the guide unit in balance. (c) The equivalent figure of guiding motion.

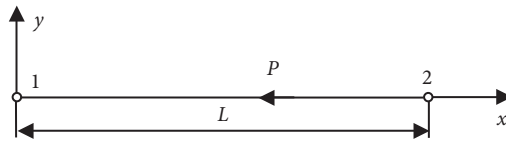


FIGURE 6: Diagram of static tension and compression for the beam element in the x - y plane.

TABLE 1: Main parameter values of static tension and compression for the beam.

Serial number of the endpoint	The x -coordinate of the endpoint	Displacement value of the boundary point	Force value of the boundary point
1	0	$U(0)$	$F(0)$
2	L	$U(L)$	$F(L)$

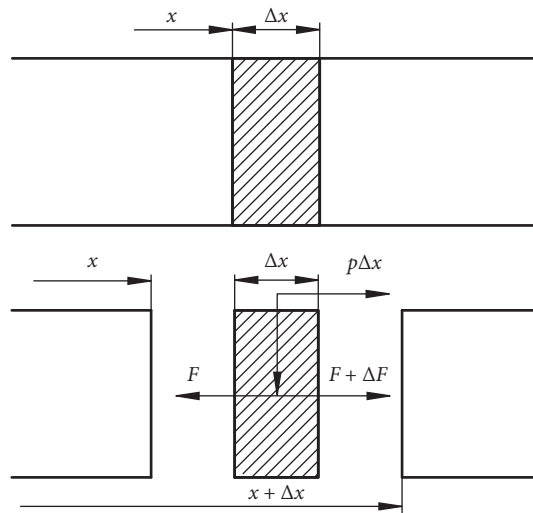


FIGURE 7: Force diagram of the beam element's infinitesimal under the stretch-press condition.

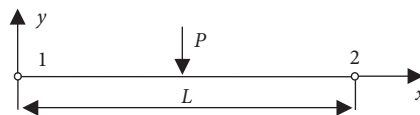


FIGURE 8: Diagram of static bending for the beam element in the x - y plane.

And, equation (6) can be transformed as

$$[K]\{U\} = \{F\} + \{P\}, \tag{7}$$

where $[K] = [G]^{-1}[H]$, $\{P\}[G]^{-1}\{P_f\}$, $[K]$ is the bending including tension and compression stiffness of the beam, $\{U\}$ is the bending including tension and compression

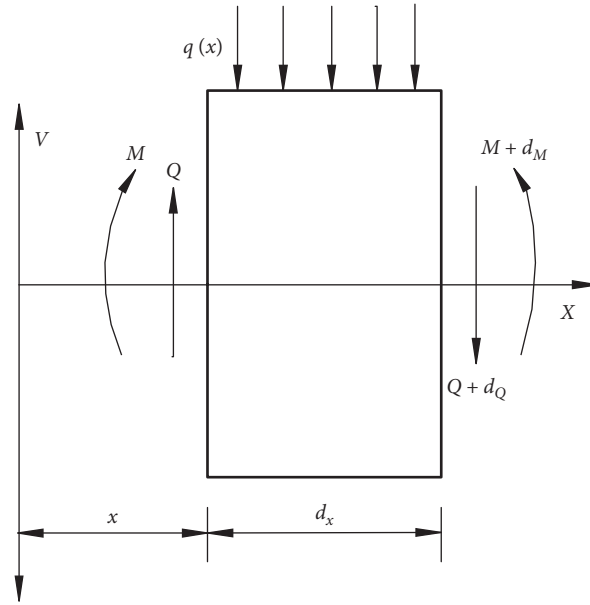


FIGURE 9: Force diagram of the beam element's infinitesimal under the static bending condition.

TABLE 2: Main parameter values of static bending for the beam.

Serial number of the endpoint	The x-coordinate of the endpoint	Displacement value of the boundary point	Force value of the boundary point
1	0	$V(0)$ $T(0)$	$Q(0)$ $M(0)$
2	L	$V(L)$ $T(L)$	$Q(L)$ $M(L)$

displacement of the beam, $\{F\}$ is the boundary force, and $\{P\}$ is the external load.

Equation (7) is the boundary stiffness equation of bending, including tension and compression for the beam element.

In equation (7), $\{U\}$ can be transformed as

$$\{U\} = [U_1 \ U_2]^T, \tag{8}$$

where

$$\begin{aligned} \{U_1\} &= [U(0) \ V(0) \ T(0)]^T, \\ \{U_2\} &= [U(L) \ V(L) \ T(L)]^T. \end{aligned} \tag{9}$$

And, $\{F\}$ can be transformed as

$$\{F\} = [F_1 \ F_2]^T, \tag{10}$$

where

$$\begin{aligned} \{F_1\} &= [F(0) \ M(0) \ Q(0)]^T, \\ \{F_2\} &= [F(L) \ M(L) \ Q(L)]^T, \end{aligned} \tag{11}$$

where U_1 and F_1 are the displacements and boundary forces of endpoint 1 and U_2 and F_2 are the displacement and boundary forces of endpoint 2.

The stiffness matrix $[K]$ can be described as

$$[K] = \begin{bmatrix} K_{11} & K_{12} \\ K_{21} & K_{22} \end{bmatrix}. \tag{12}$$

Therefore, the bending boundary stiffness equation of beam element with tension and compression can be transformed as

$$\begin{bmatrix} K_{11} & K_{12} \\ K_{21} & K_{22} \end{bmatrix} \begin{Bmatrix} U_1 \\ U_2 \end{Bmatrix} = \begin{Bmatrix} F_1 \\ F_2 \end{Bmatrix} + \{P\}. \tag{13}$$

The boundary stiffness equation (13) will be used in the rigid combination of the beam element.

3.2. Rigid Combination of the Beam Element. The method of rigid combination is shown in Figure 10. Point 1 and point 2 are the two boundaries of beam a and point 3 and point 4 are the two boundaries of beam b . The beam a and beam b are combined in boundary 3 and boundary 4, as shown in Figure 10(a). The beam c is the new beam through a rigid combination between beam a and beam b , as shown in Figure 10(b), and the beam c can be a rigid combination with other beams.

The stiffness equation of beam a is

$$\begin{bmatrix} k_{11} & k_{12} \\ k_{21} & k_{22} \end{bmatrix} \begin{Bmatrix} u_1 \\ u_2 \end{Bmatrix} = \begin{Bmatrix} f_1 \\ f_2 \end{Bmatrix} + \begin{Bmatrix} p_1 \\ p_2 \end{Bmatrix}. \tag{14}$$

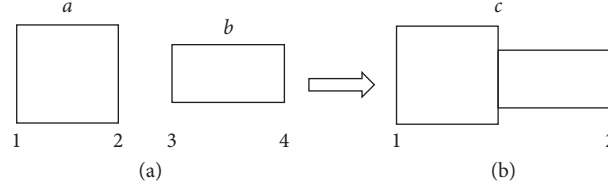


FIGURE 10: Rigid combination of series-connection components. (a) Before rigid combination. (b) After rigid combination.

And, the stiffness equation of beam b is

$$\begin{bmatrix} k_{33} & k_{34} \\ k_{43} & k_{44} \end{bmatrix} \begin{Bmatrix} u_3 \\ u_4 \end{Bmatrix} = \begin{Bmatrix} f_3 \\ f_4 \end{Bmatrix} + \begin{Bmatrix} p_3 \\ p_4 \end{Bmatrix}, \quad (15)$$

where $\begin{bmatrix} k_{11} & k_{12} \\ k_{21} & k_{22} \end{bmatrix}$ and $\begin{bmatrix} k_{33} & k_{34} \\ k_{43} & k_{44} \end{bmatrix}$ are stiffness matrixes of beam a and beam b , $\begin{bmatrix} u_1 \\ u_2 \end{bmatrix}$ and $\begin{bmatrix} u_3 \\ u_4 \end{bmatrix}$ are displacement matrixes of beam a and beam b , $\begin{bmatrix} f_1 \\ f_2 \end{bmatrix}$ and $\begin{bmatrix} f_3 \\ f_4 \end{bmatrix}$ are boundary force matrixes of beam a and beam b , and $\begin{bmatrix} p_1 \\ p_2 \end{bmatrix}$ and $\begin{bmatrix} p_3 \\ p_4 \end{bmatrix}$ are external load matrixes of beam a and beam b .

The force and displacement condition equation of the rigid combination between beam a and beam b is

$$\begin{cases} \{f_2\} = -\{f_3\}, \\ \{u_3\} = \{u_2\}. \end{cases} \quad (16)$$

The rigid combination equation between beam a and beam b with intermediate points is

$$[K]\{U\} = \{F\} + \{P\}, \quad (17)$$

where

$$\begin{aligned} [K] &= \begin{bmatrix} k_{11} & k_{12} & 0 \\ k_{21} & k_{22} + k_{33} & k_{34} \\ 0 & k_{43} & k_{44} \end{bmatrix}, \\ \{U\} &= [u_1 \ u_2 \ u_4]^T, \\ \{F\} &= [f_1 \ 0 \ f_4]^T, \\ \{P\} &= [p_1 \ p_2 + p_3 \ p_4]^T. \end{aligned} \quad (18)$$

The rigid combination equation between beam a and beam b without intermediate points is

$$[\mathbf{K}]\{\mathbf{U}\} = \{\mathbf{F}\} + \{\mathbf{P}\}, \quad (19)$$

where

$$\begin{aligned} [K] &= \begin{bmatrix} k_{11} + k_{12}Sk_{21} & k_{12}Sk_{34} \\ k_{43}Sk_{21} & k_{43}Sk_{34} + k_{44} \end{bmatrix}, \\ \{U\} &= [u_1 \ u_4]^T, \\ \{F\} &= [f_1 \ f_4]^T, \\ \{P\} &= [p_1 + k_{12}S(p_2 + p_3) \ p_4 + k_{43}S(p_2 + p_3)]^T, \\ S &= -(k_{22}k_{33})^{-1}. \end{aligned} \quad (20)$$

The stiffness model of the straight circular flexure hinge is a nonuniform beam with a continuously varying height, and the nonuniform beam consists of numerous cross-sections. It can be analyzed by stiffness equations (7) and (13), and rigid combination equations (17) and (19). Then, the guide stiffness matrix can be calculated by a rigid combination between the two straight circular flexure hinges and rod, and the guide stiffness analysis based on the boundary element method is accomplished.

4. Analysis of Guide Stiffness

4.1. Stiffness Calculation of the Straight Circular Flexure Hinge.

The stiffness model of the straight circular flexure hinge is a nonuniform beam with a continuously varying height, and the nonuniform beam consists of numerous cross sections. The elastic modulus E is the same between the sections, but section area A and the moment of inertia I are different. If x_i is the value of the x -axis for an uncertain i th point i , the variables A and I all have certain function relationships with x_i ; if $\alpha(x_i)$ is the section stiffness function at x_i , EI_0 is the datum section stiffness, and the section stiffness at x_i can be described as

$$EI_i = EI_0\alpha(x_i). \quad (21)$$

In equation (14), I_i can be solved only in a few cases (such as $\alpha(x_i) = x_i^4$). Otherwise, I_i cannot be solved. That is, I_i cannot be solved in any cases by a conventional method. When analyzing the stiffness in any case, the boundary element method is used to discretize the nonuniformity accurately, as shown in Figure 11. Figure 11(a) is the discretization model of a straight circular flexure hinge, Figure 11(b) is the height h_i and length Δl of the discretization beam element, and Figure 11(c) is the method of the height h_i . The nonuniform beam is discretized of n nonuniform beam elements with equal length. The nonuniform beam element approaches a uniform beam element when the value of n is large enough. We can improve the accuracy of the analysis by increasing the value of n , and h_i is the average height of the nonuniform beam element.

The nonuniform beam can be discretized of n uniform beams with equal length and different heights. The height of the uniform beams varies with the x_i location variation at the straight circular flexure hinge. The n uniform beams are numbered as shown in Figure 11(a).

If x_i is the x -axis value of the endpoint of the i th uniform beam, then x_{h_i} is the x -axis value of the midpoint of the i th uniform beam.

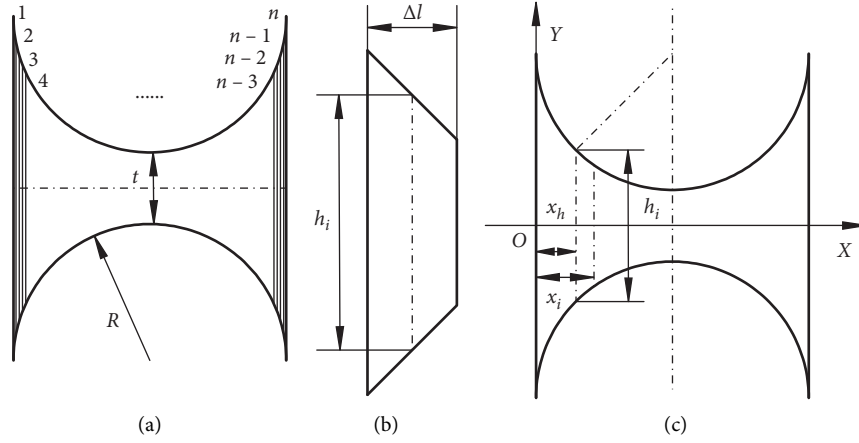


FIGURE 11: Stiffness analysis model of a straight circular flexure hinge. (a) Discretization model of a straight circular flexure hinge. (b) Height and length of the discretization beam element. (c) Solved method of the height of the discretization beam element.

In order to improve the analysis accuracy, h_i is the height of the midpoint location of the i th uniform beam, and h_i is

$$\begin{aligned} h_i &= 2\left(R - \sqrt{R^2 - (R - x_h)^2}\right) + t \\ &= 2\left(-\sqrt{R^2 - (R - x_i + 0.5\Delta l)^2}\right) + t. \end{aligned} \quad (22)$$

And, the i th uniform beam moment of inertia I_i is

$$I_i = \frac{bh_i^3}{12}, \quad (23)$$

where R is the radius of the straight circular flexure hinge, t is the minimum height of the straight circular flexure hinge, Δl is the length of each uniform beam ($\Delta l = 2R/n$), and x_h is the x -axis value of the midpoint of i th uniform beam ($x_h = x_i - 0.5\Delta l$).

Putting the values of Δl (i.e., L) and I_i (i.e., I) and the material and shape parameters of the flexure hinge into

equation (7), the stiffness equation of the uniform beam is established. Then, through the rigid combination of uniform beams in equation (13) and computer calculation, the stiffness equation and stiffness matrix of the straight circular flexure hinge are analyzed.

Therefore, the stiffness equation and stiffness matrix K_h of the straight circular flexure hinge can be analyzed as described above.

In Figure 3, the relevant parameters are described as follows: R is 5 mm, t is 2 mm, L (the length of rod 1) is 10 mm, h (the height of rod 1) is 12 mm, b (the thickness of the guide unit) is 12 mm, and the material of the mechanism is 60si2Mn with a longitudinal modulus of elasticity E of 2.06×10^{11} Pa, and $n = 1000$, while the relevant parameters are set the same as the parameters of the microguide mechanism. Then, the computed result of the stiffness matrix K_h is

$$K_h = \begin{bmatrix} 2.16 \times 10^9 & 0 & 0 & -2.16 \times 10^9 & 0 & 0 \\ 0 & 2.76 \times 10^6 & 15040 & 0 & -2.76 \times 10^6 & 12553 \\ 0 & 5.52 \times 10^8 & 2.76 \times 10^6 & 0 & -5.52 \times 10^8 & 2.76 \times 10^6 \\ -2.16 \times 10^9 & 0 & 0 & 2.16 \times 10^9 & 0 & 0 \\ 0 & 2.76 \times 10^6 & 12553 & 0 & -2.76 \times 10^6 & 15040 \\ 0 & -5.52 \times 10^8 & -2.76 \times 10^6 & 0 & 5.52 \times 10^8 & -2.76 \times 10^6 \end{bmatrix}. \quad (24)$$

In the above calculation process and the matrix K_h , the units are displacements, angular displacements, force, the moment of force in meters (m), degrees ($^\circ$), Newton (N), and Newton-meters (N·m). The units of relevant parameters of all stiffness matrixes in this paper are defined in the same manner.

4.2. Stiffness Calculation of the Guide Unit. The guide stiffness model of the micromechanism is shown in Figure 3, and the guide unit consists of flexure hinge I, rod 1, and flexure hinge II. The stiffness analysis process of the guide rail is as follows: the rigid combined flexible hinge I and rod 1 are the new rod a , and the rigid combined rod a and the flexible

hinge II are the new rod b . Therefore, rod b is the equivalent guide stiffness model of the guide unit. The stiffness matrix K_h of flexure hinge I and flexure hinge II are equal, and the calculation method of K_h is shown in Section 4.1 of this paper.

The stiffness matrix K_1 of rod 1 can be calculated by putting the relevant parameters into the matrix K of equation (7) as

$$K_1 = \begin{bmatrix} 7.91 \times 10^9 & 0 & 0 & -7.91 \times 10^9 & 0 & 0 \\ 0 & 5.70 \times 10^7 & 3.80 \times 10^5 & 0 & -5.70 \times 10^7 & 1.90 \times 10^5 \\ 0 & 1.14 \times 10^{10} & 5.70 \times 10^7 & 0 & -1.14 \times 10^{10} & 5.70 \times 10^7 \\ -7.91 \times 10^9 & 0 & 0 & 7.91 \times 10^9 & 0 & 0 \\ 0 & 5.70 \times 10^7 & 1.90 \times 10^5 & 0 & -5.70 \times 10^7 & 3.80 \times 10^5 \\ 0 & -1.14 \times 10^{10} & -5.70 \times 10^7 & 0 & 1.14 \times 10^{10} & -5.70 \times 10^7 \end{bmatrix}. \quad (25)$$

The stiffness matrixes of flexure hinge I and rod 1 are K_h and K_1 , and the stiffness matrix K_a of rod a can be calculated by equation (19) as

$$K_a = \begin{bmatrix} 1.70 \times 10^9 & 0 & 0 & -1.70 \times 10^9 & 0 & 0 \\ 0 & 1.74 \times 10^6 & 10177 & 0 & -1.74 \times 10^6 & 24720 \\ 0 & 3.40 \times 10^8 & 1.74 \times 10^6 & 0 & -3.40 \times 10^8 & 5.06 \times 10^6 \\ -1.70 \times 10^9 & 0 & 0 & 1.70 \times 10^9 & 0 & 0 \\ 0 & 5.06 \times 10^6 & 24720 & 0 & -5.06 \times 10^6 & 76453 \\ 0 & -3.40 \times 10^8 & -1.74 \times 10^6 & 0 & 3.40 \times 10^8 & -5.06 \times 10^6 \end{bmatrix}. \quad (26)$$

The stiffness matrixes of flexure rod a and hinge II are K_a and K_h , and the stiffness matrix K_b of rod b can be calculated by equation (19) as

$$K_b = \begin{bmatrix} 9.50 \times 10^8 & 0 & 0 & -9.50 \times 10^8 & 0 & 0 \\ 0 & 91100 & 1984.90 & 0 & -91100 & 749.32 \\ 0 & 6.07 \times 10^6 & 91100 & 0 & -6.08 \times 10^6 & 91143 \\ -9.50 \times 10^8 & 0 & 0 & 9.50 \times 10^8 & 0 & 0 \\ 0 & 91143 & 749.32 & 0 & -91143 & 1985.20 \\ 0 & -6.08 \times 10^6 & -91100 & 0 & 6.08 \times 10^6 & -91143 \end{bmatrix}. \quad (27)$$

Hence, the equivalent guide stiffness matrix of the mechanism is stiffness matrix K_b , and matrix K_b is the stiffness matrix of guide stiffness of the micromechanism.

If the left side of the guide unit is fixed and the right side of the guide unit is freed, then the driving force $P_y = 200$ N with a y -positive direction is loaded at the right side of the guide unit, as shown in Figure 3. When guide stiffness of the micromechanism is analyzed if we use the rigid combination equation with intermediate points as equation (17), the

bending displacement of deflection V and the bending angular displacement of deflection angle T at each intermediate point can be calculated. Sixty detection points are set and uniformly distributed in the length direction of the guide unit, and the 60 points are numbered as 1, 2, ..., 60 from left to right along the length direction of the guide unit. The deflection curve and the deflection angle curve of the guide unit are shown in Figure 12(a) (the unit of deflections is μm) and Figure 12(b) (the unit of deflection angles is $^\circ$).

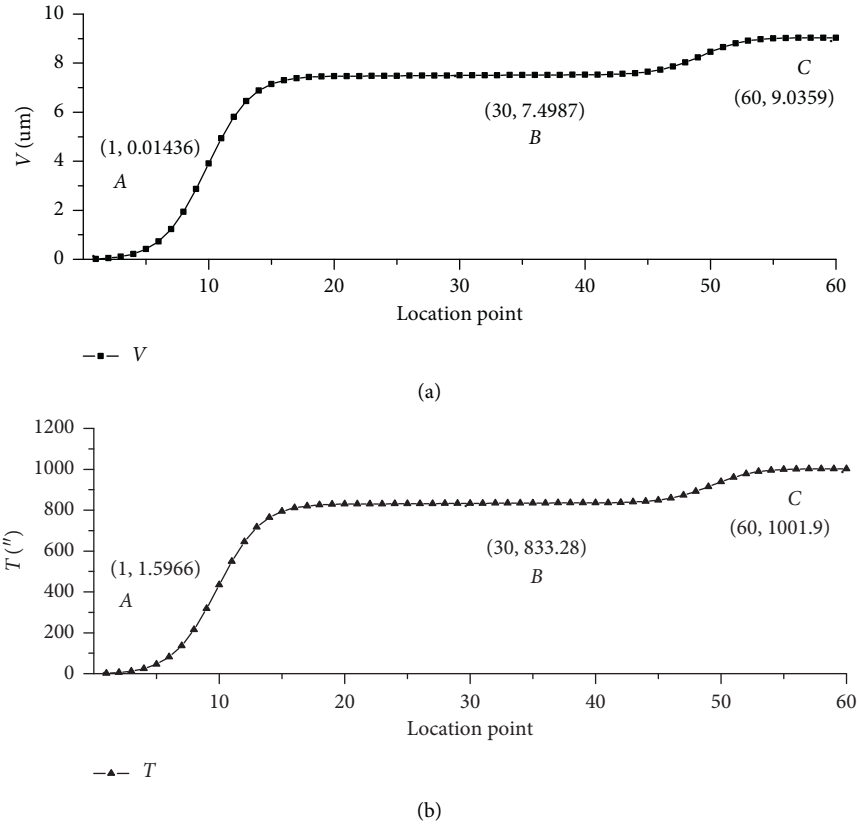


FIGURE 12: (a) The deflection curve and (b) the deflection angle curve of the guide unit.

The analysis shows that the right endpoint deflection Δu is $9.0 \mu\text{m}$ when the driving force P_y as 200 N is loaded at the right side of the guide unit, and the stiffness value of the guide unit is $K = 22.2 \text{ N}/\mu\text{m}$.

Therefore, the bending stiffness value of the guide unit K is $22.2 \text{ N}/\mu\text{m}$.

5. Experimental Verification

5.1. Experimental Scheme. A guide stiffness experiment has been carried out to verify the effectiveness of the proposed method of guide stiffness analysis. To avoid the influence of external factors such as vibration and temperature change on the experimental results, the experiment was carried out on the vibration isolation platform of the constant temperature laboratory. The guide stiffness experiment is shown in Figure 13, the principle of the guide stiffness experiment is shown in Figure 13(a), and the experiment picture is shown in Figure 13(b). In the guide stiffness experiment, the central experiment test apparatus are microguide mechanism, two displacement sensors are DGS-6C, data acquisition, force sensor is LCM500, force-loading device, and machine tool base.

In the experiment, the microguide mechanism is fixed, the different driving force P_y is loaded on the right side of the mechanism by a force-loading device, and the driving force P_y is detected by a force sensor. The right-side displacement (Δy_1) and the left-side displacement (Δy_2) of the microguide

mechanism are detected by displacement sensor 1 and displacement sensor 2. The right-side displacement (Δy_1) is the whole movement displacement of the mechanism driven by an external force. The guide stiffness (K') of the microguide mechanism in the experiment is

$$K' = \frac{P_y}{\Delta u} = \frac{P_y}{\Delta y_1 - \Delta y_2}, \quad (28)$$

where Δu is the right-side relative displacement (relative to the location of the left side) of the microguide mechanism in the y -direction.

5.2. Experimental Results and Analysis. The experimental results are shown in Figure 14. Curve *a* represents the guide stiffness performance in the loading stage, and the curve of describes the guide stiffness performance in the unloading stage.

For the guide stiffness performance in the loading stage, the linear equation fitted between driving force P_y and relative displacement Δu is

$$P_y = 22.1\Delta u + 15.0. \quad (29)$$

The linearity of the linear equation is 0.9998.

For the guide stiffness performance in the unloading stage, the linear equation fitted between driving force P_y and relative displacement Δu is

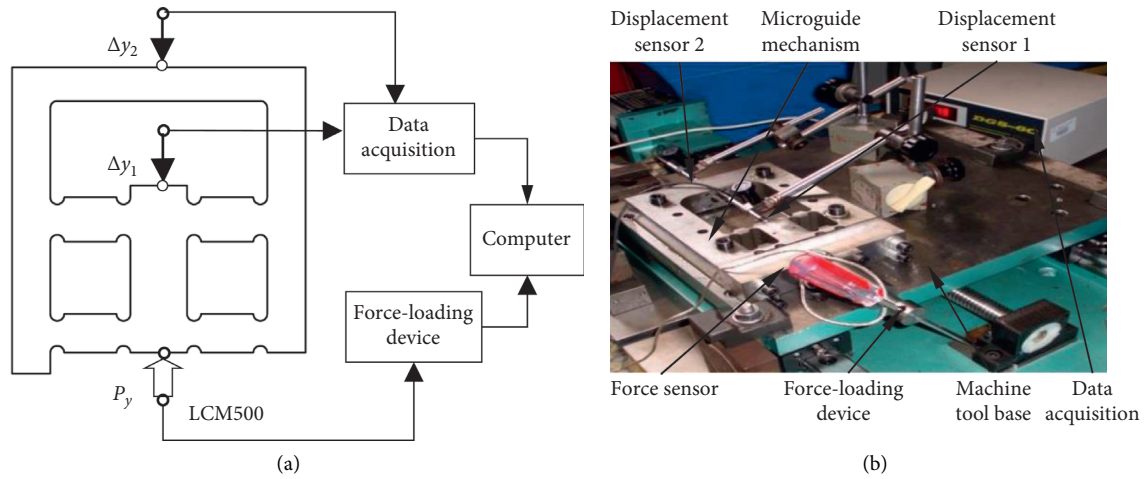


FIGURE 13: The guide stiffness experiment. (a) The principle of the guide stiffness experiment. (b) The experiment picture.

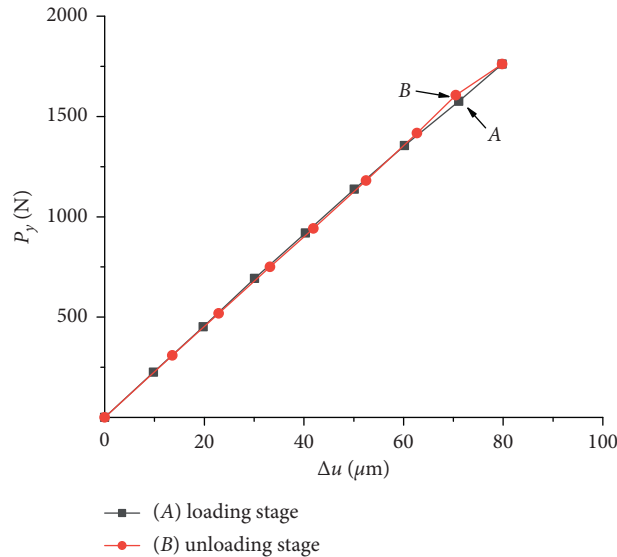


FIGURE 14: The results of the guide stiffness experiment.

$$\mathbf{P}_y = 22.4\Delta\mathbf{u} + 5.7. \quad (30)$$

The linearity of the linear equation is 0.9997.

As shown in the analysis in Section 4, the guide stiffness (K) calculated by BEM is $22.2 \text{ N}/\mu\text{m}$, and the relationship between K and the two linear equations is shown in Figure 15.

The experimental results show that the guide stiffness (K'_1 and K'_2) of the mechanism in the loading stage and unloading stage are $22.1 \text{ N}/\mu\text{m}$ and $22.4 \text{ N}/\mu\text{m}$, and the lowest linearity of the bending stiffness linear equation are 0.9998 and 0.9997, which indicates that the experiment results are accurate and believable.

In the loading stage, the experimental guide stiffness $K'_1 = 22.1 \text{ N}/\mu\text{m}$ and the calculated guide stiffness $K = 22.2 \text{ N}/\mu\text{m}$. Thus, the relative error of the guide stiffness between the two methods is -0.45% . In the unloading stage, the experimental guide stiffness $K'_2 = 22.4 \text{ N}/\mu\text{m}$ and the calculated guide stiffness $K = 22.2 \text{ N}/\mu\text{m}$. Thus, the relative error of the guide stiffness between the two methods is 0.90% .

Therefore, in the whole stage, the averages experimental guide stiffness $K' = 22.3 \text{ N}/\mu\text{m}$. Thus, the error of the guide stiffness between analysis and experiment is 0.45% . In addition, the experimental results show that the high-precision guide stiffness analysis method of the micromechanism based on BEM is adequate and accurate.

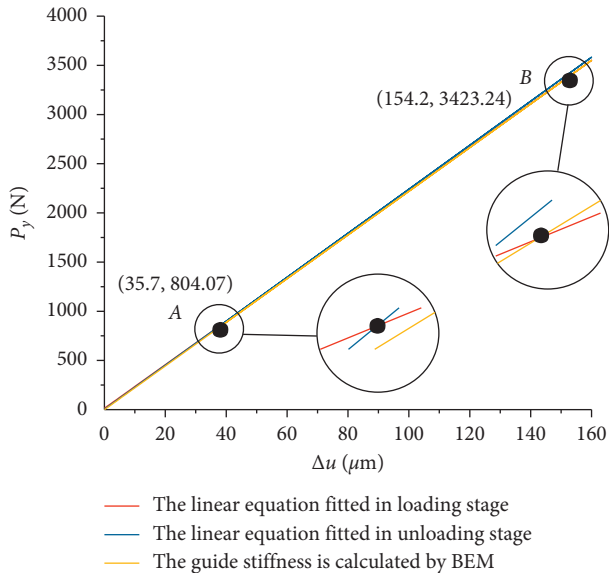


FIGURE 15: The relationship between K and the two linear equations.

6. Conclusion

This paper designs a micromechanism guiding unit to ensure the accuracy and safety of the micromechanism movement. On this basis, a method for analyzing the stiffness of the micromechanism guide rail based on BEM is proposed. In addition, the guide stiffness experiment was also carried out to test the validity and accuracy of this guide stiffness analysis method.

The guiding unit of the micromechanism is designed for the parasitic movement and the relaxation of the additional force during the movement of the micromechanism to ensure the accuracy and safety of the movement of the micromechanism. This research is conducive to the structural design of the micromechanism. The guide stiffness analysis method of the micromechanism guide rail based on BEM can better solve the special engineering problems. The guide beam stiffness analysis method of the BEM is a high-precision analysis method, and the value of the guide beam stiffness is analytical. The experimental results show that the calculated guide rail stiffness is $22.2 \text{ N}/\mu\text{m}$, the experimental guide rail stiffness is $22.3 \text{ N}/\mu\text{m}$, and the error between the methods is 0.45%. By continuing to study the method (adding rigid combination in the coordinate transformation method), the transformation stiffness of the microstructure can be analyzed. Then, the completion of two kinds of micromechanism (in Section 2.1, as shown in Figure 2) can be undertaken.

This method is suitable for other flexible units and can be used for stiffness analysis of various micromechanisms. Further work will be carried out on the stiffness analysis of the microrotary mechanism with high accuracy by BEM.

Data Availability

The data used to support the findings of this study are available from the corresponding author upon request.

Conflicts of Interest

The authors declare no potential conflicts of interest with respect to the research in this article.

Acknowledgments

The authors would like to thank the National Natural Science Foundation of China (nos. 51805428 and 51705417), the Basic Research Project of Natural Science in Shaanxi Province (nos. 2018JQ5205 and 2017JM5042), the Key Research and Development Project of Shaanxi Province (no. 2016KTZDGY4-01), the Science and Technology Plan Project of Xi'an City (no. 201805036YD14CG20(7)), the Special Scientific Research Project of the Shaanxi Province Department of Education (no. 18JK0528), and the Science and Technology Plan Project of Beilin District (no. GX2032) for their support.

References

- [1] Y. W. Sun and S. L. Jiang, "Predictive modeling of chatter stability considering force-induced deformation effect in milling thin-walled parts," *International Journal of Machine Tools and Manufacture*, vol. 135, pp. 38–52, 2018.
- [2] J. T. Xu, D. Y. Zhang, and Y. W. Sun, "Kinematics performance oriented smoothing method to plan tool orientations for 5-axis ball-end CNC machining," *International Journal of Mechanical Sciences*, vol. 157–158, pp. 293–303, 2019.
- [3] Y. Jiang and Q. Guo, "Simulation of multi-axis grinding considering runout based on envelope theory," *Chinese Journal of Aeronautics*, vol. 33, no. 12, pp. 3526–3534, 2020.
- [4] D. Bassing and A. S. Braeuer, "The lag between micro-and macro-mixing in compressed fluid flows," *Chemical Engineering Science*, vol. 163, pp. 105–113, 2017.
- [5] L. Zhang, J. Gao, X. Chen et al., "Implementation and experiment of an active vibration reduction strategy for macro-micro positioning system," *Precision Engineering*, vol. 51, pp. 319–330, 2018.
- [6] C. You, M. H. Lee, H. J. Lee et al., "The effect of macro/micro combination pore structure of biphasic calcium phosphate scaffold on bioactivity," *Ceramics International*, vol. 43, no. 4, pp. 3540–3546, 2016.
- [7] W. Tang, D. Lin, Y. Yu et al., "Bioinspired trimodal macro/micro/nano-porous scaffolds loading rhBMP-2 for complete regeneration of critical size bone defect," *Acta Biomaterialia*, vol. 32, pp. 309–323, 2016.
- [8] X. Zhuang, S. Ma, and Z. Zhao, "A microstructure-based macro-micro multi-scale fine-blanking simulation of ferrite-cementite steels," *International Journal of Mechanical Sciences*, vol. 128–129, pp. 14–427, 2017.
- [9] Y. Yang, Y. Wei, J. Lou, L. Fu, and X. Zhao, "Nonlinear dynamic analysis and optimal trajectory planning of a high-speed macro-micro manipulator," *Journal of Sound and Vibration*, vol. 405, pp. 112–132, 2017.
- [10] X. Sun and B. Yang, "A new methodology for developing flexure-hinged displacement amplifiers with micro-vibration suppression for a giant magnetostrictive micro drive system," *Sensors and Actuators A: Physical*, vol. 263, pp. 30–43, 2017.
- [11] M. Lok, E. F. Helbling, X. Zhang, R. Wood, D. Brooks, and G. Wei, "A low mass power electronics unit to drive piezoelectric actuators for flying microrobots," *IEEE Transactions on Power Electronics*, vol. 33, no. 4, pp. 3180–3191, 2018.

- [12] T. Mashimo, "Miniature preload mechanism for a micro ultrasonic motor," *Sensors and Actuators A: Physical*, vol. 257, pp. 106–112, 2017.
- [13] E. Hosseinian, P. O. Theillet, and O. N. Pierron, "Temperature and humidity effects on the quality factor of a silicon lateral rotary micro-resonator in atmospheric air," *Sensors and Actuators A Physical*, vol. 189, pp. 380–389, 2013.
- [14] D. Zhu and Y. Feng, "Structure design of a 3-DOF UPC type rotational fully spatial compliant parallel manipulator," *International Journal of Advanced Manufacturing Technology*, vol. 5, no. 8, pp. 70–81, 2013.
- [15] R. Pan, X. Zhao, P. Liu, and R. Ren, "Micro mechanism of polygonization wear on railroad wheels," *Wear*, vol. 392–393, pp. 213–220, 2013.
- [16] X. Fan, M. Sun, Z. Lin et al., "Automated noncontact micromanipulation using magnetic swimming microrobots," *IEEE Transactions on Nanotechnology*, vol. 90, p. 1, 2018.
- [17] M. A. Fenelon and T. Furukawa, "Design of an active flapping wing mechanism and a micro aerial vehicle using a rotary actuator," *Mechanism and Machine Theory*, vol. 45, no. 2, pp. 137–146, 2010.
- [18] C.-H. Liu, W.-Y. Jywe, Y.-R. Jeng, T.-H. Hsu, and Y.-t. Li, "Design and control of a long-traveling nano-positioning stage," *Precision Engineering*, vol. 34, no. 3, pp. 497–506, 2010.
- [19] D. Liu, A. J. McDaid, K. C. Aw, and S. Xie, "Position control of an ionic polymer metal composite actuated rotary joint using iterative feedback tuning," *Mechatronics*, vol. 21, no. 1, pp. 315–328, 2011.
- [20] M. A. Matin, D. Akai, N. Kawazu, M. Hanebuchi, K. Sawada, and M. Ishida, "FE Modeling of stress and deflection of PZT actuated micro-mirror: effect of crystal anisotropy," *Computational Materials Science*, vol. 48, pp. 349–359, 2010.
- [21] B. A. Gozen and O. B. Ozdoganlar, "Design and evaluation of a mechanical nanomanufacturing system for nanomilling," *Precision Engineering*, vol. 36, no. 1, pp. 19–30, 2012.
- [22] R. Majumdar and I. Paprotny, "Configurable post-release stress-engineering of surface micro-machined MEMS structures," *Journal of Microelectromechanical Systems*, vol. 26, no. 3, pp. 671–678, 2017.
- [23] C. Du, Y. Zhang, A. Kong, and Z. Yuan, "High-precision and fast response control for complex mechanical systems-servo performance of dedicated servo recording systems," *IEEE Transactions on Magnetics*, vol. 53, no. 3, pp. 1–5, 2017.
- [24] Z. Shao, S. Wu, J. Wu, and H. Fu, "A novel 5-DOF high-precision compliant parallel mechanism for large-aperture grating tiling," *International Journal of Mechanical Sciences*, vol. 8, no. 2, pp. 349–358, 2017.
- [25] F. Jiang, J. Chen, H. Bi, L. Li, W. Jing, and J. Zhang, "The underlying micro mechanism of performance enhancement of non-polar n-ZnO/p-AlGa_N ultraviolet light emitting diode with i-ZnO inserted layer," *Applied Physics Letters*, vol. 112, no. 3, Article ID 033505, 2018.
- [26] Y. Peng, S. Ito, Y. Shimizu, and W. Gao, "A micro-stage for linear-rotary positioning," *Key Engineering Materials*, vol. 523–524, pp. 650–655, 2012.
- [27] W. Xu and Y. Wu, "Piezoelectric actuator for machining on macro-to-micro cylindrical components by a precision rotary motion control," *Mechanical Systems and Signal Processing*, vol. 114, pp. 439–447, 2019.
- [28] S. R. Park and S. H. Yang, "A mathematical approach for analyzing ultra-precision positioning system with compliant mechanism," *Journal of Materials Processing Technology*, vol. 164–165, pp. 1584–1589, 2005.
- [29] H.-H. Pham and I.-M. Chen, "Stiffness modeling of flexure parallel mechanism," *Precision Engineering*, vol. 29, no. 4, pp. 467–478, 2005.
- [30] D. Wei, L. Sun, and Z. Du, "Stiffness research on a high-precision, Large-workspace parallel mechanism with compliant joints," *Precision Engineering*, vol. 32, no. 3, pp. 222–231, 2008.
- [31] K. Kyoung, A. Dahoon, and G. Daegab, "Optimal design of a 1-rotational DOF flexure joint for a 3-DOF H-type stage," *Mechatronics*, vol. 22, no. 1, pp. 24–32, 2012.
- [32] M. Liu, X. Zhang, and S. Fatikow, "Design and analysis of a multi-notched flexure hinge for compliant mechanisms," *Precision Engineering*, vol. 48, pp. 92–304, 2017.
- [33] D. F. Macheuposhti, N. Tolou, and J. L. Herder, "A statically balanced fully compliant power transmission mechanism between parallel rotational axes," *Mechanism and Machine Theory*, vol. 119, pp. 51–60, 2018.
- [34] S. Corradi, M. H. Aliabadi, and M. Marchetti, "A variable stiffness dual boundary element method for mixed-mode elastoplastic crack problems," *Theoretical and Applied Fracture Mechanics*, vol. 25, no. 1, pp. 43–49, 1996.
- [35] Y. Gong and C. Dong, "An isogeometric boundary element method using adaptive integral method for 3D potential problems," *Journal of Computational and Applied Mathematics*, vol. 319, pp. 141–158, 2017.

Research Article

Simulation of Constant-Volume Removal Rate Machining of Middle-Convex and Varying Ellipse Piston

Yanwei Xu ^{1,2}, Yin hao Wang,¹ and Tancheng Xie^{1,2}

¹School of Mechatronics Engineering, Henan University of Science and Technology, Luoyang 471003, China

²Intelligent Numerical Control Equipment Engineering Laboratory of Henan Province, Luoyang 471003, China

Correspondence should be addressed to Yanwei Xu; xuyanweiluoyang@163.com

Received 7 May 2021; Revised 19 May 2021; Accepted 21 May 2021; Published 30 May 2021

Academic Editor: Qiang Guo

Copyright © 2021 Yanwei Xu et al. This is an open access article distributed under the Creative Commons Attribution License, which permits unrestricted use, distribution, and reproduction in any medium, provided the original work is properly cited.

One kind of constant-volume removal rate machining method of the middle-convex and varying ellipse piston is proposed in this paper. By analyzing the structure and movement relationship of the middle-convex and varying ellipse piston machine, the NC machining model is built. And, the constant-volume removal rate machining model is also built by superposing the variable rotation satisfying the dynamic performance constraints on the uniform rotation of the spindle of the CNC piston lathe. Then, the instantaneous position parameters of each axis of the CNC piston lathe are obtained and turned into NC code. The functional feasibility of the method finally is verified by simulation machining.

1. Introduction

In the reciprocating process of crankshaft output torque, the piston transmits the gas pressure in the cylinder to this process through the piston pin and connecting rod, but the clearance between the piston and the cylinder sleeve should be as small and uniform as possible to prevent the piston from being “roughened” or “bitten” in the cylinder. However, in the coupled working environment of high temperature, high pressure, and alternating mechanical and thermal loads, the force acting on the top of the piston leads to the deformation of the piston skirt along the axis of the pin seat, the deformation of the side of the piston skirt, and the uneven thermal expansion. These causes lead to serious and irregular deformation of the piston, which makes the cross section of the piston skirt that is originally a round cross section cannot keep round in the working environment, and then become oval, resulting in that the “cylindrical” piston processed at room temperature presents the “elliptical cylinder” shape. This deformation directly affects the uniformity of fit clearance between piston and cylinder liner. The piston with middle-convex and varying ellipse piston skirt is designed, which can keep the ideal geometry under working conditions [1], ensure the good fit between

the piston and the cylinder wall, reduce the cylinder clearance and the impact of the piston on the cylinder wall, and reduce the specific pressure and noise of the piston skirt. Moreover, a wedge-shaped oil gap is formed between the middle-convex skirt of the piston and the cylinder wall, which ensures the good lubrication of the piston and reduces the wear of parts.

For a long time, many scholars have deeply studied the machining method of middle-convex and varying ellipse piston [2–12]. These achievements have effectively promoted the progress of machining technology of middle-convex and varying ellipse piston, but the noncircular section machining technology of piston skirt studied by these achievements is basically based on numerical control turning method. NC turning is an important method for machining the piston with middle-convex and varying ellipse piston, which can effectively improve the machining accuracy and efficiency of the piston with middle-convex and varying ellipse piston. However, in the process of cutting a circular cross-sectional workpiece into an elliptical cross-sectional workpiece on a CNC piston lathe, the workpiece will rotate at a constant speed, and the cutting tool will move with high frequency and reciprocation. Moreover, the cutting depth of the cutting tool will change continuously with the rotation position

of the workpiece, and the cutting area of the cutting tool in the same cross section will change with the processing position. The material removal rate and cutting force of the workpiece change periodically, which will form dynamic excitation force and affect the machining accuracy of piston skirt to a certain extent.

Based on the basic principle that the cutting force is approximately proportional to the cutting area, this paper studies the numerical control machining technology and simulation of the equal volume cutting rate of the middle-convex and varying ellipse piston. On the premise that the rotation position of the shaft section of the piston skirt and the cutting depth of the tool tip conform to the ellipse trajectory, the variable-speed rotation meeting the dynamic performance constraint is superimposed on the uniform speed rotation of the main shaft of the piston machine tool. The rotation speed of the main shaft of the machine tool is continuously regulated, and the material removal rate and cutting force of the middle-convex and varying ellipse piston skirt are basically constant.

2. Processing Principle of Middle-Convex and Varying Ellipse Piston Skirt

The profile characteristics of the middle-convex and varying ellipse piston skirt are as follows: the generatrix of the piston skirt is a middle-convex curve which represents the variation of the diameter of the long axis of the elliptic section along the direction of the piston axis. The shape of cross section of piston skirt is similar to an ellipse, and the ovality of different sections is different. In any section, the diameter of long axis of ellipse section is the largest diameter, the long axis is along the axis of pin seat, the diameter of short axis of this section is the smallest diameter, and the short axis is perpendicular to the axis of pin seat. The ellipticity of the elliptic section is the difference between the diameter of major axis and that of minor axis.

2.1. Elliptical Profile of Skirt Cross Section of Middle-Convex and Varying Ellipse Piston. The geometric characteristics of the skirt cross section of the piston with middle-convex and varying ellipse can be described as follows [2]:

$$R(h, \theta) = R_1(h) - \frac{G(h)}{4}C. \quad (1)$$

In the formula, $R(h, \theta)$ is polar radius value; $G(h)$ is ellipticity; and $R_1(h)$ is elliptical long half-axis.

$$R_1(h) = R_1(0) - k_1(h - h_0)^m. \quad (2)$$

In the formula, $R_1(0)$ is long half-axis of section with maximum ellipticity.

$$G(h) = G(0) - k_2h. \quad (3)$$

In the formula, $G(0)$ is the maximum ellipticity; θ is the relative rotation angle of polar radius to long axis; h is the skirt height; h_0 is the skirt height of section with maximum ellipticity; β is the dimensionless coefficient ($\beta = 0$ is an

ellipse; $\beta = 1$ is a quadratic ellipse); m is the profile shape characteristic coefficient of longitudinal profile; k_1 is the dimensionless coefficient; and k_2 is the ellipticity change rate.

$$C = 1 - k_3 \left\{ \cos 2\theta - \frac{\beta}{25} [1 - \cos 4\theta] \right\}. \quad (4)$$

In the formula, k_3 is the dimensionless coefficient (when $k_3 = 0$, the cross section is circular; when $k_3 = 1$, the cross section is elliptical).

Formula (1) is the variation of polar radius, and formula (2) is the radial variation of the middle-convex profile along the piston axis. If the piston is an elliptical piston, the formula of any elliptical cross section of the piston skirt can be obtained by substituting formula (4) into (1).

$$R(h, \theta) = R_1(h) - \frac{G(h)}{4} (1 - \cos 2\theta), \quad (5)$$

among which, $\theta = \omega t = 2\pi nt/60 = 2\pi ft$, ω is angular velocity, and

$$R(h, \theta) = R_1(h) - \frac{G(h)}{4} [(1 - \cos 2\theta) + \beta(1 - \cos 4\theta)]. \quad (6)$$

2.2. Middle-Convex Profile of Middle-Convex and Varying Ellipse Piston. The middle-convex profile of the middle-convex and varying ellipse piston skirt is usually given discrete points in design. Figure 1 is the design parameters of the middle-convex profile of the Perkins 240 piston skirt.

Usually, the discrete points of the convex profile are fitted to smooth curves by cubic spline interpolation, and then the equation of the middle-convex profile is obtained. In the process of fitting the discrete points of middle-convex profile in piston skirt shown in Figure 2, N discrete points are put into the XOZ coordinate system in which the X -axis is parallel to the piston cross section and the Z -axis is the piston axis (X represents the long half-axis of elliptical cross section and Z represents the piston skirt height). If the first derivatives of the curve composed of discrete points are x'_0 and x'_n at the beginning and end points, respectively, the function value $x(z)$ of any point $z_{i-1} < z < z_i$ on the Z -axis can be expressed as follows [13]:

$$x(z) = M_{i-1} \frac{(z_i - z)^3}{6L_i} - \frac{(z - z_{i-1})^3}{6L_i} + \left(\frac{x_i}{L_i} - \frac{M_i L_i}{6} \right) \cdot (z - z_{i-1}) + \left(\frac{x_{i-1}}{L_i} - \frac{L_i M_{i-1}}{6} \right) \cdot (z_i - z). \quad (7)$$

In the formula, M_i satisfies the equation

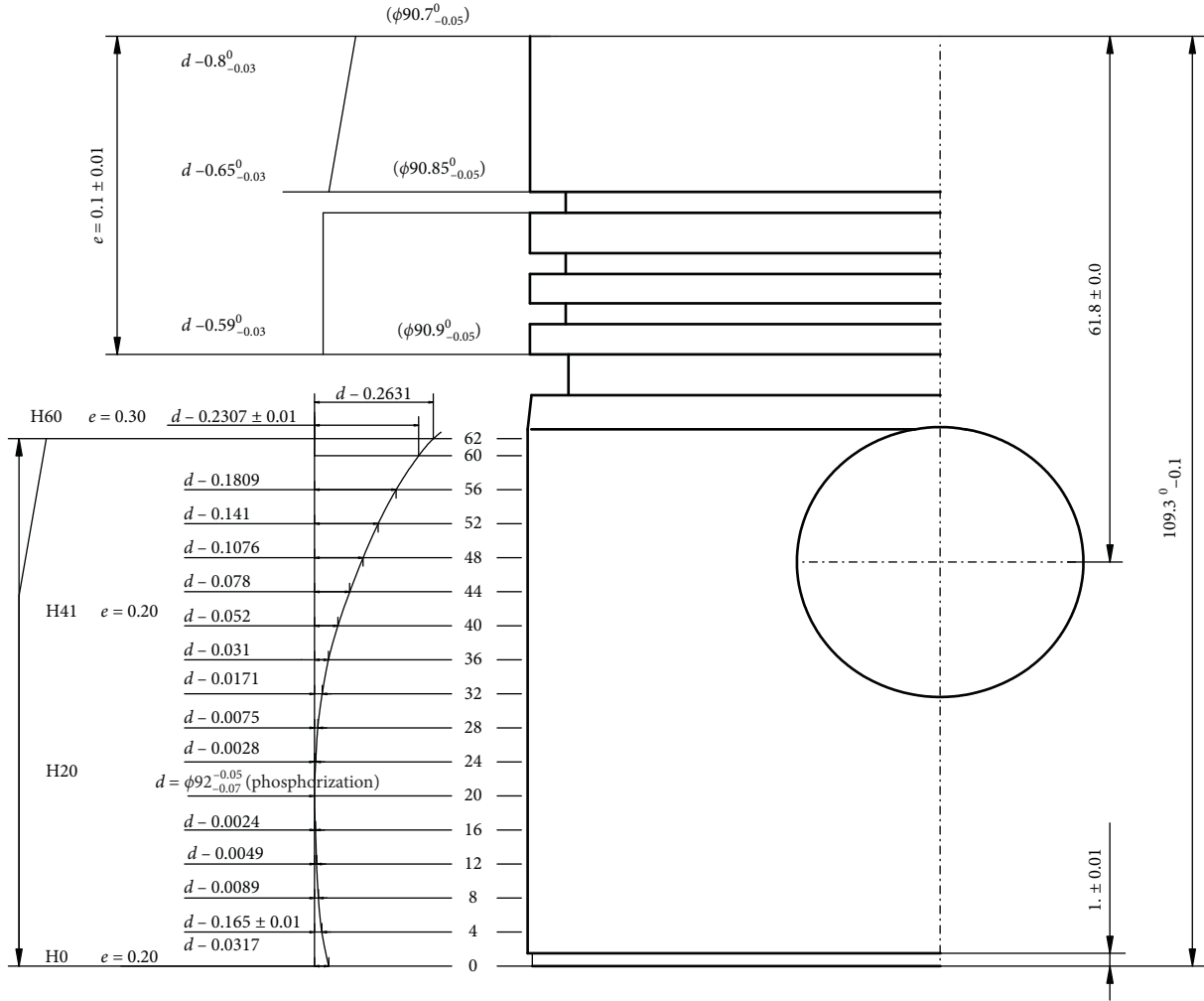


FIGURE 1: Geometric parameters of the Perkins 240 piston skirt.

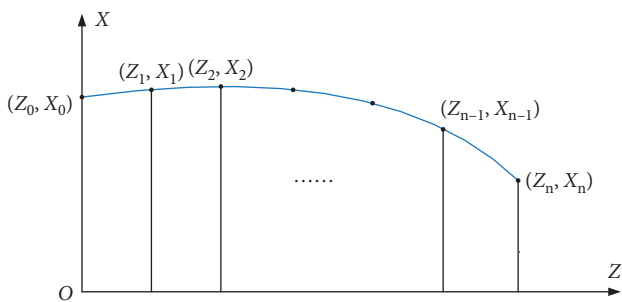


FIGURE 2: Fitting of discrete points of middle-convex profile in piston section.

$$\begin{cases} 2M_0 + M_1 = \frac{6}{L_1} \left(\frac{x_1 - x_0}{L_1} - x'_0 \right), \\ M_{n-1} + 2M_n = \frac{6}{L_n} \left(x'_n - \frac{x_n - x_{n-1}}{L_n} \right), \\ U_i + 2M_i + \lambda M_{i+1} = 6 \frac{(x_{i+1} - x_i/L_{i-1}) - (x_i - x_{i-1}/L_i)}{L_i + L_{i+1}}, \end{cases} \quad (8)$$

among which, $L_i = z_i - z_{i-1}$, $\lambda_i = (L_{i+1}/L_i + L_{i+1})$, and $U_i = 1 - \lambda_i$. Solution M_i , the fitting equation $x(z)$ of middle-convex profile in piston skirt can be obtained by substitution formula (1).

2.3. Analysis of Processing Process of Middle-Convex and Varying Ellipse Piston Skirt. The structure of CNC piston machine tool is shown in Figure 3. Machine motion consists of workpiece (spindle C-axis) rotary motion, tool holder slider linear motion along the Z-axis (parallel to workpiece rotary axis), tool holder linear motion along the X axis (perpendicular to workpiece rotary axis), and tool holder U-axis reciprocating linear motion (control tool high-frequency reciprocating microdisplacement linear motion), X-axis. The cutting depth is controlled by U-axis, and the travel of the tool in high-speed reciprocating linear motion depends on the ellipticity of elliptical cross section at different skirt heights of piston skirt.

The process of turning skirt profile of middle-convex and varying ellipse piston by motion synthesis method can be divided into two independent motions: (1) the motion of tool relative to workpiece forming middle-convex profile is

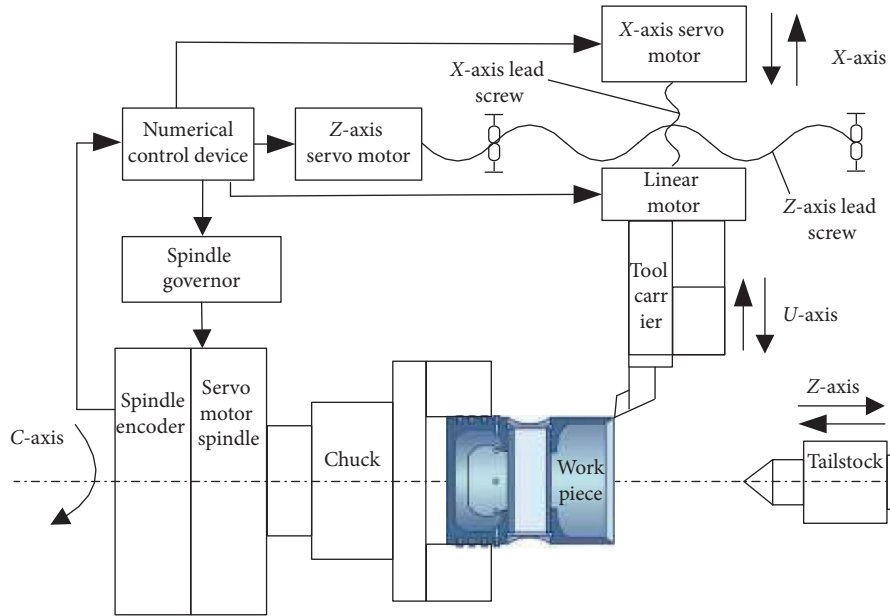


FIGURE 3: Structure sketch of CNC piston machine tool.

realized by the joint motion of X -axis and Z -axis driven by servo motor; (2) the motion of tool relative to workpiece forming elliptical profile, the reciprocating linear motion of U -axis driven by linear motor, and the motion of spindle.

2.3.1. Middle-Convex Profile Processing. The motion of forming the middle-convex profile is synthesized by the motion of the tool in the piston axis (Z -axis) and the radial direction (X -axis). After the fitting equation of discrete points on the middle-convex profile is obtained, the middle-convex profile is interpolated, and the cubic spline curve is approximated and fitted by micro line segments. According to the requirements of piston skirt surface processing accuracy and tool feed, the number of interpolation points is determined, and the middle-convex profile is interpolated in the piston axis direction. In this paper, the interpolation points are divided by equal interval method. Each step of interpolation, the workpiece rotates one week to complete a micro-short elliptical cylinder processing. Then, the Z -axis position is calculated, and the Z -axis servo motor drives the trawler to the next interpolation point. Figure 4 is a schematic diagram of NC machining of middle-convex profile in piston skirt.

2.3.2. Elliptical Profile Processing. The forming motion of the elliptical section of the piston skirt can be decomposed into a high-speed rotational motion of the workpiece and a high-speed reciprocating linear feed motion of the tool in the radial direction of the piston. During the forming process, the piston rotates with the spindle every one revolution, and the tool sequentially processes the long axis of the elliptical section \rightarrow the short axis \rightarrow the long axis \rightarrow the short axis \rightarrow the long axis, and the tool feeds twice in rapid reciprocating direction. The higher the spindle speed, the higher the tool feed frequency; the greater the ellipticity of

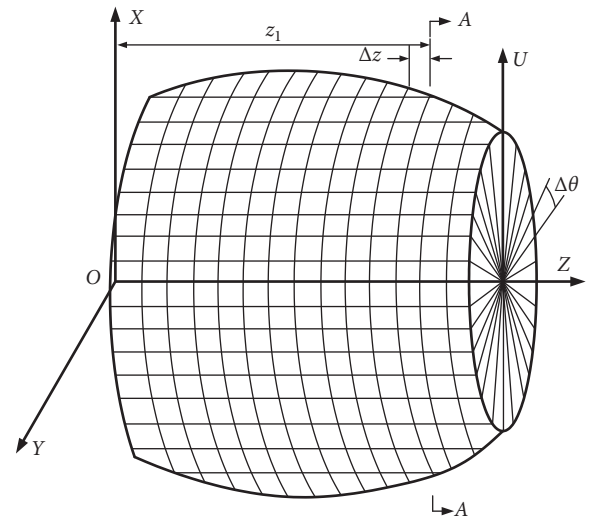


FIGURE 4: NC machining schematic diagram of middle-convex profile.

the elliptical section, the greater the turning radius change, the greater the displacement of the tool's fast reciprocating linear feed, and the greater the speed and acceleration of the tool. The key to the elliptical section turning of the piston skirt is the control of the tool path: (1) the high-frequency reciprocating linear motion of the tool; (2) the micro-displacement of the tool reciprocating linear feed motion and the angular displacement of the workpiece high-speed rotation maintain a strict one-to-one correspondence. The schematic diagram of the elliptical section machining process of the piston is shown in Figure 5.

Assuming that the starting position of the tool tip is located at the apex B of the ellipse long axis, the expression of the motion displacement of the tool tip vertex can be described as follows:

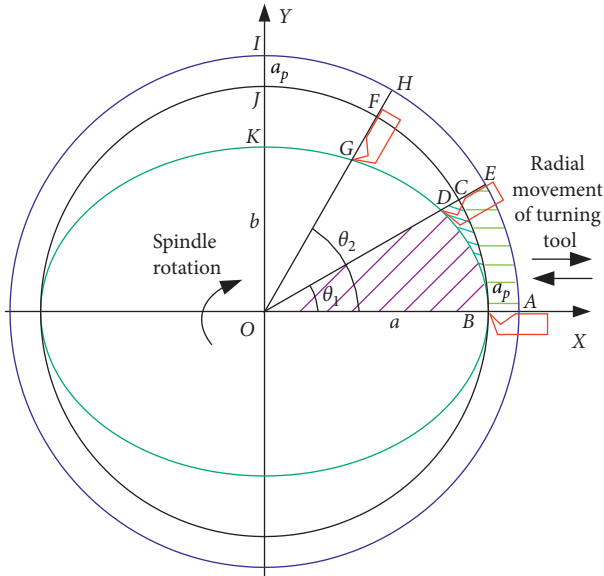


FIGURE 5: Schematic diagram of elliptical section processing.

$$x = a - R = a - \sqrt{a^2 \cos^2(2\pi ft) + b^2 \sin^2(2\pi ft)}. \quad (9)$$

In the formula, f is the rotation frequency of the lathe spindle and t is time.

When the workpiece rotates with the spindle at a constant speed to turn the piston skirt contour with middle-convex and varying ellipse, the displacement relationship of the four moving axes of the machine tool can be expressed as follows:

$$\left\{ \begin{array}{l} C: \theta = \frac{2\pi nt}{60} = 2\pi ft, \\ Z: z = f(t), \\ X: x = F(z) = F(f(t)), \\ U: u = a - \sqrt{a^2 \cos^2(2\pi ft) + b^2 \sin^2(2\pi ft)}. \end{array} \right. \quad (10)$$

This is the NC machining model of the middle-convex and varying ellipse piston skirt in the uniform turning of the workpiece.

2.4. Distribution Law of Cutting Area of Elliptical Section.

In the NC machining process of the middle-convex and varying ellipse piston, the rough machining of the piston is completed on an ordinary CNC lathe, and the final forming finishing is completed by a numerical control piston lathe. During the conventional forming and finishing of the piston skirt, the workpiece rotates at a constant speed. The area cut-off in the same elliptical cross section varies with the machining position.

In Figure 5, it is assumed that the cutting depth is changed from the workpiece diameter dimension A of the previous process to the long axis B of the elliptical cross section, and the

cutting depth is a_p from 0° to 90° , and the tool is continuously advanced, 90° . When the time is fed to the short axis K of the elliptical cross section, the path of the cutting edge along the surface of the workpiece is substantially like a smooth curve $BDGK$. During the process of moving the workpiece from 0° to 90° , the area cut by the workpiece through the same corner gradually increases. When the workpiece is turned from 0° to angle, the area to be cut is

$$S_{ABDE} = S_{ABCE} + S_{BOC} - S_{BOD}. \quad (11)$$

In the formula, the elliptical sector area S_{BOD} is calculated as follows:

$$S_{BOD} = \frac{1}{2} ab \cdot \arctan\left(\frac{a}{b} \tan \theta\right). \quad (12)$$

When the workpiece is turned from 1 to 2, the area to be cut is

$$S_{CDGF} = S_{CFHE} + S_{COF} - S_{DOG}. \quad (13)$$

Select the Perkins 240 piston skirt height $H = 20$ elliptical section in Figure 1 (diameter $d = \Phi 92$, corresponding to ellipticity $G = 0.20$). Take the cutting depth $a_p = 0.1$. Calculate the workpiece in the first quadrant every revolution. The depth of cut a_p and its variation a_p and the area cut within the same corner. The results are shown in Table 1.

It can be seen from Table 1 that in the first quadrant, the cutter starts to cut from the long semi-axis of the elliptical section, and the cutting depth a_p gradually increases as the workpiece rotation angle changes; the amount of change in the cutting depth gradually increases at the beginning of the angle a_p at 45° . The vicinity a_p increases to the maximum value and then gradually decreases; the area cut by the workpiece rotating through the same angle (3°) gradually increases. In the first quadrant, the cutting depth a_p , the cutting depth variation a_p , and the change trend of the cutting area in the workpiece rotating through the same angle (3°) are shown in Figures 6–8, respectively.

3. Processing Principle of Equal-Volume Excision Rate

During the process of uniform turning of the elliptical cross section of the middle-convex and varying ellipse piston skirt during uniform turning, the resection area changes periodically with the workpiece rotation angle per unit time, resulting in periodic changes in material removal rate and cutting force, and processing of the piston skirt to some extent. Accuracy has an impact. In order to reduce this effect, this paper proposes the NC machining concept of equal-volume resection rate of middle-convex and varying ellipse piston—the volume ρV of the material removed per unit time is equal during the elliptical cross section of the middle-convex and varying ellipse piston skirt during processing.

The projected area ΔS of the volume ΔV on the elliptical section is

$$\Delta S = \frac{\Delta V}{f}. \quad (14)$$

TABLE 1: Cutting depth and its variation and the area cut in the same corner.

Angle (°)	a_p (mm)	Δa_p (μm)	Equal-angle cut area (mm^2)
3	0.10027	0.27	0.24134
6	0.10109	0.82	0.24266
9	0.10244	1.35	0.24529
12	0.10432	1.87	0.24919
15	0.10669	2.37	0.25433
18	0.10954	2.85	0.26065
21	0.11283	3.29	0.26807
24	0.11653	3.70	0.27652
27	0.12059	4.06	0.28590
30	0.12498	4.39	0.29611
33	0.12964	4.66	0.30703
36	0.13452	4.88	0.31855
39	0.13958	5.05	0.33054
42	0.14475	5.17	0.34286
45	0.14997	5.23	0.35538
48	0.15520	5.23	0.36797
51	0.16037	5.17	0.38048
54	0.16543	5.06	0.39278
57	0.17031	4.89	0.40473
60	0.17498	4.67	0.41621
63	0.17937	4.39	0.42709
66	0.18344	4.07	0.43724
69	0.18715	3.70	0.44657
72	0.19044	3.30	0.45496
75	0.19329	2.85	0.46233
78	0.19567	2.38	0.46860
81	0.19755	1.88	0.47370
84	0.19891	1.36	0.47758
87	0.19973	0.82	0.48018
90	0.2	0.27	0.48149

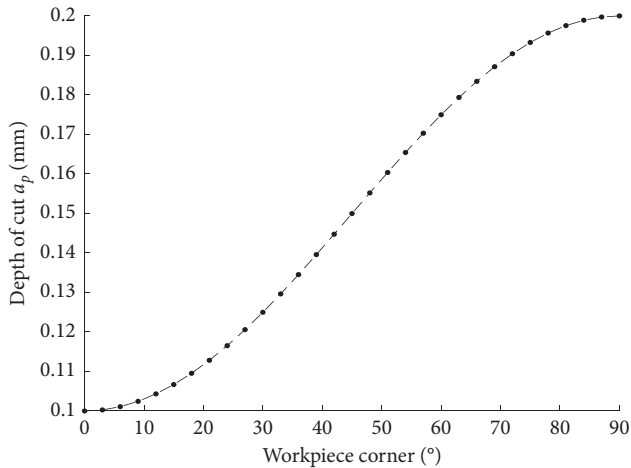


FIGURE 6: Cutting depth a_p change trend.

The projected area ΔS_{\max} of the maximum volume ΔV_{\max} allowed to be cut per unit time in the elliptical section is

$$\Delta S_{\max} = \frac{\Delta V_{\max}}{f}. \quad (15)$$

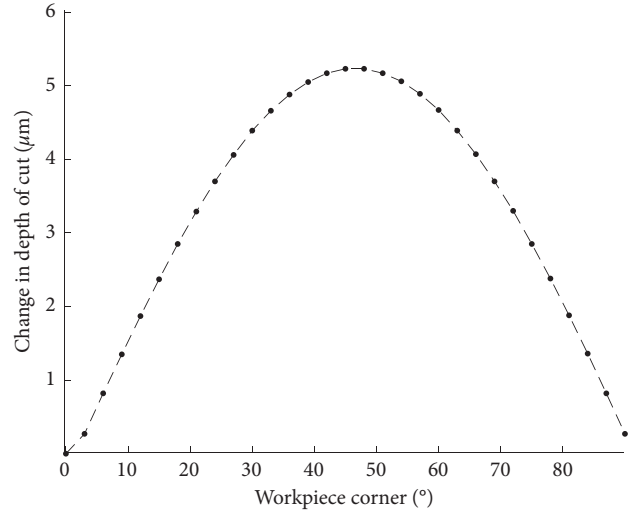


FIGURE 7: Change in cutting depth a_p change trend.

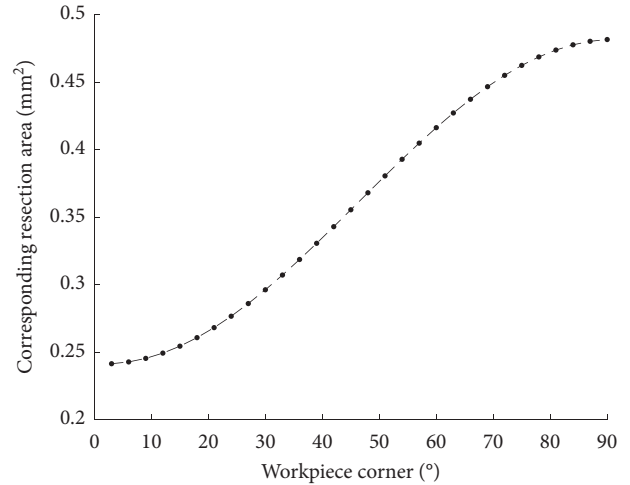


FIGURE 8: Area cut in the same corner.

In the schematic diagram of the elliptical cross section machining of the middle-convex and varying ellipse piston shown in Figure 4, the total area cut-off in the first quadrant is equal to the difference between the quarter circle area SAOI and the quarter ellipse area SBOK. Then, there is

$$S_{\text{cut}} = S_{AOI} - S_{BOK} = \frac{1}{4}\pi(a + a_p)^2 - \frac{1}{4}\pi ab. \quad (16)$$

The total area cut out in the first quadrant is divided into n equal parts for processing, so that the time taken to cut each aliquot area ΔS is the same.

$$\Delta S = \frac{S_{\text{cut}}}{n} = \frac{\pi \left[(a + a_p)^2 - ab \right]}{4n}. \quad (17)$$

In the formula, n must meet the conditions

$$n \geq \frac{S_{\text{cut}}}{\Delta S_{\max}} = \frac{\pi \left[(a + a_p)^2 - ab \right]}{4\Delta S_{\max}}. \quad (18)$$

In the first quadrant, the area cut-off from $0 \sim \theta_1, \theta_1 \sim \theta_2, \dots, \theta_{n-1} \sim \theta_n$ is equal to ΔS . Then, there is

$$i\Delta S = \frac{1}{2}\theta_i(a + a_p)^2 - \frac{1}{2}ab \cdot \arctan\left(\frac{a}{b}\tan\theta_i\right). \quad (19)$$

Combining (17) and (19) gives

$$\frac{i\pi\left[(a + a_p)^2 - ab\right]}{4n} = \frac{\theta_i(a + a_p)^2 - ab \cdot \arctan\left(\frac{a}{b}\tan\theta_i\right)}{2}. \quad (20)$$

Solving the equation yields angle values of $\theta_1, \theta_2, \theta_3, \dots, \theta_{n-1}, \theta_n$.

When the elliptical section of the middle-convex and varying ellipse piston skirt is machined by the equal-volume resection rate method, the displacement relationship of the four axes of motion of the machine tool can be expressed as follows:

$$\begin{cases} C: \theta_i = F(i, a, b, a_p), \\ Z: z = f(t), \\ X: x = F(z) = F(f(t)), \\ U: u_i = a - \sqrt{a^2 \cos^2 \theta_i + b^2 \sin^2 \theta_i}. \end{cases} \quad (21)$$

This is the numerical control machining model when machining the middle-convex and varying ellipse piston skirt in the same volume resection rate method.

4. Equal-Volume Resection Rate Simulation Processing and Experiment

The skirt height H of the middle-convex and varying ellipse piston in Perkins 240 is shown in Figure 1 and its corresponding elliptical cross-sectional long axis value and ellipticity value are shown in Tables 2 and 3, respectively.

According to Table 2, using cubic spline interpolation, the fitting equation and fitting curve of the ellipse long axis value of the Perkins 240 piston skirt can be obtained by MATLAB program fitting (Figure 9).

$$d = 2.73 \times 10^{-3}z - 4.23424 \times 10^{-5}z^2 - 9.93358 \times 10^{-7}z^3 + 91.97066. \quad (22)$$

According to Table 3, using linear interpolation, the equation for the ellipticity of the elliptical section G with the height of the skirt is

$$G = \begin{cases} 0.2, & (0 \leq z \leq 41), \\ 4.7619 \times 10^{-3}z + 4.7619 \times 10^{-3}, & (41 \leq z \leq 62). \end{cases} \quad (23)$$

Take the elliptical cross-sectional long axis maximum value plus twice the depth of cut a_p as the cylinder workpiece diameter d_0 before the piston skirt forming process, starting from the skirt height $H=0$, according to the feed amount $f=0.001$ [14], calculate the different ellipse values of the long semiaxis a , the ellipticity G , and the short semiaxis b of the

TABLE 2: Piston skirt height H and corresponding elliptical section long axis value.

Skirt height H (mm)	Long axis (mm)	Skirt height H (mm)	Long axis (mm)
4	91.9835	36	91.969
8	91.9911	40	91.948
12	91.9951	44	91.922
16	91.9976	48	91.8924
20	92	52	91.859
24	91.9972	56	91.8191
28	91.9925	60	91.7693
32	91.9829	62	91.737

TABLE 3: Piston skirt height H and corresponding cross-sectional ellipticity values.

Skirt height H	Cross-sectional ellipticity
0-41	0.2
41-62	Linear gradient to 0.3

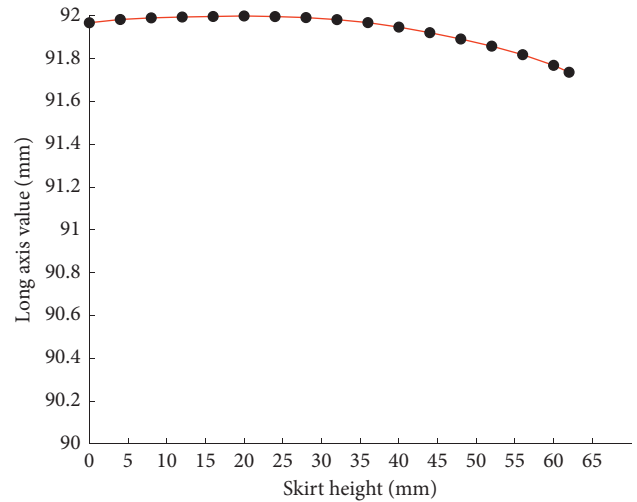


FIGURE 9: Contour line fitting curve in the Perkins 240 piston skirt.

section, and calculate the feed of the tool from the skirt height $H=0$, the tool is cut from $d_0/2$ to the long semiaxis of each different elliptical section. For each different elliptical section, divide the area cut-off in the first quadrant into n equal parts, and obtain the angle corresponding to each aliquot and the corresponding tool feed amount; then, according to the principle of symmetry, the workpiece is rotated within one week. The angle corresponding to each aliquot and the tool feed. Then, the numerical values of workpiece rotation angle and tool feed per equal part are transformed into corresponding NC machining program. According to the NC machining model of equal volume removal rate for middle-convex and varying ellipse piston, the piston skirt can be machined with equal-volume removal rate.

Taking the maximum elliptical section of the Perkins 240 piston as an example, the skirt height $H=20$, the long axis diameter, the ellipticity $G=0.20$, the long half axis $a=46$, the short half-axis $b=45.9$, and the first quadrant 0-degree cutting allowance $a_p=0.1$. According to these parameters,

TABLE 4: Equal-volume resection rate processing calculation results.

No.	a_p (mm)	Δa_p (μm)	Every aliquot ($^\circ$)	Actual corner ($^\circ$)
1	0.1006	0.612	4.4897	4.4897
2	0.1024	1.793	4.4358	8.9255
3	0.1053	2.852	4.3361	13.2617
4	0.1090	3.74	4.2015	17.4632
5	0.1134	4.434	4.0463	21.5094
6	0.1184	4.939	3.8818	25.3912
7	0.1236	5.275	3.7174	29.1085
8	0.1291	5.467	3.5592	32.6678
9	0.1347	5.542	3.4102	36.0780
10	0.1402	5.525	3.2733	39.3513
11	0.1456	5.435	3.1478	42.4991
12	0.1509	5.289	3.0338	45.5330
13	0.1560	5.102	2.9313	48.4642
14	0.1609	4.882	2.8390	51.3032
15	0.1655	4.639	2.7565	54.0597
16	0.1699	4.377	2.6826	56.7423
17	0.1740	4.102	2.6167	59.3590
18	0.1778	3.817	2.5583	61.9173
19	0.1813	3.524	2.5061	64.4234
20	0.1846	3.227	2.4603	66.8837
21	0.1875	2.925	2.4196	69.3033
22	0.1901	2.621	2.3841	71.6873
23	0.1924	2.315	2.3537	74.0410
24	0.1944	2.007	2.3274	76.3684
25	0.1961	1.699	2.3056	78.6740
26	0.1975	1.391	2.2878	80.9618
27	0.1986	1.081	2.2735	83.2353
28	0.1994	0.772	2.2632	85.4985
29	0.1998	0.463	2.2557	87.7542
30	0.2	0.154	2.2458	90.0000

the angle corresponding to the area of each aliquot and the actual rotation angle of the workpiece and the corresponding depth of cut a_p and its variation Δa_p can be obtained. Take $n = 30$ aliquots, and the calculation results are shown in Table 4.

According to Table 4, when the maximum elliptical cross section of the middle-convex and varying ellipse piston skirt in Perkins 240 is processed by equal-volume resection; in the first quadrant, the change trend of the workpiece turning angle of each aliquot is as shown in Figure 10. The trend of the actual turning angle is shown in Figure 11; the change trend of each cutting area corresponding to the cutting depth is shown in Figure 12, and the corresponding cutting depth is shown in Figure 13.

The obtained actual cutting angle and the tool feed amount corresponding to each aliquot area and the positional parameters of the corresponding X-axis and Z-axis are converted into a numerical control machining program, and the elliptical section of the middle-convex and varying ellipse piston skirt can be obtained. Perform equal-volume resection rate processing. Skirt height $H = 20$ elliptical section first image inner limit equal volume resection rate machine tool motion parameters when middle-convex and varying ellipse piston skirt is processed as shown in Table 5.

According to the machine motion parameters, based on the VERICUT CNC machining simulation platform, the equal-volume resection rate simulation was performed on

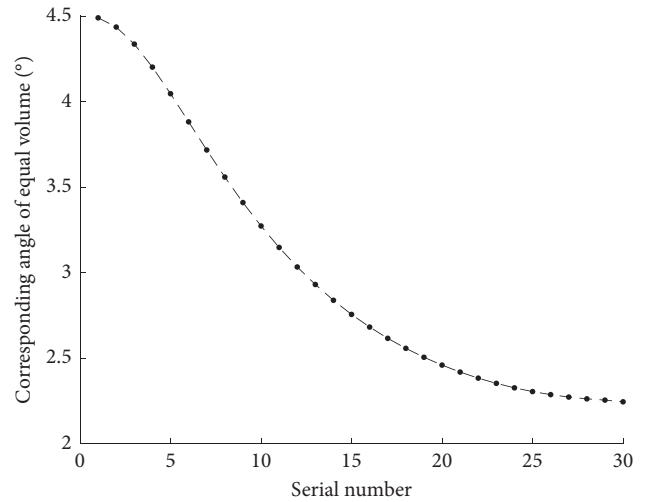


FIGURE 10: Each resection area corresponds to the workpiece rotation angle.

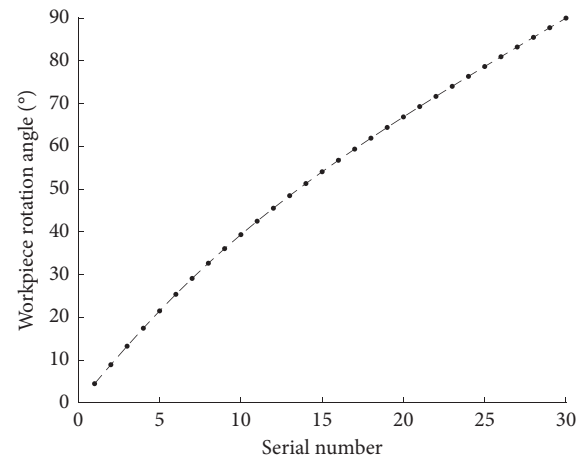


FIGURE 11: The cut area corresponds to the actual rotation angle of the workpiece.

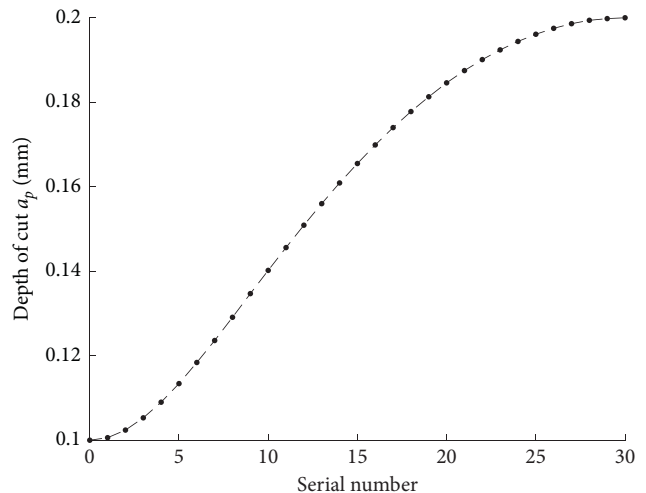


FIGURE 12: Cut area corresponds to the depth of cut.

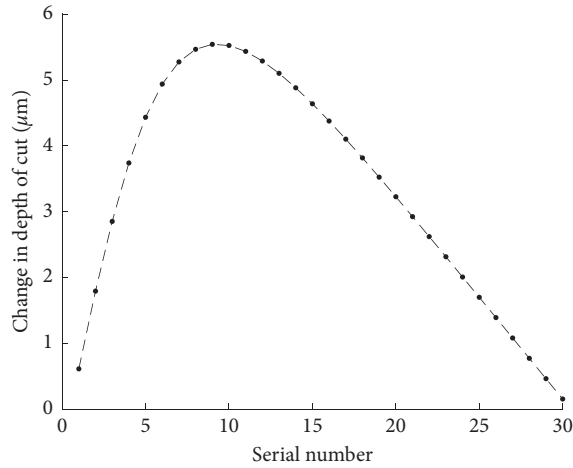


FIGURE 13: Cut area corresponds to the change in the depth of cut.

TABLE 5: Machine tool motion parameters for equal-volume resection rate machining in the first quadrant.

No.	Z (mm)	X (mm)	$\angle C(^{\circ})$	U (mm)
N 3310	20.00	46.100	4.4897	0.1006
N 3320	20.00	46.100	8.9256	0.1024
N 3330	20.00	46.100	13.2617	0.1053
N 3340	20.00	46.100	17.4632	0.1090
N 3350	20.00	46.100	21.5094	0.1134
N 3360	20.00	46.100	25.3912	0.1184
N 3370	20.00	46.100	29.1086	0.1236
N 3380	20.00	46.100	32.6678	0.1291
N 3390	20.00	46.100	36.0780	0.1347
N 3400	20.00	46.100	39.3513	0.1402
N 3410	20.00	46.100	42.4991	0.1456
N 3420	20.00	46.100	45.5330	0.1509
N 3430	20.00	46.100	48.4642	0.1560
N 3440	20.00	46.100	51.3032	0.1609
N 3450	20.00	46.100	54.0597	0.1655
N 3460	20.00	46.100	56.7423	0.1699
N 3470	20.00	46.100	59.3590	0.1740
N 3480	20.00	46.100	61.9173	0.1778
N 3490	20.00	46.100	64.4234	0.1813
N 3500	20.00	46.100	66.8837	0.1846
N 3510	20.00	46.100	69.3033	0.1875
N 3520	20.00	46.100	71.6873	0.1901
N 3530	20.00	46.100	74.0410	0.1924
N 3540	20.00	46.100	76.3684	0.1944
N 3550	20.00	46.100	78.6740	0.1961
N 3560	20.00	46.100	80.9618	0.1975
N 3570	20.00	46.100	83.2353	0.1986
N 3580	20.00	46.100	85.4985	0.1994
N 3590	20.00	46.100	87.7542	0.1998
N 3600	20.00	46.100	90.0000	0.2000

the Perkins 240 piston skirt in Figure 1 (as shown in Figure 14).

The ellipticity value of the geometric parameters of the middle-convex and varying ellipse piston skirt in Perkins 240 is magnified 30 times, the remaining parameters are unchanged, recalculated, and simulated, and the simulation processing effect of the middle-convex line and the variable elliptic section can be clearly seen (as shown in Figure 15).

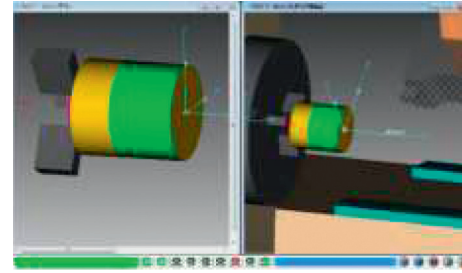


FIGURE 14: Perkins 240 piston skirt equal volume resection rate simulation processing.

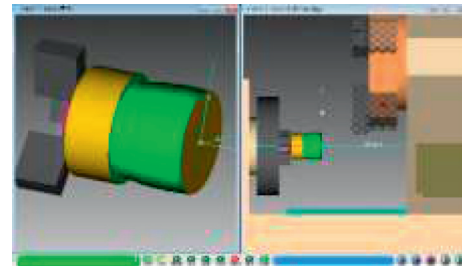


FIGURE 15: Perkins 240 piston skirt ovality magnification 30 times simulation processing.

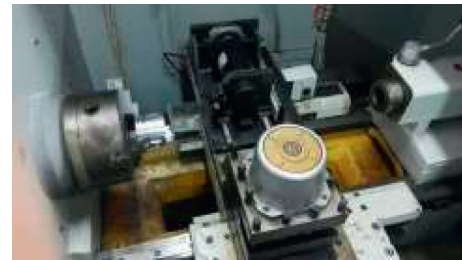


FIGURE 16: The experimental process of the Perkins 240 piston skirt.

The simulation processing of Perkins 240 piston meets the functional verification requirements of the middle-convex and varying ellipse piston machine. The results show that the simulation machining can simulate the actual machining process of the medium-convex elliptical piston machine tool and also verify the volume of the middle-convex and varying ellipse piston skirt.

By the maximum speed 2500 r/min of the workpiece and the feed rate 0.001 mm/r, the equal-volume cutting rate machining test was carried out on Perkins 240 piston based on the middle-convex and varying ellipse piston NC machining test platform. The machining test results show that the simulation can meet the requirements of the actual machining process of the medium-convex elliptical piston machine tool, and the method is feasible. The experimental process is shown in Figure 16.

5. Conclusion

This paper analyzes the forming principle of the oval section profile of the middle-convex and varying ellipse piston skirt.

The middle-convex profile and ellipse profile of the middle-convex and varying ellipse piston are described mathematically, and the NC machining model of turning piston skirt is established. The distribution of the cutting area in the process of the ellipse section is analyzed. The numerical control machining model of equal-volume cutting rate for middle-convex and varying ellipse piston is established, and the machining method of equal volume cutting rate for middle-convex and varying ellipse piston is verified by simulation.

Data Availability

The data used to support the findings of this study are included within the article.

Conflicts of Interest

The authors declare that they have no conflicts of interest regarding the publication of this paper.

Acknowledgments

The authors are grateful for the financial support of the National Natural Science Foundation of China under Grant no. 51805151 and the Key Scientific Research Project of the University of Henan Province of China under Grant no. 21B460004.

References

- [1] A. Li, J. Zhao, Z. Gong et al., "Optimal selection of cutting tool materials based on multi-criteria decision-making methods in machining Al-Si piston alloy," *International Journal of Advanced Manufacturing Technology*, vol. 86, no. 1-4, pp. 1055–1062, 2016.
- [2] S. Jiang, X. Wang, Z. Shi et al., "Study on the high performance linear servo system for middle-convex and varying ellipse piston machining," *Chinese Journal of Mechanical Engineering*, vol. 37, no. 9, pp. 58–61, 2001.
- [3] S. Pan, R. Zhang, M. Cheng et al., "The shaping method of middle convex and varied elliptic pattern with NC turning," *China Mechanical Engineering*, vol. 12, no. 8, pp. 911–914, 2001.
- [4] X. Wang, S. Yong, C. Liu et al., "The analysis for real-time performance and realization of CNC system on middle-convex and varying ellipse piston machining," *Manufacturing Technology and Machine Tool*, no. 3, pp. 15–18, 2004.
- [5] Y. Qin, X. Song, Q. Wang et al., "Research on error control method of noncircular piston turning," *China Mechanical Engineering*, vol. 18, no. 5, pp. 517–519, 2007.
- [6] B. Zhang and T. Zhu, "Research on CNC lathe for middle-convex and varying ellipse piston," *Machine Tool and Hydraulics*, vol. 38, no. 20, pp. 15–17, 2010.
- [7] X. Ma, B. Zhang, and H. Xu, "NC turning processing principle and realization for convex oval piston," *Machine Building and Automation*, vol. 41, no. 5, pp. 63–65, 2012.
- [8] K. Liu, Z. Wang, and G. Gui, "Processing technology of middle-convex and varying ellipse piston turning," *Journal of Hefei University of Technology (Natural Science)*, vol. 35, no. 10, pp. 1316–1319, 2012.
- [9] C. Gong, "The research and development of CNC system for varying ellipse piston lathe," Master Thesis, Huazhong University of Science and Technology, Wuhan, China, 2012.
- [10] X. Tian, "Variable oval convex surface of the piston-type CNC turning technology innovation into research," Master Thesis, Shandong University, Jinan, China, 2014.
- [11] H. Wu, T. Jiang, X. Chang et al., "Optimizing process algorithm and calculating data points of the skirt part of piston that combination of elliptical part and eccentric circular," *Journal of Xiamen University (Natural Science)*, vol. 53, no. 2, pp. 212–216, 2014.
- [12] S. Yun, "Research on the key technology of middle-convex and varying ellipse piston machining," Thesis, Jiangsu University of Science and Technology, Zhen Jiang, China, 2013.
- [13] Y. Zhang, Y. Huang, W. J. Shao et al., "Research on MCVE piston machining and process parameter optimization," *International Journal of Advanced Manufacturing Technology*, vol. 93, no. 9–12, pp. 3955–3966, 2017.
- [14] L. Peng and H. Zhang, *Quick Search Manual for Machining Parameters*, Chemical Industry Press, Beijing, China, 2010.